UiT The Arctic University of Norway

Faculty of Science and Technology, Department of Physics and Technology

Radio wave propagation through the ionosphere

Plasma experiments at the topside ionosphere

Theresa Rexer

A dissertation for the degree of Philosophiae Doctor – September 2021

Radio wave propagation through the Ionosphere

Plasma experiments at the topside ionosphere

Theresa Rexer

A dissertation for the degree of Philosophiae Doctor (PhD)
at UiT The Arctic University of Norway

September 2021

Cover:
Artistic rendition of space physics using radars. Artist: Rosa Leni Fee Fischer

For me.....und für mein Opi Bernd

Highly organized research is guaranteed to produce nothing new.
— Frank Herbert, Dune

Abstract

The non-transient plasma that is closest to Earth is found in the ionosphere at altitudes above approximately 60 km. It is observed either by ground-based, in-situ, or space-borne instrumentation and utilized to study and determine plasma phenomena and dynamics and the near-Earth space. Through active modification experiments, transmitting high-power, high-frequency radio waves into the ionospheric plasma, the interaction between waves and particles in a plasma can be studied in controllable and repeatable experiments.

The transmitted radio wave is usually assumed to propagate either in the left-handed O mode or right-handed X mode. When encountering the respective cutoff or reflection condition in the ionosphere, the incident wave is reflected and does not propagate further into the ionospheric plasma. However, multiple experiments show that transionospheric wave propagation, beyond the reflection altitude and to the topside ionosphere, is possible for certain conditions.

This thesis investigates the conditions and characteristics of transionospheric wave propagation in the polar ionosphere. Multiple experiments conducted at the EISCAT facilities near Tromsø, were performed transmitting an O-mode wave in the magnetic zenith direction. The findings show evidence of the incident wave propagating beyond its cutoff altitude and continuing propagation. Systematically recurring enhancements of the ion line spectra, generated by the modification wave, at the topside ionosphere are presented, as well as electron temperature enhancements consistent with wave propagation to higher altitudes.

Further, a method for determining the electron density to a higher accuracy than previously achieved, has been developed. This permitted the calculation of altitude profiles of the plasma- , upper hybrid- , and multiple cutoff frequencies, enabling the identification of two separate cases of topside ion line enhancements. With this, a gyroharmonic effect at the top- and bottomside ionosphere has been identified for both cases, as well as the characteristics of transionospheric wave propagation. The observations are consistent with wave propagation in the L mode rather than the O mode. This thesis suggests a plausible propagation process and discusses the involved plasma processes. The results firmly establish the possibility of transionospheric wave propagation outside the standard radio window and thus expand our current understanding of wave-particle interaction and wave propagation in a plasma.

Acknowledgments

First, I would like to thank my supervisor, Björn Gustavsson, for his encouragement and help and also the freedom to pursue my own ideas. Maybe most of all, for his patience to try and understand the real questions every time I asked what the radar does and the long discussions that followed. Secondly, I would like to thank my co-supervisor, Thomas Leyser, for his hospitality at IRF in Uppsala, the discussions we had and for sharing his insights and knowledge, and for helping me to gain my own. Also, his proofreading and comments, with frightening attention to detail, have taught me much that I did not realize until I began writing this thesis. A heartfelt thank you to you both.

One of the great things about academia is that there is always someone you can ask or discuss with about the many many questions, confusions, and ideas that arise. So this is a big *thank you* to everybody that has been a part of the many times of wondering, discussing, questioning, and imagining. To Mike Rietveld at EISCAT and Tom Grydeland at NORCE. To Chris Fallen at UAF, who let me come to the magical Fairbanks, Alaska for six months, introducing me to the world of ionospheric modeling and patiently helping me with all the things that moving to a new country and learning new complicated things entails. To all my colleagues in the Space Physics Group at UiT for making work a fun and interesting place to go. To my former colleagues at UiB, Paul, Kalle, Christine, and Jone, that continue to be my good friends. You got me into this. To the co-authors of my publications that I have had the pleasure to work with and to all the people that have helped me in some form with this thesis. Malin, Tinna, Inga, Juha, Unni Pia, Ingrid, Maxime — and many more, too numerous to list. To the EISCAT and space physics community that have been so welcoming, and to the people I was so lucky to meet during the EISCAT summer school and CaNoRock STEP PhD School in 2016. Thank you all.

A special thanks to Derek McKay and Andreas Kvammen, without their company I am not sure this would have been possible. I would like to list all the things you have helped me with during the last few years, like writing bash-scripts, printing double-sided sheets of paper and providing flawless colored lighting, but there is not enough space here and you already know everything. You answered my call for aid with endless proofreading and companionship. Your friendship is the best part of all the PhD-rules, and your support and encouragement has been invaluable. Thank you!

To my family, responsible for both nature and nurture, giving me all the im-

portant things in life a person could ever want or need. Thank you for always supporting me. Thank you for always tolerating me.

Every thesis requires more than just academic support and I am lucky to have good friends who, even though they have seen less and less of me toward the end, have pulled my head out of the deep, dark corners of my office, programming holes and thesis-writing. I am grateful for all the skiing, cabin trips, camping, climbing, dinners, visits, sewing-meetings, dog-watching, fishing, quiz-nights, long phone calls, watching the kids together, for just good coffee-breaks, and so so much more. Thank you for all the adventures and your wonderful company and support.

Lastly, my deepest gratitude goes to Knut Ola, my partner and favorite person. This achievement belongs to you as well.

Theresa Rexer,
Tromsø, 2021

List of publications

This thesis consists of a subject introduction and the following peer-reviewed and published papers. Papers will be referred to by their Roman numerals.

Paper I **Rexer, T.**, Gustavsson, B., Leyser, T., Rietveld, M., Yeoman, T., and Grydeland, T.: First Observations of Recurring HF-Enhanced Topside Ion Line Spectra Near the Fourth Gyroharmonic, Journal of Geophysical Research, Space Physics, 123, 1–15, doi: 10.1029/2018JA025822, 2018a

Paper II **Rexer, T.**, Leyser, T., Gustavsson, B., and Rietveld, M.: Conditions for topside ion line enhancements, Journal of Geophysical Research: Space Physics, doi: 10.1029/2021ja029379, 2021

Paper III Leyser, T. T., Gustavsson, B., **Rexer, T.**, and Rietveld, M. M.: Electron heating by HF pumping of high-latitude ionospheric F-region plasma near magnetic zenith, Annales Geophysicae, 38, 297–307, doi: 10.5194/angeo-38-297-2020, 2020

Invited conference talks

The following invited oral presentations on the topic of this thesis, were given during the PhD program:

- **Rexer, T.**, Gustavsson, B., Leyser, T., Rietveld, M., Yeoman, T., and Grydeland, T.: Observations of systematically recurring topside ion line enhancements during multiple HF modification experiments near multiples of the electron gyro frequency, in: 19th International EISCAT Symposium, p. 4, Invited Speaker, Oulu, Finland, URL `https://www.sgo.fi/Events/EISCAT46AM/prog.php`, 2019
- **Rexer, T.**, Leyser, T., Rietveld, M., Gustavsson, B., and Grydeland, T.: Observations of systematically recurring topside ionline enhancements during HF modification experiments near electron gyroharmonic frequencies, in: 42nd COSPAR Scientific Assembly, vol. 42, pp. C5.1–22–18, Solicited talk, Pasadena, Calif., URL `https://www.cospar-assembly.org/abstractcd/COSPAR-18/`, 2018b

Additional publications

The following peer-reviewed and published papers were completed during the PhD program, but are not included as part of this thesis:

- Kvammen, A., Gustavsson, B., Sergienko, T., Brändström, U., Rietveld, M., **Rexer, T.**, and Vierinen, J.: The 3-D Distribution of Artificial Aurora Induced by HF Radio Waves in the Ionosphere, Journal of Geophysical Research: Space Physics, 124, 2992–3006, doi: 10.1029/2018JA025988, 2019
- Østgaard, N., Reistad, J. P., Tenfjord, P., Laundal, K. M., **Rexer, T.**, Haaland, S. E., Snekvik, K., Hesse, M., Milan, S. E., and Ohma, A.: The asymmetric geospace as displayed during the geomagnetic storm on 17 August 2001, Annales Geophysicae, 36, 1577–1596, doi: 10.5194/angeo-36-1577-2018, 2018

Contents

Chapter 1

Introduction

It is strange to think that $\sim$99.9% of the matter in the universe consists of plasma, when we normally do not frequently encounter it in our everyday life. Distant stars and planetary nebulas consist of plasma, as does our closest star, the Sun. There is plasma in the interplanetary space of our solar system called the solar wind, streaming and expanding radially outward from the Sun. Closer to Earth, there is plasma in the Earth's magnetosphere. Closer still, plasma is found in Earth's upper atmosphere, where ultraviolet radiation from the Sun ionizes the neutral gas in the atmosphere and creates a layer of dense plasma. This is the ionosphere and if one could drive straight up towards space, it would only be a short drive of $\sim$100 km. Studying space, how our Earth is coupled to it and understanding the phenomena and dynamics we observe in the near-Earth space, is thus innately about understanding the phenomena, characteristics and dynamics of plasma.

A plasma is a electrically neutral substance often referred to as the fourth state of matter, although there are distinct differences to the other three states. It contains electrically charged particles, ions and electrons, and strongly interacts with electric and magnetic fields, both internal and external while appearing neutral on a large scale. Each particle is affected by other charged particles simultaneously, and in turn it affects those, resulting in complex collective behavior. A variety of physical phenomena can be observed in a natural plasma, of which the best known is the aurora, visible to the naked eye in the night sky of the polar regions. Plasmas are highly conductive and carry energy, momentum and charge. A characteristic of plasma is that a large number of discreet electrostatic and electromagnetic wave modes can exist in it. The propagation characteristics of a wave can be described by its dispersion relation, giving the relationship between the wave frequency ω and the wavenumber $\mathbf{k}$, and its polarization. An understanding of waves and the interactions between waves and particles can be used to understand the dynamics and behavior of a plasma.

Since plasma consists of a highly ionized gas it requires very high temperature or pressure and consequently it only occurs naturally on the surface of the Earth during sporadic events such as in a lighting strike or in very hot flames.

There are different alternatives to observe and study a plasma. It can be observed *in-situ* in space, using satellites, a plasma can be generated in a plasma laboratory, or one can study the ionospheric plasma, the closest, continuously existing natural plasma to Earth. The ionosphere plays an important role in communication systems, Earth observation and space physics. It can easily be observed through both ground-based and in-situ instrumentation and observations, like radars, radio antennas, imaging, rockets and satellites. One method to actively research the ionospheric plasma is through modification experiments. This is done by transmitting high power, high frequency (HF) radio waves into the ionosphere, modifying its plasma and observing the induced changes with auxiliary instrumentation. By adjusting the parameters of the transmitted wave it is possible to study the wave-plasma interactions through systematic, controlled and repeatable experiments. Since the accidental discovery of this possibility (Tellegen, 1933), a variety of plasma phenomena and effects have been investigated and radio waves have been central in probing and studying natural plasmas in the Earth's atmosphere and the near-Earth space ever since.

This thesis is concerned with a specific phenomenon that can be observed during ionospheric modification experiments, when the transmitted radio wave frequency is lower than the maximum plasma frequency in the ionosphere. Generally, high-frequency modification waves transmitted into the ionosphere in the direction anti-parallel to the Earth's magnetic field, are reflected at the cutoff altitude, which depends on the polarization and frequency of the transmitted wave. Only a few instances of waves propagating beyond this cutoff altitude have be sporadically observed in the past. Here, systematically recurring observations of transionospheric wave propagation are presented. An extensive analysis and discussion of all observations and the conditions and characteristics for this phenomenon are studied in detail. The physical background is explained and a plausible development of the propagation process is established in this thesis and the accompanying papers. These findings are important since a comprehensive understanding of electromagnetic wave-plasma interactions are central in plasma dynamics and thus in understanding the near-Earth space and how Earth is coupled to it. Further, radio wave propagation in ionospheres is essential for communication and navigation systems, both on Earth and increasingly in space based infrastructure as human activity in space and on other planets in our solar system increases.

About this thesis

To discuss transionospheric radio wave propagation in the ionosphere, which is the central topic of this thesis, and to understand the analyses of the experimental results, some background knowledge is required. In the first part of Chapter 2, some fundamentals of space plasma physics are introduced, while the second part briefly describes the connection between the plasmas in the near-Earth space and the Earth's ionosphere, thus establishing our connection to space.

The radar techniques and instrumentation used for the experiments forming the basis of this thesis are described in Chapter 3. In the first part, the discovery and early development of the incoherent scatter radar is given, followed by an introduction of the theory and facilities used. The second part introduces the historical background, the facility used for this thesis and the underlying technique and physics of ionospheric modification experiments. The effects and phenomena specially relevant to the results of this thesis, as well as some of the most recent theoretical and experimental results, are summarized toward the end of this chapter.

Chapter 4 discusses the theory of transionospheric wave propagation in detail. The different, relevant, plasma wave modes and their dispersion relation are shown and their propagation and interaction in a plasma are considered. Different mechanisms proposed for transionospheric radio wave propagation are introduced, focusing particularly on L mode propagation through density striations in the plasma. In the last part of this chapter, past observations and the new observations forming the basis of this thesis are summarized.

A technique for obtaining a high-accuracy estimate of the electron density profile from the plasma line spectra of the incoherent scatter radar measurements is described in Chapter 5. A step-by-step explanation is given and the results are compared to the typical electron density measurements as obtained from the ion line spectra.

Chapter 6 summarizes the findings and key points of the thesis and gives some suggestions for future research and experimental work.

The reader should be aware that the notation in the different chapters varies slightly. The standard notation for the respective fields of research that the different chapters discuss is used, meaning that in Chapter 2 and 4 the angular frequency ω will be used to describe any wave frequency, rather than frequency f which is used in Chapter 3 and 5. However, ω and f are easily related by $\omega = 2\pi f$, and any subscripts or definitions given in one notation are valid also for the other.

Chapter 2

Plasma and space physics

The fundamental connection between plasma physics and space research was gradually recognized as studies from separate branches merged to form what is now known as space plasma physics.

Before the era of spaceflight, with rockets and satellites making in-situ measurements in space, observations were limited to ground-based measurements. Some of the earliest studies that can be categorized as scientific came with the invention of the compass. In the 16th and 17th century the Earth's magnetic field was first described and it was discovered to be variable and dynamic. The term ”Magnetische Ungewitter”, or ”magnetic storms”, describing periods of large, prolonged disturbances to the Earth's magnetic field, and variations of which are still in use today, was identified and named by Alexander von Humboldt (1808). In 1839, Carl Friedrich Gauss showed that a part of the magnetic disturbance was not intrinsic to the Earth, but originated from the upper atmosphere (Gauss, 1839). A few years later the relation between the solar sunspot cycle and solar flares and an increase in magnetic disturbance was discovered by Carrington (1859).

During this period the aurora borealis, or northern lights, were studied in parallel, as an entirely separate field of research. In 1741 Olof Hjorter and Anders Celsius discovered that strong auroral displays are connected to strong magnetic disturbances and thus the two fields of research merged (Collinder, 1970; Prölss, 2004). The connection between the auroral events and charged particles originating from solar flares at the Sun was first suggested by Birkeland (1908). Birkeland proposed that a horizontal current system in the upper atmosphere is related to the aurora and that this is coupled to currents along the magnetic field of the Earth, allowing for charged particles to reach the atmosphere.

The existence of the ionosphere, a conducting layer in the atmosphere, consisting of an ionized gas, was suggested by Kennelly (1902) and Heaviside (1902) following the first ever transatlantic radio transmission by Marconi (1901). This was experimentally confirmed by Appleton and Barnett (1925) and Breit and Tuve (1926). Correlations between the magnetic storms and

variations in the ionosphere were soon made. Thus, studies of the upper atmosphere and ionosphere were firmly coupled to research of the near-Earth space and the Sun, and the importance of charged particles in this system was established. The extent of this importance became especially clear when Biermann (1951) proposed that the interplanetary space is not a vacuum with intermittently emitted streams of charged particles from the Sun, but rather that a continuous plasma flow is streaming outward from it, in all directions at supersonic speed.

The physics of the Sun, Earth's magnetosphere and ionosphere, their coupling and the role of plasma in this system, have since been studied extensively, both through ground based observations and in-situ with the advent of the space flight era. This branch in geophysics is termed space plasma physics and knowledge of plasma physics is necessary to understand phenomena and dynamics of the near-Earth space.

In the first part of this chapter, the basics of space plasma physics are introduced. The second part of this chapter introduces the plasma flow in the near-Earth space system briefly before focusing on the Earth's upper polar ionosphere, where the research in this thesis is focused. Multiple comprehensive books have been written on these subjects, including thorough introductions and derivations of the concepts only mentioned here. Some worth mentioning are Baumjohann and Treumann (2012), Chen (1983), Bittencourt (2013) and Prölss (2004). The basic principles and concepts outlined in this chapter can be found in any one of these and so no further explicit citations will be given in this chapter, unless necessary for some specific content.

2.1 Basic space plasma physics

The basic concepts of space plasma physics that are important to this thesis are outlined in this section. The definition of a plasma is given and its fundamental properties are outlined. The motion of plasma under the influence of electric and magnetic fields is described briefly and plasma waves are introduced, establishing the background for later chapters and the topic of this thesis.

Plasma properties

A plasma is a gas consisting of charged particles. However, a small degree of ionization may exist in any gas so to be considered a plasma it should also be quasi-neutral and display collective behavior. The meaning of this is explained as follows. A plasma is quasi-neutral or macroscopically neutral when it consists of approximately an equal number of positive and negative charges. Local deviations from this charge neutrality can occur. These are usually small in amplitude and short-lived since a charge imbalance will generate electric fields in the plasma, that act to restore the charge neutrality. Particles in a plasma are "free", meaning that the average potential energy of one particle, due to its

nearest neighbor, is much smaller than its random kinetic energy, $\mathbf{E}_{kin} > \mathbf{E}_{\phi}$. In a collisionless plasma, the long-range, macroscopic Coulomb forces thus dominate over the Coulomb forces between neighbors. The result is that a plasma moves collectively. Since the kinetic energy (thermal energy) of the particles is large enough to overcome the electrostatic forces to their neighbors, a plasma is typically hot and as the ionization of atoms and molecules happens at varying temperatures[1], at approximately a few thousand Kelvin, it is often called ”the fourth state of matter”.

Debye shielding

The distance at which the random kinetic energy of a particle and its electrostatic energy due to neighboring particles are equal, is called the *Debye length*. Thus, it is a measure of the sphere of influence of electrostatic potential around a given particle. It is given by:

$$\lambda_D = \left(\frac{\epsilon_0 k_B T_e}{n_e q^2} \right)^2 \tag{2.1}$$

where T_e is the electron temperature, k_B is the Boltzman constant, q is the particle charge, n_e is the electron density of the plasma and ϵ_0 is the free space permittivity. This means that if a positive test charge q, like an ion, is inserted into a quasi-neutral plasma, its electrostatic potential will be counterbalanced by the electrons in the plasma, that are temporarily in the vicinity of the charge, forming a shielding cloud around it. This collective behavior of the particles maintains the charge neutrality and the plasma appears electrically neutral at distances greater than λ_D.

The collective behavior leads to two necessary requirements for a plasma. Firstly, the characteristic dimensions of the plasma system, L, must be large compared to the Debye length, $L \gg \lambda_D$. This is known as the first plasma criterion. Secondly, there must be enough particles in the Debye sphere to efficiently shield the electrostatic potential. The number of particles in a Debye sphere is $N_D = \frac{4\pi}{3} n_e \lambda_D^3$ and accordingly the second plasma criterion is given by $n_e \lambda_D^3 \gg 1$.

In partially ionized plasmas like that of the ionosphere, a third criterion arises. The average time between collisions of electrons and neutrals, τ_n, must be

[1]The temperature of the plasma can be somewhat counter intuitive in itself. As the charged particles in the plasma are collisionless, that is elastic collisions between electrons and ions are almost perfectly energy conserving due to their great difference in mass, ions and electrons can have different temperatures. That is, a plasma may have multiple temperatures. Further, since charged particles are affected by magnetic fields, a plasma species can have different temperatures in different directions to **B**. Additionally, as the density of a typical plasma is very low and has a very low heat capacity, it may have a temperature of many thousand Kelvin, but contain relatively little energy or ”does not feel hot”. This is one of the reasons for why the ionospheric heating experiments, introduced in Chapter 3.2, are slightly misnamed.

much larger than the reciprocal of the typical plasma oscillation frequency, ω_P (see Equation 2.8). This means that if the motion of the charged particles in a weakly-ionized gas is controlled by hydrodynamic forces and the collisions, rather than the electromagnetic forces, it is not a plasma. This is quantified by the requirement that $\omega_P \tau_n \gg 1$.

Plasma motion

The motion of a plasma is influenced by forces from electric and magnetic fields, **E** and **B**. While the dynamics of each charged particle are dominated by forces from electric and magnetic fields, they are simultaneously also a source of electric and magnetic fields. The relation between charged particles and fields, and the spatiotemporal variations of the coupling between the electromagnetic fields, are given by Maxwell's equations:

$$\begin{aligned} \nabla \times \mathbf{B} &= \mu_0 \mathbf{j} + \epsilon_0 \mu_0 \frac{\partial \mathbf{E}}{\partial t} \\ \nabla \times \mathbf{E} &= -\frac{\partial \mathbf{B}}{\partial t} \\ \nabla \cdot \mathbf{B} &= 0 \\ \nabla \cdot \mathbf{E} &= \frac{\rho}{\epsilon_0} \end{aligned} \tag{2.2}$$

where **j** is the electric current density, ϵ_0 and μ_0 are the vacuum permittivity and susceptibility, respectively, and ρ is the electric space charge density. By introducing a linear wave disturbance and determining solutions of Maxwell's equations, one can find expressions for a general plasma wave equation and its dispersion relation.

Single particle motion

Describing the motion of a plasma can be done through several different approaches depending on the state of the plasma. In very low density plasmas with prescribed, strong **E** and **B** fields, only the motion of the individual particles needs to be considered. This microscopic approach gives some insight to the dynamic processes in a plasma. It does not describe the collective behavior of the plasma, but some components of microscopic single particle motion contributes to important macroscopic effects in the collective plasma behavior. One example that is specially relevant for the this thesis is the gyro motion of particles.

The equation of motion for a charged particle q can be written as

$$m \frac{d\mathbf{v}}{dt} = q(\mathbf{E} + \mathbf{v} \times \mathbf{B}) \tag{2.3}$$

where m is the particle mass and **v** is its velocity. Assuming a uniform magnetic field $\mathbf{B} = B\hat{\mathbf{z}}$ and $\mathbf{E} = 0$, one can solve for the particle motion in the x, y-plane. The velocity components are

$$\begin{aligned} \ddot{v}_x &= -\omega_G^2 v_x \\ \ddot{v}_x &= -\omega_G^2 v_y \end{aligned} \tag{2.4}$$

where ω_G is the gyro frequency or cyclotron frequency.

$$\omega_G = \frac{qB}{m} \tag{2.5}$$

These equations describe the circular motion of the particles around the magnetic field with the direction of the motion dependent on the sign of the charge. The electrons gyrate right-handedly while the ions gyrate left-handedly. Both the gyro frequency and the gyro radius, given by $r = mv/|q|B$, depend on the particle mass and charge, and therefore the gyro motion for electrons and ions differs. The electron gyro frequency is important for high frequency wave propagation in magnetized plasma. Because the direction of gyration is opposite for electrons and ions it affects waves of different polarization differently, as will be discussed in the next section and in Chapter 4. Somewhat surprisingly, it also shows to be relevant for the observations presented in Paper I and II.

Collective motion of a plasma

When considering a plasma with a large number of particles and varying **E** and **B** fields, the single particle approach is not efficient. If the individual particles are neglected and only their distribution function is considered, one can use a statistical approach using kinetic theory to describe macroscopic plasma phenomena and calculate the average motion of a large number of particles. This can be further approximated if one does not need to know the evolution of the distribution functions, but is only interested in the spatiotemporal change of the macroscopic plasma parameters like density, velocity and temperatures. The plasma can then be treated as a fluid and equations for electrically conducting fluids can be found. For a plasma containing different particle species, or more precisely, if the species in a plasma have different distribution functions (in equilibrium), the multi-fluid theory equations are as follows.

The continuity equation of species s in the plasma is given by

$$\frac{\partial n_s}{\partial t} + \nabla \cdot (n_s \mathbf{v}_s) = 0 \tag{2.6}$$

where n_s is the number density and the subscript s indicates the species. The physical interpretation of this equation is that, if no particles are added or re-

moved from the species through some interaction process, the number density, mass and the charge density are conserved.

The equation of motion or momentum equation of the plasma is given by

$$\frac{\partial n_s \mathbf{v}_s}{\partial t} + \nabla \cdot (n_s \mathbf{v}_s \mathbf{v}_s) + \frac{1}{m_s} \nabla \cdot \mathbf{P}_s - \frac{q_s}{m_s} n_s (\mathbf{E} + \mathbf{v}_s \times \mathbf{B}) = 0 \tag{2.7}$$

where $\mathbf{P}_s$ and m_s are the fluid pressure tensor and the mass of the species, respectively. This equation relates the fluid velocity to the density and the electromagnetic forces acting on a given fluid element. In fact, one can recognize this equation as the Navier-Stokes equation from conventional hydrodynamics, but additionally including the Lorenz force $(\mathbf{E} + \mathbf{v}_s \times \mathbf{B})$. The Lorenz force relates the plasma fluid to the full set of electromagnetic equations acting on the fluid. Its appearance also couples all fluid components together as the **E** and **B** fields act on all components, while simultaneously all components contribute to **E** and **B**.

These two equations contain three unknowns, n_s, $\mathbf{v}_s$ and $\mathbf{P}_s$. To solve these one can either derive the Energy equation, the next higher order moment of the fluid equations for a plasma introduced above, introducing yet another unknown, or one can obtain a closed system of macroscopic transport equations by making assumptions about one of the unknown variables[2]. The simplest assumption is that of an *equation of state* for the fluid pressure tensor, implying that the plasma is in thermodynamic equilibrium and the thermal fluctuations of the particles can be neglected. This is called the *cold plasma approximation* and the specific form of the equation of state depends on the assumptions made about a given plasma species. The equation of state relates the pressure and density of a plasma species, depending on if the plasma evolves, for example, isothermally, adiabatically or anisotropically. In that case the pressure tensor $\mathbf{P}_s$ in Equation 2.7 degenerates to the scalar pressure p_s and the appropriate equation for it, and together with Equation 2.6 this forms a closed system of equations for the macroscopic transport of a plasma species.

Waves in plasma

Waves and periodic effects play an important role in plasma physics and a variety of wave phenomena exist. A minimum amount of fluctuations always exist in a plasma in thermal equilibrium, and the amount of fluctuations depends on the temperatures of the plasma. When the plasma is disturbed by some external force, the energy of the disturbance will propagate through the plasma in the form of waves superposed on the thermal fluctuations. As for pressure waves in neutral gas, the restoring force is the change in pressure from density disturbances. In addition the restoring force in plasma waves may include the electric and magnetic forces. Plasma waves can be generated at a large

[2]Depending on the level of detail needed, the system of equations may be truncated at any next, higher order equation by making some appropriate assumptions.

range of frequencies from several millihertz to tens of kilohertz. However, they do not occur continuously. There are a finite number of wave modes that can propagate in a plasma. These are found by solving the plasma fluid and Maxwell equations introduced above, for small fluctuations and perturbations in a plasma. In this section the fundamental electrostatic and electromagnetic wave modes relevant to this thesis are introduced.

Electrostatic waves

There are two electrostatic waves that can propagate in a plasma that are specially important for the topic of this thesis. The first are internal plasma oscillations that are a specific property of the plasma. Considering a quasi-neutral plasma that is slightly disturbed, either by external forces or simply by fluctuations in the particle density distribution, the electrons will accelerate to restore charge neutrality. Due to their inertia, they will overshoot their original position however. The result is a high frequency oscillation around the heavier ions, which can be treated as stationary at these high frequencies. This characteristic oscillation is know as the plasma frequency and is given by

$$\omega_P = \sqrt{\frac{n_e q^2}{m_e \epsilon_0}} \tag{2.8}$$

These plasma oscillations will propagate in the plasma due to their initial thermal motion. The resulting waves are high frequency, electrostatic Langmuir waves. Their dispersion relation, found by linearizing the solution of the fluid and Maxwells equations for a small perturbation and solving for ω is

$$\omega^2 = \omega_P^2 + \frac{3}{2} k^2 v_{the}^2 \tag{2.9}$$

where k is the wavenumber and v_{the} is the electron thermal velocity $v_{the} = \sqrt{\frac{2k_B T_e}{m_e}}$.

The second fundamental electrostatic wave is the ion-acoustic wave. The dispersion relation for the ion acoustic waves is found in the same way as before, but including the motion of the ions. It is given by

$$\omega^2 = \frac{k^2 c_{ia}^2}{1 + \gamma_e k^2 \lambda_D^2} \tag{2.10}$$

where γ_e is the specific heat index. The ion-acoustic wave speed c_{ia}, is given by

$$c_{ia} = \sqrt{\frac{\gamma_e k_B T_e}{m_i}} \tag{2.11}$$

For small k, or long wavelengths, this becomes a linear expression

$$\omega^2 \simeq k^2 c_{ia}^2 \tag{2.12}$$

which is analogous to sound waves in a gas consisting of pure density fluctuations. For very short wavelengths approaching the Debye length, the character of the sound wave is lost and the wave frequency approaches that of the ion plasma frequency

$$\omega_I = \sqrt{\frac{n_i q^2}{m_i \epsilon_0}} \tag{2.13}$$

Electromagnetic waves

A large, finite number of electromagnetic waves can propagate in a plasma. The interactions between the wave perturbation and the ambient fields is more complex for electromagnetic waves and the dispersion relations of the possible wave modes depend on the direction of propagation relative to the ambient magnetic field, $\mathbf{B}_0$. The direction of wave propagation is given by the wave vector $\mathbf{k} = k\hat{k}$, where k is the wavenumber as before. Here, the limiting cases of perpendicular propagation, $\mathbf{k} \perp \mathbf{B}_0$, and parallel propagation, $\mathbf{k} \parallel \mathbf{B}_0$, for the relevant wave modes in this thesis are given, while propagation at arbitrary angles and changes in the direction of propagation are discussed in detail in Chapter 4.

There are two important electromagnetic wave modes that propagate perpendicular to the magnetic field, $\mathbf{k} \perp \mathbf{B}_0$. The first is known as the ordinary or O-mode wave, where the wave electric field, $\mathbf{E}_1$, is parallel to $\mathbf{B}_0$. Its dispersion relation is given by

$$\omega^2 = \omega_P^2 + c^2 k^2 \tag{2.14}$$

where c is the speed of light. It has the same dispersion relation as an electromagnetic wave in an unmagnetized plasma and, thus propagates as if it is not affected by the ambient magnetic field. When this wave is propagating in a vacuum rather than a plasma ($\omega_P \to 0$) it is the usual free space electromagnetic wave. The O-mode wave is linearly polarized as $\mathbf{E}_1$ is always parallel to $\mathbf{B}_0$.

The second electromagnetic wave where $\mathbf{k} \perp \mathbf{B}_0$ is the extraordinary or X-mode wave. Here, $\mathbf{E}_1$ is not parallel to $\mathbf{B}_0$, but lies in the plane perpendicular to $\mathbf{B}_0$. Its dispersion relation is given by

$$\frac{c^2 k^2}{\omega^2} = 1 - \frac{\omega_P^2}{\omega^2} \frac{\omega^2 - \omega_P^2}{\omega^2 - \omega_{UH}} \tag{2.15}$$

where

$$\omega_{UH}^2 = \omega_G^2 + \omega_P^2 \tag{2.16}$$

is the upper hybrid frequency. This wave is partly transverse and partly longitudinal. The X-mode wave has two separate branches, sometimes referred to as the ”slow” and the ”fast” X mode. In Chapter 4 it will be shown that the fast X mode is generally in a right-handed (RH) polarization, while the slow X mode is generally in a left-handed (LH) polarization. In the rest of this thesis, the terms RH X mode and LH X mode will be used interchangeably with the terms ”fast” X mode and ”slow” X mode, respectively, for the two branches.

For waves propagating parallel to the magnetic field, $\mathbf{k} \parallel \mathbf{B}_0$, there are three important wave modes. As for perpendicular wave propagation, the first wave mode is that where $\mathbf{E}_1 \parallel \mathbf{B}_0$. This wave is the same as the electrostatic wave of the plasma oscillations in a cold plasma, with the dispersion relation given by $\omega^2 = \omega_P^2$ (see Equation 2.9).

The second and third important wave modes are the two possible solutions to the dispersion relation where $\mathbf{E}_1 \perp \mathbf{B}_0$.

These are the R-mode wave given by

$$\frac{c^2k^2}{\omega^2} = 1 - \frac{\omega_P^2/\omega^2}{1 - (\omega_G/\omega)} \tag{2.17}$$

and the L-mode wave given by

$$\frac{c^2k^2}{\omega^2} = 1 - \frac{\omega_P^2/\omega^2}{1 + (\omega_G/\omega)} \tag{2.18}$$

Both wave modes are circularly polarized with ”R” and ”L” indicating a right-hand and left-hand circular polarization, respectively.

Plasma wave cutoffs and resonances

As a wave propagates through a plasma, its wavelength, direction and amplitude may change depending on changes in the plasma density and electron gyro frequency. If the wave approaches a region in the plasma where the cutoff frequency is close to the wave frequency, the wave can not propagate beyond this point and is generally reflected here. A *cutoff* is encountered at the frequency at which $k \to 0$ and $\lambda \to \infty$. Similarly, a wave experiences a *resonance* when $k \to \infty$ and $\lambda \to 0$, and here the wave energy is generally absorbed.

The O-mode wave has a cutoff when

$$\omega = \omega_P \tag{2.19}$$

The RH X-mode branch of the perpendicular propagating wave and the R-mode wave both have a cutoff when

$$\omega_{R-cut} = \frac{1}{2}(\omega_G + \sqrt{\omega_G^2 + 4\omega_P^2}) \tag{2.20}$$

while the LH X-mode branch of the perpendicular propagating wave and the L-mode wave both have a cutoff when

$$\omega_{L-cut} = \frac{1}{2}(-\omega_G + \sqrt{\omega_G^2 + 4\omega_P^2}) \tag{2.21}$$

The LH X-mode wave has a resonance when $\omega = \omega_{UH}$.

The dispersion curves for all wave modes mentioned in the above are indicated in Figure 4.1 in Chapter 4. The most relevant wave modes have only been briefly introduced here. They are further discussed in detail in Chapter 4, and the significance of their polarization, the cutoff frequencies and their impact on wave propagation in a plasma is the topic of that Chapter.

2.2 Plasma in the near-Earth space

In near-Earth space, comprising the inner solar system, including the Sun, the solar wind, Earth's magnetosphere and ionosphere, plasma is the dominant state of matter. The plasmas' density and temperature varies by many orders of magnitude in the different regions. How they are coupled, the dynamics of the interaction between the different populations and the different environments and where they exist, form the fundamental questions of space research. In this section the geophysical background is presented to define the relevant parameters and concepts for this thesis. The coupling of the Sun, solar wind and Earth's magnetosphere is briefly introduced before focusing on the upper polar ionosphere, where the phenomena central to this thesis occur. For a comprehensive introduction to the concepts and phenomena mentioned here some alternatives include (but are not limited to) the books by Baumjohann and Treumann (2012); Kelley (2009); Russell et al. (2016); Spohn et al. (2014) and Prölss (2004).

The Sun, solar wind and Earth's magnetosphere

The Sun, located approximately 1.496×10^8 km from Earth at the center of our solar system, with a core estimated to have a temperature around 15×10^6 K, plays a central role in all aspects of space physics. Electromagnetic radiation is constantly emitted from the Sun in a broad range of wavelengths. Additionally, a continuous stream of hot plasma, called the solar wind, is emitted from the Sun's corona, its upper atmosphere, consisting of a fully ionized hydrogen and helium plasma. The solar wind is highly variable in space and time with an average speed of $\sim$500 km/s, although it may vary from 300 km/s up to 800 km/s during events of increased solar activity (Russell et al., 2016). As the highly conductive plasma expands outward continuously, the temperature and density decrease. At the distance of Earth the typical density and temperature of the solar wind is approximately $n_e = 8.7\,\mathrm{cm}^{-3}$ and $T_e = 1.4 \times 10^5$ K, respectively. The magnetic field of the Sun is "frozen in" to the particle stream and drawn outward, extending the magnetic field originating at the Sun and forming the interplanetary magnetic field (IMF). The Sun, and thus its entire magnetic field, rotates with a period of 27 days, switching polarity with the 11 year solar cycle. The general direction of the IMF is toward and away from the Sun, above and below the heliospheric current sheet (HCS) indicated by the green line in Figure 2.1, where a schematic of the solar magnetic field is shown. Close to Earth the IMF alternates depending on whether it is above or below the current sheet. As the Sun's magnetic field changes in polarity, and the solar radiation changes as well as the ejection of plasma particles and number and size of sunspots, the IMF also varies significantly.

The Earth's magnetic field is generated by processes in its interior and to a first order it can be approximated by a dipole field. The dipole axis is tilted relative to the Earth's rotational axis by $\sim 10^\circ$ and currently the magnetic pole in the northern hemisphere is located toward Russia. This dipole field is im-

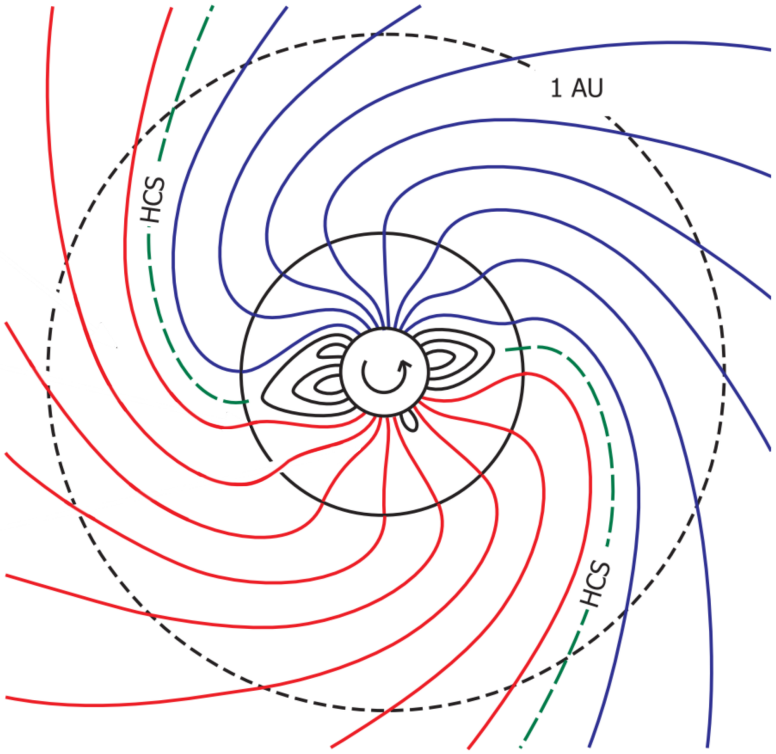

Figure 2.1: The shape and structure of the steady-state solar magnetic field. Regions of opposite magnetic polarity are indicated by red and blue lines. These are separated by the heliospheric current sheet indicated by the green lines. The Earth's orbit around the Sun, at a distance of 1 AU, is also indicated. Figure adapted from (Owens and Forsyth, 2013, Fig. 1).

mersed in the solar wind flow, forming a cavity in the IMF, and as a result the shape of the magnetosphere is greatly affected. A sketch of the cross section of the magnetosphere is shown in Figure 2.2. The pressure from the solar wind compresses the magnetosphere on the dayside and stretches it out several hundred Earth radii on the nightside. The distortion of the magnetic field is associated with large-scale electric currents in the magnetosphere, transporting mass, charge, momentum and energy. Generally these currents can be classified into two groups, magnetic field aligned currents and currents perpendicular to the magnetic field. The magnetic field aligned currents connect the magnetospheric currents to the ionospheric currents. These can be enhanced and additional currents can be induced in the polar regions during different dynamic solar wind and IMF conditions, allowing plasma in the magnetosphere to precipitate into the ionosphere. The plasma inside the magnetosphere consists mostly of electrons and protons, distributed in regions with varying densities and energy distributions.

For certain configurations of the IMF, the solar wind can couple to the Earth's magnetic field and plasma populations originating from the Sun can enter the magnetosphere. Kristian Birkeland was the first to suggest that the visible phenomena known as aurora in the polar regions, were coupled to particles

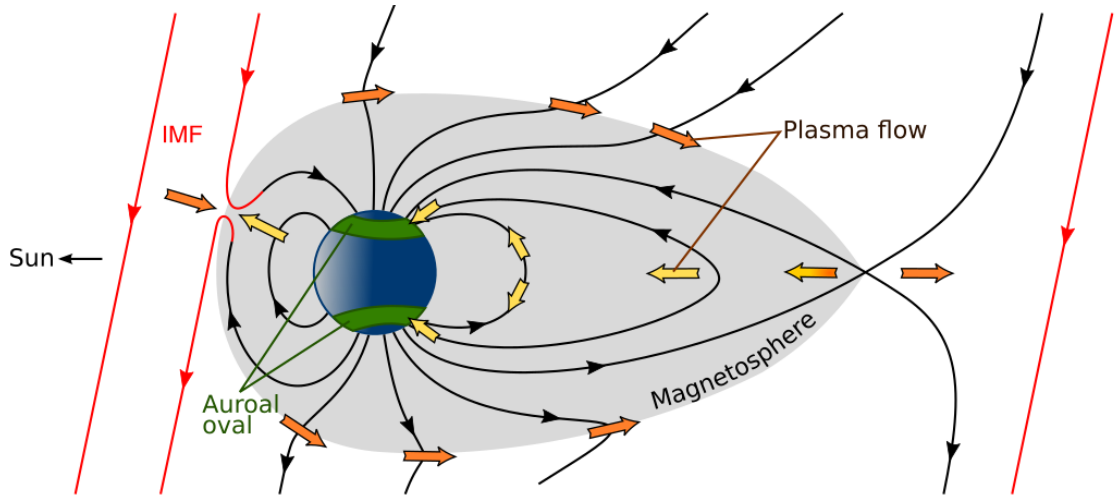

Figure 2.2: Conceptual schematic of the Earth's magnetosphere and the magnetospheric convection and reconnection transporting plasma from the solar wind into the Earth's magnetosphere, effectively connecting the solar wind to the Earth's ionosphere. Orange and yellow arrows indicate the solar wind plasma and magnetospheric plasma convection, respectively. The auroral zones in the northern and southern hemisphere, where the plasma may be accelerated into the ionosphere and generate the aurora, are indicated in green. [Not to scale]

originating from the Sun. The dominant parameter coupling the two is the direction of the IMF. When and where the IMF is approximately antiparallel to the Earth's magnetic field, the two separated magnetic fields can couple through a process called *magnetic reconnection* and change the topology of the magnetic fields. This is illustrated in Figure 2.2 where the Earth's magnetic field is indicated in black while the IMF is shown in red. When the magnetic field of the IMF and the closed magnetic field of the Earth reconnect and merge at the dayside, the Earth's magnetic field is essentially open to the solar wind. The plasma transported in the IMF from the Sun can thus penetrate into the magnetosphere along the newly connected magnetospheric field here. In Figure 2.2 the plasma flow is indicated by the orange and yellow arrows. Due to the momentum of the solar wind the plasma and thus magnetic field is transported toward the nightside and it is this process that forms the tail of the magnetosphere. In the tail, magnetic reconnection can occur again, as additional energy and magnetic flux is added to the magnetotail. The plasma flow splits and the magnetic field of Earth and the IMF will close. The magnetic tension in the stretched and newly closed field will relax and transport the frozen in plasma with it, toward Earth. This conceptual picture of the magnetic and plasma convection is known as the Dungey cycle, after Dungey (1961), and it effectively connects the IMF to the Earth's magnetosphere and ionosphere.

On Earth, the region of open field lines in the northern and southern hemispheres are known as polar cap regions. In Figure 2.2, this is the region poleward of the auroral ovals. The auroral oval is the region where the solar wind plasma that has entered the magnetosphere, becomes energized and

can enter the ionoshpere and excite the aurora. It is an oval shaped region, somewhat compressed on the dayside and streched out on the nightside ionosphere. The term polar ionosphere commonly refers to the auroral oval and polar cap regions. All EISCAT radars (see Chapter 3.1) are located under the polar ionosphere, ideal for studies of its dynamics and processes.

The polar ionosphere

The ionosphere is the ionized component of the upper atmosphere and thus the transition region between the fully ionized plasma in the magnetosphere and the neutral atmosphere. It is not a sharp boundary but a stratified layer with different plasma densities, ion compositions, temperatures and degrees of ionization. It enables the flow of electric currents, thus leading to magnetic field perturbations and electrodynamic heating effects, and it modifies the propagation characteristics of electromagnetic waves. It is formed by ionization of the neutral atmosphere and can stretch from $\sim$60 km to above 1000 km, depending on the variations in solar radiation, magnetospheric conditions and the recombination of charged particles.

Formation

There are two main processes that ionize the neutral atmosphere. The dominant process is photoionization by solar ultraviolet (UV), extreme ultraviolet (EUV) and X-ray radiation. Incident photons, with higher energies than the ionization energy of the atmospheric atoms and molecules, are absorbed by the neutral gases, producing electron-ion pairs. Because of this absorption, the photons are lost with increasing depth (decreasing altitude). Additionally, the neutral density increases with decreasing altitude. As a result, there is a peak of ionization depending greatly on both the energy spectrum of the incident radiation and the altitude variations of the constituents of the neutral atmosphere. The solar radiation varies with the day-night, seasonal and solar cycle, while the atmospheric constituents vary primarily with altitude.

The second prominent ionization process is the impact of precipitating particles. As briefly introduced in the previous section, plasma particles from the solar wind can enter the magnetosphere. Plasma particles with a range of energies precipitate along the magnetic field and into the upper atmosphere in the auroral oval and polar cap. The ionization from these is mainly due to collisions. A given incident particle will loose energy for every electron-ion pair it creates through collisions. Thus, higher energy particles can produce more ionization and penetrate deeper into the atmosphere and cause ionization at lower altitudes. Precipitating particles not only add charged particles to the upper atmosphere and cause ionization, but are also responsible for the aurora. As the precipitating particles collide with neutrals in the atmosphere a fraction of the particles are excited. When the excited particles return to their ground energy state the excess energy is released as radiation at discreet, vis-

ible, UV and infrared wavelengths, depending on the type of the excited atom or molecule.

The ionization of the upper atmosphere would continue until it is fully ionized if it were not counteracted. There are two main processes that limit the ionization and hence an equilibrium exists and large daily, seasonal and solar cycle variations are observed. The first is recombination of electrons and molecular ions producing neutral atoms. At F region altitudes the recombination is a two stage process, where O^+ charge exchanges with O_2, producing O_2^+ molecular ions, and then rapidly recombines with electrons, resulting in 2 O atoms. The second is attachment of electrons to atoms to form negative ions. Recombination of electrons and molecular ions is proportional to the square of the electron density, while attachment of electrons to atoms is a linear process proportional to the number of available electrons to attach to neutral particles. At high altitudes the reattachment process dominates, while lower in the ionosphere the recombination of electron-molecular ion pairs is the dominant process.

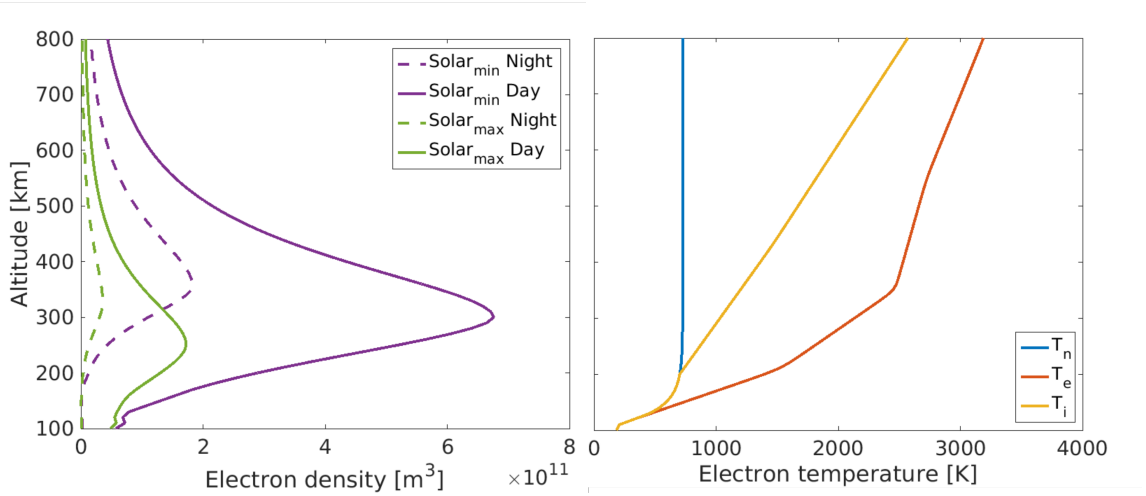

Figure 2.3: Typical altitude profiles for the electron density (left) and temperature (right) during spring. The electron densities are shown for one solar maximum (green) and one solar minimum (purple) year. Temperature variations are not as pronounced as density variations, so only one set of typical daytime values is shown. Values are calculated for the high latitude ionosphere over Tromsø, Norway, using the International Reference Ionosphere model (IRI).

Density, temperature and composition

The processes in the magnetosphere, the solar radiation and particle precipitation and recombination all contribute to the density and temperature variations in the ionosphere. Figure 2.3 shows typical spring values for the electron density (left panel) during daytime and nighttime for Solar maximum and Solar minimum years, and the altitude profile of the atmospheric temperatures (right panel) in the ionosphere above Tromsø, Norway. These variations are largely predictable as solar radiation is the dominant ionization process.

The ion composition varies with altitude and is largely determined by the composition of the neutral atmosphere. Naturally, heavier molecular ions are found at lower altitudes while lighter atomic ions are found at higher altitudes. The varying electron density and ion composition results in a layered structure in the ionosphere. These layers do not have defined sharp boundaries and are commonly referred to as ionospheric regions. The D-region is the lowest layer and it is highly variable due to the large number of different species and high density in this region. The dominating ion species here are NO^+ and O_2^+ and the region can extend from as low as $\sim$60 km to $\sim$90 km. The E-region extends from $\sim$90 km to $\sim$160 km and is also mainly composed of NO^+ and O_2^+. Ionization in these two regions is mainly from solar X-rays, UV radiation and high energy particle precipitation in the high latitude regions. As solar radiation is the dominating factor it commonly disappears at night if there is no particle precipitation to sustain it.

The F region is the region of the ionosphere that contains the bulk of the electron density. It stretches from $\sim$160 km to 500-600 km. The main ion species here is O^+ resulting from photo-ionization of O. During daytime at mid and low latitudes, the F-region is commonly split in two parts, the F1 and F2 regions. At high latitudes the lower F1 region is only observed occasionally. The electron density peak is found in the F-region and the related plasma frequency peak is commonly denoted f_{OF2} regardless of the existence of an F1 region. The F-region weakens during nighttime but does not disappear completely. Recombination in this region is less efficient than at lower altitudes and plasma convection from the dayside to the nightside ionosphere, associated with the magnetospheric convection introduced previously, is significant. The research discussed and presented in this thesis is from this region in the ionosphere.

Chapter 3

Ionospheric modification experiments

Shortly after the discovery of the ionosphere, Breit and Tuve (1925) developed the first version of an ionosonde to study it. An ionosonde is a radar consisting of an antenna and a nearby receiver. The transmitted frequency is swept from typically 1 to 20 MHz, in short radio wave pulses. Radio waves are reflected in the ionosphere at an altitude where the transmitted frequency is equal to the ionospheric plasma frequency. From the time delay of the reflected signal when it reaches the receiver, the altitude of the reflection layer for the range of frequencies that were transmitted can be calculated. Since the plasma frequency is proportional to the square root of the electron density (see Equation 2.8), it is possible to estimate an altitude profile for the electron density from the ionosonde measurements. In early studies, this was used to investigate the ionosphere itself and the effect of charged particles in a magnetic field on radio wave propagation. Variations of the electron density with local time, latitude, solar cycle and season were discovered and theories for the formation and loss of the plasma were developed.

Advances in ionospheric and space physics were made during the Space Race between the Soviet Union and the USA. During this time instrumentation for in-situ measurements, like balloons, rockets and satellites, was developed in parallel to the continued study of plasma, magnetospheric and atmospheric physics. A breakthrough came with the development of the incoherent scatter technique by Gordon (1958) and the following pioneering experiment by Bowles (1958) proving the concept. For the first time, studies of multiple ionospheric parameters at altitudes otherwise inaccessible were possible. There are numerous active incoherent scatter (IS) radars in world and they are an essential element in space physics research.

The possibility to modify the ionosphere through active experiments was discovered by accident, when the radio program of the powerful Luxembourg radio station could be heard by a receiver tuned to the frequency of the Beomünster station in Switzerland (Tellegen, 1933). The first intentional modification experiments were conducted in the Soviet Union. However, these were highly

classified until 1973, and although the possibility was discovered much earlier, the first open modification experiments were done in Platteville, Colorado in 1970 (Streltsov et al., 2018). In these experiments a high frequency (HF) radio wave is transmitted into the ionosphere by a high power radar. The radio waves affect and are affected by the plasma and a wealth of linear and non-linear processes occur and can be studied. These experiments are commonly referred to as "heating experiments" as HF waves can enhance the ionospheric temperature locally. There are currently only three such HF facilities and only one that is collocated with IS radars.

In this chapter a short introduction the two radar techniques at the center of this thesis, the IS technique and active HF ionospheric modification, are given. A comprehensive history of ionospheric physics and research is given by Rishbeth et al. (1996), while Streltsov et al. (2018) give a comprehensive review of active HF modification experiments.

3.1 Incoherent scatter technique

Incoherent scatter radars are an important ground-based tool to study ionospheric physics. It was first proposed by Gordon (1958) and has since developed into a large field of research. The historical background is outlined in the fist part of this section. The second part introduces the incoherent scatter technique and underlying physics, while the last part focuses on the facility and its capabilities that is used for the work presented in this thesis.

Historical background

Shortly after the launch of the first Sputnik satellite in October 1957, during the Space Race, Gordon (1958) first proposed the use of radar systems to study the ionosphere. He predicted theoretically that scatter from individual electrons, moving incoherently in the ionosphere can be used to derive the electron density and temperature as a function of altitude and time. At the time there where few methods for observing the ionosphere as there were no rockets or satellites and regions above the F-region peak are not accessible by ionosondes.

The theoretical calculations of Gordon were based on the assumption of backscatter from completely free electrons in the ionosphere. Further, he suggested that the electron temperature could be estimated by measuring the frequency spread or doppler shift of the returned signal as that would be dependent on the thermal motion of these free electrons. This lead to a size estimate for a suitable ionospheric radar system with a 300 meter diameter antenna dish and a transmitting frequency around 400 MHz.

A few months later, Bowles (1958) verified Gordon's predictions, making the first observations of incoherent scatter. An excerpt of his observations are shown in Figure 3.1. This was done by transmitting a signal with a makeshift

radar he and his friend built, using an array of 1024 half-wave dipole antennas and a 41 MHz transmitter. The backscattered signal, originating from the daytime ionosphere, was measured by an oscilloscope and was documented by taking photographs of superimposed oscilloscope traces of the powerspectra (Farley, 1996). Surprisingly, the experiment showed a frequency spread smaller by an order of magnitude than Gordon's predictions from the Doppler shift of "free" electrons. This, eventually lead to the realization that the ionospheric electrons are not completely free, but their motion is governed by electrostatic forces between the ions and electrons.

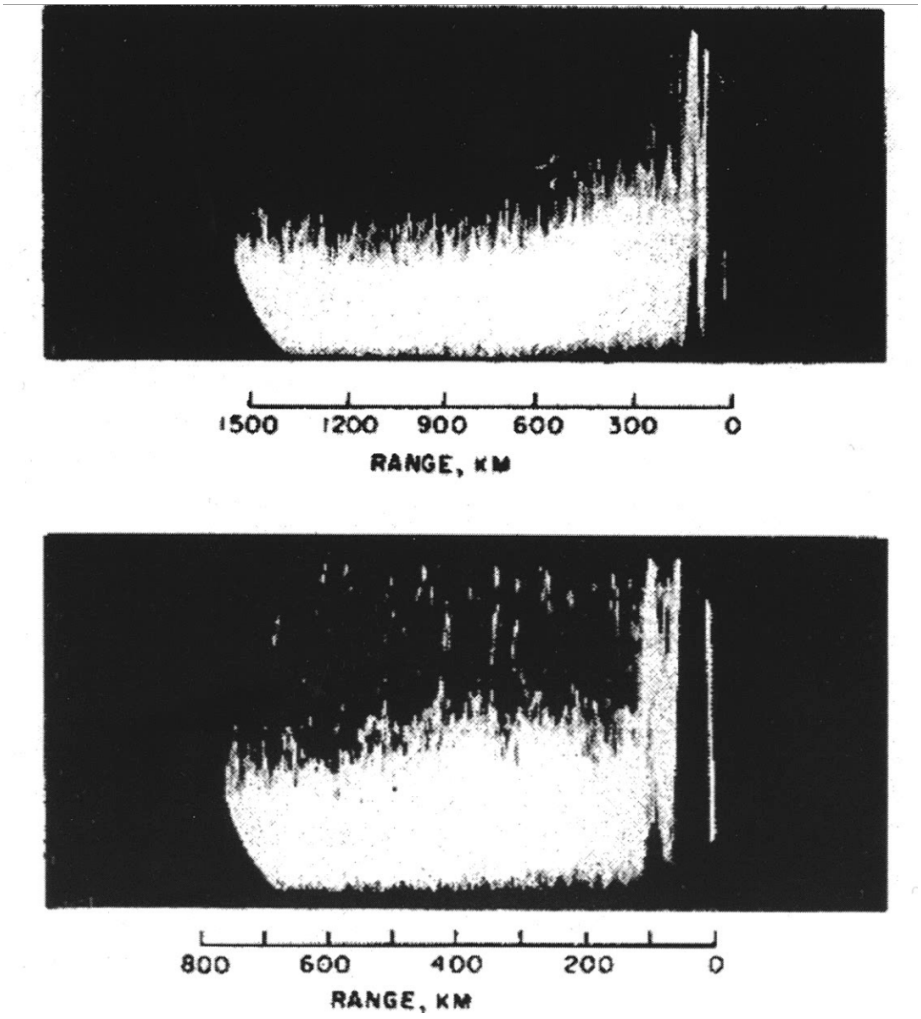

Figure 3.1: The first incoherent scatter radar observations made by Bowles (1958). The figures are made by taking photographs of superimposed oscilloscope traces of the receiver amplitude vs time (range). Figure from (Bowles, 1958, Fig. 1)

Coincidentally, the day Bowles made his historic observations was also the day that Gordon gave his first formal presentation of his theoretical predictions at the Union Radio-Scientifique Internationale meeting. After a telephone call with Bowles early in the day, Gordon then began his talk with this, now well-know anecdote (Farley, 1996):

My purpose in speaking today is to tell you about incoherent back scatter from the ionosphere, and about the possibility of building a tool to make use of it in studying the ionosphere. And then I want to tell you about a telephone call that I just had.

Although the original "free electron" theory by Gordon (1958) was oversimplified and the scattering is not in fact completely *incoherent*, this marked the beginning of what is known as the incoherent scatter (IS) radar technique as a powerful ground-based diagnostics tool to study near-Earth-space.

The fundamental principle for the incoherent scatter technique is the realization that an incident electromagnetic wave on plasma irregularities will scatter and that the scattered wave contains information about the plasma that can be extracted from the received signal. When the transmitted radar wave frequency is far above the maximum plasma frequency in the ionosphere, $f_{radar} \gg f_{OF2}$, the wave energy travels almost undisturbed through the ionosphere and into space. A small fraction of the wave energy is absorbed and scattered by ions and electrons in the plasma. These will oscillate at f_{radar} and emit radiation as small dipoles. As the ions have a much larger mass, their radiation is small compared to that of the electrons and thus their contribution to the received scattered signal is negligible. The radar scattering cross section of an individual electron, defined as the projection of a perfectly isotropically reflecting sphere producing the same electromagnetic signature as an electron, is on the order of $1.0 \times 10^{-28}\,\mathrm{m}^2$. With typical radar scattering volumes and electron densities in the ionosphere, powerful radars capable of detecting a target of a few centimeters in diameter at 300 km distance, are needed. It was these considerations that prompted Gordon's suggestion for the very large antenna. A suggestion that only a few years later resulted in the Arecibo Observatory. Built in a sinkhole in Puerto Rico in 1963, is was operational for 57 years until it collapsed following a cable failure in December 2020.

After it became clear that the electrons are not completely "free", following the first measurements by Bowles (1958), the existing theory had to be revised. Several authors (Dougherty and Farley, 1960; Farley et al., 1961; Fejer, 1960; Hagfors, 1961; Renau, 1960; Rosenbluth and Rostoker, 1962; Salpeter, 1960) approached this problem independently, using a variety of methods, which all lead to the same result: For an electrically neutral plasma, the frequency spread of the observed backscattered spectra corresponds to the thermal motion of the ions rather than the electrons. Thus, for radar wave lengths that are much larger than the Debye length (Equation 2.1) the backscattered signal contains information about both the ions and the electrons. For radar wavelengths shorter than the Debye length the electrons appear "free" and the backscattered signal is truly incoherent and the spectrum will agree with the predictions by Gordon, containing the electron phase velocity and with a spectral width corresponding to the thermal velocity distribution of the electrons.

The revised theory has been successful in quantitatively explaining all observations and has since been extended to include a wide range of effects, including for example unequal ion and electron temperatures and non-Maxwellian electron and ion velocity distributions. From the power, spectrum and polarization of the returned signal of incoherent scatter radars it is now possible to determine multiple parameters of the ionospheric plasma, such as plasma density, electron and ion temperatures, ion composition, relative motion of electrons and ions and the effects of collisions. Further details of the history, development and techniques are described in numerous review papers and books (e.g. Bauer, 1975; Beynon and Williams, 1978; Farley, 1970, 1996; Hunsucker, 1991; Rishbeth et al., 1996).

Brief radar theory

The scattering mechanism mentioned above is Thompson scatter by the individual electrons. As the lighter electrons move to preserve the charge neutrality of the plasma, the spectral shape of the scattered signal is determined by the motion of the heavier ions rather then the electrons. When the wavelength of the radar, λ_{radar}, is much larger than λ_D, waves are scattered from density fluctuations in the plasma. Small density fluctuations always exist due to the thermal motion of the plasma and collectively these give rise to the scattered signal. The power spectrum of the scattered signal is directly proportional to the power spectrum of the random thermal electron density fluctuations in the plasma, where the radar frequency and scattering geometry dictate the density fluctuations that can be observed. Scattered waves from the electrons are constructively interfering when the wavelength of the density fluctuations, Λ, satisfies the *Bragg scattering* condition:

$$\Lambda = \frac{\lambda_{radar}}{2\cos\theta}$$

where θ is the angle between the incident wave and the scattered wave. The thermal fluctuations in the plasma are composed of plane waves at all wave numbers k, in all directions, including waves traveling toward and away from the radar at a wavelength of $\Lambda = \lambda_{radar}/2$. In a monostatic radar systems, meaning that the transmitter and receiver of the radar are co-located, only scattering from waves in the radar beam can be detected. In a multistatic radar system, meaning that there are more than one receiver at different locations from the transmitter, the plasma motion in different directions can be observed for the scattering volume where the radar beams intersect. The discussion and results presented in this thesis consider a monostatic radar system only.

Several wave modes exist inherently in the ionospheric plasma due to the thermal fluctuations. The two modes important for IS radar observations, are the ion-acoustic waves and electron acoustic or plasma waves. The phase velocity, ν_{ph}, of these waves is determined by their dispersion relations (see Chapter 2.1 and 4.1). The scattered signal from a traveling wave will be

Doppler shifted from the incident frequency, f_{radar}, depending on the direction of wave propagation. As a result the scattered signal spectrum contains four main components, consisting of the upward and downward traveling, ion acoustic and plasma waves. The Doppler shift for the ion acoustic wave is $f_{ia} = \pm 2\nu_{ia}/\lambda_{radar} = \pm\nu_{ia}/\Lambda$ and similarly $f_P = \pm 2\nu_P/\lambda_{radar} = \pm\nu_P/\Lambda$ is the Doppler shift for the plasma wave. Here, ν_{ia} and ν_P are the phase velocity of the ion acoustic and plasma waves, respectively, and f_P is the plasma frequency (see Equation 2.8). Figure 3.2 shows a schematic of the scattering spectrum containing the up- and downshifted, ion (green) and plasma (purple) lines, as they would appear from a monochromatic, purely sinusoidal density fluctuation. The actual shape of the signal is spread out in frequency, as illustrated by the green and purple curves in the figure. The frequency broadening and the shape of the spectra depend on the damping of the wave. In steady state, new thermal waves are continually generated in a plasma and then attenuated mainly through *Landau damping* and collisional damping depending on the altitude.

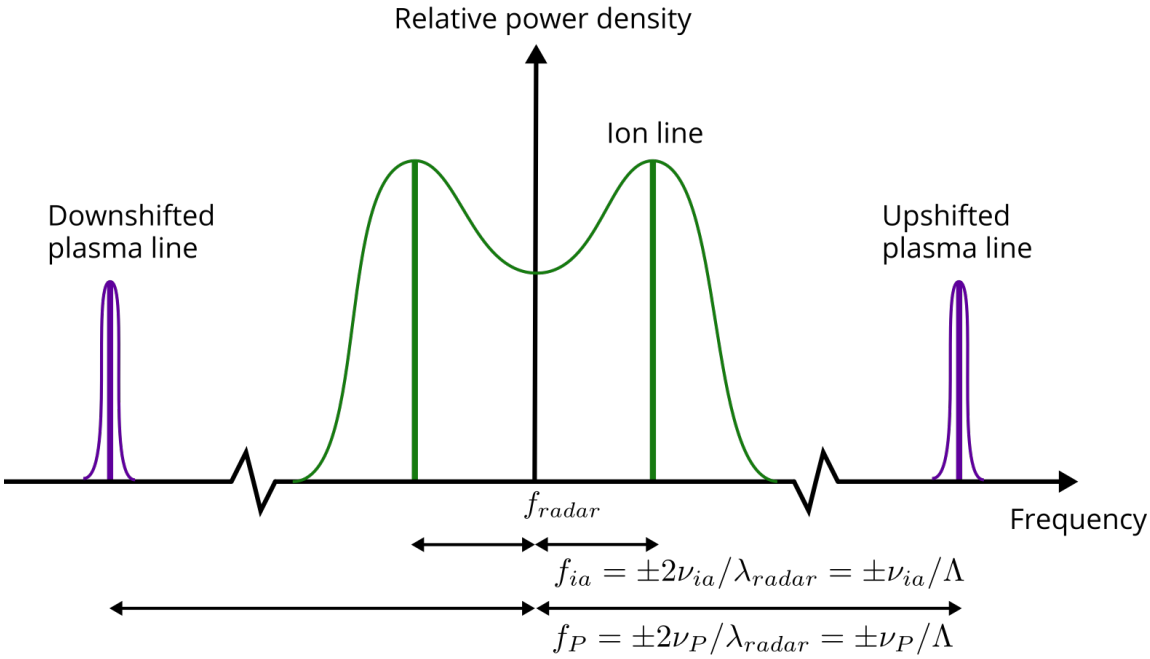

Figure 3.2: Schematic of the general shape of the incoherent scatter spectra of the ion (green) and plasma (purple) lines. The frequency scale on the horizontal axis is relative to the radar frequency, f_{radar}. Typically the plasma lines are on the order of megahertz while the ion lines are typically on the order of tens of kilohertz. The solid bold lines indicate the appearance of the ion and plasma lines in the absence of Landau damping, while the curved lines indicate the shape of a typical incoherent scatter spectrum from the F-region ionosphere. [Not to scale]

Landau damping is collisionless and results from the velocity difference between particles and waves in the plasma. In a plasma with a Maxwellian velocity distribution, some particles will have velocities very close to the phase velocity of a wave, and will interact with it. For these, energy will be transferred

from one to the other. ”Fast” particles, compared to the wave, will increase the waves energy and momentum while ”slower” particles will gain energy from the wave. In a Maxwellian distribution there are more particles with lower velocities than higher, so that the net result is a damping of the wave. This leads to a broadening of the frequency spectrum of the scattered signal. For the ion line from the E and F regions in the ionosphere, the broadening is often such that the spectra of the up- and downshifted waves overlap and form the characteristic ”double hump” or ”shoulder” shape, illustrated by the green line in Figure 3.2. It is not difficult to interpret how for example a change in the electron temperature would change the shape of the ion line spectrum. For an increase in electron temperature, T_e, it can be seen from Equation 2.11 that the ion acoustic wave speed increases. At this new speed, the difference between the number of fast and slow particles with respect to the wave is smaller, and the wave damping is reduced. Thus, the peaks of the ion line become sharper.

The plasma line experiences much less damping since plasma waves typically propagate at much higher phase velocities than the thermal velocity of the electrons. Therefore, the plasma line has a much narrower spectrum than the ion line. In fact, the plasma waves are easily excited or enhanced by for example photoelectrons or an influx of energetic precipitating particles from the magnetosphere, and the plasma line spectrum will typically be enhanced and remain sharp. When f_{radar} is much greater than λ_D, the phase velocity of the plasma wave can be approximated $\nu_P = f_P\Lambda$ and observations of the plasma line spectrum can be used to calculate the electron density independent of the ion line observation. A detailed description of this is given in Chapter 5.

Most important parameters of the plasma affect the power spectrum of the scattered signal, and as a result it contains a wealth of information that can be extracted through careful analyses. To calculate these, a number of strong assumptions about the state of the plasma have to be made and the data processing and signal analyses is complex. However, the rewarding outcome is that the following plasma parameters can be determined in a range of altitudes, along the radar beam:

- **Electron density:** The electron density, n_e, can be determined in three ways. It is proportional to the total power of the scattered signal (1), it can be calculated from the *Faraday rotation* of the signal when $\mathbf{B}_0$ is known (2), and it can be determined from the plasma line (3). When the plasma line is detectable, this method gives the highest level of accuracy and precision (see Chapter 5).

- **Electron and ion temperature:** The temperature ratio, T_e/T_i, can be found from the ratio between the peaks and the trough of the ion line spectra.

- **Ion mass:** The ion mass, m_i, can be determined from the width of the ion line spectrum by making some assumptions on the temperature. Vice

versa, if the ion mass can be estimated reliably, one can determine T_e and T_i.

- **Plasma drift velocity:** The drift velocity of the plasma, v_p, can be determined from the Doppler shift of the whole spectrum. That is, if the ion line is shifted, but otherwise unchanged from the transmitted frequency, the line-of-sight velocity from the mean shift can be calculated. The true drift velocity vector can be found if independent measurements from at least three directions are combined. For example by using a tri-static radar system, giving three components of the drift, simultaneously.
- **Ion-neutral collision frequency:** The Ion-neutral collision frequency, ν_{in}, increases as we move lower in the atmosphere and the neutral density increases. As T_i decreases and m_i increases for lower altitudes, f_{ia} will decrease and the ion acoustic wave will not be able to propagate far. The two shoulders of the ion line spectrum will merge and with measurements of the width and shape of this, ν_{in} can be determined.

Combining the parameters with measurements from multiple IS radars with different f_{radar}, models and measurements of the geomagnetic field and the neutral atmosphere it is possible to derive several other valuable parameters. The Hall and Pedersen conductivities, the electric field in the ionosphere, currents parallel and perpendicular to $\mathbf{B}_0$, joule heating, the motion of the neutral atmosphere and the energy spectra of auroral precipitation are some examples. Radar theory and the accompanying signal processing and analyses is an active field of study and research in its own right. Further information and detailed descriptions and derivations are given in the book by Nygrén (1996) and several scientific review papers including Bauer (1975); Beynon and Williams (1978); Farley (1996); Milla and Kudeki (2011) and Kudeki and Milla (2011).

The EISCAT Radar

There are currently six incoherent scatter radars operational in the high latitude region in the northern hemisphere. RISR-N and RISR-C are two radars pointing deep into the polar cap region, in Resolute Bay, Canada. The PFISR radar is located at the Poker Flat Research Range close to Fairbanks, Alaska, in the auroral zone, participating and supporting rocket launches in addition to ionospheric studies. All three radars are phased array radars of mobile, modular building block panels and are part of the Advanced Modular Incoherent Scatter Radar (AMISR) system. The other three incoherent scatter radars in the polar region, are all part of the European Incoherent SCATter (EISCAT) scientific Association. The EISCAT Svalbard Radar (ESR) consists of two parabolic antennas located near Longyearbyen, Svalbard. Its position in this very high latitude region allows for studies of the cusp region of the low altitude magnetosphere. On the Norwegian mainland, the EISCAT UHF and VHF radars are located in Ramfjordmoen close to Tromsø. There are two additional receiving antennas located in Kiruna, Sweden and Sodankylä, Finland, for the VHF radar,

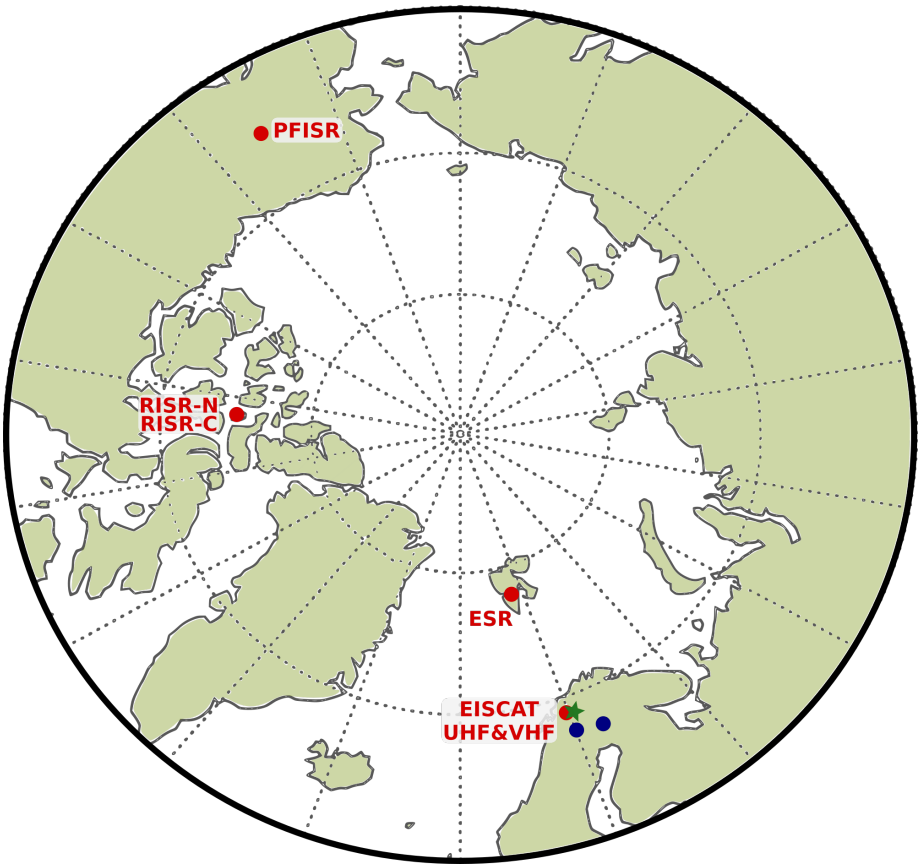

Figure 3.3: Geographic map of the northern polar hemisphere showing the current incoherent scatter radars in auroral region. AMISR radars (PFISR, RISR-N and RISR-C) are located in Northern America, while all EISCAT radars are in Northern Scandinavia and Svalbard. Red dots indicate IS radars with transmit and receive capabilities, while blue dots show facilities with receive capabilities only. The green star indicates the main location of the new EISCAT3D radar currently in construction.

and together they form the only tri-static incoherent scatter radar system in the world. Additionally, EISCAT is planning and currently building a new radar system, EISCAT3D, that will be located in Skibotn, Norway, which will have exceptional new capabilities. For this thesis the EISCAT UHF radar has been used in a monostatic setup to observe the ionosphere during multiple experiments.

EISCAT is an international scientific organization operating incoherent and coherent scatter radars, researching the polar ionosphere and upper atmosphere. The UHF radar was the first to become operational in 1981. It is a parabolic antenna with a 32-meter diameter dish, fully steerable in azimuth and elevation, with a theoretical maximum peak power of 2 MW at a frequency of 930 MHz. The direction of the radar beam can thus be changed for different experiments and can also be run with a scanning pattern, scanning or alternating between directions. An image of the UHF radar antenna is shown in Figure 3.4. By modulating the transmitted wave or the pulse code of the beam, different range and time resolutions of the scattered signal can be obtained.

Utilizing a combination of all these options the radar parameters can be chosen and optimized for the phenomena of interest. A description of the possible experiments and the corresponding radar parameters in given by Tjulin (2017).

Figure 3.4: The 32-meter diameter dish of the EISCAT UHF radar in Ramfjormoen, Norway on a sunny winter day.

The scattered power spectrum measured by the EISCAT radars is commonly analysed using the Grand Unified Incoherent Scatter Design and Analysis Package (GUISDAP), a MATLAB package develeoped by Lehtinen and Huuskonen (1996) and EISCAT for designing and analyzing incoherent scatter measurements. GUISDAP works by fitting a theoretically calculated spectrum to the measured spectrum and provides the physical plasma parameters in range and time, making research and analyses of EISCAT data smooth and user-friendly. All EISCAT data, as well as the GUISDAP software, is freely available online through the online MADRIGAL database and GitLab, respectively, with current links found on the EISCAT web site (EISCAT Scientific Association, 2021).

3.2 Ionospheric heating in the polar ionosphere

Active ionospheric modification experiments provide the possibility to study the ionospheric plasma dynamics and processes in controllable and repeatable experiments. High-power, high-frequency radio waves are transmitted into the ionosphere and the effects of this can be observed and studied with ground-based, in-situ or space-borne instrumentation. The transmitted wave is commonly referred to as the pump wave, HF wave, heating wave or modification wave in the literature. In the rest of this thesis these terms are used interchangeably. The first part of this section is concerned with the historical background of ionospheric modification experiments . The facilities used for the experiments central to this thesis are introduced in the second part. The last part outlines the underlying physics and some of the commonly observed phenomena, that are specially relevant for this thesis.

Historical background

The discovery that the ionospheric plasma could be modified and possibly used for scientific research was made by accident. Two standard broadcasting radio stations were transmitting their radio program simultaneously at two different locations in Europe. The amplitude modulation of the powerful low-frequency radio signal from the Luxembourg radio station was impressed on the medium frequency radio signal from Beromünster in Switzerland. The observation was made by Tellegen (1933) who noticed an unusual effect while listening to the radio, which he reported in the Nature journal with the title *Interaction between Radio-Waves?*. He stated that:

> *For the first time on April 10 of this year it was observed at Eindhoven, Holland, that when a radio-receiver was tuned to Beromünster (460 m), the modulation of the Luxembourg station [1190 m] could be heard on the background to such an intensity that during the weak passages of the programme of Beromünster, the programme of Luxembourg was heard with an annoying strength.*

Within a year, Bailey and Martyn (1934) confirmed this quantitatively and reported their findings in the same journal with the title *Interaction of Radio waves*, leaving out the question mark. This became known as the *Luxembourg* effect.

Following this discovery, the potential of using radio waves as a means to modify and study the ionosphere in controlled experiments was recognized by several scientists in the 1960s (e.g. Farley, 1963; Ginzburg and Gurevich, 1960). The first[1] of several dedicated ionospheric modification facilities using high frequency radio waves, was finally built in 1971 in Plattevile, Colorado,

[1] Actually the first experiments were conducted in 1961 in the Soviet Union near Moscow, Russia, but the results remained classified until 1973. (Streltsov et al., 2018)

USA (Fejer, 1979). Utilizing the ionosphere as a large-scale, wall-less plasma laboratory, enabling controlled, repeatable experiments in near-Earth-space has since been an active field of research (e.g. Robinson, 1989; Stubbe and Hagfors, 1997; Wong and Brandt, 1990, and references therein).

A large variety of ionospheric experiments have been designed and performed to study a range of phenomena and the mechanisms causing them, including fundamental properties of the plasma, wave-plasma interactions, properties of the near-Earth-space and the coupling to the atmosphere and magnetosphere system. The last section of this chapter, briefly introduces some of the important and recent advancements. There are several comprehensive review articles summarizing the theoretical and experimental findings, for example Leyser and Wong (2009); Rietveld et al. (2016); Robinson (1989) and Streltsov et al. (2018). An historical overview of the early development and research of ionosphereic modification experiments is given by Gordon and Duncan (1990).

Currently, there are only three active ionospheric modification facilities. The Sura facility in Vasilsursk, Russia (Belikovich et al., 2007), the High Frequency Active Auroral Research Program (HAARP) (Pedersen and Carlson, 2001) in Gakona, Alaska, and the EISCAT Heating facility (Rietveld et al., 1993, 2016) in Tromsø, Norway. Of the three, EISCAT Heating is the only one co-located with IS radars to observe the effects of the transmitted radio waves.

EISCAT Heating

The experiments that form the basis of the this thesis were carried out during campaigns at the EISCAT Heating facility, located in Ramfjordmoen near Tromsø, Norway. An overview of the arrays, control room and transmitter hall is shown in Figure 3.5. Its location is well within the auroral zone in the northern hemisphere and the angle between the geomagnetic field and zenith is approximately $\sim 12^\circ$ here. The facility was built by the Max-Planck-Institut für Aeronomie in Germany from 1977 to 1980. It is currently the only ionospheric modification facility that is co-located with incoherent scatter radars. Since its transfer to EISCAT in 1993, 356 publications have come out of the facility from a total of 479 (numbers as of April 2021).

EISCAT Heating operates with twelve transmitters capable of generating a total theoretical effective radiated power (ERP) of 1200 MW with a transmitted frequency, f_{HF}, in the range from 5.05 – 8 MHz. There are three crossed dipole antenna arrays that may be connected to the transmitters depending on the frequency and antenna gain needed for a specific experiment. The arrays where originally built to cover the frequency range of 2.75 – 8 MHz. In 1985, a storm damaged Array 1 that was built for the 2.7 – 4.1 MHz frequency range. It was rebuilt in 1990 and now consists of 12×12 antennas, covering frequencies from 5.4 – 8 MHz with an 28 – 31 dBi antenna gain, providing the maximum ERP and a full-width-half-maximum beam width of $\sim 7^\circ$, varying slightly with frequency. Array 2 and 3 have 6×6 antennas each, covering a frequency

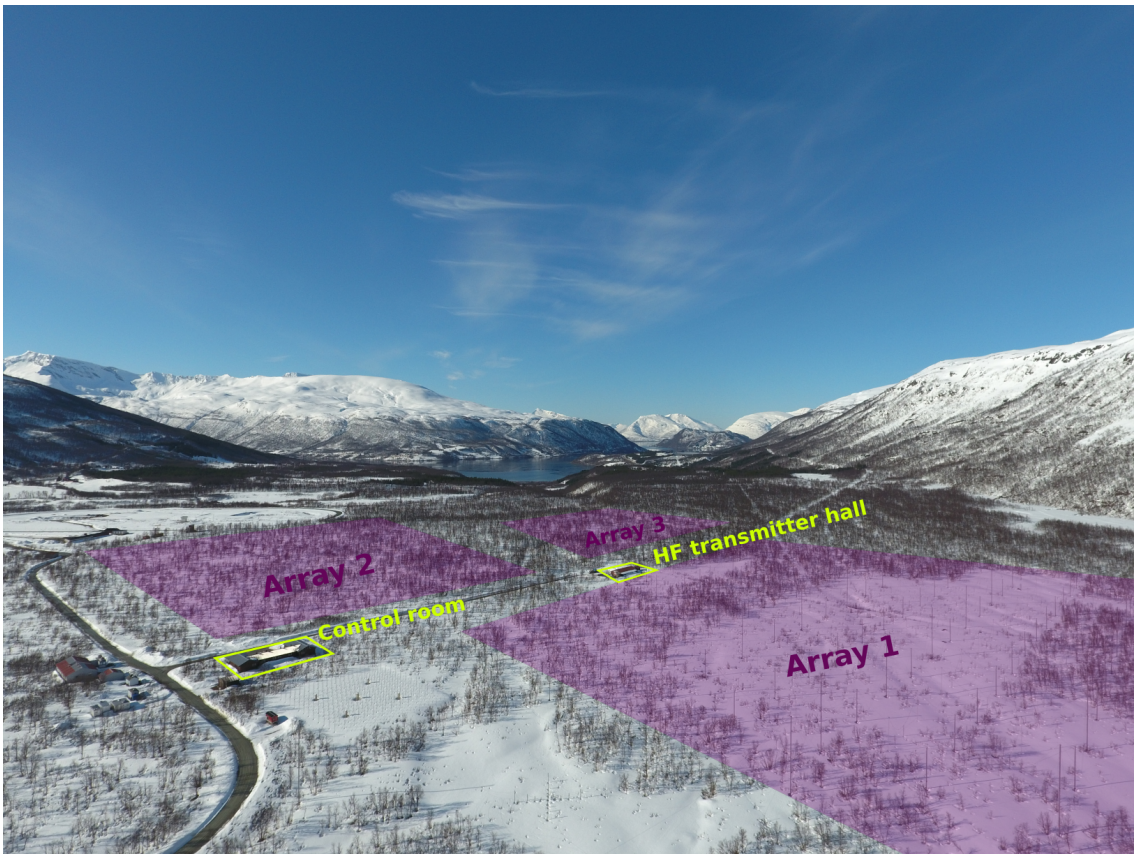

Figure 3.5: The EISCAT Heating facilities with the arrays, control room and transmitter hall indicated. Photo: Craig Heinselman

range from 3.85 – 5.65 MHz and 5.5 – 8 MHz, respectively, with a 24 dBi antenna gain. The maximum ERP for these arrays is 300 MW and the full-width-half-maximum of the beam is $\sim$14.5°.

Using subsets of the arrays and setting the transmitters to different frequencies it is possible to transmit multiple frequencies simultaneously. Up to six frequencies with circular polarization are possible, while for a linear polarization all twelve transmitters can be set to a different frequency, although this will affect the shape of the transmitted beam. In addition to the transmitted frequency, f_{HF}, a number of other beam parameters can be selected, these include the wave polarization, beam direction and width and maximum power. Intricate on-off, frequency stepping- or power stepping- schemes are also commonly used. Figure 3.6 shows a schematic of the co-located setup for a possible experiment using the EISCAT Heating and the EISCAT UHF radar, indicating the beamwidth of both radars and the angle of the magnetic field. This setup was used for the experiments that form the basis of this thesis.

During experiments, it is sometimes difficult to achieve a perfectly left- or right-handed circular polarization. Slightly uneven powers or phases of the transmitters will affect the transmitted beam. An example of the beam pattern from a magnetic field aligned experiment in March 2016 (presented in Paper

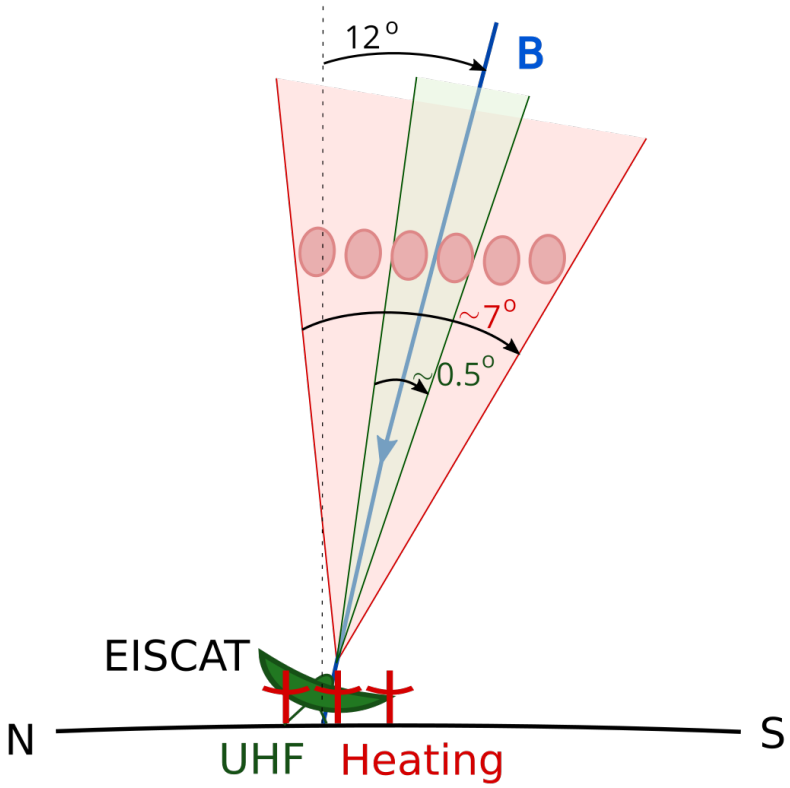

Figure 3.6: Schematic of the colocated EISCAT UHF radar and Heating facilities for active experiments. Both Heating and radar beam are steerable and are shown in a magnetic field aligned direction here. This setup was used for the experiments presented in this thesis. [Not to scale]

I) is shown in Figure 3.7. The intention of this experiment was to transmit a pure O-mode wave. A small part, about 4%, of the radiated power leaked in the X mode. This might be of consequence for some experiments and thus the beam pattern is one of the standard data products available for experiments at EISCAT Heating.

This is only a brief summary of the most relevant capabilities and parameters of the facility to provide context for the presented work. Thorough technical reports and detailed description of EISCAT Heating are given by Rietveld et al. (1993); Stubbe (1996); Stubbe et al. (1982) and most recently and updated for the facilities by Rietveld et al. (2016).

Transmitting radio waves in the ionosphere

When a high frequency (HF) wave is transmitted toward space, it will propagate and reflect at an altitude that depends on the ionospheric plasma frequency (proportional to the electron density), the angle-of-incidence of the wave in the ionosphere and its polarization relative to the magnetic field. The most efficient interaction with the ionospheric plasma is achieved when the wave frequency is less than the maximum plasma frequency in the ionosphere,

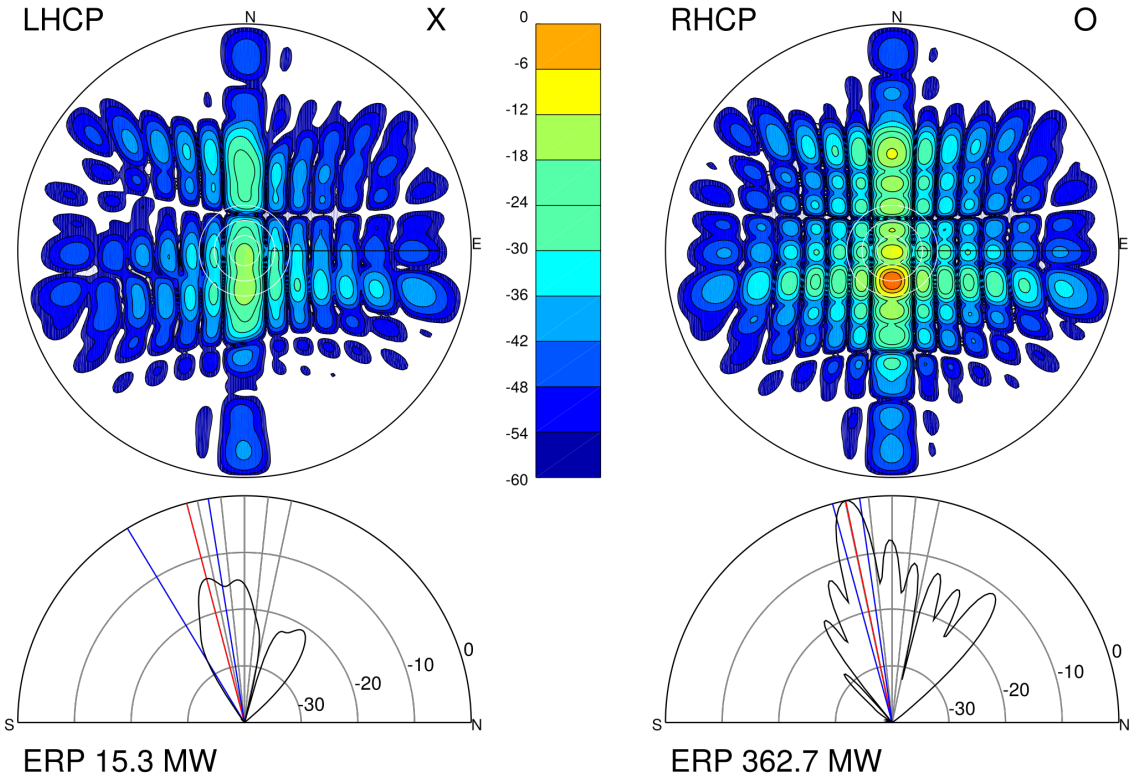

Figure 3.7: An example of a calculated beam pattern and effective radiated power of the transmitters for the two circular polarized modes during the experiment presented in Paper I. It should be noted that the O and X-mode wave in these figures are labeled as RHCP (right hand circular polarized) and LHCP (left hand circular polarized), respectively, as they are defined by the direction of **k**. This is contrary to the notation of this thesis where the handedness of the wave modes is defined by the direction of $\mathbf{B}_0$ (see Chapter4).

f_{OF2}. An O-mode wave will interact most efficiently near the ionospheric layers where f_{HF} approaches the plasma and upper hybrid frequencies and consequently these are of special interest during experiments.

The basic principle of linear, HF wave propagation when $f_{HF} < f_{OF2}$ is illustrated in Figure 3.8. Waves transmitted at an angle away from the vertical will reflect at a lower altitude due to refraction in the ionosphere. A vertically transmitted wave in the O mode will reflect when it has reached the reflection altitude where the transmitted frequency is equal to the local plasma frequency (see also Equation 2.8).

$$f_{HF} = f_P \tag{3.1}$$

An X-mode wave transmitted vertically has two reflection altitudes when

$$f_{HF} = \pm\frac{f_G}{2} + \frac{1}{2}\sqrt{f_G^2 + 4f_P^2} \tag{3.2}$$

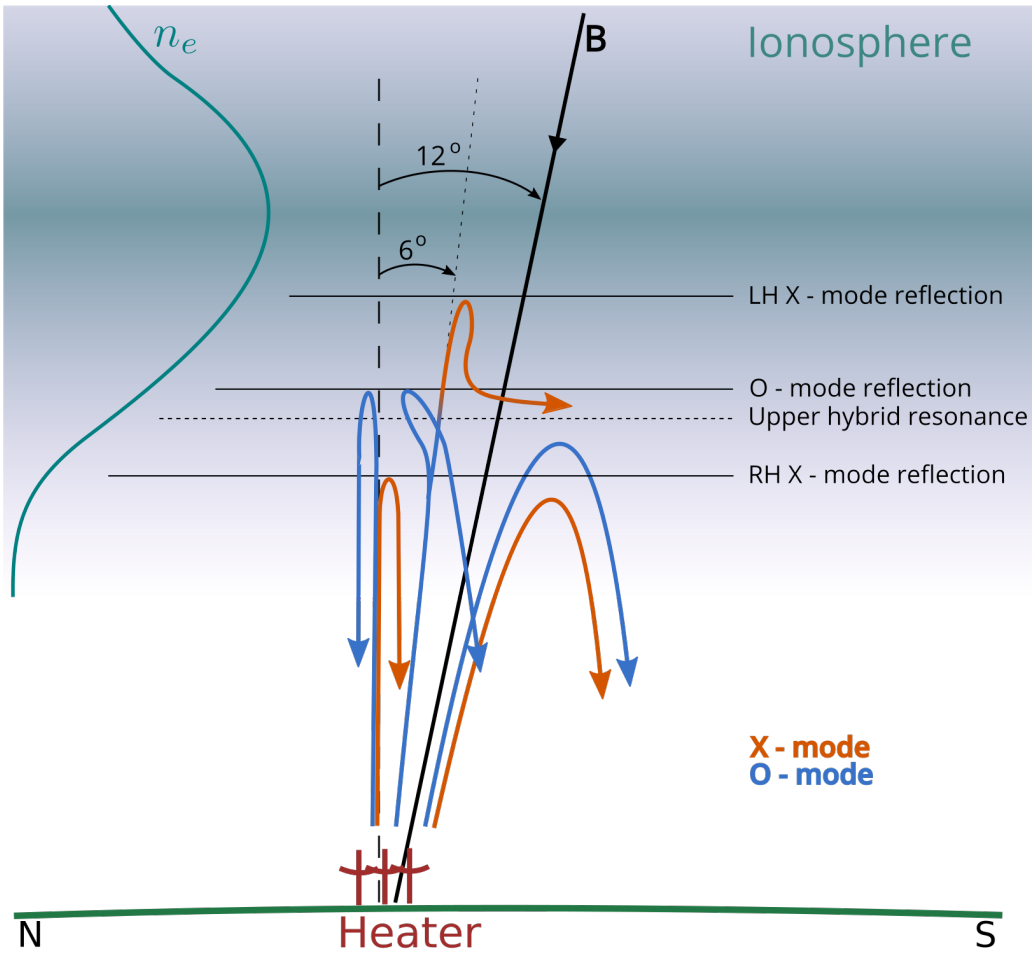

Figure 3.8: Schematic of raypaths of HF radio waves transmitted at various angles of incidence in the ionosphere at the EISCAT facilities. At 6° south of vertical an O-mode wave (blue) may convert to the Z mode (also called the slow or LH X mode) and pass through the radio window. RH X-mode waves will reflect at lower altitudes than the O-mode waves. [Not to scale]

where the negative solution applies to the LH X mode and the positive solution applies to the RH X mode. The wave transmitted from a ground-based antenna is not actually in a plasma wave mode until it reaches the ionospheric plasma. It is either an LHCP or a RHCP electromagnetic wave. In ionospheric modification experiments a transmitted LHCP wave is commonly referred to as an O-mode wave also before it reaches the ionosphere, and likewise a transmitted RHCP wave is referred to as an X-mode wave. As these are the only circular polarization available, it is not possible to transmit a LH X-mode wave from a ground-based antenna. The reflection altitudes in Equation 3.1 and 3.2 correspond to the O, R and L mode cutoff frequencies given in Equation 2.19, 2.20 and 2.21, respectively. The schematic Figure 3.9 indicates the cutoff or reflection and resonance frequencies for the two wave modes, as well as harmonics of the electron gyro frequency (see Equation 2.5). In an inhomogeneous plasma the reflections and resonances occur in very narrow height ranges.

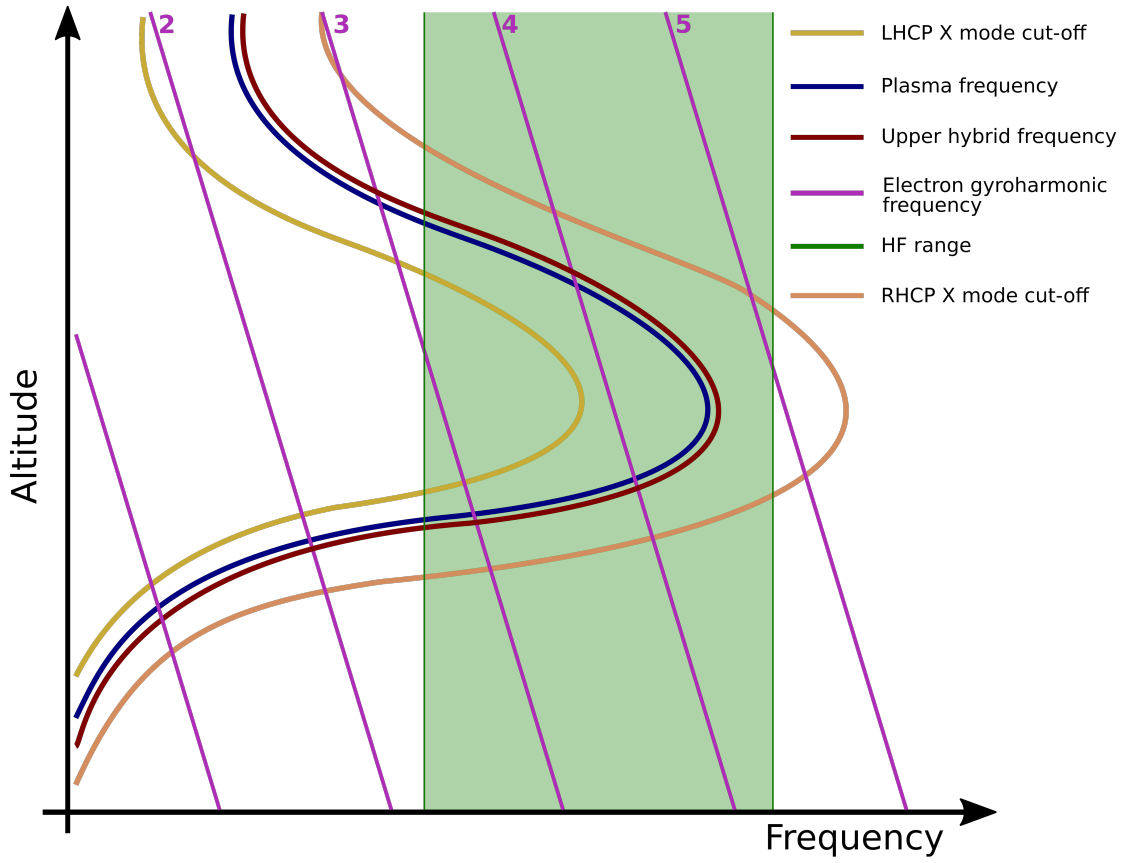

Figure 3.9: Schematic of the frequency-altitude profile of important ionospheric frequencies in relation to the range of the pump frequencies available in EISCAT Heating experiments. The EISCAT Heating facility can easily reach the third and fourth electron gyroharmonic frequencies (pink), nf_G. The plasma frequency (blue), f_P, upper hybrid frequency (red), f_{UH}, and the two X mode cutoff frequencies, f_{L-cut} (yellow) and f_{R-cut} (orange), are indicated. The region where the electron gyroharmonic frequencies intersect the upper hybrid frequency is defined as the double resonance frequency, f_{dbl} (see Equation 3.4).

An exception to this refraction and reflection of incident waves is for O-mode waves transmitted at the *Spitze angle*, θ_c. These have a *radio window* here, meaning the phenomenon or region where an incident wave can pass through and beyond a region where it, according to simple ray theory, would be evanescent (Budden, 1980). For an O mode transmitted at the Spitze angle this means that the incident wave can pass through to higher altitudes and plasma densities in the ionosphere, here. The Spitze angle is defined as

$$\sin\theta_c = \sin\alpha\sqrt{\frac{Y}{1+Y}} \tag{3.3}$$

where $Y = f_G/f_{HF}$ and α is the angle of the magnetic field to the vertical. At the EISCAT Heating facility θ_c varies between 6° and 4.5° for frequencies between

4 MHz and 8 MHz.

When approaching the plasma resonance region, an O-mode wave is refracted such that the electric field of the wave, $\mathbf{E}_1$, becomes parallel, and **k** becomes perpendicular, to the magnetic field $\mathbf{B}_0$. Since f_{HF} is equal or very close to the local plasma frequency here, the transmitted wave can efficiently couple to plasma wave eigenmodes in this region, initiating Langmuir turbulence and other instabilities. At the upper hybrid resonance altitude, also indicated in Figure 3.9 and usually found a few kilometers below the plasma resonance, $\mathbf{E}_1$ is mostly perpendicular to $\mathbf{B}_0$. Here, the wave can generate magnetic field aligned density irregularities called striations that are discussed in detail later in this chapter. New wave modes, like electron Bernstein waves may also be enhanced and generated.

Especially interesting effects are sometimes observed for waves transmitted at or near a multiple of the *double resonance frequency*, where the local upper hybrid frequency and a harmonic of the electron gyro frequency are equal,

$$f_{dbl} = f_{UH} = nf_G \tag{3.4}$$

where n is a positive integer. Paper I and II present some of these gyroharmonic effects. These are also briefly discussed in Chapter 4.

The ionosphere as a plasma laboratory

The ionospheric plasma is easily accessible by radio waves allowing for repeatable and methodical plasma experiments. Active ionospheric modification experiments have thus lead to new insights and understanding of plasma and geophysical processes.

The transmitted wave generally modifies the plasma in the ionosphere and the plasma in turn modifies the incident waves by absorption and refraction, and the interaction between the different types of waves. Consequently most of the resulting effects and processes become nonlinear. The numerous nonlinear plasma phenomena and processes generated can be classified into two categories (Stubbe and Hagfors, 1997). The first is thermal nonlinearity where electrons are heated through collisional heating as they oscillate in the electric field of the wave. These occur on long timescales on the order of seconds and one of the effects is the generation of plasma density irregularities. The second is a result of the ponderomotive force leading to a gradient in wave intensity. Langmuir and upper hybrid turbulence are caused by this type of nonliniearity and occur on timescales of milliseconds. Through controlled and specifically designed experiments these processes can be studied and an understanding of wave propagation, wave-particle interactions, plasma turbulence and instabilities as well as geophysical phenomena in the near-Earth-space can be gained.

Since the first ionospheric modification experiments, a wealth of research has been published and experiments have been conducted to study radio physics, mesospheric and thermoshperic physics, chemistry, space weather, magnetosphere and radiation belt physics and laser fusion (e.g. Leyser and Wong, 2009; Robinson, 1989). In the following sections, some of the phenomena directly relevant to this thesis are presented in some detail. This is only a brief introduction and by no means a complete list, and more extensive reviewes are given by, for example Streltsov et al. (2018) or Gurevich (2007).

Enhanced plasma and ion lines

When a high power, HF wave illuminates the ionosphere the naturally occurring plasma waves are enhanced, and new waves are generated through different nonlinear effects. As discussed in Section 3.1, an IS radar can not observe the entire spectrum of the waves generated and enhanced by the HF pump wave. However, the ion acoustic and Langmuir waves satisfying the Bragg condition, that is waves with a wavenumber and direction such that $\mathbf{k} = \mathbf{k}_{radar}/2$, are also enhanced and are observable by the IS radar. The enhancements are largely caused by the so called parametric decay instability (e.g. Kohl et al., 1993; Najmi et al., 2016), where the incident pump wave energy is conserved in a three-wave interaction satisfying the relation

$$f_0 = f_1 + f_2 \quad , \quad k_0 = k_1 + k_2$$

where the subscripts 0, 1 and 2 indicate the pump and the two descendant waves, respectively. The descendant waves are a Langmuir wave and an ion acoustic wave, detectable by the IS radar at specific offsets from the radar frequency.

Another instability that strongly affects the enhancement of the ion acoustic waves and Langmuir waves is the oscillating two stream instability (OTSI) or purely growing mode (e.g. Kuo et al., 1997). Here, the pump wave interacts with a Langmuir wave of the same frequency. The OTSI is responsible for the central peak, often observed between the two ion acoustic shoulders in the ion line spectra (Robinson, 1989). Figure 3.10 shows an example of an enhanced ion line spectra during an HF modification experiment (details presented in Paper II). The enhanced ion acoustic shoulders are clearly seen at both altitudes in the right panels. A central peak is observed for the topside ion line enhancement and also for the weaker bottomside enhancement (not shown in detail) above the strongest enhancement. In the left panel the natural ion acoustic wave backscatter as a faint background enhancement at all altitudes, with the up- and down-shifted ion acoustic shoulders clearly identifiable above $\sim$170 km, is also seen. The frequency of the natural ion acoustic waves increases with altitude and thus the shoulders are observed to be further apart for higher altitudes.

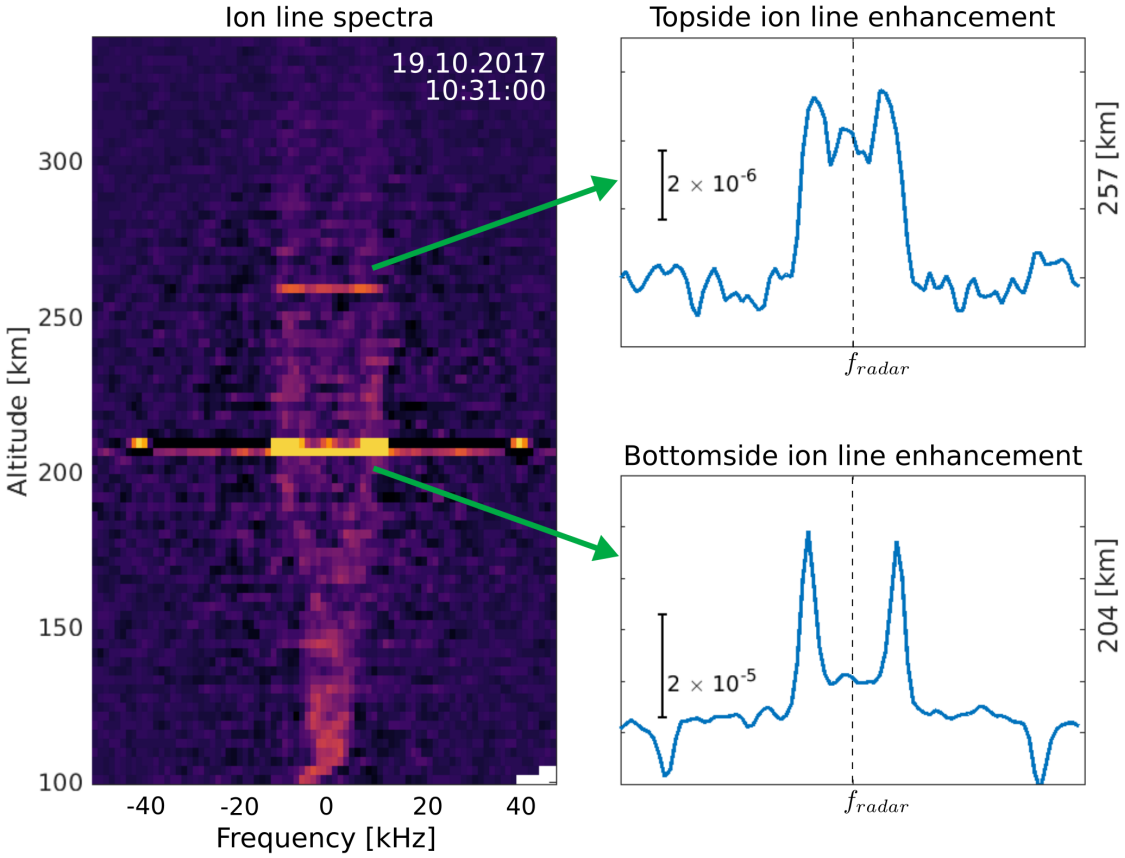

Figure 3.10: An example of enhanced ion line spectra obtained from the EISCAT UHF radar during an HF modification experiment is shown. In the left panel, the frequency spectra of the backscattered signal for every ∼3 km altitude range, is indicated in color. The natural ion acoustic wave can be detected as a faint background enhancement with the ion acoustic double shoulder feature observed at altitudes from ∼170 km to ∼300 km (see Chapter 3.1). At altitudes of 204 km, 207 km and 257 km, clear enhancements of the ion line are visible. The right panels show two of these HF induced, ion line spectra enhancements, from the topside (upper panel) and bottomside (lower panel) ionosphere. The enhancements on the topside ionosphere are approximately an order of magnitude smaller that those at the bottomside. Data from this experiment are presented in Paper II.

Density irregularities

The generation of artificial field aligned density irregularities (FAIs) and ducts by an HF modification wave, where the field referred to here is geomagnetic field $\mathbf{B}_0$, has been extensively studied. The FAIs were first observed during early experiments at Plattville, Colorado (Minkoff et al., 1974). When a pump wave is incident on a small natural density perturbation in the ionosphere, refraction of the pump wave, focusing it into the perturbation, becomes significant and upper hybrid plasma waves are generated where the frequency of the pump wave is equal to the upper hybrid frequency, f_{UH} (Gondarenko

et al., 2005). These are generated most efficiently in the direction of the density gradient ∇n_e, that is, the direction of the highest plasma density increase. As electrons can more easily move along the magnetic field, compared to perpendicular to the magnetic field, the initial small density irregularity will be elongated in the magnetic field aligned direction. Hence, the direction of ∇n_e is perpendicular to $\mathbf{B}_0$ within the striation and the generated upper hybrid waves will be too. The upper hybrid waves are trapped inside this density striation leading to an increase in electron temperature, which in turn further enhances the density striation and thereby also ∇n_e. This positive feedback process is known as the resonance or thermal instability (e.g. Gurevich, 2007; Gurevich et al., 1995; Istomin and Leyser, 1997). The scale size of these pump wave induced, small-scale density striations is 1–100 meter across $\mathbf{B}_0$, while they can stretch several tens of kilometers along $\mathbf{B}_0$, and their generation occurs within a few seconds of heating.

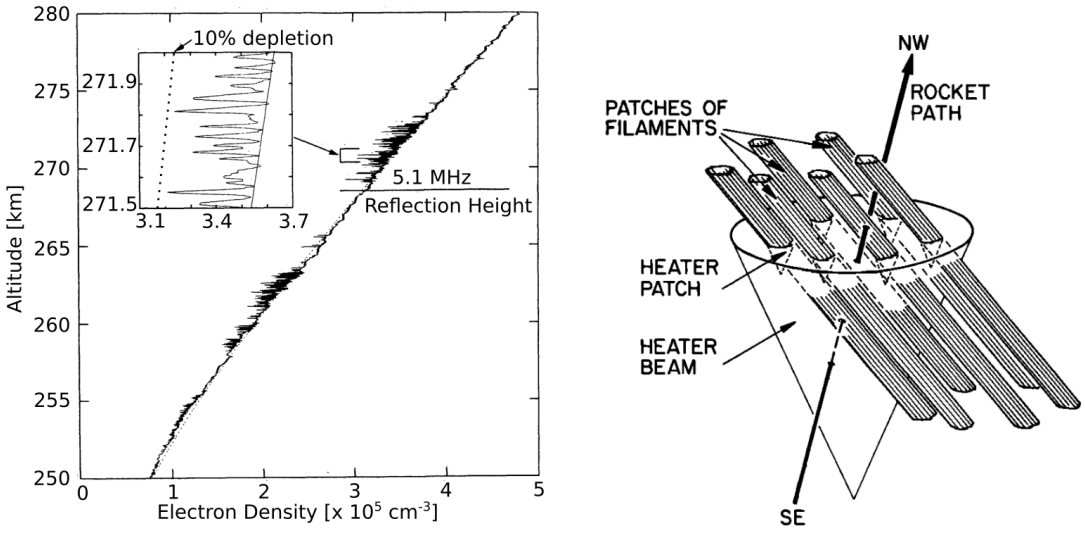

Figure 3.11: In-situ observations of plasma density striations obtained in a rocket experiment through the pump wave beam. The striations where found to be structured in bunches, extending more than 20 km in altitude. The right panel shows the sketch of the rocket trajectory relative to the bunches of density striations in the heated volume. Figures from (Kelley et al., 1995, Fig. 2 and 4).

The small, 7 – 10 meter sized striations ($\perp \mathbf{B}_0$), were observed in-situ in a rocket experiment above Arecibo at mid latitude, by Kelley et al. (1995). The striations were observed in bunches of about 1 – 2 km with regions of similar size with no striations in between them. The mechanism for this bunching has been interpreted in two ways. Either as a diffraction effect of the pump wave on the small-scale striations (Istomin and Leyser, 2001) or as nonlinear self-focusing of the pump wave (Gurevich et al., 1998), where a group of striations are excited simultaneously by the pump wave. Self-focusing may happen when the pump wave illuminates several striations, and the mean plasma density is reduced, producing a lensing effect focusing the pump wave, thus further enhancing the electron temperatures. This increases the growth of density stri-

ations further, which then further increases the focusing effect , leading to a positive feedback loop, known as the thermal self-focusing instability. The result is larger regions of density striations or density depleted ducts and a structuring of the ionospheric plasma. The term duct is used when the scale size of the density striation is large enough that the density gradient within the striation, perpendicular to $\mathbf{B}_0$, leads to total internal reflection and the incident wave is "ducted" along the magnetic field aligned "tube" (Milikh et al., 2008).

Density striations and ducts of all scale sizes are detectable by incoherent and coherent scatter, VHF and UHF radars as well as in-situ by rockets. The rocket experiment by Kelley et al. (1995) also obtained in-situ measurements where the bunching of the disturbed regions is clearly seen. Figure 3.11 presents their results, showing the measured electron density along the rocket trajectory in the left panel. The right panel illustrates the bunching of the density striations relative to the rocket path.

The temporal evolution of the striations varies with the scale size as the different instabilities influence the wave-plasma interaction. Observations of the first $\sim$100 milliseconds after pump wave transmission onset show that the signature Langmuir waves of the parametric decay instability dominate (Djuth et al., 2004). Small-scale striations generate within 1 – 10 seconds and large-scale striations grow on the order of minutes (e.g. Basu et al., 1997; Frolov et al., 1997; Hysell et al., 1996; Myasnikov et al., 2001). The generation of all striations decreases and disappears when the pump frequency approaches that of an electron gyroharmonic frequency (Honary et al., 1999; Najmi et al., 2017). Currently no complete, first-principles model for the growth, decay and bunching of the density striations exists, but many advances toward a better understanding of these processes have been made through numerical modeling (e.g. Eliasson, 2008; Gondarenko et al., 2003, 2005; Najmi et al., 2016).

Magnetic zenith effect

The magnetic zenith (MZ) effect describes the increased plasma response in the direction along the magnetic field during heating experiments and has been observed at all high power heating facilities (e.g. Gurevich, 2007; Gurevich et al., 2002; Pedersen, 2003). Figure 3.12 shows an observational example made by Rietveld et al. (2003), from an HF modification experiment where the HF beam was tilted at the Spitze angle. An image of the artificial 630 nm red auroral light generated by the HF wave, taken by a digital camera is shown. The dashed circles indicate the –3 dB and –6 dB contours of the HF beam mapped onto the assumed emission altitude at 300 km. The upper white cross marks the MZ direction while the lower cross marks the vertical direction. These optical measurements show an example of HF induced aurora that is preferably excited in the MZ direction. Other optical measurements have been made, when during a vertical heating experiment (Kosch et al., 2000) and an experiment pointed 6° south of vertical (Gustavsson et al., 2001), artificial airglow was observed to be displaced toward MZ.

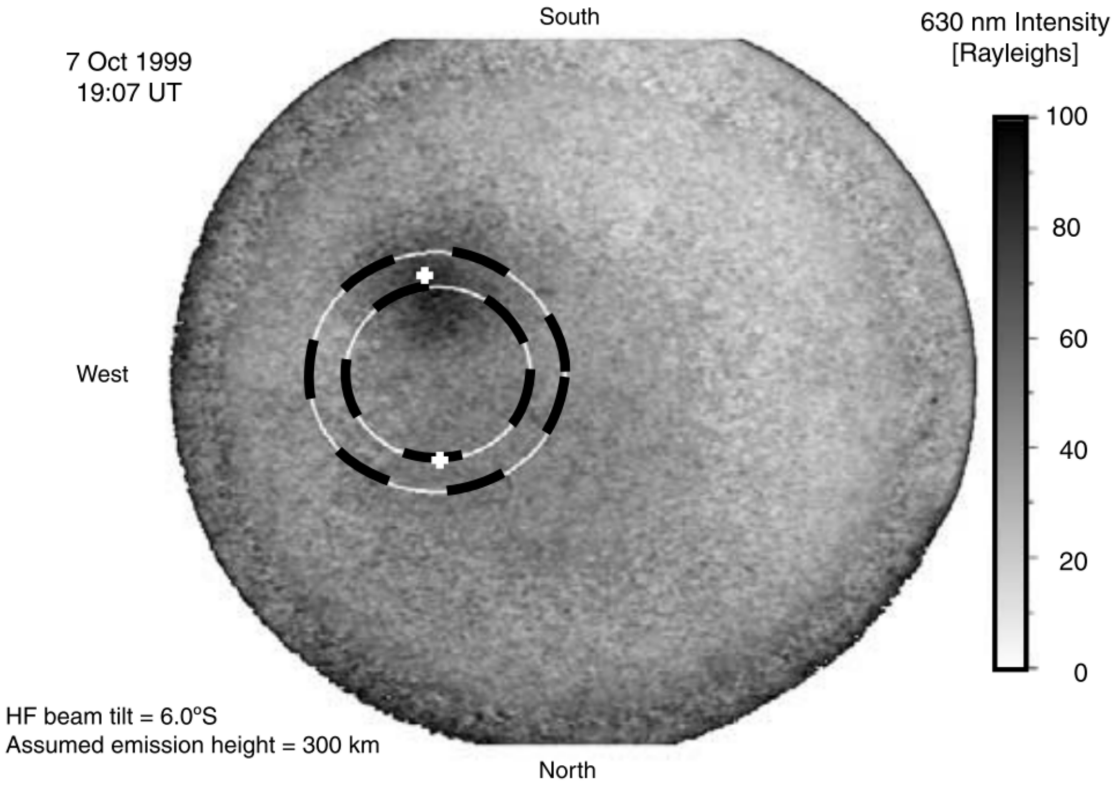

Figure 3.12: Image of HF induced auroral emissions at 630 nm during an experiment with EISCAT Heating directed in the Spitze angle, at 6° from vertical. The dashed circles indicate the projected –3 dB and –6 dB contours of the HF beam at 300 km altitude, and the upper and lower white crosses indicate the MZ direction and the vertical direction, respectively, from the HF transmitter at 300 km. The induced auroral emissions are displaced from the center of the beam toward the MZ. Figure from (Rietveld et al., 2003, Fig. 8b).

Another example of the MZ effect is presented in Paper III, where the electron heating rate in the ionosphere was calculated and compared to the transmitted heating beam. The column-integrated heating rate is at a maximum in the MZ direction and the horizontal angular extent of the heating profile is narrower than that of the pump wave beam. Figure 4.8 shows an excerpt from these results presented in detail in Paper III.

Several mechanisms have been proposed to explain the observed effect, including the thermal self-focusing effect mentioned above (Gurevich et al., 2002). Others include ionospheric tilts (Rietveld et al., 2003) and scattering of small-scale field aligned striations (Zabotin and Kovalenko, 1999). Leyser and Nordblad (2009) suggested that large-scale field aligned striations play an important role in the MZ effect. Some of their results will be discussed further in Chapter 4.

Anomalous absorption

One of the earliest result from ionospheric modification experiments was the reduced reflection of an incident radio wave, passing through a modified ionospheric volume (Cohen and Whitehead, 1970). This is referred to as anomalous absorption of the radio wave (e.g. Gurevich et al., 1996; Robinson et al., 1996; Stubbe, 1996). The conversion of the pump wave energy into upper hybrid waves, leads to effective absorption of the pump wave. Generation of density striations, discussed above, are strongly linked to anomalous absorption and bunches of density striations will give rise to almost total absorption (Dysthe et al., 1982; Gurevich et al., 1996). Similar to the generation of density striations, the anomalous absorption is also dependent on the relative proximity of the pump wave frequency to the electron gyroharmonic frequency, and anomalous absorption is reduced when $f_{HF} \rightarrow f_{dbl}$.

Other phenomena

In addition to the responses and phenomena introduced above, and relevant for this thesis, there are a multitude of other effects and observations arising from modification experiments in the ionosphere, that make up a large body of research. Streltsov et al. (2018) have written a comprehensive review of ionospheric modification experiments, including the current and most recent theoretical and experimental results. Some of the recent important scientific advances are the following:

- Stimulated Electromagnetic Emissions (SEE) where the incident HF wave causes secondary electromagnetic emissions from the perturbed volume (e.g. Leyser, 2001; Sergeev et al., 2006, and references therein). The frequency of these emissions is observed at both lower and higher frequencies than f_{HF}. The generation of SEE may involve both types of nonlinear processes.

- Artificial optical emissions excited by the pump wave. Incident O-mode waves can accelerate the electrons in the ionosphere. These suprathermal electrons in turn will collide with neutral particles in the F-layer causing artificial aurora or airglow, depending on the latitude of the experiment. The energetic electrons excite the same atomic and molecular states as the natural aurora. However, the intensities are shifted toward lower excited energy transitions (e.g Bernhardt et al., 1989; Gustavsson and Eliasson, 2008; Kvammen et al., 2019, and references therein). Observational advances are summarized by e.g. Kosch et al. (2007).

- Descending artificial ionization layers (Pedersen et al., 2010) are an ionizing wavefront caused by suprathermal electrons accelerated by the turbulence created by the incident HF wave (e.g. Mishin and Pedersen, 2011, and references therein).

- The generation and modification of magnetospheric ULF, ELF and VLF waves through different mechanisms initiated by HF heating (e.g. Cohen and Inan, 2012; Cohen et al., 2010; Robinson et al., 2000, and references therein).

- X mode modification experiments have been observed to induce strong plasma responses. Although an RHCP X-mode wave should be mostly reflected below the upper hybrid and plasma resonance region in high latitude experiments, it has been observed to generate field aligned irregularities, optical emissions, electron density enhancements due the electron acceleration well as enhanced plasma and ion lines and SEE (Blagoveshchenskaya, 2021). The mechanisms and causes behind these observed phenomena are still largely unknown.

Chapter 4

Transionospheric wave propagation

In general, an electromagnetic wave transmitted into the ionosphere at a frequency that is lower than the maximum plasma frequency, $f_{HF} < f_{OF2}$, is refracted away, reflected or absorbed. Under certain conditions, a wave can penetrate the region where it would ordinarily be evanescent, propagate to higher altitudes in the ionosphere and continue to space. This transionospheric wave propagation is most easily achieved by specific wave modes, through a radio window. To explain this process, an understanding of different wave modes, their dispersion relation and their propagation in a plasma is needed. The first section of this chapter, focuses on the wave modes specially relevant to this process, that is the O, X, L and Z modes (see also Chapter 2.1 and 3.2). Their properties and characteristics are discussed in detail in the context of wave propagation in the Earth's ionosphere. Following this, the concept of natural and artificial radio windows, as well as other possible mechanisms for transionospheric wave propagation, is considered. In the second section of this chapter, observational evidence of transionospheric propagation from previous studies is reviewed and an overview of the observations central in this thesis and the enclosed papers is given.

4.1 Plasma wave modes and wave propagation

In plasma and space plasma physics, the possible waves are labeled and categorized according to their propagation characteristics. The type of a wave is determined from the relation and direction between the defining parameters. These are the waves frequency ω, vector **k**, electric and magnetic fields, $\mathbf{E}_1$ and $\mathbf{B}_1$, and the ambient magnetic field $\mathbf{B}_0$. The limiting directions of propagation for a wave, specified by **k**, are parallel and perpendicular in relation to the undisturbed background magnetic field, $\mathbf{B}_0$. The waves can be longitudinal or transversal (or a mixture), depending on the direction of $\mathbf{E}_1$ relative to **k**, while the rotation of $\mathbf{E}_1$ determines its polarization. In a magnetized plasma, the polarization of a wave can be circular, elliptical or linear. The elec-

tric field $\mathbf{E}_1$ rotates left handedly, or counterclockwise, in relation to $\mathbf{B}_0$ in a left handed circular polarized (LHCP) wave. This is opposite to the electron gyro motion (see Equation 2.5). Right hand circular polarized (RHCP) waves, as the name implies, rotate in the opposite direction, that is, in the same sense as the electron gyro motion. Also, when a wave is elliptically polarized it is likewise called left handed (LH) or right handed (RH) depending on the rotation of $\mathbf{E}_1$.[1] The polarization determines the propagation, resonances and cutoffs of the wave, as will be shown. When the oscillating magnetic field is zero, $\mathbf{B}_1 = 0$, the wave is electrostatic, while otherwise it is electromagnetic. Along the propagation direction of small amplitude waves, the frequency remains constant while both amplitude and wavelength may change due to absorption and reflection or changes in refractive index, respectively (e.g. Baumjohann and Treumann, 2012; Chen, 1983).

Dispersion relations of relevant wave modes

The complex interaction between the plasma particles and the magnetic field allows for a finite number of wave modes to exist in a plasma. To determine these, the dispersion relation of a wave from the plasma fluid equations and Maxwell's equations for small, propagating amplitude fluctuations is derived (see Chapter 2.1). The dispersion relation of a wave relates the wave frequency ω and the wavevector $\mathbf{k}$ and contains all the information about the propagation of the wave. For high-frequency waves (where $\omega \gg \omega_{IG}$), the dispersion relation for propagation in a cold magnetized plasma, is given by the Appelton-Hartree equation (e.g. Bittencourt, 2013). When calculating ω as a function of $\mathbf{k}$ for propagation angles between $\theta = 0$ and $\theta = 90°$, i.e. covering all propagation directions from parallel to perpendicular to $\mathbf{B}_0$, the dispersion relation takes the form of a set of surfaces (Andre, 1985).

The three dispersion surfaces of the wave modes most relevant for this thesis, for a plasma where $\omega_P > \omega_G$, are shown in Figure 4.1. The relation of ω as a function of $\mathbf{k}$ is shown for wave propagation directions from $\mathbf{k} \parallel \mathbf{B}_0$ on the left edge of the plot, to $\mathbf{k} \perp \mathbf{B}_0$ along the right side of the plot, for $\omega_P = \omega_G$. The colors of the surfaces indicate the polarization of the waves from left handed shown in blue, to right handed shown in yellow. Along the edges on each side of the surfaces, one recognizes the two dimensional dispersion relations commonly shown in plasma physics textbooks (e.g. Baumjohann and Treumann, 2012; Bittencourt, 2013; Chen, 1983; Swanson, 2003). The dispersion relation of a given wave $\omega(\mathbf{k}, \theta)$ is represented as a point on one of the surfaces. The phase velocity ν_{ph}, of the wave is given by the slope of the line from the origin

[1] It should be noted here, that in some fields of research (like engineering), the polarization is defined by the rotation of $\mathbf{E}_1$ relative to $\mathbf{k}$, not $\mathbf{B}_0$. This results in opposite definitions for for example RHCP and LHCP waves propagating antiparallel to $\mathbf{B}_0$. Additionally, the names that many of the different waves have are different in different fields, also in adjacent fields like laboratory plasma physics and space plasma physics. This can be very confusing, and hence determining the definitions that are used is essential for studying literature on waves in plasmas.

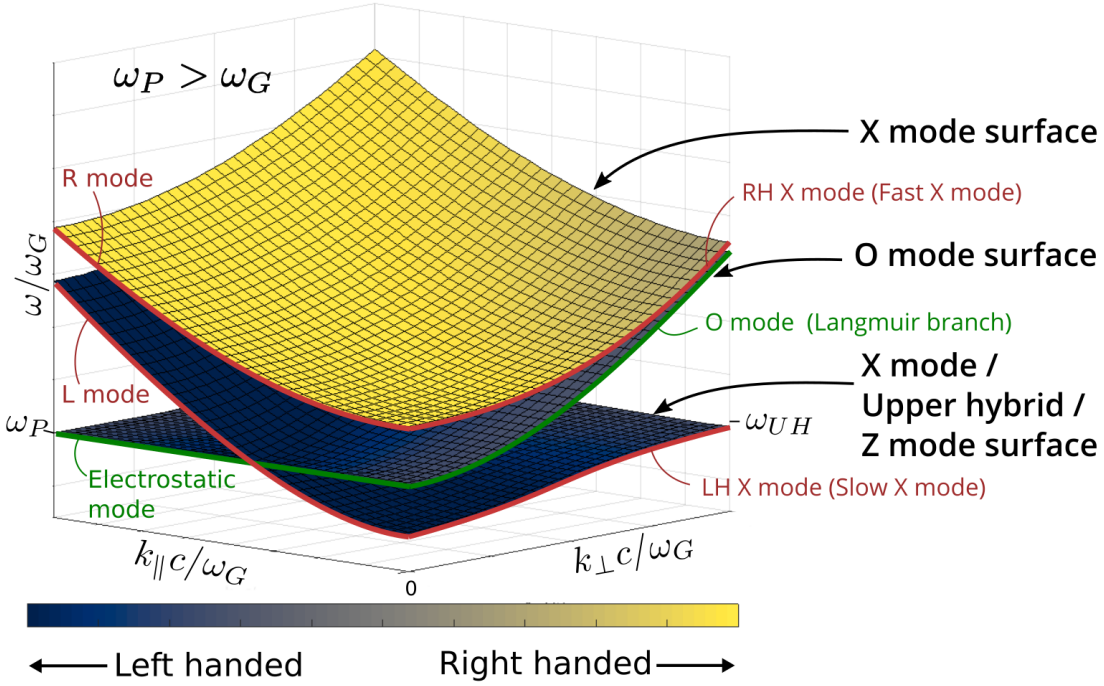

Figure 4.1: Dispersion surfaces of the RH X mode (upper), O mode (middle) and LH X mode (lower). the lower LH X-mode surface is also called the slow X-mode or upper hybrid surface, and the Z-mode surface for small **k**) plasma waves. Wave propagation perpendicular to $\mathbf{B}_0$ is found on the right edge of the plot, while propagation parallel to $\mathbf{B}_0$ is found on the left edge of the plot. The names of the wave modes on these edges are indicated. The color of the surfaces indicate the polarization of the waves from left handed (blue) to right handed (yellow) in relation to $\mathbf{B}_0$. Dispersion surface plot produced with IRFU-Matlab analysis package (IRFU, 2003).

to that point on the surface, while the group velocity ν_g of the wave is given by the tangent to the surface in the direction of the steepest ascent at that point. While the ν_{ph} is always parallel to **k**, ν_g is not necessarily in the same direction.

The upper dispersion surface is that of the RH X-mode or fast X-mode waves with the purely electromagnetic RHCP R mode along the $\mathbf{k} \parallel \mathbf{B}_0$ edge (the R-mode dispersion relation is given in Equation 2.17). These X-mode waves are partially longitudinal and partially transverse and they approach the speed of light, c, for $(\omega, \mathbf{k} \rightarrow \infty)$, for all angles of propagation. The second surface is that of the O mode. For small values of **k** and approaching parallel propagation the wave turns gradually more electrostatic and ω approaches the electrostatic wave mode. When the O-mode wave is propagating perpendicular to $\mathbf{B}_0$ (along right edge of the plot), then $\mathbf{E}_1 \parallel \mathbf{B}_0$ and the plasma response is unaffected by the magnetic field. The dispersion relation then, is the same as for an electromagnetic wave in an unmagnetized plasma and the wave propagates as if $\mathbf{B}_0 = 0$ (see Equation 2.9). The lower dispersion surface is the lower branch X-mode surface. This is sometimes called the upper hybrid surface and Z-mode or slow X-mode surface for small **k** (Andre, 1985). O-mode waves and

waves on this lower X-mode surface are generally left handed while the upper branch X mode is generally right handed, as seen from the colored surfaces in Figure 4.1. In the rest of this thesis the upper surface will be referred to as the RH X-mode surface while the lower surface will be referred to as the LH X-mode surface. Similarly, a wave will be referred to as an RH X-mode wave for waves with dispersion relations on the upper surface, and LH X-mode wave for waves with dispersion relations on the lower X-mode surface. Along the $\mathbf{k} \parallel \mathbf{B}_0$ edge, the L-mode wave dispersion curve connects the O-mode and LH X-mode surfaces at $\omega = \omega_P$. When $\mathbf{k} \perp \mathbf{B}_0$ the wave on the LH X-mode surface edge has a resonance at the upper hybrid frequency (see Equation 2.16), and it connects to electrostatic Bernstein waves (not shown) for high values of $\mathbf{k}_\perp$ (Rönnmark, 1990).

Wave propagation in a plasma

A radio wave incident in the ionosphere, with frequency ω_{HF}, will be continuously refracted as it propagates, since the ionospheric plasma density varies, and consequently $\mathbf{k}$ will change (ω_{HF} does not change). The two limiting cases for the propagation of a wave are when $\mathbf{k} \to 0$ and when $\mathbf{k} \to \infty$. A propagating wave has a cutoff or reflection point when $\mathbf{k} \to 0$ and the direction of propagation is reversed. A resonance is encountered when $\mathbf{k} \to \infty$, which also implies that the phase velocity of the wave becomes zero and the energy of an incident wave is absorbed. In the ionospheric plasma where ω_P and ω_G are changing as the altitude changes, a propagating wave will encounter cutoffs and resonances at different altitudes depending on the wave mode. For the O, L, R and both RH and LH X-mode waves, these are given by Equation 2.19, 2.21 and 2.20 in Chapter 2.1. The refraction of the wave also affects the wave electric field $\mathbf{E}_1$ which will change from being mostly perpendicular to being directed essentially parallel to $\mathbf{B}_0$, where the wave is reflected (e.g. Rietveld et al., 1993).

Figure 4.2 shows a schematic example of how an incident O-mode wave may be refracted in the ionosphere. In the upper left panel the altitude profile of the upper hybrid frequency and the fourth harmonic of the electron gyro frequency are shown. The transmitted pump frequency is indicated, as well as 3 positions, A, B and C, in altitude. Two sets of dots, green and blue, are indicated to illustrate two different incident rays of the pump wave at these altitudes. The difference between the two sets may for example be a small difference in $\mathbf{k}$ or angle of incidence θ. As a wave propagates between the altitudes A, B and C, it will refract and both $\mathbf{k}_\perp$ and $\mathbf{k}_\parallel$ will change. Hence, a wave at altitudes A, B and C in the upper left panel, will correspond to a point on a set of dispersion surfaces, with ω_P and ω_G at that respective altitude. These are depicted in panels A, B and C in the figure. The dispersion surfaces of the O mode and LH X mode are shown as before, in greater detail. Colors now indicate the direction of $\mathbf{E}_1$ relative to $\mathbf{B}_0$. The incident waves, defined by ω_{HF} and $\mathbf{k}$, are each represented by a point on one of the dispersion surfaces, showing how a propagating wave is refracted.

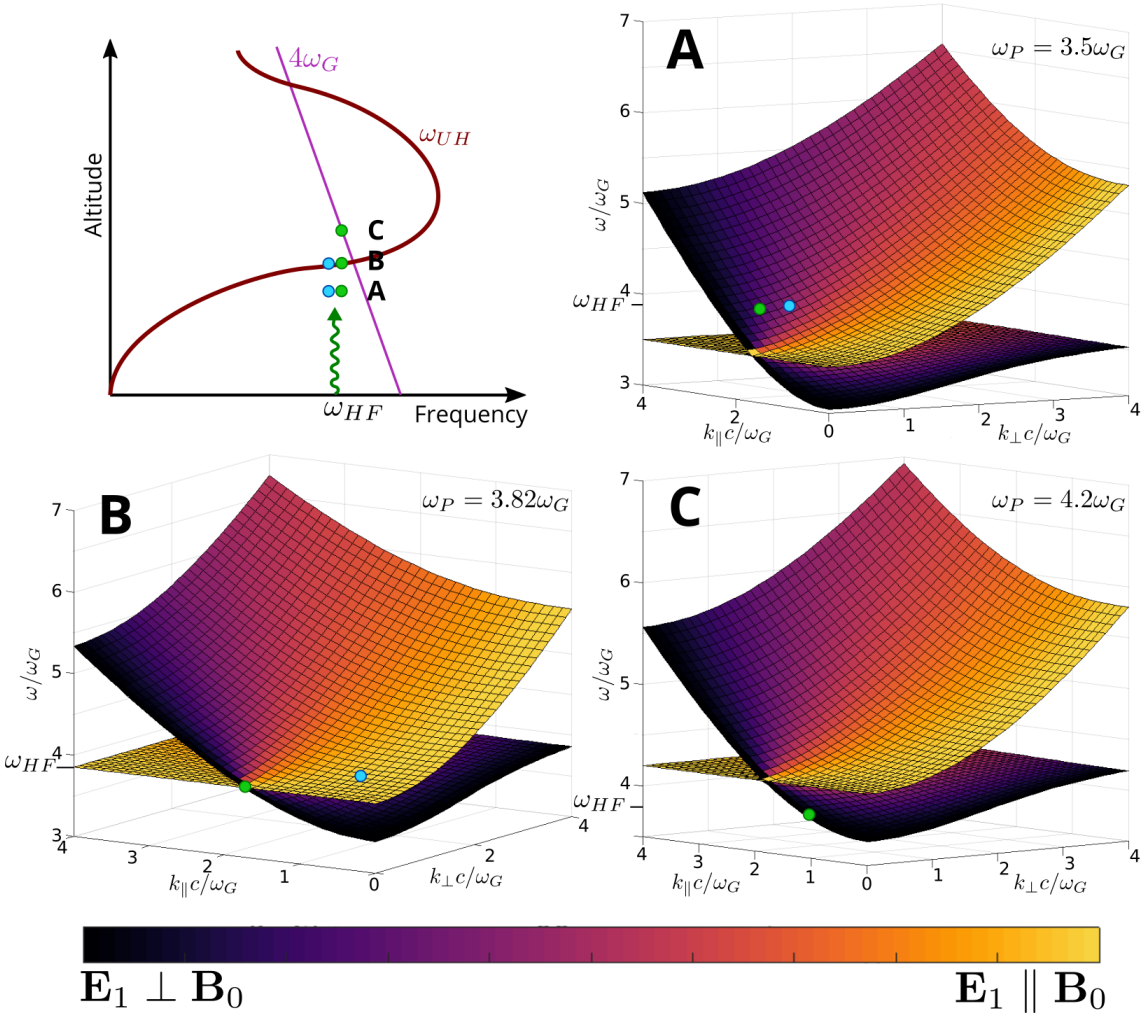

Figure 4.2: Schematic of the dispersion relations of a propagating wave. The upper left panel, showing the altitude profile of the upper hybrid frequency and the fourth harmonic of the electron gyro frequency, indicates three points where an incident O-mode wave may pass through. Each point corresponds to one of the other three panels denoted by the letters. In these panels the dispersion surface of the O and LH X-mode/upper hybrid (Z mode) is shown and the point of the dispersion relation for the incident O-mode wave is indicated. An incident LHCP wave propagating strictly field aligned at the radio window may pass from one surface to the other and continue propagation, without mode conversion or being reflected. The wave will continue propagation unless it encounters the L-mode cutoff (see Equation 2.21). The values in this schematic example are arbitrarily chosen to represent conditions close to the double resonance frequency (see Equation 3.4) and do not present real data. Dispersion surface plot produced with IRFU-Matlab analysis package (IRFU, 2003).

As the wave propagates in the ionosphere, the surrounding plasma density and gyro frequency change, so the frequency-ratio ω/ω_G changes. Hence, the dispersion surfaces in Figure 4.2 shift on the frequency-axis (vertical axis in the figure). For conditions similar to those at point A in the upper left panel, the corresponding points for the two waves on the dispersion surfaces might

be somewhere close to that shown in the upper right panel, labeled A. An O-mode wave with $\mathbf{k}_\perp \neq 0$ and $\mathbf{k}_\parallel \neq 0$, approaching the upper hybrid resonance region, will have a point somewhere on the O mode dispersion surface, depending on the angle of incidence relative to $\mathbf{B}_0$ and the plasma density. In the illustration in Figure 4.2, the two wave rays might differ slightly in angle of incidence θ. They might, for example, originate from two different positions within the same HF beam, and therefore have a slightly different propagation, thus corresponding to two different points on the surface.

The waves will be continuously refracted in the increasing plasma density, and if $\mathbf{k}_\perp$ remains unequal to zero, the wave will eventually be reflected when $\mathbf{E}_1 \parallel \mathbf{B}_0$ and $\mathbf{k}_\parallel = 0$. This corresponds to a change in color from black to yellow on the O mode dispersion surface. In the lower left panel (B) this is illustrated by the incident wave depicted by the blue point, which has refracted such that the dispersion relation of the wave is now on the area of the O-mode surface where $\mathbf{E}_1 \parallel \mathbf{B}_0$ (yellow). This wave is reflected and can not propagate to higher altitudes than where $\omega_P > \omega_{HF}$.

If, by refraction, the wave has $\mathbf{k}_\perp = 0$, that is it is now propagating strictly field aligned in the L mode, at the point where $\omega_{HF} = 3.8\omega_P$ [2], as illustrated by the green point in the lower left panel (B), the incident wave is not reflected (or absorbed). At the point where the two surfaces touch an incident L-mode wave may pass from one surface to the other and continue propagation. The wave can then propagate to altitudes where $\omega_P > \omega_{HF}$ and the dispersion relation, now on the LH X-mode (Z-mode) surface might correspond to a point as illustrated in the lower right panel (C). This is the radio window. If the propagating wave does not encounter the L-mode cutoff (see Equation 2.21 and Figure 3.8) it will continue propagation to the topside ionosphere, through the topside radio window and into space.

Wave propagation through the ionosphere

Different mechanisms for transionospheric wave propagation have been proposed. These are considered in this section, starting with wave propagation through the standard radio window at the Spitze angle and through artificial radio windows. Other proposed mechanisms for wave propagation through the ionosphere are introduced briefly in the last part of this section.

The standard radio window

A vertically transmitted wave in the O mode will reflect at the O-mode cutoff altitude, while a wave transmitted in the RH X mode will reflect at the corresponding X-mode cutoff altitude (see Chapter 3.2, Equation 2.19 and 2.20 and Figure 3.8). Waves transmitted at angles between the vertical and the Spitze will also reflect at these respective cutoff altitudes, while waves transmitted at

[2] The value $\omega_{HF} = 3.8\omega_P$ is chosen arbitrarily for this schematic example, but corresponds to conditions close to the double resonance frequency (see Equation 3.4).

larger angles, relative to zenith, will reflect at successively lower altitudes. The exception to this are waves transmitted at the Spitze angle. In Figure 3.8, propagation through the standard radio window at the EISCAT facilities is illustrated by the central O-mode ray. When transmitted at the Spitze angle, a propagating O-mode wave will have refracted through the increasing plasma density such that it is in the L mode when it reaches the point where $\omega_{HF} = \omega_P$, where it can pass through the radio window and continue propagation to higher altitudes (regions where $\omega_P > \omega_{HF}$). If the pump frequency is larger than the L-mode cutoff frequency, $\omega_{HF} > \omega_{L-cut}$, the wave will continue propagation to the topside radio window and space. The theory of linear conversion of an incident radio wave was first adapted to ionospheric modification experiments by Mjølhus and Flå (1984). The linear conversion of the wave mode is illustrated by the change in color of the ray in Figure 3.8. In Figure 4.2, the green points on the dispersion surfaces illustrates this refraction process, and after passing through the radio window it is apparent that the dispersion relation of the wave ,$(\omega_{HF}, \mathbf{k})$ now is a point on the LH X-mode (Z-mode) dispersion surface. For a wave with ω_{HF} and $\mathbf{k}$ on the L-mode curve, it is apparent that $\mathbf{E}_1$ relative to $\mathbf{B}_0$ does not change (no change in color), in Figure 4.2.

A wave that is at or in close vicinity of the radio window will be transmitted completely or partially transmitted and partially reflected (Mjølhus, 1990). Partially penetrating waves will propagate slightly off the Spitze angle after passing the radio window and refract on the LH X-mode (Z-mode) surface. Thus they will not meet the topside radio window or only partially and be partially reflected at the topside radio window into a northward propagation path (Mjølhus, 1990; Mjølhus and Flå, 1984).

Artificial radio windows

Artificial radio windows can be generated at locations away from the standard radio window, by large-scale, field aligned density striations and ducts. In a ray-tracing study, Nordblad and Leyser (2010) show that refraction on duct walls, and self-focusing of the incident LHCP wave can affect the polarization and refraction such that the wave is guided into the L mode in kilometer scale density ducts in an otherwise horizontally stratified ionosphere. Thus guided, the wave can pass the O-mode cutoff altitude, where it would otherwise be reflected and continue propagating to regions with higher plasma density. If the wave frequency is above the L-mode cutoff frequency (Equation 2.21) the wave will continue propagation to the topside ionosphere. The large-scale density striations facilitating this can be generated by the pump wave on naturally existing small-scale density striations (Gurevich et al., 1995) or created by the pump wave (e.g. Gondarenko et al., 2005; Gurevich et al., 1998; Istomin and Leyser, 2001)(see also Section 3.2).

Other mechanisms for transionospheric wave propagation

In addition to propagation through the standard or artificial radio windows, several other mechanisms have been proposed for O-mode wave propagation beyond the cutoff altitude. A resonant scattering mechanism for modification experiments with low duty cycles was suggested by Mishin et al. (2001). They propose that an O-mode wave can efficiently scatter into Z-modes waves on small-scale density striations incident above the upper hybrid resonance region . Such small-scale density striations are generated (see Section 3.2) within a few seconds (e.g. Myasnikov et al., 2001) by the pump wave through the resonant instability (e.g. Vas'kov and Gurevich, 1977).

Eliasson (2008) conducted a simulation for low duty cycle experiments and an ambient magnetic field tilted to 13°, replicating conditions during EISCAT Heating experiments. The simulations were done for low duty-cycle experiments to minimize the effect of density striations generated by the pump wave. A vertically propagating, large amplitude, O-mode wave was shown to reach the reflection altitude, where it decayed into a Langmuir wave and an ion acoustic wave through the parametric decay instability (see Section 3.2). This was followed by strong Langmuir turbulence and excitation of large amplitude Z-mode waves. The Z-mode wave continued propagation beyond the O-mode reflection altitude.

Vodyanitskij et al. (1974) suggested that resonant electrons, excited by an X-mode pump wave, can carry the plasma oscillations across the reflection altitude. This mechanism is proposed for mid latitudes, where the ambient magnetic field is tilted significantly compared to high latitudes.

4.2 Observations

Observations of transmitted electromagnetic waves propagating beyond the cutoff altitude have been made multiple times in the past. The first observations of this phenomenon were made in and ionogram, almost a decade after the development of the first ionosonde. Since, sporadic evidence of wave propagation beyond the cutoff altitude and also through the ionosphere and to the topside, and further into space has been presented in ISR and satellite measurements. In the first section of this chapter, all past observations are listed and presented. In the second section, the new, systematically recurring observations of transionospheric wave propagation that form the basis of this thesis, are summarized.

Past observations of transionospheric radio wave propagation

The first observations of a transmitted radio wave propagating beyond its cutoff altitude were reported by Toshniwal (1935) who presented a very short-lived third trace, observed during sunset, in addition to the usual two traces in ionosonde measurements. Shortly after, Harang (1936) confirmed these with the first direct observations. He observed the third trace, that became known as the F region triple splitting, in ionograms from the Tromsø ionosonde. The two common traces observed in ionograms from ionosondes, are reflections of the transmitted radio wave at RH X-mode cutoff altitude and the O-mode cutoff altitude (orange and blue lines in Figure 3.9). Several attempts were made to explain the third trace in the ionograms and to understand how an incident wave can propagate beyond both the RH X and O-mode cutoff altitude. They were attributed to the Z-mode wave and wave reflections from the Z-mode (or LH X-mode) cutoff (yellow line in Figure 3.9) by Poeverlein (1949) and Millington (1954). An example of an ionogram from the Tromsø Dynasonde, showing the three traces, is shown in Figure 4.3. The turquoise dotted line indicates the RH X-mode reflections while the two red dotted lines indicate the O-mode (right) and Z-mode (left) reflections. The idea of a ”hole” in the ionosphere for transmitted radio waves to pass through, was first proposed by Ellis (1956), who noted that the angle of arrival of the wave in the ionosphere was critical for the observation of Z-mode traces, and that the ”hole” had a very narrow angular extent. Thus the radio window was found.

The first evidence of radio wave propagation beyond the RH X-mode and O-mode cutoff altitude in IS radar measurements was presented by Ganguly and Gordon (1983). During an ionospheric modification experiment, transmitting an HF pump wave in the O mode, at the mid latitude Arecibo Observatory, an enhanced plasma line signature was observed $\sim$50 km above the bottomside cutoff altitude of the O-mode wave. The ionospheric plasma frequency was not measured during the experiment and hence it is unclear if the enhanced plasma line appeared at the topside ionosphere or below.

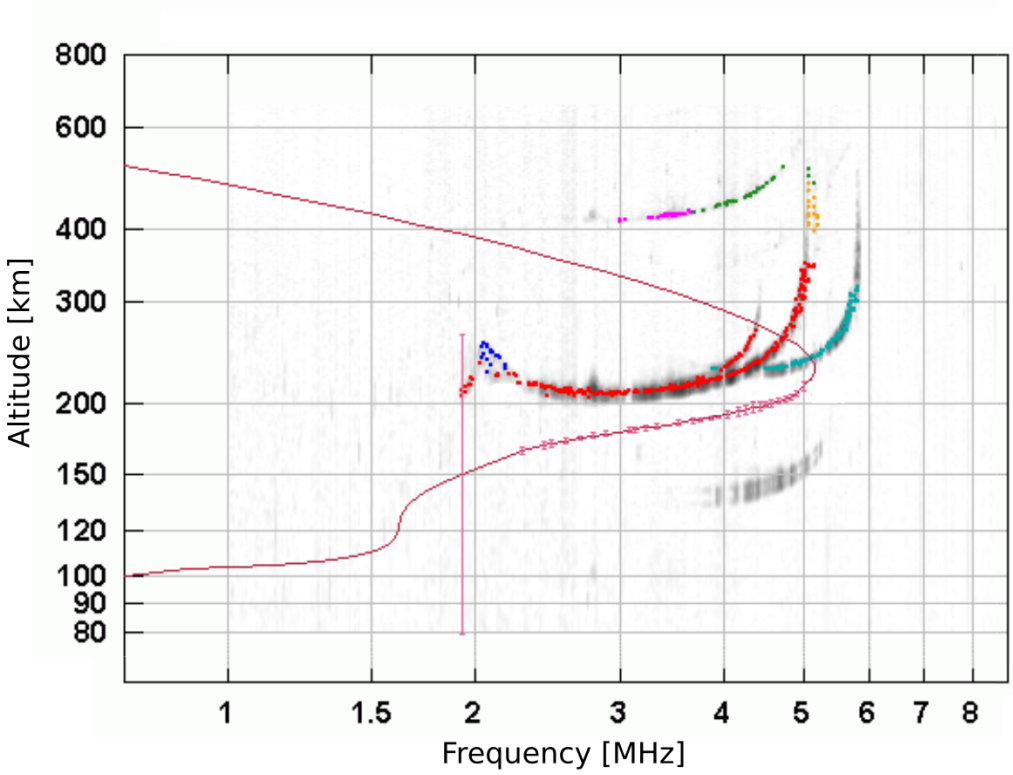

Figure 4.3: Example of an ionogram from the Tromsø Dynasonde showing the three traces of the RH X mode (bluegreen), O mode (red right) and Z mode (red left) reflections on the bottomside ionosphere.

The Z-mode traces in ionograms and possibly the observations of enhanced plasma lines made by Ganguly and Gordon (1983), do not provide evidence of transionospheric wave propagation, but only show that an incident wave may pass the bottomside cutoff altitudes of the O- and RH X-mode waves. The first clear measurements of transmitted HF pump wave propagating to the topside ionosphere were presented by Isham et al. (1990). Coincidentally, these were also the first observations of transionospheric wave propagation outside the standard radio window. In an experiment using EISCAT Heating and the UHF radar facilities, in a magnetic field aligned direction, ion line power profiles showed evidence of the existence of topside HF enhanced ion lines (THFIL). These appeared for the first ten seconds after HF transmission on, for some of the transmitted HF pulses. Figure 4.4 shows the ion line power profile with clear enhancements at the bottom and topside ionosphere, presented by them.

In a follow up experiment a few years later, Isham et al. (1999a,b) observed THFIL with both the EISCAT UHF radar, scanning between the vertical and field aligned direction, and the EISCAT VHF radar pointing in the vertical direction. The EISCAT Heating facility was transmitting and O-mode wave in the direction of the Spitze angle for 200 milliseconds every 10 seconds. Interestingly, the THFIL were clearly observed with both radars and topside plasma line en-

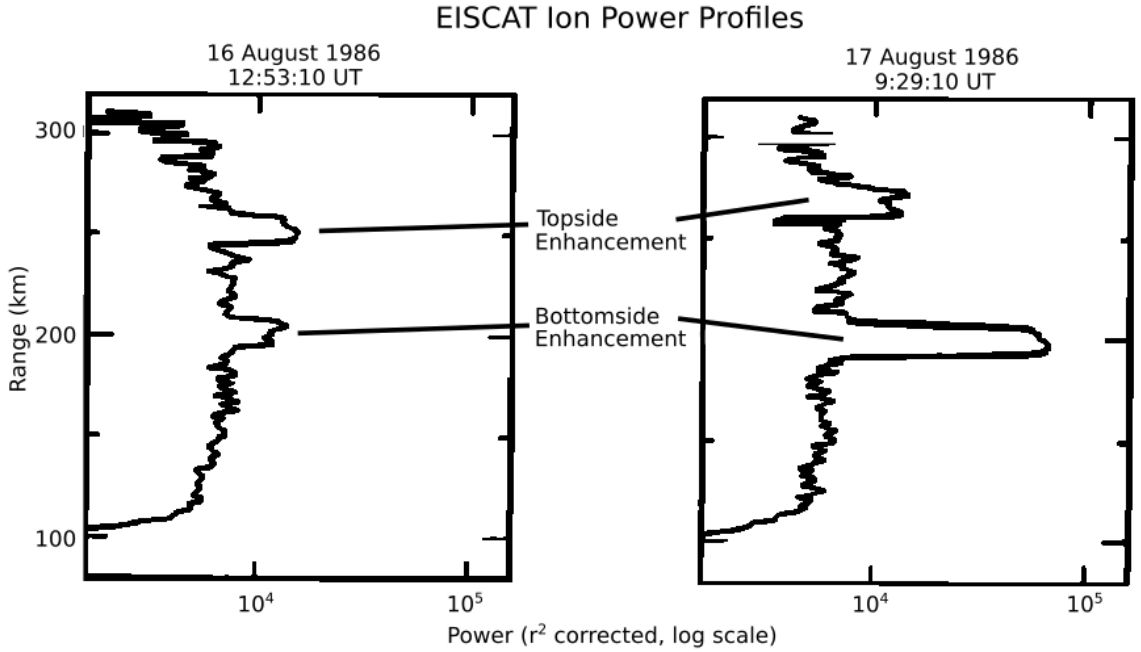

Figure 4.4: Ion line power profiles measured during HF modification experiments at EISCAT Tromsø. Clear enhancements at the bottom and topside ionosphere can be seen. Adapted from Isham et al. (1990, Fig. 6).

hancements were observed in the VHF data. In the UHF measurements, THFIL occurred predominantly at an angle between the Spitze and the magnetic field aligned direction. The authors remark on this result and the apparent evidence of pump wave propagation beyond the reflection altitude, outside the normal radio window, and attribute these observations to an O to Z mode conversion of the wave. However, they note that theoretical explanations for the mechanism producing the THFIL and the angular extent at which they appear, were insufficient that time (Isham et al., 1999a).

THFIL were first observed in a vertically directed modification experiment by Rietveld et al. (2002). Here, the THFIL were observed at the topside of a strongly enhanced E region. In this experiment too, the authors attribute the observations to a coupling of the O mode to the Z mode allowing for wave propagation through the E-region peak, although outside the standard radio window. Eliasson (2008) proposed a mechanism for transionospheric propagation of a radio wave, specifically for low duty cycle experiments (see also Section 4.1) in their simulation study, to explain the observations made by Isham et al. (1999a,b) and Rietveld et al. (2002).

THFIL were again observed when Kosch et al. (2011) studied the angular extent of the standard radio window. EISCAT Heating was directed 9° south of zenith while the EISCAT UHF radar was scanned in small steps, along the magnetic meridian. THFIL were consistently observed and their observations showed the radio window to be shifted to $\sim$7 – 8° south of zenith instead of $\sim$6°. Additionally, the observations of the THFIL are displaced 2° – 3° equator-ward,

relative to the bottomside HF induced ion line enhancements (BHFIL). They suggest that this is the result of a tilted ionosphere, observed in Dynasonde data obtained simultaneously. This displacement was also theoretically predicted by Mjølhus and Flå (1984).

The first space borne observations of transionospheric wave propagation during HF modification experiments were presented by Leyser et al. (2018). During a fly-by, the magnetic field aligned transmitted pump wave was detected on the CASSIOPE satellite, although the pump frequency was well below the maximum plasma frequency in the ionosphere. The transmitted wave is interpreted to propagate in the L mode, through an artificial radio window, generated by pump wave induced density depletion (see Section 4.1).

Borisova et al. (2020) present THFIL observations as well as simultaneously enhanced plasma lines at the topside ionosphere during an experiment in 2013. In the experiment, the O-mode pump wave was directed in a magnetic field aligned direction with a 60% duty cycle (20 minutes on – 10 minutes off). The author attribute the observations to the propagation mechanism suggested by Eliasson (2008). However, Eliasson (2008) propose a mechanism for the generation of topside enhancements for very low duty cycles and vertically propagating pump wave experiments. Considering the long HF-on pulse and the direction of propagation in the experiments performed by Borisova et al. (2020), it is likely that upper hybrid waves and density striations are generated. Hence, it is possible that the wave is guided into the L mode by the density striations and propagates to the topside ionosphere thus Their results are therefore consistent with propagation through an artificial radio window in the L mode (see Chapter 4.1). Since Eliasson (2008) modeled only the first few milliseconds of vertical experiments, it is unclear if that proposed mechanism is applicable to the observations made by Borisova et al. (2020).

New observations of recurring transionospheric wave propagation

Observations from multiple HF modification experiments performed at the EISCAT facilities form the basis of this thesis. During all experiments, evidence of wave propagation beyond the cutoff altitude of the transmitted wave mode was observed. The details are presented and their possible generation mechanisms and involved physics are thoroughly discussed in the accompanying papers. In this section some of these results are summarized, focusing on the observations demonstrating transiononspheric wave propagation repeatedly.

In Paper I and II, evidence of transionospheric wave propagation was observed as THFIL in the EISCAT UHF radar measurements. The THFIL were observed consistently during multiple experiments, under different conditions. During the experiments an O-mode pump wave was transmitted in a magnetic field aligned direction while the pump frequency, f_{HF}, was stepped in small steps around the fourth harmonic of the double resonance frequency, $4f_{dbl}$ (see Equation 3.4). A typical example of the observations from one experi-

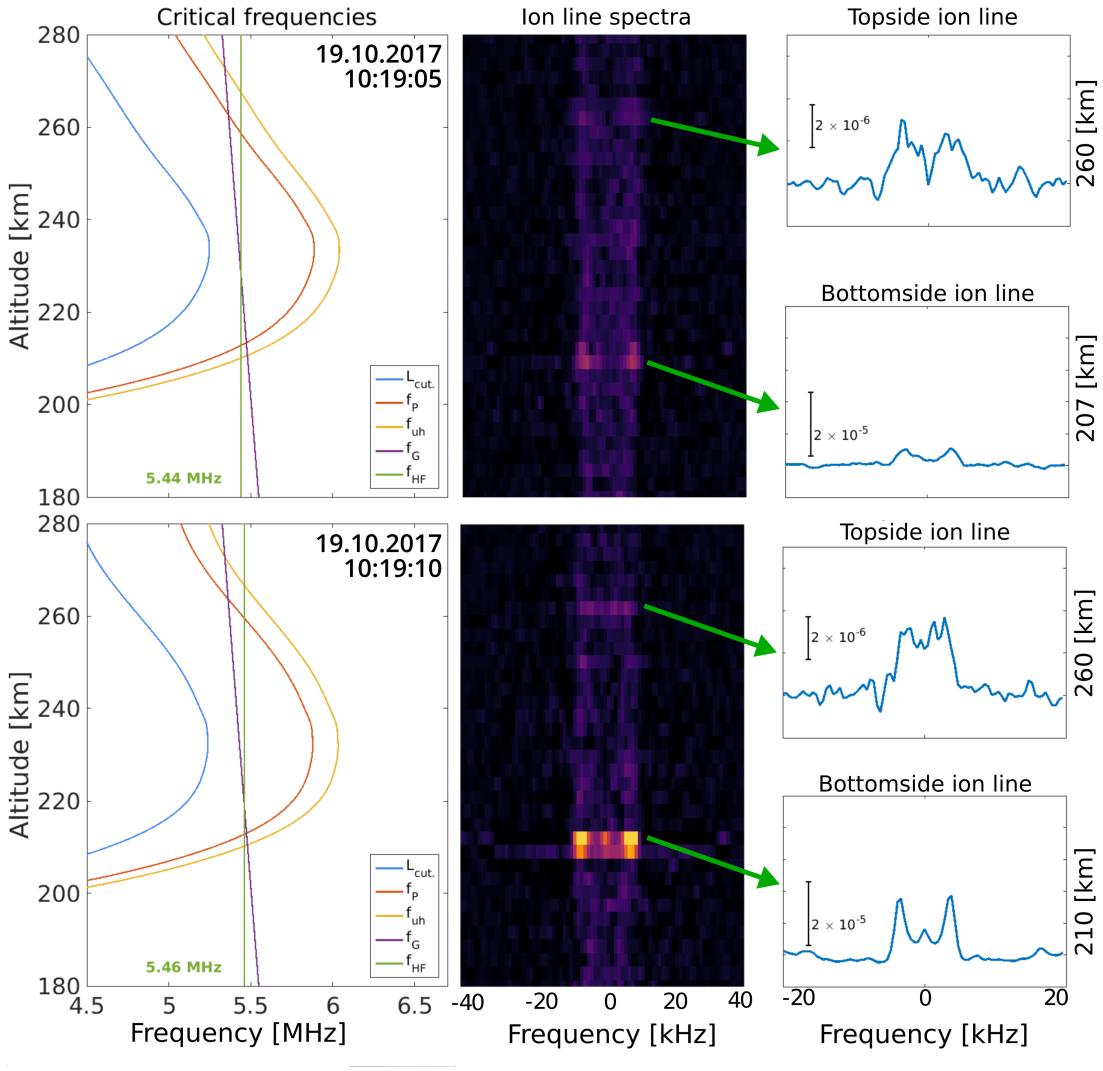

Figure 4.5: Example of enhanced ion line spectra at two subsequent instances in time during an experiment, transmitting an O mode pump wave in the MZ direction. Left panels show the critical frequencies, f_P (red), f_UH (yellow), f_{L-cut} (blue), f_{HF} (green) and $4f_G$ (purple). The middle panels show the ion line frequency spectra at altitudes from 180 km to 280 km, while the right panels show the frequency line spectra at the enhanced altitudes. The THFIL at the first time-step (first right panel) are weaker than the THFIL at the next time step (third right panel), where it becomes clearly visible as a brighter purple color, also in the lower middle panel. The altitude of the strongest BHFIL increases from 207 km to 210 km in the second time-step, where the "double shoulder" shape and a central feature are clearly seen in the line spectra of the corresponding right panel.

ment, at two subsequent instances in time are shown in Figure 4.5. In the left panels the altitude profiles of the plasma (red), upper hybrid (yellow) and L-mode cutoff (blue) frequencies are shown. These are calculated from observations of the natural Langmuir waves observed in the plasma line spectra measurements of the radar (see Chapter 5 for details). The fourth harmonic

of the electron gyro frequency (purple) and the pump frequency (green) are also indicated. The middle and right panels are as in Figure 3.10, with the ion line frequency spectra in the middle and the line spectra of the enhanced altitudes to the right. In the left panels it is evident that f_{HF} is well above the L-mode cutoff, and well below the maximum plasma frequency f_{OF2}. So here, an incident L-mode wave, first passing through an artificial radio window (see Section 4.1), can propagate from the bottomside ionosphere to the topside ionosphere without encountering the cutoff. The THFIL, seen at 260 km in the middle panels of Figure 4.5 and growing from one time-step to the next (upper to lower panel), are interpreted as evidence of this transionospheric wave propagation. Comparing the line spectra of the THFIL in the first and third panel on the right, to the line spectra of the BHFIL in the second and fourth panel on the right, it can be seen that the THFIL are approximately an order of magnitude smaller than the BHFIL. The example presented in this figure is illustrative for all observations of THFIL during the experiments. THFIL occurred repeatedly, and one of the important parameters was found to be that $f_{HF} > f_{L-cut}$.

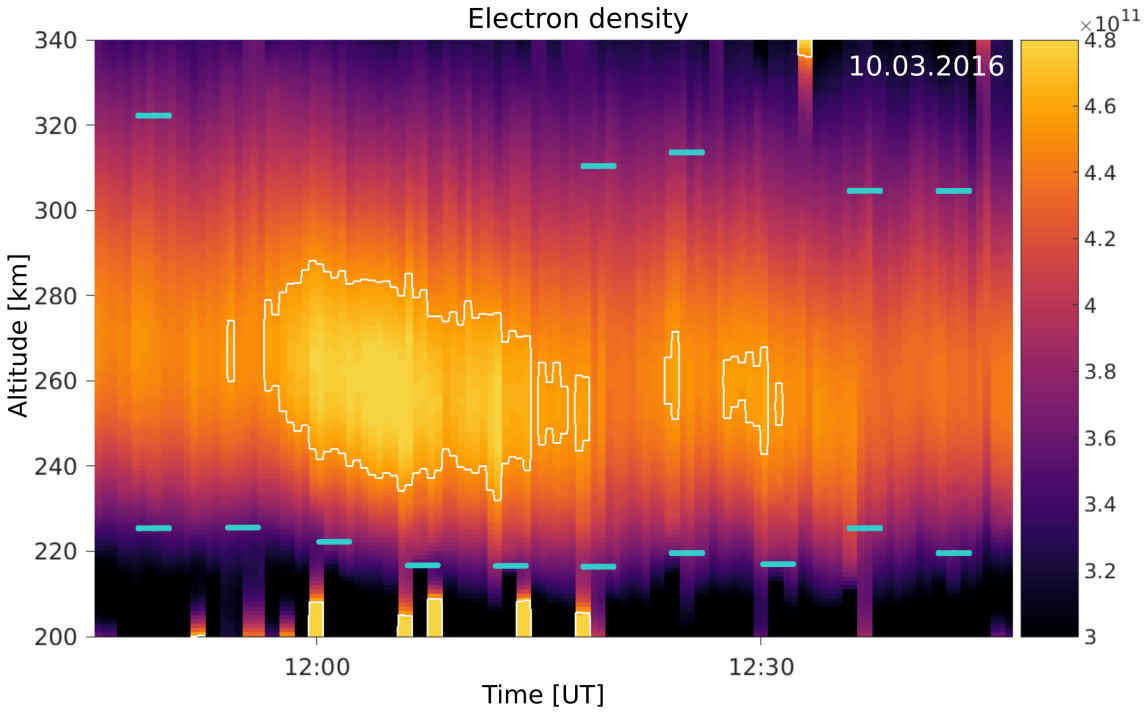

Figure 4.6: Electron density calculated from the plasma line observations of the natural Langmuir waves in the EISCAT UHF radar measurements. The altitude and time of the observations of the THFIL and BHFIL are indicated by the blue bars. The L-mode cutoff, when it is 5.42 MHz or above, is superposed on the electron density by the white contour line. this indicated when f_{HF} approaches the cutoff frequency during the frequency stepping in the experiment.

An example demonstrating this is given in Figure 4.6 showing a $\sim$1 hour segment of the electron density measurements during one experiment. The time

and altitude of the THFIL and BHFIL are superposed as blue bars on the figure. The maximum L-mode cutoff frequency changes naturally with the changing ionospheric plasma density and the white contour line superposed on the figure, indicates when the L-mode cutoff frequency reached 5.42 MHz or above. The value of 5.42 MHz was chosen as this was the mean pump frequency during the experiment and is intended to give an indication of when f_{HF} was close to or below f_{L-cut}. If the frequency f_{HF} of an incident pump wave in the L mode, is below that of f_{L-cut}, the wave can not propagate further. In the figure this is seen as THFIL are only observed when $f_{HF} > f_{L-cut}$, while BHFIL are observed for all heating pulses in this experiment. The altitude of THFIL and BHFIL follow the variations in the ionospheric electron density, as would be expected. This example illustrates that THFIL can be generated repeatedly under certain conditions. However, not all important parameters that affect the generation of THFIL and transionospheric wave propagation are known and the experiments presented in Paper I and II lead to several new unanswered questions (see Chapter 6).

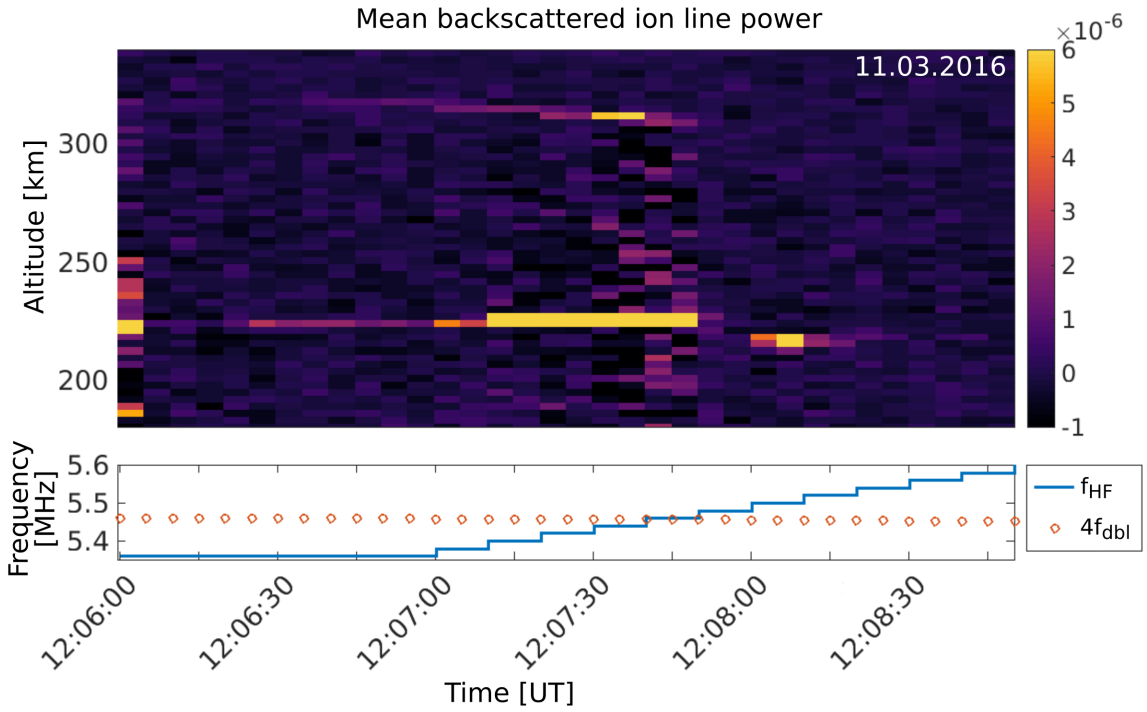

Figure 4.7: Mean backscattered power of the ion line spectra from the EISCAT UHF radar measurements, showing the development of THFIL (∼315 km) and BHFIL (∼225 km) during one 3 minute, HF modification pulse. The enhancements can be clearly seen as brighter purple and yellow. The bottom panel shows the corresponding f_{HF} and $4f_{dbl}$ at the bottomside ionosphere.

Figure 4.7 shows the development of THFIL and BHFIL during one, 3 minute, HF modification pulse, including an example of one of the yet unexplained features. The change in the mean backscattered power of the 5 second integrated ion line spectra, of the UHF radar measurements, is seen in the upper panel.

The bottom panel shows the pump frequency as well as $4f_{dbl}$ on the bottom side ionosphere. The magnitude of the ion line enhancements at both the topside (314 km) and the bottomside (215 km), varies throughout a heating pulse as f_{HF} is stepped around $4f_{dbl}$.

The decrease and slight increases of the altitude of the enhancements, at the topside and bottomside respectively, is consistent with the stepping of f_{HF} and the resulting change of altitude of the cutoff altitude. Both THFIL and BHFIL enhancements appear to increase as f_{HF} is stepped upward toward $4f_{dbl}$. As f_{HF} is stepped above $4f_{dbl}$, both THFIL and BHFIL abruptly disappear. The appearance of both BHFIL and THFIL seem to be affected by the proximity of f_{HF} to $4f_{dbl}$ on the bottom ionosphere. The example given in Figure 4.7 is characteristic for what is defined as Case B observations in Paper II. Case A observations (not shown here), defined in the same paper, also show a curios feature where the appearance of THFIL seem to be conditioned by the proximity of f_{HF} to $4f_{dbl}$ on the topside ionosphere. The analyses of these data and details are discussed at length in Paper I and II.

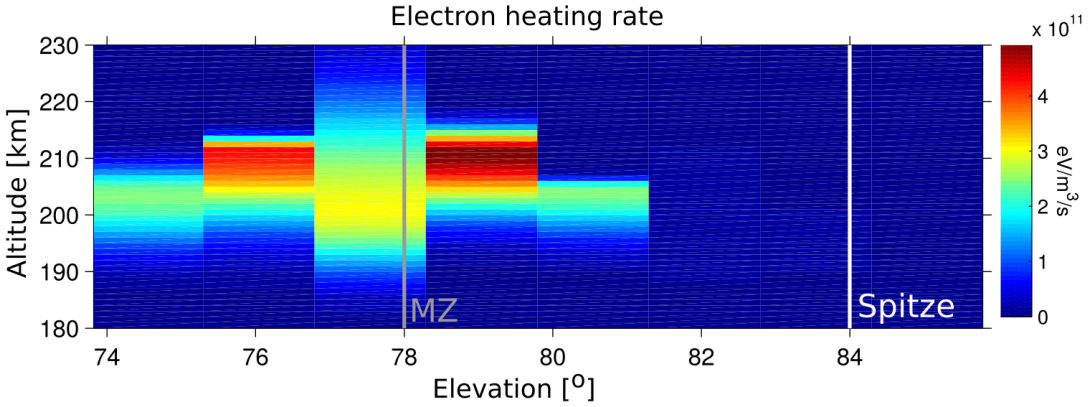

Figure 4.8: Altitude profiles of the modeled electron heating rate at radar elevation from 74 – 84° during O mode HF modification in the MZ direction. The MZ and Spitze angles are indicated in grey and white, respectively. The electron heating rate in the MZ direction clearly differs from the heating rate at other elevations.

The findings presented in Paper III are consistent with the results and conclusions of Paper I and II, even though the experiment and calculations were different. In this experiment the EISCAT UHF radar was scanned through eight positions around magnetic zenith (MZ), measuring the plasma parameters at each elevation, as an HF pump wave in the O mode was transmitted in the MZ direction. The electron temperature and heating rate were then modeled from the energy equation (see Chapter 2.1) and fitted to the measurements of the plasma parameters. A difference in the electron heating rate at different radar elevation steps was detected. Figure 4.8 shows an excerpt of these results. The altitude profile of the heating rate is shown for the different radar elevations and the MZ and Spitze angles are indicated. With the exception of the MZ direction the heating rate at all elevation angles is asymmetric, with a

sharp decrease above the maximum and a gradual decrease below the maximum heating. In the MZ direction the heating rate is extended over a larger range of altitudes and the asymmetric decrease above and below the maximum is not observed. This is consistent with a propagating L-mode pump wave in the MZ direction and an O-mode wave at angles away from MZ. An L-mode wave can propagate to higher altitudes than an O-mode wave, and thus the wave plasma interaction generating the increase in electron heating can occur at a larger range of altitudes.

The experimental results and their interpretation presented above, demonstrate and establish the possibility of transionospheric wave propagation in the polar ionosphere, outside the standard radio window. Further details and observations that were made are examined and discussed at length in the accompanying papers. These results could be achieved as a method was developed, to calculate the ionospheric electron density to a higher accuracy than previously achieved. This has enabled the calculation of high-accuracy altitude profiles of the plasma- , upper hybrid- and multiple cutoff frequencies. The method for these calculations is explained in detail in the next chapter.

Chapter 5

Determination of electron density from plasma line frequency spectra

Electron density is typically determined from the total power of the ion line spectra of the backscattered signal, measured by the radar. The accuracy of the electron density is thus limited by the accuracy of the power measurement, which may vary significantly depending on the signal-to-noise ratio. It is also possible to calculate the electron density from the natural Langmuir waves in the ionosphere (see Chapter 3.1). These can be observed in the plasma line spectra of the EISCAT UHF radar. The accuracy then is limited by the accuracy of the enhanced frequency observations rather than power. A method for determining the ionospheric electron density profile from the natural Langmuir wave frequency observations in the plasma line spectra was derived and forms an important step in the data analysis done for results presented in this thesis. The accuracy and range resolution is significantly higher than previously achieved. In this chapter, this method is described in detail and the accuracies of the new method are compared to that of the previous method.

The natural Langmuir wave frequency can be observed in the plasma line spectra of the EISCAT UHF radar, as enhancements at a narrow range of frequencies and varying with altitude. During the experiments presented in this thesis, these spectra had a minimum time resolution of 5 seconds, range span from 107 to 374 km with a minimum range gate resolution of 3 km, and a spectral range of $\pm$1.25 MHz with a resolution of 3.125 kHz for the three plasma line channels available, centered at –3.6 MHz, –6 MHz and –8.4 MHz (Tjulin, 2017). A typical observation of one downshifted plasma line spectra from the second channel, centered at –6 MHz, when no HF modification wave is transmitted, is shown in Figure 5.1. In the left panel, the unfiltered spectra are shown, while the right panel shows the filtered spectra with the simple filter, shown in the insert, used at all altitudes. A very weak trace of the naturally enhanced Langmuir wave frequency-altitude profile can be detected by visual inspection.

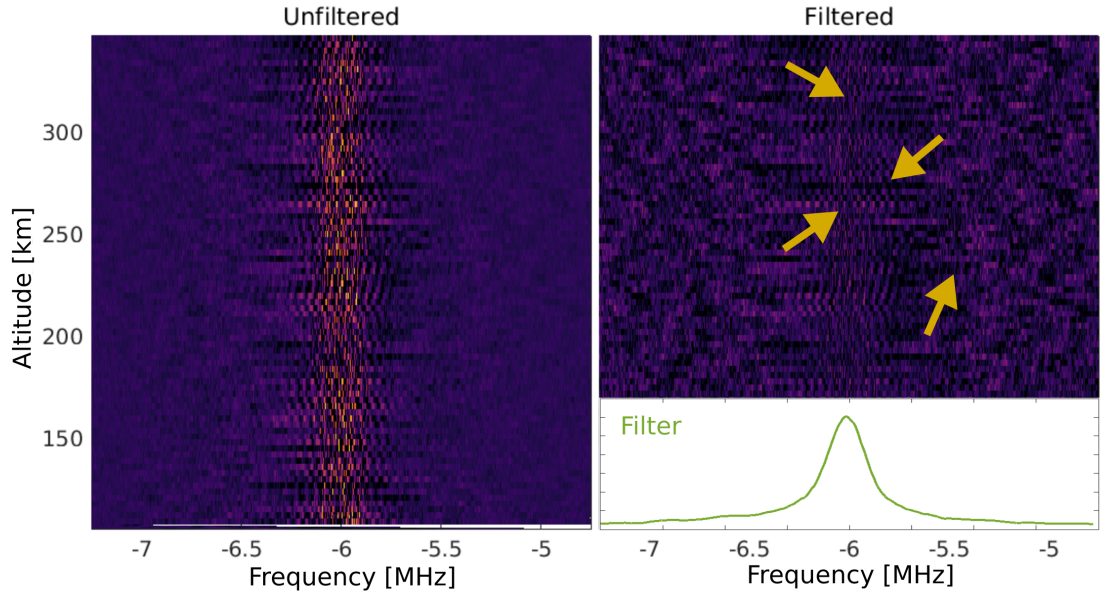

Figure 5.1: Example of 5-second integrated plasma line spectra for altitudes from ∼111 km to ∼350 km. The left panel shows the unfiltered spectra centered at –6 MHz. The noise in this measurement increases toward the center of this frequency channel. The right panel shows the same spectra with the simple filter, shown in the inset, applied at all altitudes, to reduce noise. A very faint trace of the naturally enhanced Langmuir wave signal can be seen between the arrows.

The plasma line spectra thus filtered, are integrated over one minute and further low-pass-filtered. The naturally, photo-electron enhanced, Langmuir waves are now clearly visible, as the random background noise changes between each frame while the naturally enhanced Langmuir wave signal remains unchanged on very short timescales. An example is shown in the left panel of Figure 5.2. The enhanced backscatter is visible from ∼220 km to ∼340 km, and includes the ionospheric peak frequency in the F layer. Signals larger than 5 standard deviations from the mean, one-minute averaged background noise are identified as enhanced plasma line backscatter. The lower right panel in the figure shows four examples of these enhancements at different altitudes around the maximum frequency in the F layer. These points are then used to create a curve fit, f_{-}^{*}, to the measured frequency altitude profile of the Langmuir waves. These are indicated by blue circles and the green curve, respectively, in the upper right panel of Figure 5.2.

The electron density is calculated from the estimate of the Langmuir wave frequency profile, f_{-}^{*}. A theoretical expression for the resonance frequency of the downshifted backscatterd signal of the natural Langmuir waves, f_{-}, was presented by Hagfors and Lehtinen (1981). It includes the dispersion relation of the waves and is dependent on the frequency, f_{radar} (and ω_{radar}), and angle of incidence, θ, for the radar wave, as well as both n_e and T_e.

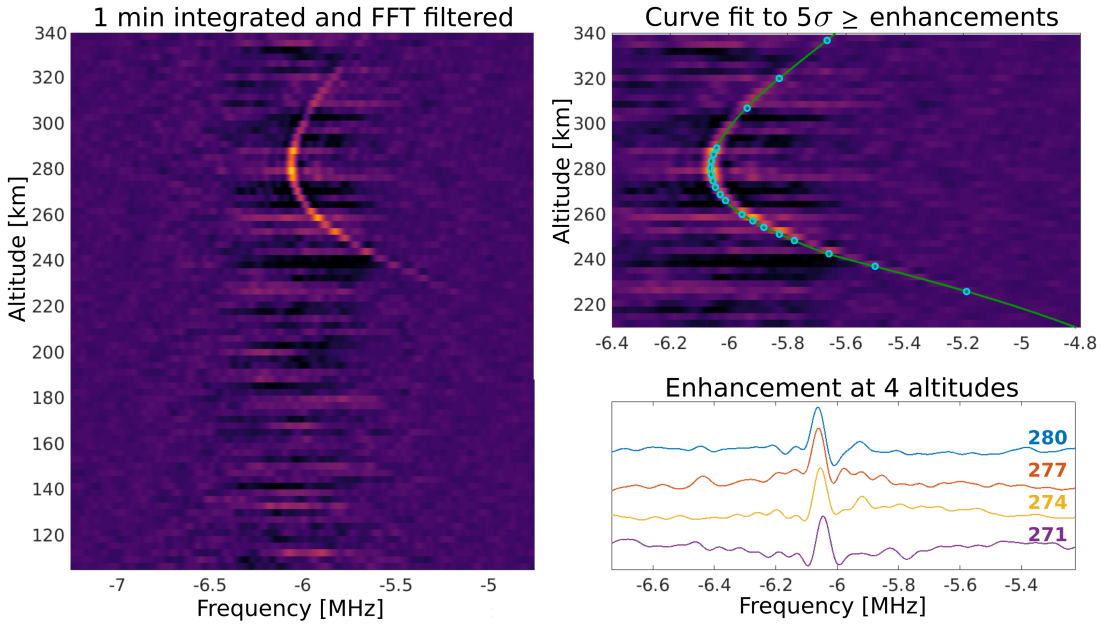

Figure 5.2: Example of the filtering and curve fitting to the natural Langmuir waves observed in the plasma line spectra. The left panel shows one-minute integrated and FFT low-pass-filtered plasma line spectra. The naturally enhanced Langmuir waves are now clearly visible. The upper right panel shows the same spectra with signals stronger than 5 standard deviations from the mean background noise indicated by light blue circles. These are then used for the curve fit, indicated in green, to estimate an expression for the frequency altitude profile of the Langmuir waves. Four examples of these enhancements, at different altitudes, indicated by the colored number on the right, are shown in the lower right panel.

It is given by

$$f_- \cong -f_P\left(1+\frac{3}{2}D^2\cdot\frac{1}{c^2}\left[(\omega_{radar}-\omega_P)^2+\omega_{radar}^2-2\cos\theta\,\omega_{radar}(\omega_{radar}-\omega_P)\right]\right)+f_{radar} \tag{5.1}$$

where $D = T_e/m_e\omega_P^2$. Higher order corrections, for example due to heat-flux and photo-electrons contributing with small shifts in f, are neglected here. From this an expression for the electron density in the magnetic field aligned direction ($\theta = 0$) is obtained,

$$n_e = \left(\frac{m_e\epsilon_0}{q^2}\right)\left[\frac{-y+\sqrt{y^2-4xz}}{2x}\right]^2 \tag{5.2}$$

where

$$x = \frac{1}{2\pi}+\frac{3T_e}{4m_e\pi c^2}, \qquad y = f_- - \frac{3T_e f_{radar}}{c^2 m_e \pi}, \qquad z = \frac{3T_e f_{radar}^2}{c^2 m_e \pi}$$

To determine n_e, f_-^* is substituted for f_- in the expression and an estimate for the electron temperature, T_e, is required. In this thesis, the 30-second in-

tegrated T_e profiles calculated from the ion line spectra (a standard measurement for all EISCAT experiments) has been used. The temporal and spatial resolution of those T_e profiles are the same as the temporal and spatial resolution of the electron density calculated from the total backscattered power of the ion line. The T_e measurements are interpolated in range for the subsequent calculations, since heat conduction along the magnetic field in the F region is efficient and no sharp gradients in T_e should exist here (when no HF modification wave is present). Nonetheless, T_e contributes only to a small correction term in Equation 5.2. This is illustrated in Figure 5.3. It shows n_e calculated for the example in Figure 5.2 in the left panel. The right panel indicates T_e obtained from the ion line, used in the calculations of n_e shown in the left panel. Dark and light orange shaded areas indicate a 10% and 30% error calculation of the temperature, respectively. It is apparent from this that a 30% error in the electron temperature estimate leads to a relatively small correction of the calculated electron density, seen in the correspondingly shaded areas in the left panel.

In addition to errors from T_e measurements, an uncertainty arises from the curve fit to the natural Langmuir wave frequency. An estimate of this error is made using the mean of the full-width-half-maximum of the enhanced backscattered plasma line signal used for the fit, of which four examples are shown in the bottom right panel of Figure 5.2. That is, all enhancements 5 standard deviations over the mean background noise indicated by the light blue circles in the upper right panel of Figure 5.2. For the example presented here and the results presented in the enclosed papers of this thesis, this corresponds to $\pm$20–30 kHz. Two factors contribute to the width, and thus the uncertainty, of the frequency measurement. The first is the low-pass filtering that is used to reduce noise, while the second is the change in electron density (and thus a change in the Langmuir wave frequency) over altitude ranges smaller than the range resolution of the measurements. The light purple shaded area in Figure 5.3 indicates the uncertainty in the n_e calculations that this calculated frequency error contributes. An estimate of a total error is obtained by adding the uncertainty from the 10% T_e error estimate and the error from the frequency fit.

A comparison between n_e obtained from the ion line measurements (red) and the plasma line measurements (blue) and their respective error estimates, are shown in Figure 5.4. There it is clearly visible that using the plasma line observations of the Langmuir waves increases the accuracy of the n_e measurements significantly. To estimate the uncertainty of n_e obtained from the ion line measurements, one standard deviation of the electron density measurements is calculated, for the same time interval that is used for the integration of the plasma line data. In addition to a more accurate n_e estimate, a major improvement is made to the altitude resolution of the estimate. When calculated from the ion line, the altitude resolution decreases with increasing altitude, typically varying between 10 and 20 km for altitudes from 200 to 300 km. When using the plasma line for the electron density calculations, the theoretical altitude

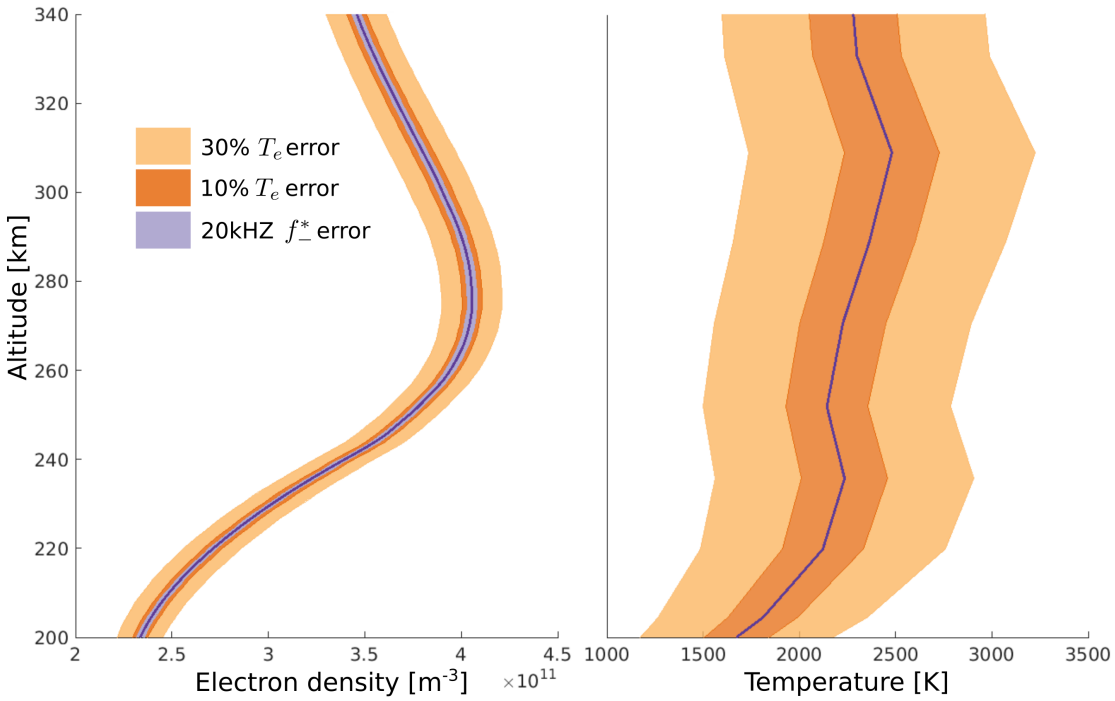

Figure 5.3: The electron density as calculated from observations of the natural Langmuir wave frequency in the plasma line spectra of the EISCAT UHF radar, from the example presented in Figure 5.1 and 5.2, and Equation 5.2, is shown in the left panel. The calculations depend on an estimate of the electron temperature, which is obtained from the 30-second integrated ion line measurements, shown in the right panel. The dark orange shaded area indicates a 10% error while the light orange shades area indicates a 30% error of the temperature estimate. The purple shaded area indicates the calculated error of the frequency estimate. Comparing the two light orange shaded areas in the left and right panels, it can be seen that a large error in the temperature estimate leads to only a small correction of the electron density estimate.

resolution is the same as that of the plasma line spectra, which is $\sim$3 km for the experiments presented in this thesis.

The frequency range and altitude range of the natural Langmuir waves in the ionosphere varies as n_e and T_e in the ionosphere vary. The electron density as estimated from the naturally enhanced Langmuir waves is only valid for altitudes where a these are observed, which is typically considerably less than the altitude range of the ion line observations. A good estimate of the altitude profile of the Langmuir wave frequency depends on a good curve fit to the natural plasma line enhancements. This can only be obtained when the natural enhancements are detectable, that is the integrated plasma line is significantly stronger than the background noise level. The integration time can be adjusted to obtain a stronger signal, depending on the temporal variability of the ionospheric parameters. That is, if the Langmuir wave frequency in the ionosphere changes on shorter time scales than the minimum integration time needed to get a sufficiently strong signal, this method can not be applied.

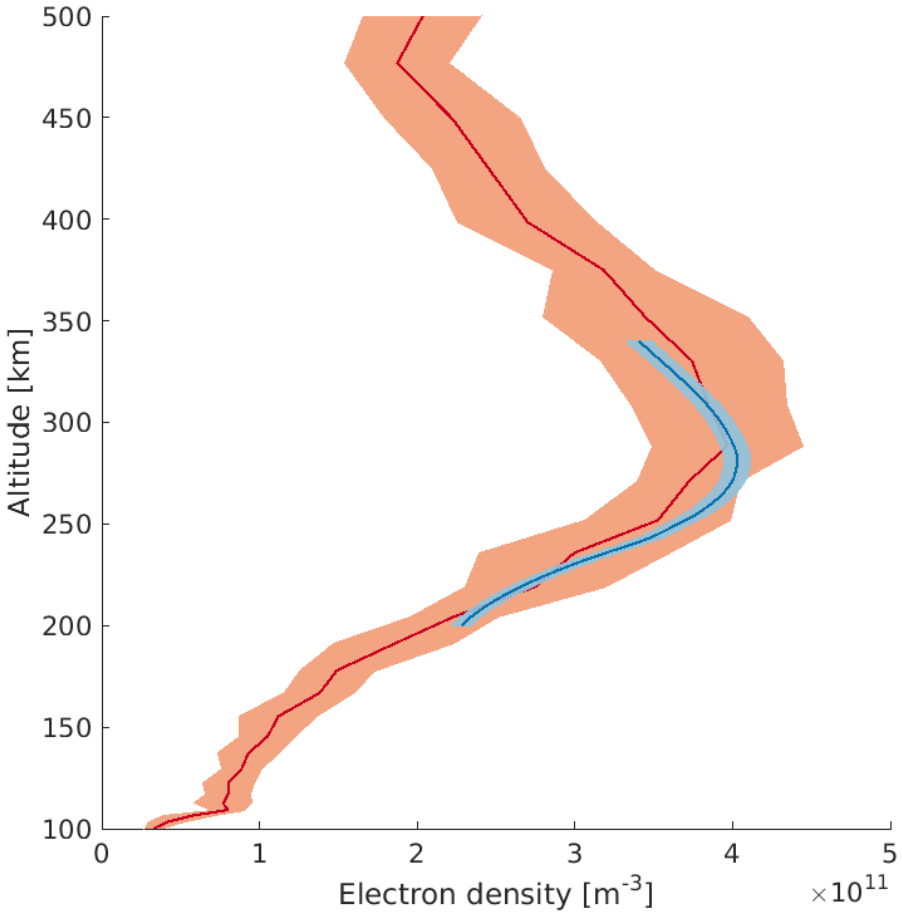

Figure 5.4: Altitude profile of the electron density as calculated from the ion line spectra (red) and from the naturally enhanced Langmuir waves in the plasma line spectra (blue). The shaded red area indicates the 1σ uncertainty calculations while the blue shaded area indicates the calculated uncertainty of the electron density calculation from the plasma line spectra.

Consequently this method does not give a good n_e measurement of the short temporal variations during ionospheric modification experiments, such as the generation of FAIs. However, neither do the electron density measurements calculated from the ion line spectra.

Ionospheric modification experiments can produce different plasma and ion line enhancements (see Chapter 3.2) that will affect the algorithm determining the signals of the natural Langmuir wave frequency. Additionally, the data resolution and quality of the plasma line spectra obtained by the EISCAT radar may vary. Hence the method for the determination of the electron density described above may be time-consuming, since some manual inspection often is needed. Nonetheless, this method is a significant improvement to the previous method, that provides the standard n_e estimate of the EISCAT data, and should be considered as an alternative in future experiments and studies.

Chapter 6

Conclusions and future work

The work presented in this thesis contributes to widen our understanding of electromagnetic wave-plasma interactions and plasma dynamics in the near-Earth-space. In this final chapter, the results and conclusions that have been reached are summarized in the first section. Suggestions for future work and some unanswered questions are raised in the second section.

6.1 Conclusion

This purpose of this thesis is to describe the generation and characteristics of transionospheric wave propagation during ionospheric modification experiments in the polar ionosphere. It includes the first observations of systematically recurring, enhanced topside ion line spectra, generated by the high-power, high-frequency modification wave propagating through the ionosphere, outside the standard radio window. Multiple experiments were conducted at the EISCAT facilities near Tromsø, Norway. The modification waves were transmitted using EISCAT Heating and plasma parameters were obtained with the collocated EISCAT UHF radar. A method and algorithm for the calculation of high-accuracy altitude profiles of the electron density has been developed, enabling the computation of altitude profiles for the plasma- , upper hybrid- , and multiple cutoff frequencies. With this, it has been possible to identify two separate cases of topside HF enhanced ion lines (THFIL), providing evidence of transionospheric wave propagation. An apparent gyroharmonic effect at the top- and bottomside ionosphere has been found for both cases, the temporal evolution of the THFIL have been characterized, as well as their location in altitude and relative to the standard radio window and magnetic zenith. Further, a plausible development of the propagation process from transmission to the observations has been established. The key findings are summarized as follows:

- Two cases of THFIL are identified. In Case A the THFIL are observed when f_{HF} is at or just below the fourth harmonic of the double resonance frequency, $4f_{dbl} = f_{UH} = 4f_G$, at the topside, while no simultaneous BHFIL

were observed at these pump frequencies. In Case B all THFIL are observed simultaneous to BHFIL, for f_{HF} at or just below $4f_{dbl}$ at the bottomside ionosphere. The THFIL spectra are similar in both cases, while BHFIL spectra appear different for the two cases.

- The enhancements develop and increase, as f_{HF} approaches $4f_{dbl}$, on the topside for Case A and bottomside for Case B. All experiments and observations of THFIL were done in the MZ direction, well outside the standard radio window. Further, the altitude at which THFIL were observed, was at or very close to the reflection altitude where $f_P = f_{HF}$.

- The following development of the process, as an HF modification wave is injected into the ionospheric plasma, is proposed. An incident O-mode wave is guided by electron density irregularities generated by the HF wave, and guided into the strictly magnetic field aligned L mode. As the incident wave approaches the altitude where $f_P = f_{HF}$, it's dispersion relation can pass from the that of the O mode dispersion surface, along the L mode edge, to that of the Z mode dispersion surface. The wave can continue propagation to regions of higher plasma density, instead of being reflected. Thus the incident wave can pass the reflection altitude and propagate to the topside ionosphere and space.

- The altitude distribution of electron heating due to an incident pump wave is affected differently depending on the direction of propagation. A pump wave propagation in the L mode along the magnetic field aligned direction can penetrate deeper into the plasma and thus facilitate electron heating to higher altitude ranges than pump waves propagating in directions deviating by as little as 1°.

Overall, the experimental results demonstrate that transionospheric wave propagation is possible in directions away from the standard radio window. The observational results were analyzed and a likely physical explanation was presented. Further, enhanced, pump wave induced, topside ion line spectra were consistently generated and these appear to be asymmetrically conditioned by the proximity of the pump wave to the double resonance frequency both on the topside and on the bottomside ionosphere, depending on the case of THFIL.

This work has investigated an intricate case of electromagnetic wave propagation in magnetized plasma. The study of electromagnetic wave and plasma interactions through ionospheric modification experiments broadens our knowledge and understanding of the underlying physics. Results in this particular field are of interest in a variety of other research fields including all parts of space research and laboratory plasma research. As large part of our modern day technology and communication is increasingly dependent on electromagnetic waves and their interaction and propagation, the understanding of these is essential and the continued research in this field is of importance.

6.2 Future work

The findings of this thesis provide a foundation for many new research ideas and opportunities. Two categories of directions appear particularly interesting for future investigations, and for these some suggestions are listed below.

Transionospheric wave propagation experiments in conjunction with other instrumentation

Although there are still numerous open questions and ideas for future experiments that can be explored using incoherent scatter radars as described in this thesis, one apparent opportunity for future investigations is to coordinate experiments with other instrumentation. This would expand the measurable parameters, effects and possible directional differences that are otherwise not observable. A variety of different instrumentation exists that is suitable for this. Below, four suggestions are given that can contribute to the current understanding of electromagnetic wave propagation through the ionosphere.

Coordinating experiments using the Hankasalmi HF radar of the Super Dual Auroral Radar Network (SuperDARN) is one such possibility. By using appropriate radar parameters for an experiment, the electron density irregularities can be measured at different scale sizes, and raytraces of backscatter from these can be obtained to investigate the spatiotemporal evolution of the irregularities that permit wave propagation through the ionosphere.

Likewise, measurements of Stimulated Electromagnetic Emissions (SEE) during transionospheric wave propagation would likely expand our understanding of the involved plasma processes and could possibly provide an insight into the observed gyroharmonic effect that has been observed.

Further, the possibillity of using satellite measurements in conjunction with transionospheric wave progagation experiments has previously been demonstrated by Leyser et al. (2018). There are numerous satellites with a suitable orbit and instrumentation (e.g. DMSP, SWARM) that would expand the range of possible experiments and potentially greatly enhance our understanding of the processes involved.

One immensely valuable opportunity would be the possibility to conduct transionospheric wave propagation experiments with the EISCAT UHF radar and upcoming EISCAT3D measuring the plasma parameters simultaneously. In fact, this would be beneficial to any ionospheric modification experiment conducted at EISCAT Heating. However, its possibility depends on the future developments of EISCAT.

Some of the open questions that could be answered by the suggestions above are:

- How much of the wave energy is propagated from the bottom to the topside ionosphere?

- How is the polarization of the propagating wave affected at the topside interaction region?
- Does the transionospheric wave generate SEE at the topside ionosphere?
- What is the relationship and importance of the transionospheric wave frequency and the effect of the proximity to the double resonance frequency that is observed?
- Why are there two separate cases of topside HF enhanced ion lines?
- What is the spatiotemporal evolution of the density striations that allow for transionospheric wave propagation?

Electron density determination algorithm

The method for determining the electron density described in Chapter 5 provides a significant improvement of the accuracy and precision of the electron density measurements. However, it involves manual inspection and depending on the data resolution and quality this can be very time consuming. The use of machine learning techniques and neural networks is well established and they can process very large data-sets and be applied to a variety of problems. Preliminary studies have shown that deep convolutional neural network techniques from machine learning can be applied to find ionospheric traces in ionogrammes (Vierinen and Kvammen, 2021). Applying these techniques to find and identify the naturally enhanced Langmuir waves in the EISCAT plasma line spectra would greatly improve the current electron density measurements and open new possibilities for research where a higher accuracy is critical. Developing this method and a robust algorithm to identify suitable plasma line spectra data, and integrating it to the current analyses tools and thus the standard plasma parameter output of the radar, has the potential to expand and enhance the usefulness of existing and future EISCAT data. It would also be highly relevant for future data from the upcoming EISCAT3D radar, where multistatic, plasma line observations will make it possible to determine the electron velocity field.

Fly on, space penguin. Fly on.
— The Gentleman's Armchair

References

Andre, M.: Dispersion surfaces, Journal of Plasma Physics, 33, 1–19, doi: 10.1017/S0022377800002270, 1985.

Appleton, E. V. and Barnett, M. A.: On some direct evidence for downward atmospheric reflection of electric rays, Proceedings of the Royal Society of London. Series A, Containing Papers of a Mathematical and Physical Character, 109, 621–641, doi: 10.1098/rspa.1925.0149, 1925.

Bailey, V. A. and Martyn, D. F.: Interaction of Radio waves, Nature, 133, 1934, doi: 10.1038/133218a0, 1934.

Basu, S., Costa, E., Livingston, R. C., Groves, K. M., and Carlson, H. C.: Evolution of subkilometer scale ionospheric irregularities generated by high-power HF waves, Journal of Geophysical Research, 102, 7469–7475, doi: 10.1029/96JA03340, 1997.

Bauer, P.: Theory of Waves Incoherently Scattered, Philosophical Transactions of the Royal Society of London. Series A, Philosophical Transactions of the Royal Society of London, 280, 167–191, 1975.

Baumjohann, W. and Treumann, R.: Basic Space Plasma Physics, Imperial College Press, revised edn., 2012.

Belikovich, V. V., Grach, S. M., Karashtin, A. N., Kotik, D. S., and Tokarev, Y. V.: The "Sura" facility: Study of the atmosphere and space (a review), Radiophysics and Quantum Electronics, 50, 497–526, doi: 10.1007/s11141-007-0046-4, 2007.

Bernhardt, P. A., Tepley, C. A., and Duncan, L. M.: Airglow enhancements associated with plasma cavities formed during Ionospheric Heating Experiments, Journal of Geophysical Research, 94, 9071, doi: 10.1029/JA094iA07p09071, 1989.

Beynon, W. J. and Williams, P. J.: Incoherent scatter of radio waves from the ionosphere, Reports on Progress in Physics, 41, 909–955, doi: 10.1088/0034-4885/41/6/003, 1978.

Biermann, L.: Kometenschweife und solare Korpuskularstrahlung, Zeitschrift fur Astrophysik, 29, 274, 1951.

Birkeland, K.: The Norwegian Aurora Polaris Expedition 1902-1903, H. Aschehoug & Co, 1908.

Bittencourt, J. A.: Fundamentals of Plasma Physics, Springer Science & Business Media, New York, 3rd edn., doi: 10.1007/978-1-4757-4030-1, 2013.

Blagoveshchenskaya, N. F.: Perturbing the high-latitude upper ionosphere (F region) with powerful HF radio waves: A 25-year collaboration with EISCAT, URSI Radio Science Bulletin, 2020, 40–55, doi: 10.23919/ursirsb.2020.9318436, 2021.

Borisova, T. D., Blagoveshchenskaya, N. F., Kalishin, A. S., Häggström, M. I., and Rietveld, M. T.: Excitation of Langmuir and Ion–Acoustic Turbulence in the High-Latitude Ionosphere by a High-Power HF Radio Wave Simultaneously Below and Above the F 2-Layer Maximum, Radiophysics and Quantum Electronics, 62, 793–806, doi: 10.1007/s11141-020-10025-z, 2020.

Bowles, K. L.: Observation of vertical-incidence scatter from the ionosphere at 41Mc/s, Physical Review Letters, 1, 454–455, doi: 10.1103/PhysRevLett.1.454, 1958.

Breit, G. and Tuve, M. A.: A Radio Method of Estimating the Height of the Conducting Layer, Nature, 116, 357, doi: 10.1038/116357a0, 1925.

Breit, G. and Tuve, M. A.: A test of the existence of the conducting layer, Physical Review, 28, 554–575, doi: 10.1103/PhysRev.28.554, 1926.

Budden, K. G.: The theory of radio windows in the ionosphere and magnetosphere, Journal of Atmospheric and Terrestrial Physics, 42, 287–298, doi: 10.1016/0021-9169(80)90036-7, 1980.

Carrington, R. C.: Description of a Singular Appearance seen in the Sun on September 1, 1859, Monthly Notices of the Royal Astronomical Society, 20, 13–15, 1859.

Chen, F.: Introduction to plasma physics and controlled fusion, Springer, second edn., 1983.

Cohen, M. B. and Inan, U. S.: Terrestrial VLF transmitter injection into the magnetosphere, Journal of Geophysical Research: Space Physics, 117, 1–11, doi: 10.1029/2012JA017992, 2012.

Cohen, M. B., Inan, U. S., Gołkowski, M., and McCarrick, M. J.: ELF/VLF wave Generation via ionospheric HF heating: Experimental comparison of amplitude modulation, beam painting, and geometric modulation, Journal of Geophysical Research: Space Physics, 115, 1–10, doi: 10.1029/2009JA014410, 2010.

Cohen, R. and Whitehead, J. D.: Radio-Reflectivity Detection of Artificial Modification of the Ionospheric F Layer, Journal of Geophysical Research, Space Physics, 75, 6439–6445, doi: 10.3109/00016486809122149, 1970.

Collinder, P.: Swedish astronomers 1477-1900, vol. 19, Acta Universitatis Upsaliensis, Uppsala, 1970.

Djuth, F. T., Isham, B., Rietveld, M. T., Hagfors, T., and La Hoz, C.: First 100 ms of HF modification at Tromso, Norway, Journal of Geophysical Research: Space Physics, 109, 1–24, doi: 10.1029/2003JA010236, 2004.

Dougherty, J. P. and Farley, D. T.: A theory of incoherent scattering of radio waves by a plasma, Proceedings of the Royal Society of London, 259, 79–99, doi: 10.1098/rspa.1960.0212, 1960.

Dungey, J. W.: Interplanetary magnetic Field and the Auroral Zones, American Physical Society Journals, 6, Pysical Research Letter, 1961.

Dysthe, K. B., Mjølhus, E., Pecseli, H., and Rypdal, K.: Thermal Cavitons, Physica Scripta, T2, 548–559, 1982.

EISCAT Scientific Association: EISCAT Webpage, URL `https://eiscat.se/scientist/data/`, 2021.

Eliasson, B.: Full-scale simulation study of the generation of topside ionospheric turbulence using a generalized Zakharov model, Geophysical Research Letters, 35, 1–5, doi: 10.1029/2008GL033866, 2008.

Ellis, G. R.: The Z propagation hole in the ionosphere, Journal of Atmospheric and Terrestrial Physics, 8, 43–54, doi: 10.1016/0021-9169(56)90090-3, 1956.

Farley, D. T.: Artificial heating of the electrons in the F region of the ionosphere , Journal of Geophysical Research, 68, 401–413, doi: 10.1029/jz068i002p00401, 1963.

Farley, D. T.: Incoherent scattering at radio frequencies, Journal of Atmospheric and Terrestrial Physics, 32, 693–704, doi: 10.1016/0021-9169(70)90215-1, 1970.

Farley, D. T.: Incoherent Scatter Radar Probing, in: Modern Ionospheric Science, edited by Kohl, H., Rüster, R., and Schlegel, K., pp. 415–439, European Geophysical Society, Kaltenburg-Lindau, Germany, 1996.

Farley, D. T., Dougherty, J. P., and Barron, D. W.: A theory of incoherent scattering of radio waves by a plasma II. Scattering in a magnetic field, Proceedings of the Royal Society of London. Series A. Mathematical and Physical Sciences, 263, 238–258, doi: 10.1098/rspa.1961.0158, 1961.

Fejer, J. A.: Radio-Wave Scattering by an Ionized Gas in Thermal Equilibrium, Journal of Geophysical Research, 65, 2635–2636, 1960.

Fejer, J. A.: Ionospheric modification and parametric instabilities, Reviews of Geophysics, 17, 135–153, doi: 10.1029/RG017i001p00135, 1979.

Frolov, V. L., Erukhimov, L. M., Metelev, S. A., and Sergeev, E. N.: Temporal behaviour of artificial small-scale ionospheric irregularities: Review of experimental results, Journal of Atmospheric and Solar-Terrestrial Physics, 59, 2317–2333, doi: 10.1016/S1364-6826(96)00126-5, 1997.

Ganguly, S. and Gordon, W. E.: Heater enhanced topside plasma line, Geophysical Research Letters, 10, 977–978, 1983.

Gauss, C. F.: Allgemeine Theorie des Erdmagnetismus, URL https://books.google.no/books?id=UdCUIgAACAAJ, 1839.

Ginzburg, V. L. and Gurevich, A. V.: Nonlinear phenomena in a plasma located in an alternating electromagnetic field, Soviet physics, Uspekhi., 3, 115–146, 1960.

Gondarenko, N. A., Guzdar, P. N., Ossakow, S. L., and Bernhardt, P. A.: Linear mode conversion in inhomogeneous magnetized plasmas during ionospheric modification by HF radio waves, Journal of Geophysical Research: Space Physics, 108, doi: 10.1029/2003JA009985, 2003.

Gondarenko, N. A., Ossakow, S. L., and Milikh, G. M.: Generation and evolution of density irregularities due to self-focusing in ionospheric modifications, Journal of Geophysical Research: Space Physics, 110, 1–13, doi: 10.1029/2005JA011142, 2005.

Gordon, W. E.: Incoherent Scattering of Radio Waves by Free Electrons with Applications to Space Exploration by Radar, Proceedings of the IRE, 46, 1824–1829, doi: 10.1109/JRPROC.1958.286852, 1958.

Gordon, W. E. and Duncan, L. M.: Historical overview of HF ionospheric research, in: Conference Proceedings on Ionospheric Modification and its Potential to Enhance or Degrade the Performance of Military Systems, pp. 3–13, 1990.

Gurevich, A., Hagfors, T., Carlson, H., Karashtin, A., and Zybin, K.: Self-oscillations and bunching of striations in ionospheric modifications, Physics Letters, Section A: General, Atomic and Solid State Physics, 239, 385–392, doi: 10.1016/S0375-9601(98)00006-1, 1998.

Gurevich, A. V.: Nonlinear effects in the ionosphere, Uspekhi Fizicheskih Nauk, Russian Academy of Sciences, 177, 1145 –1177, doi: 10.3367/UFNr.0177.200711a.1145, 2007.

Gurevich, A. V., Zybin, K. P., and Lukyanov, A. V.: Stationary Striations Developed in the Ionospheric Modification, Physical Review Letters, 75, 2622–2625, doi: 10.1103/PhysRevLett.75.2622, 1995.

Gurevich, A. V., Lukyanov, A. V., and Zybin, K. P.: Anomalous absorption of powerful radio waves on the striations developed during ionospheric modification, Physics Letters, Section A: General, Atomic and Solid State Physics, 211, 363–372, doi: 10.1016/0375-9601(95)00970-1, 1996.

Gurevich, A. V., Zybin, K. P., Carlson, H. C., and Pedersen, T.: Magnetic zenith effect in ionospheric modifications, Physics Letters, Section A: General, Atomic and Solid State Physics, 305, 264–274, doi: 10.1016/S0375-9601(02)01450-0, 2002.

Gustavsson, B. and Eliasson, B.: HF radio wave acceleration of ionospheric electrons: Analysis of HF-induced optical enhancements, Journal of Geophysical Research: Space Physics, 113, 1–14, doi: 10.1029/2008JA013752, 2008.

Gustavsson, B., Sergienko, T., Rietveld, M. T., Honary, F., Steen, A., Brandstrom, B. U. E., Leyser, T. B., Aruliah, A. L., Aso, T., Ejiri, M., and Marple, S.: First tomographic estimate of volume distribution of HF-pump enhanced airglow emission, Journal of Geophysical Research, 106, 29 105 – 29 123, doi: 10.1029/2000JA900167, 2001.

Hagfors, T.: Density fluctuations in a plasma in a magnetic field, with applications to the ionosphere, Journal of Geophysical Research, 66, 1699, doi: 10.1029/JZ066i006p01699, 1961.

Hagfors, T. and Lehtinen, M.: Electron temperature derived from incoherent scatter radar observations of the plasma line frequency, Journal of Geophysical Research, 86, 119, doi: 10.1029/JA086iA01p00119, 1981.

Harang, L.: Vertical movements of air in the upper atmosphere, Terrestrial Magnetism and Atmospheric Electricity, 41, 143–160, 1936.

Heaviside, O.: Telegraphy, in: Encyclopedia Britannica, chap. 33, p. 213, 10th edn., 1902.

Honary, F., Robinson, T., Wright, D., Stocker, A., Rietveld, M., and McCrea, I.: First direct observations of the reduced striations at pump frequencies close to the electron gyroharmonics, Annales Geophysicae, 17, 1235–1238, doi: 10.1007/s00585-999-1235-6, 1999.

Humboldt, A.: Die vollständigste aller bisherigen Beobachtungen über den Einfluss des Nordlichts auf die Magnetnadel angestellt, Annalen der Physik, 29, 425–429, doi: 10.1002/andp.18080290806, 1808.

Hunsucker, R. D.: Radio techniques for probing the terrestrial ionosphere, vol. 22, Springer Science & Business Media, doi: 10.1007/978-3-642-76257-4, 1991.

Hysell, D. L., Kelley, M. C., Yampolski, Y. M., Beley, V. S., Koloskov, A. V., Ponomarenko, P. V., and Tyrnov, O. F.: HF radar observations of decaying artificial field-aligned irregularities, Journal of Geophysical Research: Space Physics, 101, 26 981–26 993, doi: 10.1029/96ja02647, 1996.

IRFU: IRFU-Matlab analysis package, URL `https://github.com/irfu/irfu-matlab`, 2003.

Isham, B., Kofman, W., Hagfors, T., Nordling, J., Thidé, B., LaHoz, C., and Stubbe, P.: New phenomena observed by EISCAT during an RF ionospheric modification experiment, Radio Science, 25, 251–262, doi: 10.1029/RS025i003p00251, 1990.

Isham, B., Hagfors, T., Mishin, E., Rietveld, M. T., La Hoz, C., Kofman, W., and Leyser, T. B.: A search for the location of the HF excitation of enhanced ion acoustic and langmuir waves with EISCAT and the Tromsø Heater, Radiophysics and Quantum Electronics, 42, 533–534, 1999a.

Isham, B., Rietveld, M., Hagfors, T., La Hoz, C., Mishin, E., Kofman, W., Leyser, T., and Van Eyken, A.: Aspect angle dependence of HF enhanced incoherent backscatter, Advances in Space Research, 24, 1003–1006, doi: 10.1016/S0273-1177(99)00555-4, 1999b.

Istomin, Y. N. and Leyser, T. B.: Small-scale magnetic field-aligned density irregularities excited by a powerful electromagnetic wave, Physics of Plasmas, 4, 817, doi: 10.1063/1.872175, 1997.

Istomin, Y. N. and Leyser, T. B.: Diffraction of electromagnetic waves by small scale geomagnetic field-aligned density striations, Physics of Plasmas, 8, 4577–4584, doi: 10.1063/1.1399325, 2001.

Kelley, M. C.: The Earth's Ionosphere Plasma Physics and Electrodynamics, Academic Press, second edn., doi: 10.1016/B978-0-12-404013-7.50004-6, 2009.

Kelley, M. C., Arce, T. L., Salowey, J., Sulzer, M., Armstrong, W. T., Carter, M., and Duncan, L.: Density depletions at the 10-m scale induced by the Arecibo heater, Journal of Geophysical Research, 100, 17 367–17 376, 1995.

Kennelly, A. E.: On the elevation of the electrically-conducting strata of the Earth's atmosphere, Electrical world and engineer, 39, 473, 1902.

Kohl, H., Kopka, H., Stubbe, P., and Rietveld, M. T.: Introduction to ionospheric heating experiments at Tromsø-II. Scientific problems, Journal of Atmospheric and Terrestrial Physics, 55, 601–613, doi: 10.1016/0021-9169(93)90008-M, 1993.

Kosch, M. J., Rietveld, M. T., Hagfors, T., and Leyser, T. B.: High-latitude HF-induced airglow displaced equatorwards of the pump beam, Geophysical Research Letters, 27, 2817–2820, doi: 10.1029/2000GL003754, 2000.

Kosch, M. J., Pedersen, T., Rietveld, M. T., Gustavsson, B., Grach, S. M., and Hagfors, T.: Artificial optical emissions in the high-latitude thermosphere induced by powerful radio waves: An observational review, Advances in Space Research, 40, 365–376, doi: 10.1016/j.asr.2007.02.061, 2007.

Kosch, M. J., Mjlhus, E., Ashrafi, M., Rietveld, M. T., Yeoman, T., and Nozawa, S.: Angular dependence of pump-induced bottomside and topside ionospheric plasma turbulence at EISCAT, Journal of Geophysical Research: Space Physics, 116, 1–9, doi: 10.1029/2010JA016014, 2011.

Kudeki, E. and Milla, M. A.: Incoherent scatter spectral theories - Part I: A general framework and results for small magnetic aspect angles, IEEE Transactions on Geoscience and Remote Sensing, 49, 315–328, doi: 10.1109/TGRS.2010.2057252, 2011.

Kuo, S. P., Lee, M. C., and Kossey, P.: Excitation of oscillating two stream instability by upper hybrid pump waves in ionospheric heating experiments at Tromsø, Geophysical Research Letters, 24, 2969–2972, doi: 10.1029/97GL03054, 1997.

Kvammen, A., Gustavsson, B., Sergienko, T., Brändström, U., Rietveld, M., Rexer, T., and Vierinen, J.: The 3-D Distribution of Artificial Aurora Induced by HF Radio Waves in the Ionosphere, Journal of Geophysical Research: Space Physics, 124, 2992–3006, doi: 10.1029/2018JA025988, 2019.

Lehtinen, M. S. and Huuskonen, A.: General incoherent scatter analysis and GUISDAP, Journal of Atmospheric and Terrestrial Physics, 58, 435–452, doi: 10.1016/0021-9169(95)00047-X, 1996.

Leyser, T. B.: Stimulated electromagnetic emissions by high-frequency electromagnetic pumping of the ionospheric plasma, Space Science Reviews, 98, 223–328, doi: 10.1023/A:1013875603938, 2001.

Leyser, T. B. and Nordblad, E.: Self-focused radio frequency L wave pumping of localized upper hybrid oscillations in high-latitude ionospheric plasma, Geophysical Research Letters, 36, 1–4, doi: 10.1029/2009GL041438, 2009.

Leyser, T. B. and Wong, A. Y.: Powerful electromagnetic waves for active environmental research in geospace, Reviews of Geophysics, 47, 1–33, doi: 10.1029/2007RG000235, 2009.

Leyser, T. B., James, H. G., Gustavsson, B., and Rietveld, M. T.: Evidence of L-mode Electromagnetic Wave Pumping of Ionospheric Plasma in Geomagnetic Zenith, Annales Geophysicae, 36, 900 167, doi: 10.1029/2009GL041438., 2018.

Leyser, T. T., Gustavsson, B., Rexer, T., and Rietveld, M. M.: Electron heating by HF pumping of high-latitude ionospheric F-region plasma near magnetic zenith, Annales Geophysicae, 38, 297–307, doi: 10.5194/angeo-38-297-2020, 2020.

Marconi, G.: Syntonic wireless telegraphy, The Journal of the Society of Arts, 49, 505–520, 1901.

Milikh, G. M., Papadopoulos, K., Shroff, H., Chang, C. L., Wallace, T., Mishin, E. V., Parrot, M., and Berthelier, J. J.: Formation of artificial ionospheric ducts, Geophysical Research Letters, 35, 1–5, doi: 10.1029/2008GL034630, 2008.

Milla, M. A. and Kudeki, E.: Incoherent scatter spectral theories - Part II: Modeling the spectrum for modes propagating perpendicular to B, IEEE Transactions on Geoscience and Remote Sensing, 49, 329–345, doi: 10.1109/TGRS.2010.2057253, 2011.

Millington, G.: Ray-path characteristics in the ionosphere, Proceedings of the IEE - Part III: Radio and Communication Engineering, 101, 235–249, doi: 10.1049/pi-4.1954.0029, 1954.

Minkoff, J., Kugelman, P., and Weissman, I.: Radio frequency scattering from a heated ionospheric volume: 1, VHF/UHF field aligned and plasma line backscatter measurements, Radio Science, 9, 941–955, doi: 10.1029/RS009i011p00941, 1974.

Mishin, E. and Pedersen, T.: Ionizing wave via high-power HF acceleration, Geophysical Research Letters, 38, 10–13, doi: 10.1029/2010GL046045, 2011.

Mishin, E., Hagfors, T., and Isham, B.: A generation mechanism for topside enhanced incoherent backscatter during high frequency modification experiments in Tromsø, Geophysical Research Letters, 28, 479–482, doi: 10.1029/2000GL000122, 2001.

Mjølhus, E.: On linear conversion in a magnetized plasma, Radio Science, 25, 1321–1339, 1990.

Mjølhus, E. and Flå, T.: Direct Access to Plasma Resonance in Ionospheric Radio Experiments, Journal of Geophysical Research, 89, 3921–3928, 1984.

Myasnikov, E. N., Muravjeva, N. V., Sergeev, E. N., Frolov, V. L., Nasyrov, A. M., Nasyrov, I. A., Beley, V. S., Koloskov, A. V., Yampolsky, Y. M., and Groves, K. M.: Spatial spectrum of artificial ionospheric irregularities induced by powerful HF radiowaves, Radiophysics and Quantum Electronics, 44, 833–846, doi: 10.1023/A:1014257628617, 2001.

Najmi, A., Eliasson, B., Shao, X., Milikh, G. M., and Papadopoulos, K.: Simulations of ionospheric turbulence produced by HF heating near the upper hybrid layer, Radio Science, 51, 704–717, doi: 10.1002/2015RS005866, 2016.

Najmi, A., Eliasson, B., Shao, X., Milikh, G., Sharma, A. S., and Papadopoulos, K.: Vlasov simulations of electron acceleration by radio frequency heating near the upper hybrid layer, Physics of Plasmas, 24, doi: 10.1063/1.4999768, 2017.

Nordblad, E. and Leyser, T. B.: Ray tracing analysis of L mode pumping of the ionosphere, with implications for the magnetic zenith effect, Annales Geophysicae, 28, 1749–1759, doi: 10.5194/angeo-28-1749-2010, 2010.

Nygrén, T.: Introduction to Incoherent Scatter Measurements, Invers publications, Invers, 1996.

Østgaard, N., Reistad, J. P., Tenfjord, P., Laundal, K. M., Rexer, T., Haaland, S. E., Snekvik, K., Hesse, M., Milan, S. E., and Ohma, A.: The asymmetric geospace as displayed during the geomagnetic storm on 17 August 2001, Annales Geophysicae, 36, 1577–1596, doi: 10.5194/angeo-36-1577-2018, 2018.

Owens, M. J. and Forsyth, R. J.: The heliospheric magnetic field, Living Reviews in Solar Physics, 10, doi: 10.12942/lrsp-2013-5, 2013.

Pedersen, T., Gustavsson, B., Mishin, E., Kendall, E., Mills, T., Carlson, H. C., and Snyder, A. L.: Creation of artificial ionospheric layers using high-power HF waves, Geophysical Research Letters, 37, 5–8, doi: 10.1029/2009GL041895, 2010.

Pedersen, T. R.: Magnetic zenith enhancement of HF radio-induced airglow production at HAARP, Geophysical Research Letters, 30, 18–1, doi: 10.1029/2002GL016096, 2003.

Pedersen, T. R. and Carlson, H. C.: First observations of HF heater-produced airglow at the high frequency active auroral research program facility: Thermal excitation and spatial structuring, Radio Science, 36, 1013–1026, doi: 10.1029/2000RS002399, 2001.

Poeverlein, H.: Strahlwege von Radiowellen in der Ionosphäre, URL `https://publikationen.badw.de/de/016510405`, 1949.

Prölss, G.: Physics of the Earth's Space Environment, Springer-Verlag Berlin Heidelberg, 1 edn., doi: 10.1007/978-3-642-97123-5, 2004.

Renau, J.: Scattering of Electromagnetic Waves from a Nondegenerate Ionized Gas, Journal of Geophysical Research, 65, 3631–3640, 1960.

Rexer, T., Gustavsson, B., Leyser, T., Rietveld, M., Yeoman, T., and Grydeland, T.: First Observations of Recurring HF-Enhanced Topside Ion Line Spectra Near the Fourth Gyroharmonic, Journal of Geophysical Research, Space Physics, 123, 1–15, doi: 10.1029/2018JA025822, 2018a.

Rexer, T., Leyser, T., Rietveld, M., Gustavsson, B., and Grydeland, T.: Observations of systematically recurring topside ionline enhancements during HF modification experiments near electron gyroharmonic frequencies, in: 42nd COSPAR Scientific Assembly, vol. 42, pp. C5.1–22–18, Solicited talk, Pasadena, Calif., URL `https://www.cospar-assembly.org/abstractcd/COSPAR-18/`, 2018b.

Rexer, T., Gustavsson, B., Leyser, T., Rietveld, M., Yeoman, T., and Grydeland, T.: Observations of systematically recurring topside ionline enhancements during multiple HF modification experiments

near multiples of the electron gyro frequency, in: 19th International EISCAT Symposium, p. 4, Invited Speaker, Oulu, Finland, URL https://www.sgo.fi/Events/EISCAT46AM/prog.php, 2019.

Rexer, T., Leyser, T., Gustavsson, B., and Rietveld, M.: Conditions for topside ion line enhancements, Journal of Geophysical Research: Space Physics, doi: 10.1029/2021ja029379, 2021.

Rietveld, M. T., Kohl, H., Kopka, H., and Stubbe, P.: Introduction to ionospheric heating at Tromsø-I. Experimental overview, Journal of Atmospheric and Terrestrial Physics, 55, 577–599, doi: 10.1016/0021-9169(93)90007-L, 1993.

Rietveld, M. T., Isham, B., Grydeland, T., La Hoz, C., Leyser, T. B., Honary, F., Ueda, H., Kosch, M., and Hagfors, T.: HF-pump-induced parametric instabilities in the auroral E-region, Advances in Space Research, 29, 1363–1368, doi: 10.1016/S0273-1177(02)00186-2, 2002.

Rietveld, M. T., Kosch, M. J., Blagoveshchenskaya, N. F., Kornienko, V. A., Leyser, T. B., and Yeoman, T. K.: Ionospheric electron heating, optical emissions, and striations induced by powerful HF radio waves at high latitudes: Aspect angle dependence, Journal of Geophysical Research: Space Physics, 108, 1–16, doi: 10.1029/2002JA009543, 2003.

Rietveld, M. T., Senior, A., Markkanen, J., and Westman, A.: New capabilities of the upgraded EISCAT high-power HF facility, Radio Science, 51, 1533–1546, doi: 10.1002/2016RS006093, 2016.

Rishbeth, H., Kohl, H., and Barcley, L. W.: A history of ionospheric physics and radio communications, in: Modern Ionospheric Science, edited by Kohl, H., Rüster, R., and Schlegel, K., pp. 4–31, European Geophysical Society, Katlenburg-Lindau, 1996.

Robinson, T. R.: The Heating of the High Latitude Ionosphere By High Power Radio waves, Physics Reports, 179, 79 – 209, 1989.

Robinson, T. R., Honary, F., Stocker, A. J., Jones, T. B., and Stubbe, P.: First EISCAT observations of the modification of F-region electron temperatures during RF heating at harmonics of the electron gyro frequency, Journal of Atmospheric and Terrestrial Physics, 58, 385–395, doi: 10.1016/0021-9169(95)00043-7, 1996.

Robinson, T. R., Strangeway, R., Wright, D. M., Davies, J. A., Horne, R. B., Yeoman, T. K., Stocker, A. J., Lester, M., Rietveld, M. T., Mann, I. R., Carlson, C. W., and McFadden, J. P.: FAST observations of ULF waves injected into the magnetosphere by means of modulated RF heating of the auroral electrojet, Geophys. Res. Lett., 27, 3165–3168, doi: 10.1029/2000GL011882, 2000.

Rönnmark, K.: Quantitative methods for waves in space plasmas, Space Science Reviews, 54, 1–73, doi: 10.1007/BF00168020, 1990.

Rosenbluth, M. N. and Rostoker, N.: Scattering of electromagnetic waves by a nonequilibrium plasma, Physics of Fluids, 5, 776–788, doi: 10.1063/1.1724446, 1962.

Russell, C. T., Luhmann, J. G., and Strangeway, R. J.: Space Physics: An Introduction, Cambridge University Press, 2016.

Salpeter, E. E.: Electron density fluctuations in a plasma, Physical Review, 120, 1528–1535, doi: 10.1103/PhysRev.120.1528, 1960.

Sergeev, E. N., Frolov, V. L., Grach, S. M., and Kotov, P. V.: On the morphology of Stimulated Electromagnetic Emission spectra in a wide pump wave frequency range, Advances in Space Research, 38, 2518–2526, doi: 10.1016/j.asr.2005.02.046, 2006.

Spohn, T., Breuer, D., and Johnson, T.: Encyclopedia of the Solar System, Elsevier, Boston, third edn., doi: 10.1016/B978-0-12-415845-0.00056-6, 2014.

Streltsov, A. V., Berthelier, J. J., Chernyshov, A. A., Frolov, V. L., Honary, F., Kosch, M. J., McCoy, R. P., Mishin, E. V., and Rietveld, M. T.: Past, Present and Future of Active Radio Frequency Experiments in Space, vol. 214, Springer Nature B.V., doi: 10.1007/s11214-018-0549-7, 2018.

Stubbe, P.: Review of ionospheric modification experiments at Tromsø, Journal of Atmospheric and Terrestrial Physics, 58, 349–368, 1996.

Stubbe, P. and Hagfors, T.: The Earth's ionosphere: A wall-less plasma laboratory, Surveys in Geophysics, 18, 57–127, doi: 10.1023/A:1006583101811, 1997.

Stubbe, P., Kopka, H., Lauche, H., Rietveld, M. T., Brekke, A., Holt, O., Jones, T. B., Robinson, T., Hedberg, Å., Thidé, B., Crochet, M., and Lotz, H. J.: Ionospheric modification experiments in northern Scandinavia, Journal of Atmospheric and Terrestrial Physics, 44, doi: 10.1016/0021-9169(82)90015-0, 1982.

Swanson, D. G.: Plasma Waves, Institute of Physics Publishing, London, 2nd editio edn., doi: 10.1088/0741-3335/45/6/701, 2003.

Tellegen, B. D. H.: Interaction between Radio-Waves?, doi: 10.1038/131840a0, 1933.

Tjulin, A.: EISCAT Experiments, EISCAT Scientific Association, URL `https://www.eiscat.se/wp-content/uploads/2017/04/Experiments.pdf`, 2017.

Toshniwal, G. R.: Three-fold Magneto-ionic Splitting of the Radio Echoes reflected from the Ionosphere, Nature, 135, 471–472, 1935.

Vas'kov, V. V. and Gurevich, A. V.: Resonance instability of small-scale plasma perturbations, Journal of Experimental and Theoretical Physics, 46, 487, 1977.

Vierinen, J. and Kvammen, A.: Automated ionogram scaling using deep learning, in prepara, 2021.

Vodyanitskij, A., Erokhin, N. S., Lisitchenko, V., Moiseev, S. S., and Oraevskij, V.: "Transillumination" of the wave barriers in a plasma as a result of kinetic effects, Nuclear Fusion, 14, 267, 1974.

Wong, A. Y. and Brandt, R. G.: Ionospheric modification - An outdoor laboratory for plasma and atmospheric science, Radio Science, 25, 1251–1267, 1990.

Zabotin, N. A. and Kovalenko, E. S.: Simple numerical model of radio wave multiple scattering effects in the ionospheric plasma layer, Waves Random Media, 9, 393–399, doi: 10.1088/0959-7174/9/3/307, 1999.

PAPER I

First Observations of Recurring HF-Enhanced Topside Ion Line Spectra Near the Fourth Gyroharmonic

Rexer, T., Gustavsson, B., Leyser, T., Rietveld, M., Yeoman, T., and Grydeland, T., Journal of Geophysical Research, Space Physics, 123, 1–15, doi: 10.1029/2018JA025822, 2018

Journal of Geophysical Research: Space Physics

RESEARCH ARTICLE
10.1029/2018JA025822

First Observations of Recurring HF-Enhanced Topside Ion Line Spectra Near the Fourth Gyroharmonic

Theresa Rexer[1], **Björn Gustavsson**[1], **Thomas Leyser**[3], **Michael Rietveld**[1,4], **Tim Yeoman**[5], **and Tom Grydeland**[2]

[1]Institute for Physics and Technology, Arctic University of Norway UiT, Tromsø, Norway, [2]Northern Research Institute, Tromsø, Norway, [3]Swedish Institute of Space Physics, Uppsala, Sweden, [4]EISCAT Scientific Association, Ramfjordmoen, Norway, [5]Department of Physics and Astronomy, University of Leicester, Leicester, UK

Key Points:
- First observations of topside, HF-induced enhanced ion line spectra
- Systematically recurring topside enhancements at the resonance altitude during pumping outside the radio window
- Enhancements predominantly occur when pumping just below the fourth electron gyrofrequency

Correspondence to:
T. Rexer,
theresa.rexer@uit.no

Citation:
Rexer, T., Gustavsson, B., Leyser, T., Rietveld, M., Yeoman, T., & Grydeland, T. (2018). First observations of recurring HF-enhanced topside ion line spectra near the fourth gyroharmonic. *Journal of Geophysical Research: Space Physics*, *123*. https://doi.org/10.1029/2018JA025822

Received 26 JUN 2018
Accepted 21 SEP 2018
Accepted article online 28 SEP 2018

Abstract We present first incoherent scatter radar observations of systematically recurring, high-frequency (HF)-enhanced ion line spectra at the topside F-region ionosphere, during magnetic field aligned HF pumping in an O-mode polarization. The European Incoherent Scatter UHF radar was directed in magnetic zenith on 9–11 March 2016 while stepping the pump frequency across the double resonance of the fourth harmonic of the electron gyrofrequency and the local upper hybrid frequency, in a 3-min-on, 3-min-off pump cycle. Topside and bottomside enhancements occur at the respective plasma resonance altitude and seem to be asymmetrically conditioned by the relative proximity of the pump frequency to the double resonance frequency. Further, the topside HF-induced ion line enhancements predominantly appear while the pump frequency is just below the double resonance frequency and only simultaneous to strong bottomside enhancements. A powerful, HF radio wave in O-mode, transmitted in the direction of magnetic zenith is reflected a few kilometers below the plasma resonance altitude, where the pump frequency is equal to the local plasma frequency, on the bottomside F-region in the ionosphere. Transionospheric propagation of the pump wave outside the radio window can be facilitated by density striations in the plasma, and we consider, in detail, the possible mechanisms proposed for propagation outside the standard radio window.

1. Introduction

A high-power, high-frequency (HF) O-mode radio wave with frequency lower than the peak ionospheric plasma frequency can drive a number of processes when it reaches the ionosphere. Depending on the power and polarization of the HF wave and the local plasma parameters, these include generation of small scale density depletions (e.g., Kelley et al., 1995; Honary et al., 1999), enhanced electron temperatures (e.g., Robinson et al., 1996; Rietveld et al., 2003), stimulated electromagnetic emissions at frequencies around the pump frequency (Leyser, 2001, and references therein) and enhanced optical emissions (e.g., Gustavsson et al., 2006; Kosch et al., 2002; Rietveld et al., 2003). Many of these responses vary in magnitude and character when the pump frequency, f_{HF}, varies, especially so when f_{HF} is close to a multiple, n, of the electron gyrofrequency, f_g, in the upper hybrid resonance layer. A vertically propagating, O-mode polarized pump wave has a reflection point, or cutoff, when it reaches an altitude where its frequency is equal to the local plasma frequency, f_p. Due to refraction in the ionosphere, rays at angles larger than the *Spitze* angle (equation (1)) will reflect at slightly lower altitudes (Rietveld et al., 1993). Signatures of pump wave propagation beyond the reflection height to higher altitudes and regions of higher plasma frequency and density was first observed in ionograms (Ellis, 1956). In incoherent scatter radar (ISR) measurements, effects of the HF pump wave above the O-mode reflection height were first observed at midlatitudes (Ganguly & Gordon, 1983) and later at high latitudes (Isham et al., 1990). For this to occur, certain conditions have to be met.

An O-mode pump wave propagating in a strictly field aligned direction, $\mathbf{k}\|\mathbf{B_0}$ and $\mathbf{k}_\perp = 0$, is a left-hand circular polarized (LHCP) wave, and at the point where $f_p = f_{HF}$, it can pass trough a narrow ($\sim 1°$) radio window (Mjølhus, 1990). This limiting case of a wave that is strictly field aligned is known as an L-mode wave (Chen, 1983). For altitudes where the pump frequency is higher than the local plasma frequency, $f_{HF} > f_p$, the wave is in LHCP O-mode with the corresponding dispersion relation, while for altitudes where the pump frequency is lower than the local plasma frequency, $f_{HF} < f_p$ it is a LHCP X-mode wave (see Figure 1 in

Nordblad & Leyser, 2010). The X-mode branch of the L-mode wave is also known as the Z-mode (Mjølhus, 1990), but the Z-mode usually refers to all wave vectors from parallel to perpendicular to the magnetic field. The standard radio window for an O-mode pump wave is at the *Spitze* angle,

$$\sin(\theta_c) = \sin(\alpha)\sqrt{\frac{Y}{1+Y}} \tag{1}$$

with $Y = \frac{f_g}{f_{HF}}$ and α is the angle of the magnetic field from vertical, in a horizontally stratified ionosphere (Budden, 1980). The *Spitze* angle is that angle of incidence for which an O-mode wave, transmitted from the ground, has refracted to being magnetic field aligned ($\mathbf{k} \parallel \mathbf{B_0}$) when reaching the plasma resonance height. At the European Incoherent Scatter (EISCAT) facility in Tromsø the radio window is between $\theta_c = 5^\circ - 6^\circ$ south from vertical, depending on the pump frequency (Isham et al., 1996).

Four possible mechanisms for propagation of a pump wave beyond the reflection height, outside of this narrow radio window, have been proposed. The first is the introduction of new artificial radio windows by large-scale density striations in the ionosphere that guide an O-mode wave such that the transmission conditions are met outside the standard radio window (Leyser & Nordblad, 2009; Nordblad & Leyser, 2010). Such density ducts, with horizontal scales on the order of a kilometer, can exist naturally (e.g., Fejer & Kelley, 1980; Gurevich et al., 1995) or can be efficiently generated by the O-mode HF pump wave (Gurevich et al., 1998; Kelley et al., 1995; Leyser & Wong, 2009; Utlaut & Violette, 1974, and references therein). If the propagating wave does not encounter the L-mode cutoff at,

$$f_{HF} = f_L = -\frac{f_g}{2} + \frac{1}{2}\sqrt{f_g^2 + 4f_p^2} \tag{2}$$

after passing through a radio window, it continues propagating to higher altitudes and can reach the topside ionosphere (Eliasson et al., 2012; Mjølhus & Flå, 1984), and continue to propagate into space (Leyser et al., 2018).

The second mechanism is a resonant scattering process of the pump wave on small-scale, field aligned, density irregularities (Mishin et al., 2001). Here the incident O-mode pump wave can efficiently be transformed in to a Z-mode wave as a result of scattering on the field aligned striations at the bottomside ionosphere. As the propagating wave reaches the topside, several turbulent processes may occur and transform the wave to O-mode and electrostatic waves at this altitude. The small-scale density striations are strongly excited by the resonance instability (Vas'kov & Gurevich, 1977), and models for their nonlinear stabilization have been obtained (Gurevich et al., 1995; Istomin & Leyser, 1997).

Eliasson (2008) has simulated a propagation process for low duty-cycle experiments, minimizing the effect of density irregularities, with vertically propagating O-mode waves. Here the incident O-mode wave is efficiently converted to Z-mode waves within a few milliseconds, due to Langmuir turbulence, at the reflection altitude. The Z-mode wave will propagate to higher altitudes and reach the topside reflection altitude. This mechanism is effective only for low duty cycles and pump waves that reach the resonance altitude, and thus not a probable explanation for the observational results of our experiment.

A fourth mechanism for producing topside enhancements at midlatitudes (Vas'kov et al., 1995) has been proposed by Vodyanitskij et al. (1974), in which resonant electrons at the bottomside, exited by the pump wave, carry the plasma oscillations to the topside ionosphere. We consider this effect to be unlikely for our observations due to the large distance between the top and bottomside ionosphere. Neither thermal- nor photoelectrons have a long enough mean-free-path length ($\sim$ 4, 2.5, and 10 km at 220 km for 1, 10, and 100 eV, respectively) to reach the topside F-region with flux modulated by the pump frequency, at the bottomside ionosphere resonance altitude.

Enhancements of the backscattered power in the ion and plasma lines of ISR measurements in the ionosphere, due to high-power HF wave pumping, have been observed many times (e.g., Ganguly & Gordon, 1983; Isham et al., 1990; Isham, Rietveld, et al. 1999; Isham, Hagfors, et al. 1999; Kosch et al., 2011; Rietveld et al., 2002). Isham et al. (1990) reported ion-line enhancements at the topside and bottomside of the F-region observable during the first 10-s period after heating on in magnetic zenith. During their experiment, topside HF ion line enhancements (THFIL) were sporadically observed from one heating on pulse to the next. In 1997, Isham, Rietveld, et al. (1999) performed a second experiment where THFIL were clearly seen in the data from

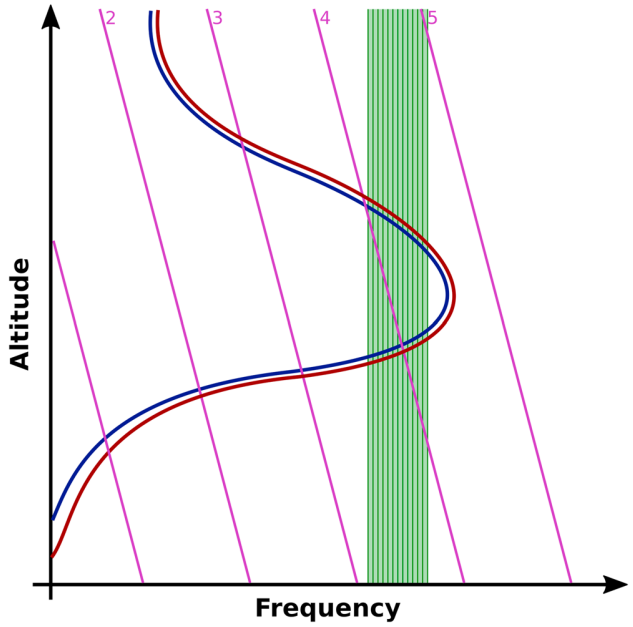

Figure 1. Schematic of the experiment setup. Red and blue lines illustrate the altitude profile of the local upper hybrid- and plasma frequency, respectively. Pink diagonal lines show harmonics of the electron gyrofrequency, while the green shaded area indicates the frequency range in which the HF pump wave stepped.

both the UHF and VHF radar at the EISCAT site in Tromsø. Again, observations showed clear THFIL and the the authors attribute the observations to a coupling of the O-mode wave to the Z-mode at the altitude where $f_p = f_{HF}$ and the pump wave is parallel to the magnetic field, $\mathbf{k} \parallel \mathbf{B_0}$, that is, the radio window. Mishin et al. (2001) suggested the resonant scatter process of the pump wave, facilitating a conversion from O-mode to Z-mode waves on small-scale field-aligned irregularities as the cause for these observations. Nordblad and Leyser (2010) also suggest that L-mode propagation through heater induced radio windows can not be ruled out as an explanation for the Isham, Rietveld, et al. (1999) observations. In an experiment studying the angular extent of the radio window in 2004, Kosch et al. (2011) observed clear topside enhancements during a low duty cycle (3.3%), heating experiment pointed in a direction 9° south of zenith. They present observations indicating the location of the bottomside radio window to be around 7°–8° south of zenith, arguing that this can be explained by a tilt in the ionosphere, that was observed in the Dynasonde data during the experiment. Interestingly, they observe the equatorward, 2°–3°, displacement of the topside enhancements relative to the bottomside radio window, first predicted by Mjølhus and Flå (1984). Most recently, Leyser et al. (2018) presented possible evidence of L-mode propagation through the F-region, where $f_{OF2} > f_{HF}$, into space.

In this paper we present first observations of systematically occurring HF-enhanced ion line spectra from the topside ionosphere when stepping through the fourth electron gyroharmonic frequency. During a heating experiment on 9–11 March 2016 at the EISCAT facility near Tromsø, Norway, clear THFIL from the F-region were observed in 33 out of 90 heating on pulses. The HF pump frequency of each on pulse was stepped through the fourth harmonic of the electron gyrofrequency. Observations of the natural ionospheric Langmuir waves, enhanced by photo electrons during daytime conditions, in the plasma line spectra of the UHF radar have been used to calculate the electron density giving the critical plasma frequencies in the ionosphere with an unprecedented accuracy. This allows us to determine that THFIL occur in the plasma resonance region where, $f_p = f_{HF}$, in the ionosphere. A gyro harmonic effect of the THFIL and bottomside ion line enhancements (BHFIL) was detected, when the pump frequency was near the double resonance of the local upper hybrid frequency and the fourth harmonic of the electron gyrofrequency. The upper hybrid resonance region has been studied extensively, and the "double resonance" frequencies of the different electron gyro harmonics have been shown to be of great importance and is the focus of a large body of research (see, e.g., Ashrafi et al., 2007; Borisova et al., 2014; Dhillon & Robinson, 2005; Grach et al., 2016; Gustavsson et al., 2006; Honary et al., 1995; Honary et al., 1999; Kosch et al., 2002; Leyser et al., 1989; Stubbe et al., 1994; Robinson et al., 1996, and references therein).

We present the first observations of topside HF-enhanced ion line spectra, as well as first experimental results of a gyro harmonic effect of the enhancements. All topside enhancements are compared and analyzed in the context of the critical plasma frequencies in the ionosphere.

2. EISCAT Heating and UHF Radar

On 9–11 March 2016 EISCAT Heating (Rietveld et al., 2016) was operated in a 3-min-on, 3-min-off cycle, transmitting LHCP HF radio waves in the magnetic zenith direction, which upon reaching the ionosphere have most of their energy in the O-mode. The experiments were conducted during quiet geomagnetic daytime conditions from 10:00 UT to 13:00 UT on all 3 days. During the 3-min-on pulse, the pump frequency, f_{HF} , was kept constant for 1 min, then increased in steps of 10 or 20 kHz every 10 s for 2 min. The pump frequency was chosen such that it was stepped through the double resonance of the local upper hybrid frequency, f_{uh}, and the fourth harmonic of the electron gyrofrequency, $4f_g$,such that the condition

$$f_{HF} = f_{uh} = 4f_g \tag{3}$$

was met at some point in the bottomside ionosphere, during the frequency stepping. Here $f_{uh}^2 = f_g^2 + f_p^2$. The effective radiated power (ERP) on 9 March was 359 MW at 5.35 MHz O-mode heating with 12.5 MW X-mode

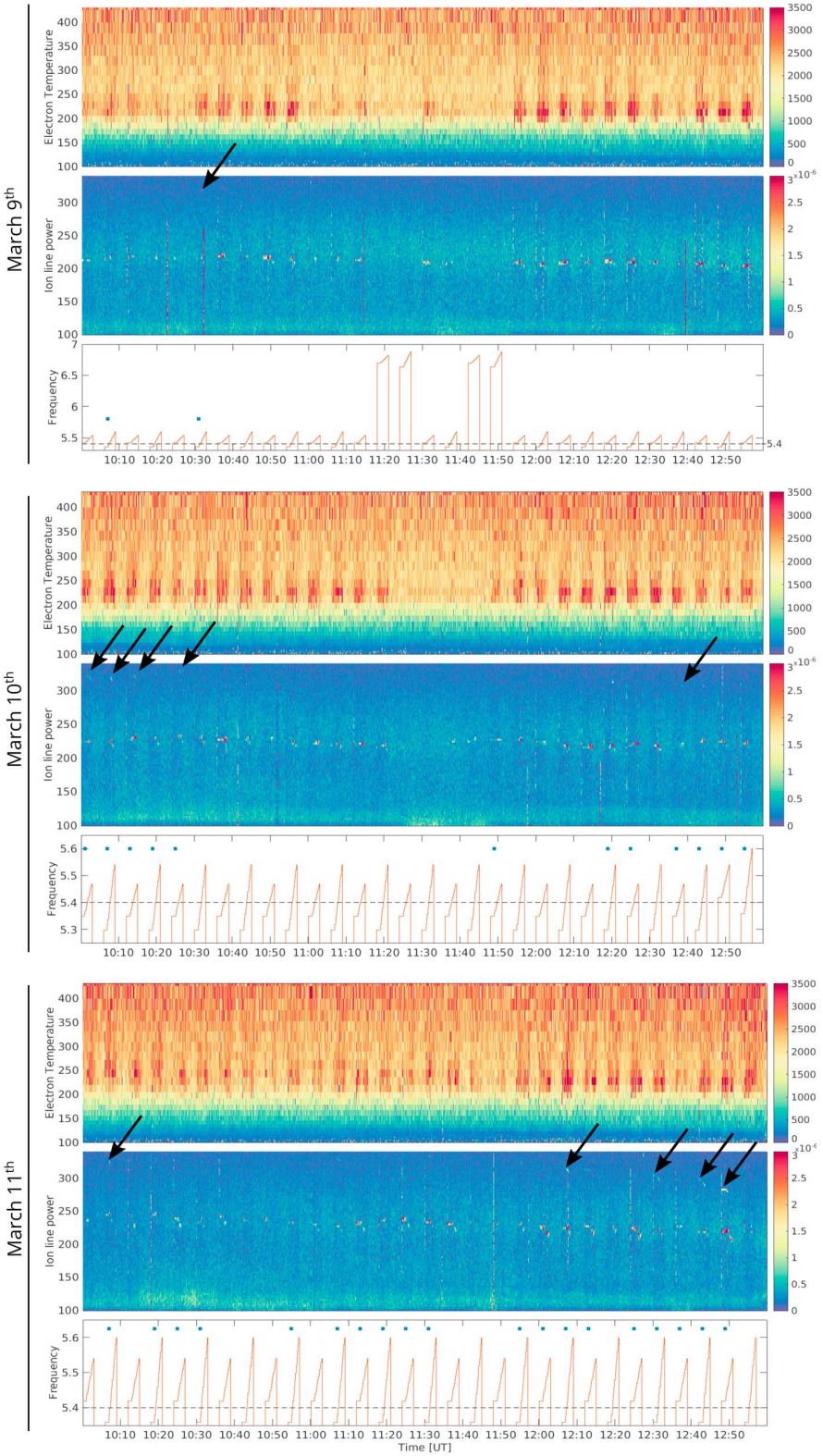

Figure 2. Electron temperature (top), backscattered ion line power (middle) and pump frequency (bottom) for 9–11 March 2016. Blue dots in the bottom panels indicate heating pulses during which topside ion line enhancements are observed. Black arrows highlight some, but not all, enhanced backscatter in the ion line power at the topside ionosphere.

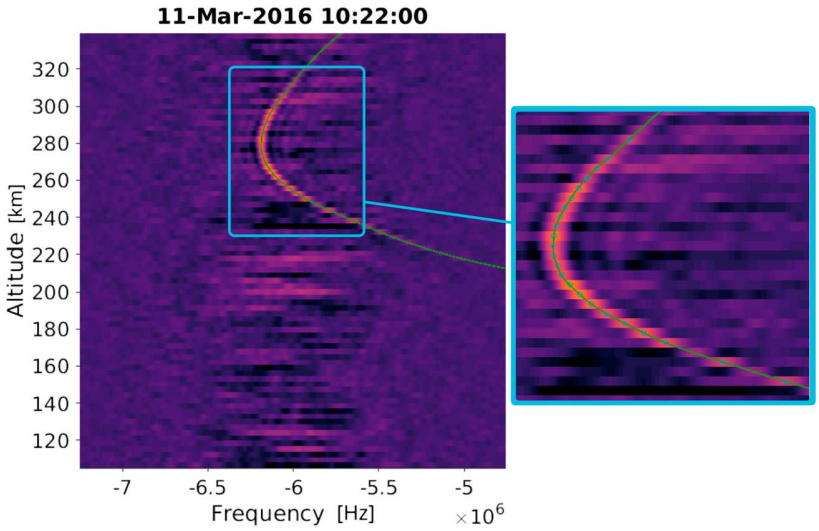

Figure 3. Example of a 1-min integrated and low-pass-filtered plasma line spectra data from 11 March 2016 at 10:22 UT, which is used to calculate a curve fit to the natural Langmuir wave enhancements. Blue circles indicate signals that are 5 standard deviations above noise level, which are used to find the fit shown in green.

"leakage" and a beamwidth of 7.0° in the north-south plane. On 10 March the ERP of the heater was 330 MW at 5.35 MHz, with a beamwidth of 7.2°, while on 11 March, the ERP was 363 MW at 5.42 MHz, and the beamwidth was 7.0°.

A schematic of the experiment setup is shown in Figure 1, where the red and blue lines illustrate the altitude profile of the upper hybrid and plasma frequency. Gyrofrequency harmonics are sketched in pink, and the frequency band in which we step the HF pump wave is shown in green to give an overview of important frequencies involved in the experiment and their relation. From this illustration we see that for a portion of each 3-min-on pulse, the pump frequency will be just below and just above the double resonance frequency, as we step through it by increasing the pump frequency.

The ionospheric response of the HF modulation wave was observed using the colocated EISCAT UHF radar, also pointing in the direction along the local magnetic field. The IS-radar measurements were done with the "beata" program (see Lehtinen & Huuskonen, 1996; Tjulin, 2017, and references therein). Only lags out to 410 μs are computed, which gives a frequency resolution of 2.4 kHz. Range gates are computed from 49 to 693 km of range, with 5-s temporal resolution and 3-km range resolution. In addition, the plasma line is sampled at 0.4 μs, covering a 2.5-MHz wide band offset from the transmit frequency by 8.4, 6, and 3.4 MHz, and covering ranges from 107 to 374 km. During the experiment strong backscatter from the natural existing Langmuir waves in the ionosphere were observed, mostly in the −6 MHz band of the downshifted plasma spectra.

Figure 2 shows summary plots of the experiment and results from 10:00 UT to 13:00 UT for 9 (top), 10 (middle), and 11 (bottom) March 2016. The upper panel for each day shows the electron temperature modulated by the HF pumping. The response in the backscattered power of the ion line is shown in the second panel. Arrows indicate some, but not all, examples of the strongest THFIL backscatter we observe, which are apparent even in these overview figures. In the bottom panel the heating on/off times and frequency are shown. Blue dots indicate all HF pump pulses where clear topside ion line enhancements are found during the analysis. Several plasma line spectra are observed, where strong enhancements at different frequencies and altitudes, coincidental with the HF pump wave. These are not discussed in detail in this paper.

3. Determination of Electron Density From Plasma Line Frequency Spectra

From the downshifted UHF power spectra it was possible to identify the frequency of peak power from the backscatter of natural Langmuir waves in range gates from about 180 to 320 km. This made it possible to obtain an accurate estimate of the electron density. From the Langmuir wave altitude profile we calculate the electron density, adapting the relevant parts of the method for temperature determination from plasma line

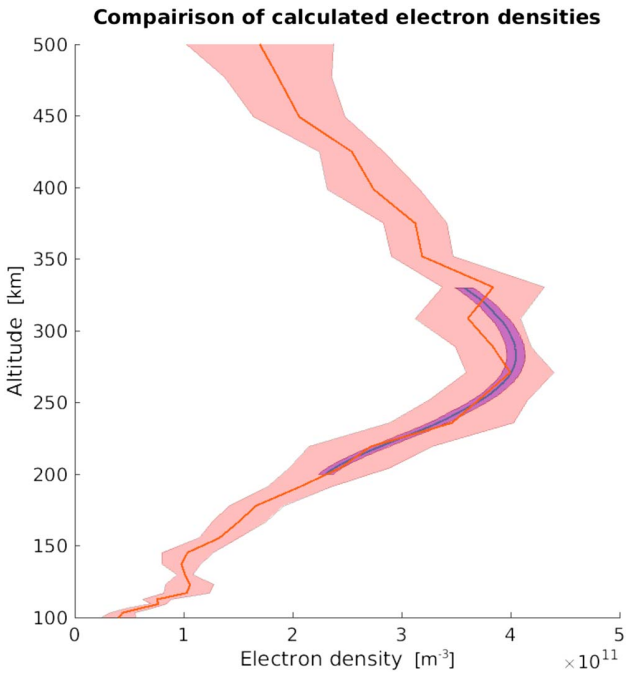

Figure 4. Altitude profile of electron density calculated during heating off from the ion line and plasma line spectra obtained from the UHF EISCAT radar on 11 March 2016 at 10:17:00 UT. The red shaded area shows the 1σ uncertainty level for the ion line density calculations, while the blue area shows the reasonable uncertainty for the electron density as calculated from the plasma line.

observation described by Hagfors and Lehtinen (1981). Solving the dispersion relation for the downshifted plasma line, $f\_$, for the density, N_e we obtain the physically relevant solution:

$$N_e = \left(\frac{m_e \epsilon_0}{q^2}\right)\left[\frac{-y + \sqrt{y^2 - 4xz}}{2x}\right]^2 \tag{4}$$

where

$$x = \frac{1}{2\pi} + \frac{3T_e}{4m_e\pi c^2}, \qquad y = f\_ - \frac{6T_e f_0}{c^2 m_e}, \qquad z = \frac{12\pi T_e f_0^2}{c^2 m_e}$$

where f_0 is the UHF radar frequency and c the speed of light. T_e and m_e are the electron temperature and mass respectively.

We used standard ISR parameters estimated from 30 s integrated ion line data for the electron temperature, necessary for these calculations. Although the altitude resolution of this electron temperature data is the same as for the estimated electron density parameter, obtained from the ion line, N_e is weakly dependent on T_e. Thus, T_e only contributes with a small correction term to N_e in equation (4). The densities obtained from this calculation are used to calculate O-, X-, and L-mode cutoff frequencies and the plasma- and upper hybrid- frequency, which are used in the analyses presented in this paper.

An example of 1-min integrated and low-pass-filtered, plasma spectra from 100 to 340 km, between −7.25 and −4.75 MHz, on 11 March 2016 at 10:22 UT are shown in Figure 3. The green line indicates the calculated curve fit to the signal of the natural Langmuir waves. Backscatter from the natural Langmuir waves are clearly visible for 80–90 km in altitude around the F-layer maximum frequency, around 280 km. Weaker backscatter from these is distinguishable well above the background noise, also for altitudes down to around 220 km and up to around 320 km, for this time interval. For most spectra from this experiment, the range where a clear power enhancements from Langmuir waves was detected was between 180 and 320 km and for frequencies below −5.25 MHz. The curve fit in frequency and altitude is obtained from signals where the power enhancements are 5 standard deviations or more above the mean noise level, at that altitude.

Previously, the electron densities have been obtained from ion-acoustic waves detected in the ion line spectra of the EISCAT radar. The altitude resolution obtained through this method decreases with height and is ≈20–25 km around 150–350 km, and hence, the accuracy and precision of the densities calculated from these is restricted. In Figure 4 we compare the altitude profile of the electron density as calculated from the ion and plasma line on 11 March 2016 at 10:17:00 UT. The red shaded area indicates 1 standard deviation for the ion line density data as calculated from the same time interval as was used for the curve fit to the natural Langmuir wave enhancements in the plasma line. The blue shaded area indicates the uncertainty of the electron density calculated from the plasma line. This uncertainty was obtained by combining 1 standard deviation for the temperature, σ_{Te}, with an assumed frequency uncertainty, σ_f, of 20 kHz, which corresponds to the mean half width, half maximum of the power enhancement signals of the plasma line. Comparing the altitude resolution and the calculated accuracy of these, as in the example in Figure 4, it is clear that the densities calculated by this method, from the natural Langmuir wave signatures observed in the plasma spectra, improve our results significantly for the altitudes where naturally enhanced plasma line data are available.

4. Data Analyses and Results

We now look at the observations made by the UHF radar during the frequency stepping of the pump wave, focusing only on the 3-min-on pulses where we observe topside enhancements of the ion line spectra. Clear topside enhancements were detected during 33 heating on pulses on 9–11 March 2016. The examples of the enhancements on the topside ionosphere shown in the following section are all from separate heating on pulses, in order to emphasize and demonstrate the systematic occurrence of the THFIL with respect to the double resonance frequency.

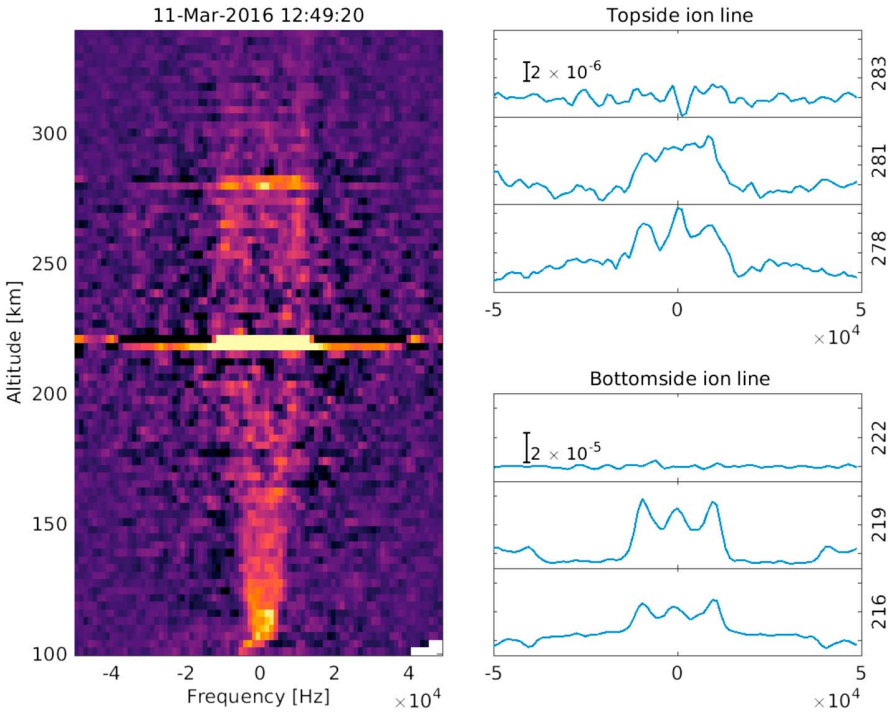

Figure 5. Example of an ion spectra showing topside enhancements on 11 March at 12:49:20 UT (left). The top and bottom panels on the right show the line spectra at the altitude of the strongest enhancements for the top and bottomside ionosphere, respectively.

Figure 5 shows a typical example of the ion line enhancements from 12:49:20 on 11 March at the instant during the on pulse where the topside enhancement is the strongest. The figure shows the first published observations of the THFIL spectra. The left panel shows an instant in time, of the backscattered power in the ion spectra range, where the bottom and topside enhancements are clearly visible during HF pumping. The upper and lower right panel show line plots, of the same spectra as in the left panel, at the altitude of the strongest enhancement for the topside and bottomside, respectively. Note that the scales of the line plots for the topside and bottomside enhancement are different and that the backscattered power from the topside is weaker by an order of magnitude. We observe this difference in backscattered power for most pulses. Signatures of the natural ion line spectra are seen at all altitudes. To isolate the HF-enhanced backscatter, the

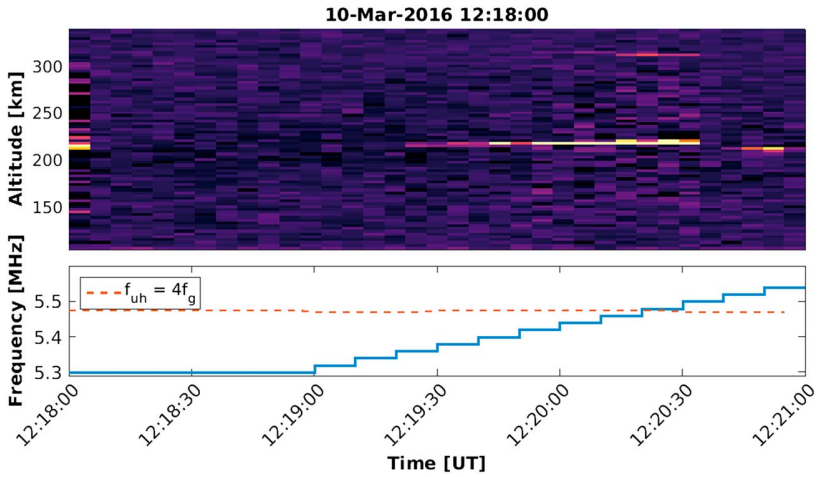

Figure 6. The time evolution of the averaged backscattered power in the ion line spectra for one 3-min-on pulse from 10 March at 12:18 UT. The bottom panel shows the pump frequency and double resonance frequency.

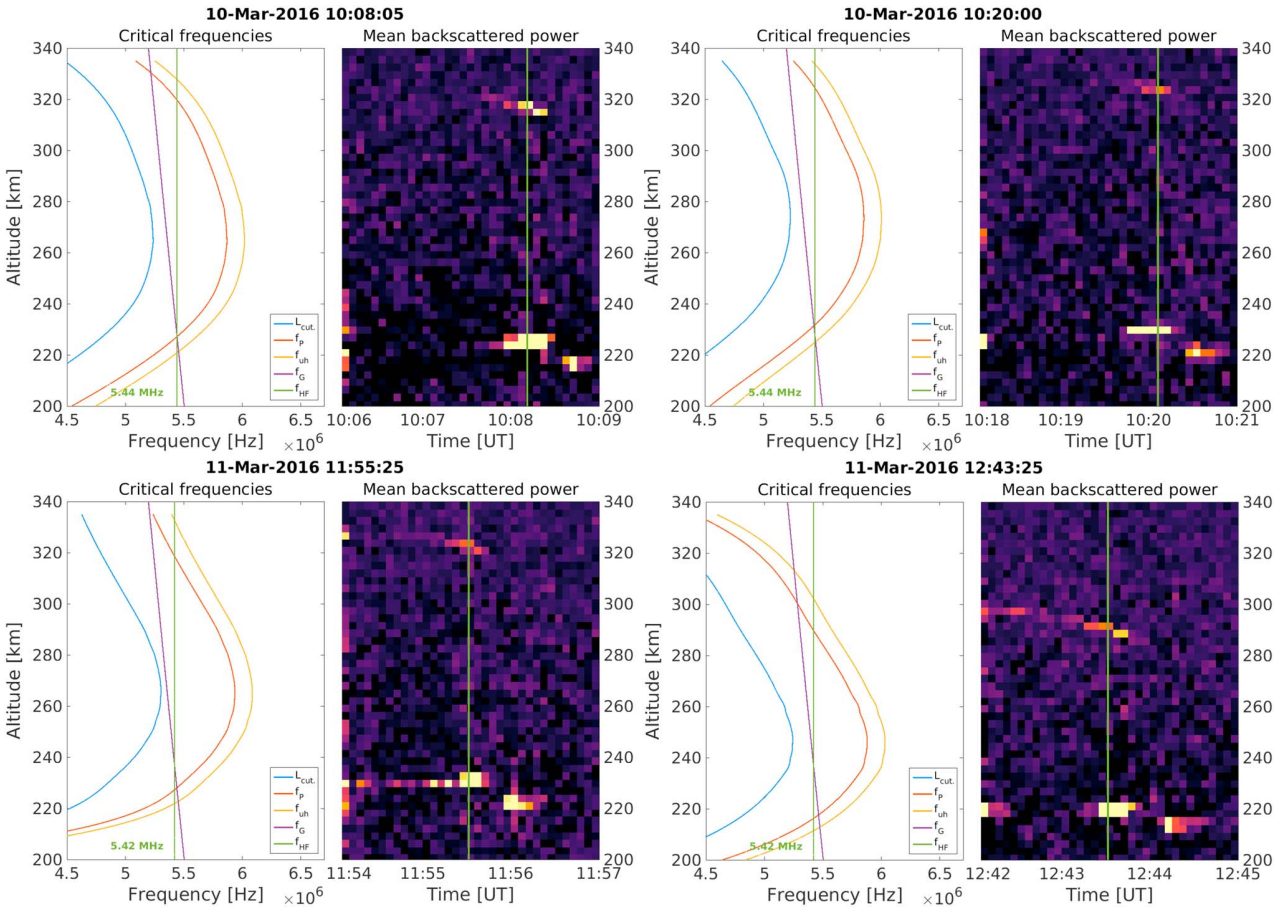

Figure 7. Four examples of 3-min pulses where we see clear topside enhancements. The left plot in each panel shows the critical frequencies calculated from the observed natural Langmuir waves. The blue line indicates the L-mode cutoff (equation (2)), the red is the local plasma frequency, purple shows the fourth harmonic of the electron gyrofrequency, while the green vertical line indicates the frequency of the transmitted O-mode pump wave. Right panel shows the 5-s mean backscattered ion line power during a 3-min-on pulse. The vertical green line indicates the time corresponding to the left panel plot.

natural ion line backscatter is calculated from a 1-min heating off period immediately before start of a new heating on period and subtracted from all ion spectra in the following 3 min of heating on. This background subtraction is done for all following ion spectra presented here.

Figure 6 shows the temporal evolution of the mean, 5-s integrated, ion line power during the on pulse starting at 12:18:00 UT on 11 March. The transmitted pump frequency is indicated in blue in the lower panel along with the frequency of the double resonance in red. The overshoot effect (Stubbe, 1996) is apparent in the first 5 s of the heating on period. Starting at 12:19:20 UT in the 213-km altitude range gate, the BHFIL is clearly seen until 12:20:35 UT where the strongest enhancement is in the 222-km altitude range gate. The topside enhancement, for this pulse, appears weakly first at 12:20:05 UT at 316 km and is visible for 30 s until 12:20:35 UT, where it is strongest at 310 km. The altitude resolution of the radar in this experiment is around 3 km so the respective decrease and increase in the altitude of the strongest THFIL and BHFIL corresponds to 3 and 2 steps in altitude. That is ~9 and ~6 km, respectively. The increase and decrease of altitude of the enhancements is consistent with the respective increase and decrease of the resonance altitude, where $f_P = f_{HF}$, as we step the pump frequency up during the 3-min pulse, and we observe this in most pulses. At the time of the appearance of the first bottomside enhancement, the pump frequency is 5.36 MHz. At 12:20:40 UT, where both topside and bottomside enhancements abruptly disappear the pump frequency is 5.5 MHz after having been stepped every 10 s in 20-kHz increments. A second bottomside enhancement appears at 12:20:45 UT in the 210-km range gate and lasts for 15 s before the pump is turned off.

Four further examples, out of the 33 pulses with clear THFIL observations, are shown in Figure 7. All left-hand plots show the altitude profile of the critical frequencies, f_p, f_{UH}, $4f_g$, and the L-mode cutoff frequency

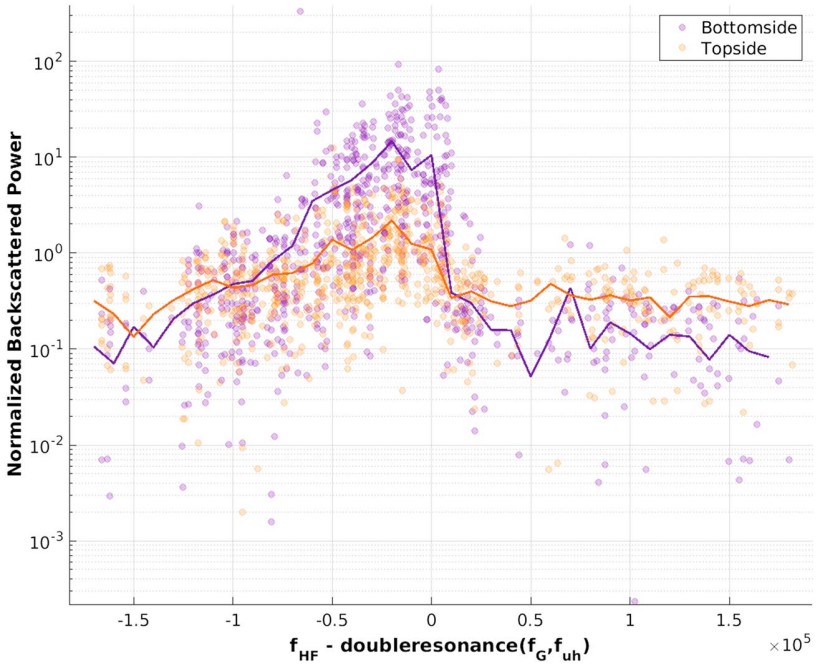

Figure 8. Comparison of all 33 heating pulses. Backscattered ion line power relative to the difference of the pump and double resonance frequency. Topside enhancements are shown in orange while bottomside enhancements are shown in purple. The superposed lines show the mean of the observation.

(equation (2)) calculated from enhanced backscatter from natural Langmuir waves observed in the plasma line of the radar (see section 3). The green number toward the bottom of the plot indicates the pump frequency at this instant. The corresponding right plots, as in Figure 6, show the temporal evolution of the mean backscattered power from −15 to 15 kHz, in the ion line for the 3-min HF on period, with the time indicated on the *x*-axis. The vertical green line indicates the time of the strongest backscatter from the THFIL, to which the left plot corresponds for each pulse.

For all 33 pulses with identified THFIL we see consistent responses. This is seen in Figure 8 where we compare the normalized backscattered power of all data points of the 33 pulses, at the altitude of the strongest BHFIL and THFIL. We relate this, to the difference between the pump frequency and the double resonance frequency, that is, how close the HF pump frequency is to the double resonance. Negative values indicate an HF pump just below the double resonance frequency. BHFIL are shown in violet, while the THFIL are orange. The mean of these observations is shown by the solid lines in the same color coding. Comparing these and illustrated by the four pulses shown in Figure 7, we observe the following similarities for THFIL:

1. Signatures of the overshoot effect are easily identified in the first 5-s integration period after heating on, as seen in the four right-hand plots of Figure 7.
2. After the overshoot with the pump frequency still kept constant, very little or no enhancement of backscattered power is seen.
3. As the HF pump frequency is increased throughout the pulse the BHFIL intensity increase until they reach a maximum and decrease significantly, then disappear completely (Figure 8).
4. Simultaneous to the increase in the BHFIL we observe clear enhancements at the topside ionosphere.
5. The strongest backscatter from the THFIL coincides with the strongest backscatter from the BHFIL.
6. For the two pulses shown in the bottom panels of Figure 7 we can recognize a THFIL also before the strongest BHFIL, while for the two pulses in top panels, the THFIL seems to appear simultaneous to the strongest BHFIL.
7. A decrease and increase of altitude of the THFIL and BHFIL, respectively, is clearly visible in the figure and corresponds to the increasing altitudes of resonance for increasing f_{HF}.
8. Comparing this observation to the left plots of Figure 7, which all show the critical frequencies calculated for the instant at which the strongest THFIL is observed, in all panels, we see that the BHFIL and THFIL occur close

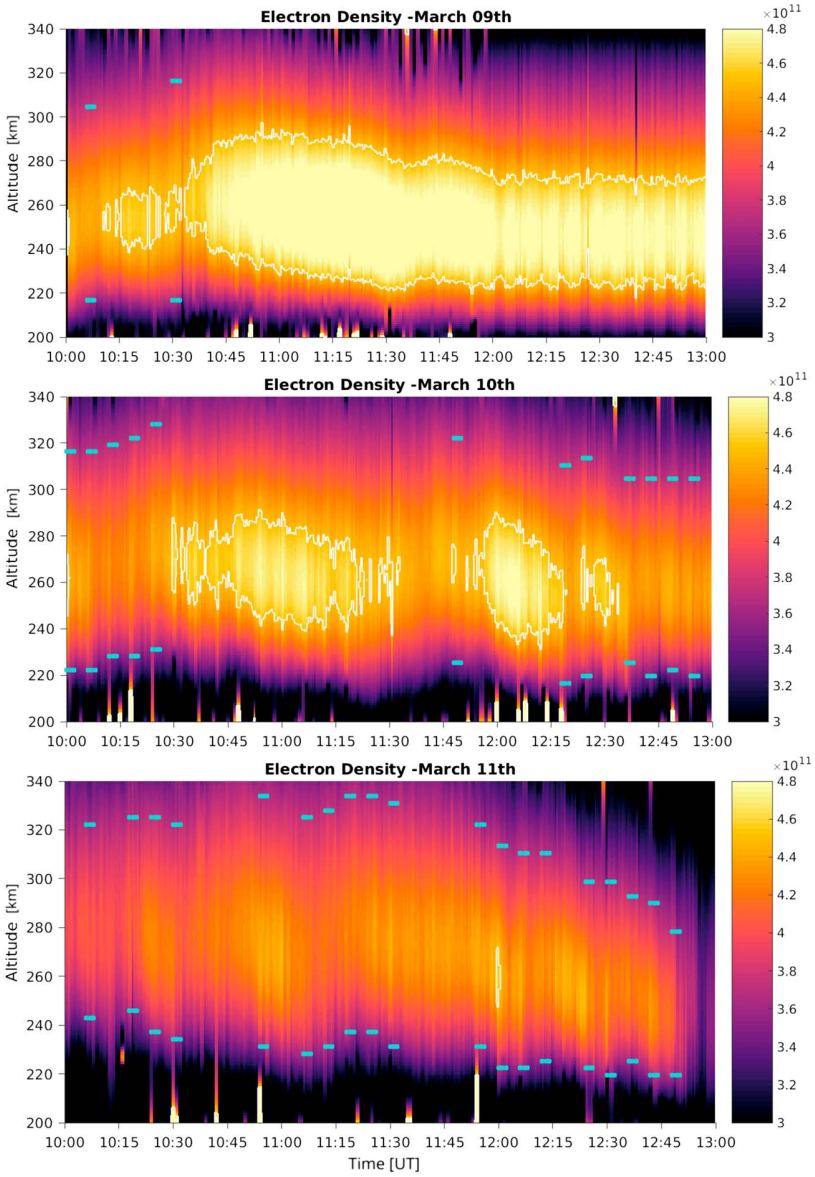

Figure 9. Electron density (color) calculated from the UHF plasma line observations of the natural Langmuir wave enhancements on 9–11 March 2016. A white contour indicates the superposed L-mode cutoff frequency of 5.4 MHz, and the altitude and occurrence of BHFIL and THFIL for pulses where THFIL are observed are shown by blue bars.

to the altitude where the HF pump frequency (green) is equal (or close to) the the local plasma frequency f_P (red) at the topside and bottomside ionosphere.

9. The second BHFIL, appearing at lower altitudes, is seen for all of the shown pulses after the main BHFIL.

The electron density at altitudes from 200 to 340 km, for the duration of the experiment on all 3 days is shown in Figure 9. As for Figure 7, the density is calculated as described in section 3. Blue bars show the altitude and time of the BHFIL and THFIL for all pulses where THFIL where observed. The white contour in these three figures indicates where the L-mode cutoff frequency (see equation (2)) is 5.4 MHz and is intended to give an indication of when the cutoff frequency was close to or at the pump frequency. In the bottom panels for all days in Figure 2 we have marked this frequency, for comparison to the pump frequency, by the dashed line. For three heating on pulses with observed THFIL (9 March at 10:30 UT and 10 March at 12:18 UT and 12:24 UT), the pump frequency is below the L-mode cutoff for the beginning of the pulse. As we step the pump frequency up, it increases above the local L-mode cutoff frequency toward the end of the heating pulse,

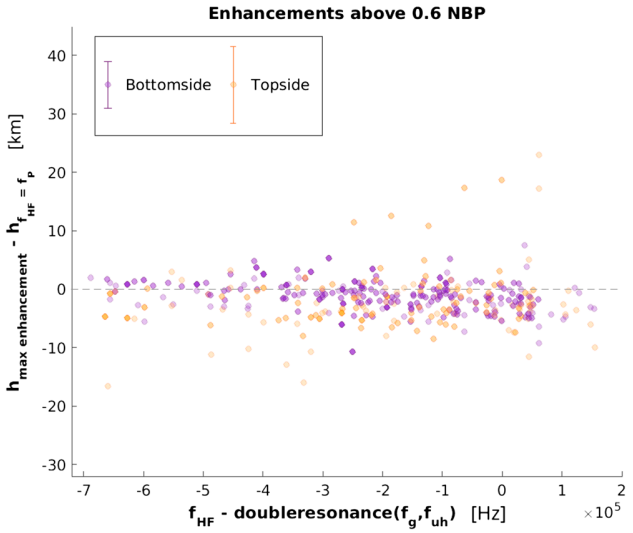

Figure 10. Comparison of the altitude of the appearance of the THFIL and BHFIL above 0.6 NBP in the ion line spectra, and the altitude of the plasma resonance, $f_P = f_{HF}$ as calculated from the plasma line. The mean error of ±4 km for the bottomside and ±6.6 km, for for the topside, for all points is indicated in the legend.

permitting trans-ionospheric propagation. It is nevertheless evident in Figure 9 that THFIL is generally only observed when the L-mode cutoff is sufficiently low, that is, below the frequency at which the pump wave can propagate as an L-mode wave without encountering a cutoff. In this figure we also see that the altitude of the observed BHFIL and THFIL fluctuates with the observed density variations on all 3 days.

The altitude of the observed enhancements and the altitude of the resonance heights, $f_p = f_{HF}$ at the top and bottomside ionosphere, obtained from the calculations discussed in section 3, is shown in Figure 10. The altitude of data points, where the normalized backscattered power is stronger than 0.6, is compared to the altitude of the resonance height, at that time, for the THFIL and BHFIL separately. It is clear from the figure that the enhancements at both altitudes occur at or close to, their respective resonance heights. Mean errors of ±4 and ±6.6 km, indicated in the figure, for the bottomside and topside altitudes, respectively, are due to the uncertainty in the plasma line fit and the difference in temporal resolution of the plasma line fit and the ion line spectra. The discrepancy in the temporal resolution also accounts for the slight negative trend of the altitude differences.

5. Discussion

We present the first observations of THFIL spectra from EISCAT UHF radar measurements during HF modulation experiments. The EISCAT Heating facilities transmitted a LHCP electromagnetic wave into the ionosphere directed in magnetic zenith, in a 3-min-on, 3-min-off cycle while stepping the pump frequency across the double resonance frequency at the fourth gyroharmonic. The different aspects of the observations are discussed systematically in the following.

5.1. Appearance of THFIL

Thirty-three cases of THFILs are clearly identified in our observations during HF-pumping with frequency stepping through the double resonance frequency. In Figure 9 the altitude of the THFIL and BHFIL for all 33 pulses are indicated. It is clear that no THFIL are observed when electron densities are high enough, such that there is a cutoff for the L-mode waves at f_{HF}. We see that the altitudes of both the THFIL and the BHFIL match the plasma resonance altitude of $f_P = f_{HF}$.

As apparent, from Figure 9, there are a number of heating on pulses (14) on 10 and 11 March, where no THFIL are observed, even though the L(Z)-mode cutoff frequency is lower than the pump frequency. On 10 March the L(Z)-mode cutoff frequency is below the double resonance frequency, from 11:30 UT to 11:51 UT, but only for the last (starting at 11:48 UT), of the four on pulses transmitted during that period, do we observe topside enhancements. Comparing the electron temperature during this period, shown in the middle panel of Figure 2, we see no temperature enhancements during these heating pulses. However, we do see an increased backscattered power in the ion line around 100-km altitude, in the middle panel, possibly due to E-region absorption. As a result of partial absorption at lower altitudes, less HF-wave power reaches the F-region and we observe very weak or no BHFIL for those three pulses.

On 11 March, 11 HF pulses were transmitted (10:00, 10:12, 10:36, 10:42, 10:48, 11:00, 11:36, 11:42, 11:48, 12:18, and 12:54 UT), where no THFIL were observed. For four of these (10:12, 10:42, 11:36, 12:18 UT), faint traces of THFIL can perhaps be detected. However, these were very weak and below the threshold we set for THFIL and were thus not included in our analysis. Noticeably the backscattered power of the ion line and temperature modulations (see bottom panels Figure 2), on the bottomside ionosphere for these four pulses was much lower than for pulses with observed THFIL enhancements. For the pulses at 10:36, 11:00, 11:42, and 11:48 UT we observed significantly weaker BHFIL than for pulses with THFIL. The electron temperature enhancements shown in Figure 2, during these pulses are also lower then for other pulses. Figure 8 indicates that THFIL primarily occur simultaneously to the BHFIL enhancements. It seems likely that there exists a threshold that has to be exceeded, such that a large enough fraction of wave energy can propagate beyond the bottomside reflection height and that this was not achieved during the pulses where the BHFIL were weak.

For the absence of the THFIL enhancement in the remaining three pulses, there are several possible explanations. The lack of a THFIL from the HF pulses starting 10:00 and 10:48 UT on 11 March are particularly interesting as they had an initial frequency of 5.42 MHz closely matching our estimate of the double resonance frequency for that time. For the pulse at 10:48 UT we initially observe clear BHFIL for 1 min, but no THFIL. For the pulse at 10:00 UT, no HFIL at any altitude was observed until the pump frequency was well above the double resonance.

Generation of density striations is significantly reduced for HF-pumping at the double resonance frequency. If propagation to the topside ionosphere is facilitated by small- or large-scale density striations in the ionospheric plasma, generated by the pump wave, then no THFIL are expected for this pulse. This could indicate that some period of heating on, at a frequency where small- or large-scale striations are effectively generated, is necessary prior to pumping at the double resonance frequency, were less wave energy is absorbed by turbulent upper hybrid processes such that the wave can propagate further. Further experiments are required to clarify this.

For the last HF pulse transmitted on 11 March at 12:54 UT, the electron density in the ionosphere had decreased such that the double resonance frequency was below the lowest pump frequency.

5.2. Evolution of THFIL

Four conclusions can be drawn from Figure 8:

1. Enhancements are observed when the pump frequency is between ∼ 80 kHz below the double resonance frequency and ∼ 9.8 kHz above the double resonance frequency.
2. All pulses have a similar development of the enhancements in relation to the relative proximity of the HF pump wave to the double resonance.
3. BHFIL are stronger than THFIL, sometimes up to an order of magnitude.
4. THFIL predominantly occur when we observe BHFIL.

A likely interpretation of the development of the observations is the following. During the first 5 s after heating on we observe the overshoot effect in all pulses, consistent with previous observations (e.g., Fejer, 1979; Honary et al., 1999; Showen & Behnke, 1978), which is rapidly suppressed within a few seconds, as the HF wave energy is absorbed through other processes (Robinson, 1989). Small-scale field-aligned striations are generated within a few seconds, as the HF pump wave is converted to UH electrostatic waves perpendicular to the geomagnetic field, at the upper hybrid resonance height (Robinson, 1989). Throughout this process no, or very little, enhanced ion acoustic or Langmuir waves are observed as most of the pump energy is absorbed by upper hybrid turbulence, leading to the formation of the density striations (e.g., Stubbe et al., 1994; Thidė et al., 2005), and significantly less reaches the resonance altitude.

As a result of the linear dispersion properties of upper hybrid waves around harmonics of the electron gyrofrequency, the growth of striations diminishes as the HF pump approaches the double resonance frequency (Mjølhus, 1993; Huang & Kuo, 1994; Robinson et al., 1996; Honary et al., 1999). The HF-pump energy can then be guided by the density irregularities and reach the resonance altitude, where coupling to Langmuir and ion acoustic waves is possible. This manifests itself, in the presented data, in the increase in ion line backscattered power on the bottomside ionosphere as the HF pump frequency approaches the double resonance. The enhancements increase while approaching the double resonance and abruptly disappear when the HF pump frequency increases beyond this, mirroring the asymmetric properties of the upper hybrid mode about the double resonance. Although the backscattered power of the THFIL is significantly less than that of the BHFIL, the THFIL show the same behavior as the BHFIL on approach of the double resonance as is seen in Figure 8.

5.3. Position and Altitude of the THFIL

As mentioned, there are two possibilities proposed for propagation of the incident wave to the topside ionosphere. The wave can pass through a radio window (Mjølhus, 1990), or the wave can be transformed into a Z-mode through the resonant scatter process (Mishin et al., 2001). While artificial, heater-induced radio windows can exist at multiple angles (Nordblad & Leyser, 2010), the standard radio window in a horizontally stratified ionosphere is located at the Spitze angle, around ∼5° – 6° at EISCAT depending on the pump frequency (Isham et al., 1996).

Both the heater and the UHF radar were pointed in the magnetic field-aligned direction, at 12° south of zenith, for our experiment. This is well outside of the standard radio window at ∼ 6° at EISCAT. The heating beam at full width, half maximum (FWHM) for this experiment was ∼ 7°, such that angles from ∼ 9° to ∼ 16° were

effectively illuminated by the beam. Kosch et al. (2011) report observations showing the radio window appearing around 7° – 8° with a spatial extent of 2° and a corresponding topside enhancement displaced further south by 2° – 3°, appearing around 8° – 12° and with and angular extent of 2° – 3°. As their experiment was run with a very low-duty cycle (3.3%), minimizing the generation of pump-induced striations, they attribute this southward displacement of the standard radio window to a local tilt in the ionosphere.

The heating beam in our experiment does not extend far enough at FWHM, to reach the radio window observed by Kosch et al. (2011) at 7° – 8°, but it is possible that parts of the beam at lower ERP do extend to this angle and propagate though the radio window. In this case the ionospheric tilt would have to be somewhat comparable to the tilt observed by Kosch et al. (2011). Also, as we observe topside enhancements multiple times on three consecutive days, any tilt during our experiment would have to occur systematically on all days and for the duration of all pulses where we do observe THFIL, in the same direction and with similar magnitude. In Figure 9, we see that the density varies considerably throughout the 3 hr on all 3 days. Especially on 10 and 11 March, we see signatures of periodic electron density variations. These variations are on timescales on the order of 10 – 40 mins, matching that of atmospheric gravity waves or traveling ionospheric disturbances (Hunsucker, 1982).

During our experiment the THFIL seem to occur independent of tilt angle when studying the five consecutive pulses on 11 March starting at 11:06:00 UT. Here we observe THFIL enhancement for every HF pulse while the electron density varies from high, $\sim 4.3 \times 10^{11}$ (lower altitude BHFIL), to low, $\sim 3.5 \times 10^{11}$, and back to higher density, possibly indicating a large-scale TID moving past the radar beam. During that period the ionospheric tilt angle would vary between opposites. Based on these considerations, we argue that it is unlikely that the propagation of the HF pump wave to the topside ionosphere occurs though the standard radio window but rather is a result of one of the proposed mechanisms for propagation outside the radio window.

Supporting our interpretation of the evolution of the THFIL observations (see section 5.2), and consistent with simulations done by Eliasson (2008), Figures 7 and 10 show that the altitude of both enhancements is at or close to the respective topside and bottomside plasma resonance altitude where $f_P = f_{HF}$. This is consistent with the shape of the enhanced ion line spectra of which we show examples for one instant in time, in the left panels of Figure 5. Two well-developed shoulders are observed in the ion line spectra at the altitudes of strongest enhancements of the topside and bottomside ionosphere, at 278 and 219 km, respectively. A prominent central feature characteristic for the oscillating two stream instability (e.g., Stubbe et al., 1992; Stubbe, 1996) is also visible for both enhancements. We observe the corresponding enhancement just below the pump wave frequency, in the plasma line spectrum at the bottomside ionosphere (not shown).

5.4. Propagation Outside the Radio Window

For both Z-mode scattering (Mishin et al., 2001) and L-mode propagation through artificial radio windows (Nordblad & Leyser, 2010), field-aligned electron density striations are essential for wave propagation outside the standard radio window. The resonant scatter process proposed by Mishin et al. (2001) should be effective when small-scale density irregularities are present at the reflection height of the pump wave. Small-scale density striations, on the order of several meters, are rapidly generated within a few seconds (Basu et al., 1997), by the pump wave itself and thus there is no "buildup" time or very little delay from heating on to the possible occurrence of THFIL. The characteristic timescales in the case of the L-mode propagation though artificially generated radio windows depends on the temporal evolution of kilometer-scale density striations. The L-mode wave is guided by large-scale density ducts that can be generated by the pump wave. Generation of large-scale density ducts is on the order of minutes (Basu et al., 1997).

Considering, as an example, the four pulses shown in Figure 7, we see that the two pulses from 10 March (top) are slightly different from the two bottom panel examples from 11 March. The temporal evolution of the two top panels is consistent with the generation of large-scale density striations facilitating L-mode propagation in artificial radio windows (Nordblad & Leyser, 2010), while the observations shown in the bottom panels are consistent with the Z-mode scattering process (Mishin et al., 2001). If large-scale density ducts exist before heating on, possibly from a previous heating on pulse, L-mode propagation is possible immediately. As exemplified in Figure 7, it is not unambiguously clear which of the two mechanisms is dominating from the observation made during our experiment. However, the topside enhancements were the strongest for pump frequencies near the double resonance (see Figure 8). It may be noted that for such conditions excitation of small-scale density striations is suppressed (Honary et al., 1999). This would thus also suppress the scattering of the pump wave into the Z-mode. As larger-scale ducts have a longer lifetime than small-scale striations

these may still facilitate guiding of the pump wave in the L-mode during the time near double resonance. Further, as the anomalous absorption of the pump wave is minimum at the double resonance (Stubbe et al., 1994), this may explain why the THFIL are the strongest for such frequencies. Further experiments are needed to study the physics involved.

6. Summary and Conclusions

We have shown systematically recurring ion line enhancements appearing at the topside ionospheric plasma resonance altitude, in the polar ionosphere on the three consecutive days, from 9 to 11 March 2016. These are the first observations of HF-enhanced ion line spectra at the topside ionosphere. The enhancements present evidence of radio wave propagation outside the standard radio window (∼ 6°) during O-mode, HF radio wave pumping along the local geomagnetic field (∼ 12°). Stepping the pump frequency across the double resonance of the fourth harmonic of the electron gyrofrequency and the local upper hybrid frequency, the enhancements seem to be asymmetrically conditioned by the relative proximity of the HF-pump frequency to the double resonance. THFILs predominantly appear while the HF-pump frequency is just below or at the double resonance frequency and the L-mode cutoff frequency is below the pump frequency. Approaching the double resonance frequency by the HF-pump frequency, the backscattered power of the THFIL and BHFIL increases until both enhancements abruptly disappear completely when the HF-pump frequency is larger than the double resonance frequency. Further, the THFIL only appear simultaneous to strong bottomside enhancements. We have considered the possible mechanisms proposed for radio wave propagation outside the standard radio window in detail. However, further experiments are needed to determine the dominating processes involved in HF pump wave propagation beyond the reflection height outside the radio window.

Acknowledgments
The data of EISCAT UHF radar during the experiment can be obtained from EISCAT http://www.eiscat.se/schedule/schedule.cgi. The EISCAT ISR analysis tool GUISDAP is available at https://www.eiscat.se/scientist/user-documentation/guisdap-9-0/. EISCAT is an international association supported by research organisations in China (CRIRP), Finland (SA), Japan (NIPR and STEL), Norway (NFR), Sweden (VR), and the United Kingdom (NERC). We thank K. M. Laundal for finding the best color maps. This paper includes color specifications and designs developed by Cynthia Brewer (http://colorbrewer.org/) and colormaps by Nathaniel J. Smith and Stefan van der Walt.

References

Ashrafi, M., Kosch, M. J., Kaila, K., & Isham, B. (2007). Spatiotemporal evolution of radio wave pump-induced ionospheric phenomena near the fourth electron gyroharmonic. *Journal of Geophysical Research*, *112*, A05314. https://doi.org/10.1029/2006JA011938

Basu, S., Costa, E., Livingston, R. C., Groves, K. M., & Carlson, H. C. (1997). Evolution of subkilometer scale ionospheric irregularities generated by high-power HF waves. *Journal of Geophysical Research*, *102*(A4), 7469–7475.

Borisova, T. D., Blagoveshchenskaya, N. F., Kalishin, A. S., Kosch, M. J., Senior, A., Rietveld, M., et al. (2014). Phenomena in the high-latitude ionospheric F region induced by a HF heater wave at frequencies near the fourth electron gyroharmonic. *Radiophysics and Quantum Electronics*, *57*(1), 1–19.

Budden, K. G. (1980). The theory of radio windows in the ionosphere and magnetosphere. *Journal of Atmospheric and Terrestrial Physics*, *42*(3), 287–298. https://doi.org/10.1016/0021-9169(80)90036-7

Chen, F. (1983). *Introduction to Plasma Physics and Controlled Fusion* (2nd ed.). Los Angeles, CA: Electrical Engineering Department School of Engineering and Applied Science University of California, Los Angeles.

Dhillon, R. S., & Robinson, T. R. (2005). Observations of time dependence and aspect sensitivity of regions of enhanced UHF backscatter associated with RF heating. *Annales Geophysicae*, *23*(1), 75–85. https://doi.org/10.5194/angeo-23-75-2005

Eliasson, B. (2008). Full-scale simulation study of the generation of topside ionospheric turbulence using a generalized Zakharov model. *Geophysical Research Letters*, *35*, L11104. https://doi.org/10.1029/2008GL033866

Eliasson, B., Shao, X., Milikh, G., Mishin, E. V., & Papadopoulos, K. (2012). Numerical modeling of artificial ionospheric layers driven by high-power HF heating. *Journal of Geophysical Research*, *117*, A10321. https://doi.org/10.1029/2012JA018105

Ellis, G. R. (1956). The Z propagation hole in the ionosphere. *Journal of Atmospheric and Terrestrial Physics*, *8*, 43–54.

Fejer, J. A. (1979). Ionospheric modification and parametric instabilities. *Reviews of Geophysics*, *17*(1), 135–153. https://doi.org/10.1029/RG017i001p00135

Fejer, B., & Kelley, C. (1980). Ionospheric Irregularities. *Reviews of Geophysics*, *18*(2), 401–454.

Ganguly, S., & Gordon, W. E. (1983). Heater enhanced topside plasma line. *Geophysical Research Letters*, *10*(10), 977–978.

Grach, S., Sergeev, E., Mishin, E., & Shindin, A. V. (2016). Dynamic properties of ionospheric plasma turbulence driven by high-power high-frequency radiowaves. *Uspekhi Fizicheskih Nauk*, *186*(11), 1189–1228. https://doi.org/10.3367/UFNr.2016.07.037868

Gurevich, A., Hagfors, T., Carlson, H., Karashtin, A., & Zybin, K. (1998). Self-oscillations and bunching of striations in ionospheric modifications. *Physics Letters, Section A: General, Atomic and Solid State Physics*, *239*(6), 385–392. https://doi.org/10.1016/S0375-9601(98)00006-1

Gurevich, A. V., Zybin, K. P., & Lukyanov, A. V. (1995). Stationary striations developed in the ionospheric modification. *Physical Review Letters*, *75*(13), 2622–2625.

Gustavsson, B., Leyser, T. B., Kosch, M., Rietveld, M. T., Steen, Å., Brändström, B. U. E., & Aso, T. (2006). Electron gyroharmonic effects in ionization and electron acceleration during high-frequency pumping in the ionosphere. *Physical Review Letters*, *97*(19), 1–4. https://doi.org/10.1103/PhysRevLett.97.195002

Hagfors, T., & Lehtinen, M. (1981). Electron temperature derived from incoherent scatter radar observations of the plasma line frequency. *Journal of Geophysical Research*, *86*(A1), 119–124. https://doi.org/10.1029/JA086iA01p00119

Honary, F., Robinson, T., Wright, D., Stocker, A., Rietveld, M., & McCrea, I. (1999). First direct observations of the reduced striations at pump frequencies close to the electron gyroharmonics. *Annales Geophysicae*, *17*, 1235–1238. https://doi.org/10.1007/s00585-999-1235-6

Honary, F., Stocker, A. J., Robinson, T. R., Jones, T. B., & Stubbe, P. (1995). Ionospheric plasma response to HF radio waves operating at frequencies close to the third harmonic of the electron gyrofrequency. *Journal of Geophysical Research*, *100*(A11), 21,489–21,501.

Huang, J., & Kuo, S. P. (1994). A theoretical model for the broad upshifted maximum in the stimulated electromagnetic emission spectrum. *Journal of Geophysical Research*, *99*(A10), 19,569–19,576.

Hunsucker, R. D. (1982). Atmospheric gravity waves generated in the high-latitude ionosphere: A review. *Reviews of Geophysics*, *20*(2), 293–315. https://doi.org/10.1029/RG020i002p00293

Isham, B., Hagfors, T., Mishin, E., Rietveld, M. T., La Hoz, C., Kofman, W., & Leyser, T. B. (1999). A search for the location of the HF excitation of enhanced ion acoustic and langmuir waves with EISCAT and the Tromso Heater. *Radiophysics and Quantum Electronics*, *42*(7), 533–534.

Isham, B., Kofman, W., Hagfors, T., Nordling, J., Thidė, B., LaHoz, C., & Stubbe, P. (1990). New phenomena observed by EISCAT during an RF ionospheric modification experiment. *Radio Science*, *25*(3), 251–262. https://doi.org/10.1029/RS025i003p00251

Isham, B., La Hoz, C., Kohl, H., Hagfors, T., Leyser, T. B., & Rietveld, M. T. (1996). Recent EISCAT heating results using chirped ISR. *Journal of Atmospheric and Terrestrial Physics*, *58*(1-4), 369–383. https://doi.org/10.1016/0021-9169(95)00042-9

Isham, B., Rietveld, M., Hagfors, T., La Hoz, C., Mishin, E., Kofman, W., et al. (1999). Aspect angle dependence of HF enhanced incoherent backscatter. *Advances in Space Research*, *24*(8), 1003–1006. https://doi.org/10.1016/S0273-1177(99)00555-4

Istomin, Y. N., & Leyser, T. B. (1997). Small-scale magnetic field-aligned density irregularities excited by a powerful electromagnetic wave. *Physics of Plasmas*, *4*(3), 817. https://doi.org/10.1063/1.872175

Kelley, M. C., Arce, T. L., Salowey, J., Sulzer, M., Armstrong, W. T., Carter, M., & Duncan, L. (1995). Density depletions at the 10-m scale induced by the Arecibo heater. *Journal of Geophysical Research*, *100*(A9), 17,367–17,376.

Kosch, M. J., Mjlhus, E., Ashrafi, M., Rietveld, M. T., Yeoman, T., & Nozawa, S. (2011). Angular dependence of pump-induced bottomside and topside ionospheric plasma turbulence at EISCAT. *Journal of Geophysical Research*, *116*, A03322. https://doi.org/10.1029/2010JA016014

Kosch, M., Rietveld, M., Kavanagh, A., Davis, C., Yeoman, T., Honary, F., & Hagfors, T. (2002). High-latitude pump-induced optical emissions for frequencies close to the third electron gyro-harmonic. *Geophysical Research Letters*, *29*(23), 2112. https://doi.org/10.1029/2002GL015744

Lehtinen, M. S., & Huuskonen, A. (1996). General incoherent scatter analysis and GUISDAP. *Journal of Atmospheric and Terrestrial Physics*, *58*(1-4), 435–452. https://doi.org/10.1016/0021-9169(95)00047-X

Leyser, T. B. (2001). Stimulated electromagnetic emissions by high-frequency electromagnetic pumping of the ionospheric plasma. *Space Science Reviews*, *98*(3-4), 223–328. https://doi.org/10.1023/A:1013875603938

Leyser, T. B., James, H. G., Gustavsson, B., & Rietveld, M. T. (2018). Possible evidence of L-mode electromagnetic wave pumping of ionospheric plasma in geomagnetic zenith. *Annales Geophysicae*, *36*(900), 167. https://doi.org/10.1029/2009GL041438

Leyser, T. B., & Nordblad, E. (2009). Self-focused radio frequency L wave pumping of localized upper hybrid oscillations in high-latitude ionospheric plasma. *Geophysical Research Letters*, *36*, L24105. https://doi.org/10.1029/2009GL041438

Leyser, T. B., Thidė, B., Derblom, H., Hedberg, Å., Lundborg, B., Stubbe, P., & Kopka, H. (1989). Stimulated Electromagnetic Emission near Electron Cyclotron Harmonics in the Ionosphere. *Physical Review Letters*, *66*(11), 1441–1443. https://doi.org/10.1103/PhysRevLett.21.1441

Leyser, T. B., & Wong, A. Y. (2009). Powerful electromagnetic waves for active environmental research in geospace. *Reviews of Geophysics*, *47*, RG1001. https://doi.org/10.1029/2007RG000235

Mishin, E., Hagfors, T., & Isham, B. (2001). A generation mechanism for topside enhanced incoherent backscatter during high frequency modification experiments in Tromsø. *Geophysical Research Letters*, *28*(3), 479–482. https://doi.org/10.1029/2000GL000122

Mjølhus, E. (1990). On linear conversion in a magnetized plasma. *Radio Science*, *25*(6), 1321–1339.

Mjølhus, E. (1993). On the small scale striation effect in ionospheric radio modification experiments near harmonics of the electron gyro frequency. *Journal of Atmospheric and Terrestrial Physics*, *55*(6), 907–918. https://doi.org/10.1016/0021-9169(93)90030-3

Mjølhus, E., & Flå, T. (1984). Direct access to plasma resonance in ionospheric radio experiments. *Journal of Geophysical Research*, *89*(A6), 3921–3928.

Nordblad, E., & Leyser, T. B. (2010). Ray tracing analysis of L mode pumping of the ionosphere, with implications for the magnetic zenith effect. *Annales Geophysicae*, *28*(9), 1749–1759. https://doi.org/10.5194/angeo-28-1749-2010

Rietveld, M. T., Isham, B., Grydeland, T., La Hoz, C., Leyser, T. B., Honary, F., et al. (2002). HF-pump-induced parametric instabilities in the auroral E-region. *Advances in Space Research*, *29*(9), 1363–1368. https://doi.org/10.1016/S0273-1177(02)00186-2

Rietveld, M. T., Kohl, H., Kopka, H., & Stubbe, P. (1993). Introduction to ionospheric heating at Tromsø-I. Experimental overview. *Journal of Atmospheric and Terrestrial Physics*, *55*(4-5), 577–599. https://doi.org/10.1016/0021-9169(93)90007-L

Rietveld, M. T., Kosch, M. J., Blagoveshchenskaya, N. F., Kornienko, V. A., Leyser, T. B., & Yeoman, T. K. (2003). Ionospheric electron heating, optical emissions, and striations induced by powerful HF radio waves at high latitudes: Aspect angle dependence. *Journal of Geophysical Research*, *108*(A4), 1–16. https://doi.org/10.1029/2002JA009543

Rietveld, M. T., Senior, A., Markkanen, J., & Westman, A. (2016). New capabilities of the upgraded EISCAT high-power HF facility. *Radio Science*, *51*, 1533–1546. https://doi.org/10.1002/2016RS006093

Robinson, T. R. (1989). The heating of the high latitude ionosphere by high power radio waves. *Physics Reports*, *179*(2 - 3), 79–209.

Robinson, T. R., Honary, F., Stocker, A. J., Jones, T. B., & Stubbe, P. (1996). First EISCAT observations of the modification of F-region electron temperatures during RF heating at harmonics of the electron gyro frequency. *Journal of Atmospheric and Terrestrial Physics*, *58*(1-4), 385–395. https://doi.org/10.1016/0021-9169(95)00043-7

Showen, R. L., & Behnke, R. A. (1978). The effect of HF-induced plasma instabilities on ionospheric electron temperatures. *Journal of Geophysical Research*, *83*(A1), 207–209.

Stubbe, P. (1996). Review of ionospheric modification experiments at Tromsø. *Journal of Atmospheric and Terrestrial Physics*, *58*(1-4), 349–368. https://doi.org/10.1016/0021-9169(95)00041-0

Stubbe, P., Kohl, H., & Rietveld, M. T. (1992). Langmuir turbulence and ionospheric modification. *Journal of Geophysical Research*, *97*(A5), 6285–6297.

Stubbe, P., Stocker, A. J., Honary, F., Robinson, T. R., & Jones, T. B. (1994). Stimulated electromagnetic emissions an anomalous HF wave absorption near electron gyroharmonics. *Journal of Geophysical Research*, *99*(A4), 6233–6246.

Thidė, B., Sergeev, E. N., Grach, S. M., Leyser, T. B., & Carozzi, T. D. (2005). Competition between Langmuir and upper-hybrid turbulence in a high-frequency-pumped ionosphere. *Physical Review Letters*, *95*(25), 1–4. https://doi.org/10.1103/PhysRevLett.95.255002

Tjulin, A. (2017). EISCAT Experiments, EISCAT Scientific Association, (March).

Utlaut, W. F., & Violette, E. J. (1974). A summary of vertical incidence radio observations of ionospheric modification. *Radio Science*, *9*(11), 895–903. https://doi.org/10.1029/RS009i011p00895

Vas'kov, V. V., Bud'ko, N. I., Kapustina, O. V., Mikhailov, Y. M., Ryabova, N. A., Komrakov, G. P., et al. (1995). Appearance of VLF and ELF-noises in topside ionosphere under the action of high power radio wave from data of satellite intercosmos-24. *Advances in Space Research*, *15*(12), 49–56. https://doi.org/10.1016/0273-1177(95)00011-3

Vas'kov, V. V., & Gurevich, A. V. (1977). Resonance instability of small-scale plasma perturbations. *Journal of Experimental and Theoretical Physics*, *46*(3), 487–494.

Vodyanitskij, A., Erokhin, N. S., Lisitchenko, V., Moiseev, S. S., & Oraevskij, V. (1974). "Transillumination" of the wave barriers in a plasma as a result of kinetic effects. *Nuclear Fusion*, *14*, 267–275.

PAPER II

Conditions for topside ion line enhancements

Rexer, T., Leyser, T., Gustavsson, B., and Rietveld, M., Journal of Geophysical Research: Space Physics, doi: 10.1029/2021ja029379, 2021

JGR Space Physics

RESEARCH ARTICLE
10.1029/2021JA029379

Conditions for Topside Ion Line Enhancements

Theresa Rexer[1], Thomas Leyser[2], Björn Gustavsson[1], and Michael Rietveld[3]

[1]Institute for Physics and Technology, Arctic University of Norway UiT, Tromsø, Norway, [2]Swedish Institute of Space Physics, Uppsala, Sweden, [3]EISCAT Scientific Association, Ramfjordmoen, Norway

Key Points:

- Observations of high frequency enhanced ion line spectra at the topside ionosphere
- The appearance of the topside enhancements are affected by the proximity to the topside double resonance frequency
- We interpret the observations as a result of *L* mode wave propagation through artificial radio windows

Correspondence to:

T. Rexer,
theresa.rexer@uit.no

Citation:

Rexer, T., Leyser, T., Gustavsson, B., & Rietveld, M. (2021). Conditions for topside ion line enhancements. *Journal of Geophysical Research: Space Physics*, *126*, e2021JA029379. https://doi.org/10.1029/2021JA029379

Received 25 MAR 2021
Accepted 10 JUN 2021

Abstract Enhanced ion line spectra as a response to magnetic field-aligned high frequency (HF) pumping of the overdense polar ionosphere with left-handed circular polarization, can be observed at the top and bottomside F-region ionosphere under certain conditions. The European Incoherent Scatter (EISCAT) UHF radar was directed in magnetic zenith on October 18th and 19th, 2017 while stepping the pump frequency of the EISCAT Heating facility both upward and downward across the double resonance frequency of the fourth harmonic of the electron gyrofrequency and the local upper hybrid frequency, in a 2-min-on, 5-min-30-s-off pump cycle. We present observations of two separate cases of topside HF-enhanced ion lines (THFIL). THFIL simultaneous to bottomside HFIL (BHFIL), and conditioned by the relative proximity of the HF pump frequency to the bottomside double resonance frequency, consistent with previous observations (Rexer et al., 2018, https://doi.org/10.1029/2018JA025822) were observed for HF pulses on 19th October. Recurring THFIL appearing after BHFIL have faded and conditioned by the relative proximity to the double resonance frequency on the topside ionosphere, were observed on 18th October. The THFIL are consistent with transionospheric propagation through artificial radio windows by *L* mode guiding of the pump wave, facilitated by large scale density ducts present in the plasma.

1. Introduction

High power radio waves transmitted from the ground into the high-latitude ionosphere at frequencies below the critical frequency, are reflected, at altitudes depending on the plasma density and the polarization of the incident wave. Vertically propagating waves with an *O* mode polarization will reflect at the altitude where the pump frequency, f_{HF} is equal to the local plasma frequency, f_P. Pump waves in a horizontally stratified ionosphere transmitted at the Spitze angle, defined by $\sin(\theta_c) = \sin(\alpha)\sqrt{\frac{Y}{1+Y}}$, where $Y = \frac{f_{HF}}{f_G}$ and α is the angle of the magnetic field, in the magnetic meridian plane, from vertical (Budden, 1980), can pass through the radio window and continue to propagate to regions of higher plasma density and frequency (Mjølhus, 1990). Here f_G is the electron gyro frequency. Pump waves transmitted at larger angles to the vertical than the Spitze angle are reflected at progressively lower altitudes.

In this paper, we present observations of high frequency (HF) enhanced ion line spectra from the top and bottomside ionosphere during magnetic field-aligned, high-power pumping of the polar ionosphere. Ellis (1956) first observed ionogram signatures of pump wave propagation to altitudes beyond the *O* mode reflection height. Subsequently Ganguly and Gordon (1983) and Isham et al. (1990) presented incoherent scatter radar (ISR) measurements of HF modification experiments, showing effects of an HF pump wave above the *O* mode reflection altitude, at mid- and high-latitudes, respectively. Several studies have since reported ISR measurements showing effects of HF pumping above the reflection altitude of the ionospheric *F*-region (Isham, Hagfors, et al., 1999; Isham, Rietveld, et al., 1999; Kosch et al., 2011; Rietveld et al., 2002). Leyser et al. (2018) present signatures of transionospheric HF pump wave propagation into space in CASSIOPE spacecraft data. The first consistently recurring topside HF enhanced ion line (THFIL) spectra and their relation to pump frequencies close to the fourth gyroharmonic frequency were shown by Rexer et al. (2018). Observations of THFIL from an experiment in 2013 were also reported by Borisova et al. (2020).

An *O* mode wave, that is propagating strictly in a field-aligned direction is a left-hand circular polarized (LHCP) wave for which the electric field rotates opposite to the electron gyro motion, known as an *L* mode wave (i.e., Chen, 1983). The *L* mode dispersion curve follows the edge of the O mode dispersion surface where k is parallel to B for $f_{\mathrm{HF}} > f_P$ and the slow *X* mode band dispersion surface for $f_P > f_{\mathrm{HF}}$ (see for example

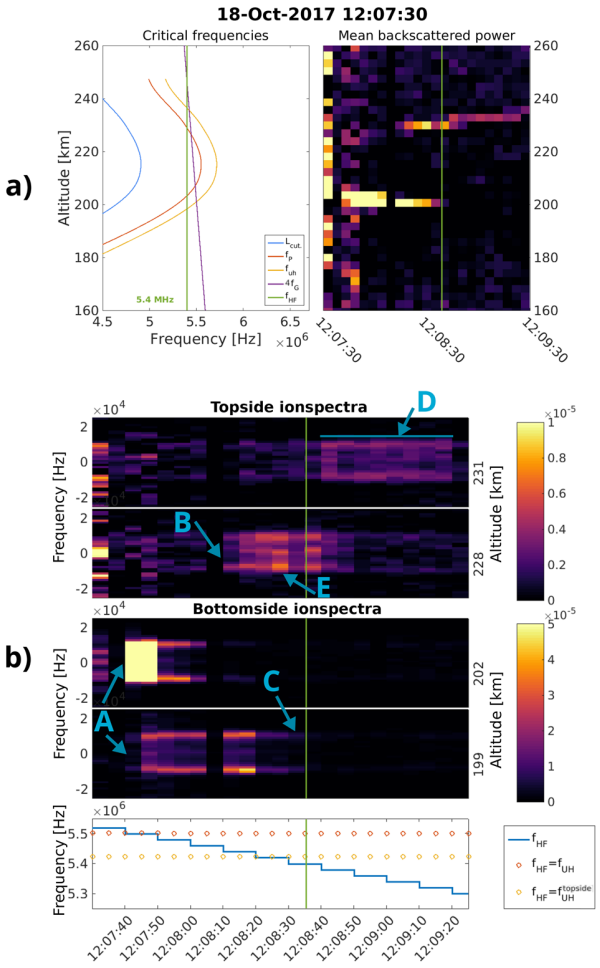

Figure 1. Example of a typical observation of case A topside high frequency enhanced ion lines (THFIL). (a) The top left panel shows the critical frequencies calculated from the observed natural Langmuir waves. The blue, red and yellow lines indicate the *L* mode cutoff, the local plasma frequency, and the local upper hybrid frequency, respectively. The purple line shows the fourth harmonic of the electron gyrofrequency, while the green vertical line indicates the frequency of the transmitted *O* mode pump wave. On the right the 5-s mean backscattered ion line power, with a 3 km altitude resolution, during a 2-min-on pulse is shown. The vertical green line in the top right panel plot indicates the time to which the left panel plot corresponds. (b) The four upper panels show the topside ion line spectra and the bottomside ion line spectra with the frequency on the vertical axis, for the two altitudes of the strongest THFIL (228 and 231 km) and bottomside high frequency enhanced ion lines (199 and 202 km). The bottom panel shows f_{HF} and the top- and bottom-side fourth harmonic of the double resonance frequency, corresponding to the panels above. Green vertical lines indicate the time corresponding to the top left panel in (a) of the critical frequencies.

Figure 1 in Nordblad & Leyser, 2010). The *X* mode branch of the *L* mode is sometimes called the *Z* mode (Mjølhus, 1990). However, this usually refers to all wave vectors at angles between the parallel and perpendicular to the ambient magnetic field, whereas the *L* mode only refers to wave vectors parallel and anti-parallel to the magnetic field. When mapped out for all angles of k to B, the two wave modes form two dispersion surfaces that connect at the Spitze angle when $f_P = f_{\mathrm{HF}}$ forming a radio window (Mjølhus, 1990). A strictly field-aligned incident wave in the *L* mode moves from one to the other dispersion surface at this point without a change in polarization. At the EISCAT facility in Tromsø, Norway, the Spitze angle, is around $\theta_c = 5°–6°$ south of zenith. An incident wave that passes through a radio window in the *L* mode will continue to propagate to higher altitudes and regions of higher plasma density and frequency until it encounters its cutoff at $f_{L-cut} = -\frac{f_G}{2} + \frac{1}{2}\sqrt{f_G^2 + 4f_P^2}$ (Leyser et al., 2018; Mjølhus & Flå, 1984).

For an *O* mode wave transmitted in magnetic zenith in the high-latitude ionosphere, propagating beyond the plasma resonance height, outside the natural radio window is possible by two mechanisms. New radio windows in the form of large scale density ducts, generated by small scale density striations existing naturally (A. V. Gurevich et al., 1995) or created by the pump wave (i.e., Eliasson & Leyser, 2015; A. Gurevich et al., 1998; Istomin & Leyser, 2001), can guide the incident *O* mode wave into the *L* mode at locations outside the standard radio window (Leyser & Nordblad, 2009; Nordblad & Leyser, 2010). Alternatively, resonant scatter on small-scale field-aligned density irregularities can transform an incident *O* mode pump wave to a *Z* mode wave in the region above the upper hybrid resonance layer, where $f_{UH}^2 = f_G^2 + f_P^2$, close to the bottomside reflection altitude (Mishin et al., 2001). While *L* mode propagation through artificial radio windows (Nordblad & Leyser, 2010) is possible through large scale density ducts, the *Z* mode scattering process (Mishin et al., 2001) is facilitated by small scale density striations. Meter-scale density striations are generated within seconds, while kilometer-scale density ducts form in timescales on the order of minutes (Basu et al., 1997). The formation of small-scale density striations also depends on f_{HF}, and for f_{HF} close to multiples of the electron gyro harmonic frequency the generation of striations is greatly reduced (Honary et al., 1999). A mechanism for generating THFIL for a vertically propagating O mode wave has been proposed by Eliasson (2008). They simulated a propagation process where an incident wave reaches the resonance altitude and efficiently converts to the *Z* mode, for low duty-cycle experiments (2%), minimizing the effect of density irregularities in an attempt to explain the observations by (Isham, Rietveld, et al., 1999). In the present experiments the duty-cycle was significantly higher (~26%) and the direction of propagation along the magnetic field. Hence it is unlikely to explain our current observations.

In the following paper we present ISR observations forming two separate cases of recurring THFIL during comparable ionospheric conditions and HF pump schemes, from experiments on October 18th and 19th, 2017 at the EISCAT facilities in Tromsø, Norway. Strong THFIL occurred repeatedly while stepping f_{HF} through the fourth harmonic of f_G and a possible, previously undetected, relation to the topside double resonance frequency of the local f_{UH} and $4f_G$ has been observed. Observations of the naturally existing Langmuir waves, made in the plasma line spectra of the EISCAT UHF radar, are used to calculate the electron density and critical frequencies during the experiments.

2. Experiment

On October 18th and 19th, 2017, during quiet geomagnetic daytime conditions, the EISCAT Heating facility (Rietveld et al., 2016) in Tromsø was transmitting a LHCP HF radio wave in the magnetic zenith direction (78° elevation south), in a 2 min on - 5 min 30 s off cycle. Upon reaching the ionosphere most of the wave energy is in the *O* mode.

Different frequency stepping schemes were used on the two days, aiming to meet the double resonance frequency f_{dbl} on the bottomside ionosphere at some point during each heating cycle. The double resonance frequency is defined as

$$f_{dbl} = f_{UH} = 4f_G$$

and can be met by f_{HF} twice, once at the topside and once at the bottomside ionosphere. In this experiment, f_{HF} was changed in steps of 10 kHz every 10 s within the 2 min HF pulse, such that it crossed f_{dbl} on the bottomside. Because f_{HF} is stepped throughout each HF pulse and f_G decreases with increasing altitude, the numeric value for f_{dbl} on the topside will be different from the numeric value of f_{dbl} on the bottomside. On October 18th, 2017 the effective radiated power (ERP) in the *O* mode was estimated to be 378 MW and the frequency stepping was done from a few tens of kilohertz above f_{dbl} to a few tens of kilohertz below f_{dbl} on the bottomside ionosphere. The mean difference between the maximum ionospheric plasma frequency and the pump frequency, $\overline{m} = f_{OF2} - f_{HF}$, had a minimum value of $\overline{m}_{min} = 152$ kHz during HF pulses, while the maximum was $\overline{m}_{max} = 396$ kHz. On October 19th, 2017 the ERP in the O mode was estimated to be 460 MW with one extra transmitter running. The frequency stepping, alternated between stepping up from below to above f_{dbl} and stepping down from above to below f_{dbl}. For pulses on the 19th October, $\overline{m}_{min} = 603$ kHz, while $\overline{m}_{max} = 810$ kHz.

The EISCAT UHF radar, pointing in the magnetic field aligned direction, was used to obtain the ionospheric plasma parameters for the background and HF-modulated conditions. Measurements were done with the beata modulation scheme (i.e., Tjulin, 2017), giving a frequency resolution of 2.4 kHz, range resolution of 3 km and a temporal resolution of 5 s for ion line measurements. In addition, the plasma line is sampled at 0.4 μs lag profiles, averaged over 5 s, covering a 3.125 MHz wide band offset from the transmit frequency by 8.4, 6.0, and 3.4 MHz, and covering ranges from 107 to 374 km. Backscatter from natural existing Langmuir waves is observed during the experiment in the downshifted plasma line spectra that is −6.0 MHz offset from the radar transmit frequency. The electron density used for the calculation of relevant resonance and cut-off frequencies (f_P, f_{UH}, $f_{L-\mathrm{cut}}$) is obtained from these observed natural Langmuir waves in the plasma line spectra and adapting the method described by Hagfors and Lehtinen (1981) (see Section 3 of Rexer et al., 2018, for a detailed description).

3. Experimental Results

Observations made during the experiments show characteristic differences with respect to the appearance of bottomside HF enhanced ion lines (BHFIL) and the proximity of f_{HF} to the top- and bottomside f_{dbl} on October 18th and 19th. We have identified two cases for excitation of THFIL. In the following two sections, these observations are presented separately

3.1. Case A: October 18th Observations

On October 18th 2017, 16 HF pulses with clear THFIL were observed. Figure 1 shows an example of one of these. In the left panel of Figure 1a, the altitude profiles of, f_P, f_{UH}, $4f_G$, and $f_{L-\mathrm{cut}}$ are shown, for an altitude range from 180 to 280 km, at the time of strong THFIL (indicated by the vertical green line in the right panel). The right panel shows the altitude profile from 180 to 280 km of the mean ion line spectra power for the 2 min HF pulse with a 5 s temporal resolution. The development of the BHFIL and THFIL for the duration of the HF pulse as f_{HF} is stepped downward, is seen at altitudes around 202 and 228 km respectively.

The development of the ion line spectra of the BHFIL and THFIL for the duration of the HF pulse are shown in more detail in Figure 1b. Ion line spectra at the two altitude ranges of the strongest THFIL (228 and 231 km) and BHFIL (199 and 202 km) are shown in the four upper panels, while the f_{HF} stepping

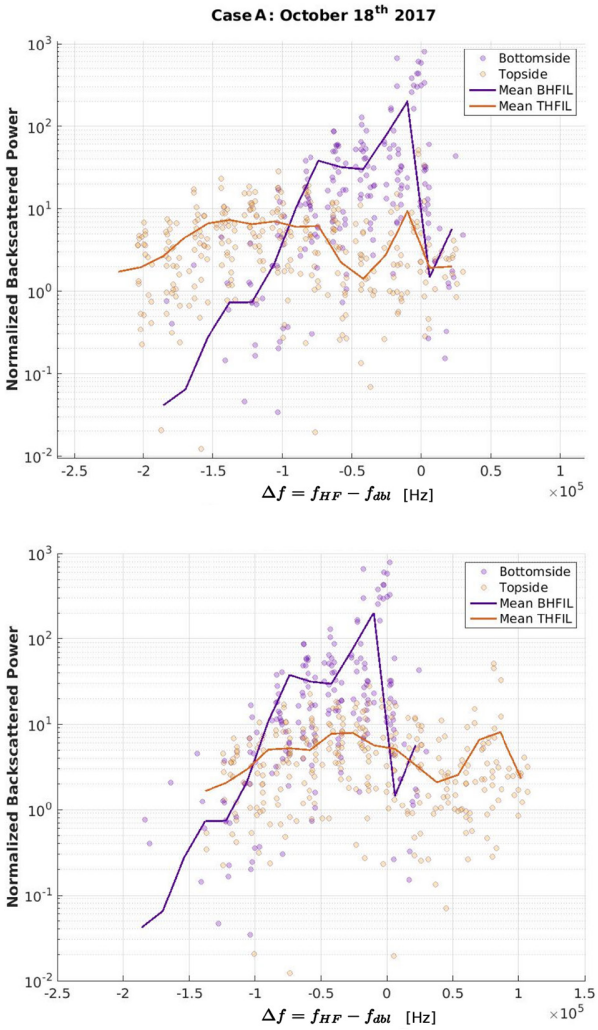

Figure 2. Comparison of all 16 high frequency pulses of case A. Normalized backscattered ion line power relative to the difference of the pump and bottomside double resonance frequency are shown upper panel. The lower panel shows the backscattered ion line power for the topside high frequency enhanced ion lines related to the topside double resonance frequency and the bottomside high enhanced ion lines related to the bottomside double resonance frequency. Topside enhancements are shown in orange while bottomside enhancements are shown in purple. The superposed solid lines show the mean of the observations.

scheme of 20 kHz decrements every 10 s is indicated in the bottom panel. The f_{dbl} at the bottomside (red) and topside (yellow) are also indicated. Green vertical lines indicate the time corresponding to the left panel in (a). In the first 5 s after Heating on, of the four upper panels in (b) (and the right panel in [a]), the commonly observed overshoot (Stubbe, 1996) is clearly visible. Five features are indicated in (b). (A) At 12:07:40 UT, as $f_{\mathrm{HF}} = 5.50$ MHz, after a first 20 kHz downward frequency step toward the bottomside f_{dbl}, the BHFIL appear strongly at 202 km and somewhat weaker at 199 km. (B) THFIL appear, faintly at first, around 228 km as $f_{\mathrm{HF}} = 5.44$ MHz, 50–60 kHz below $f_{dbl} \approx 5.5$ MHz at the bottomside. (C) BHFIL decrease in intensity and fade completely as $f_{HF} = 5.40$ MHz and lower. (D) The THFIL are visible for the remaining steps of f_{HF} of the HF pulse, increasing in altitude to 231 km (and 234 km as seen in the right panel of (a)) as f_{HF} is stepped further downward to 5.3 MHz. (E) The strongest THFIL were observed when $f_{\mathrm{HF}} = 5.42$ MHz at which only weak BHFIL were observed, during 3 steps ($f_{\mathrm{HF}} = 5.44$, 5.42 and 5.40 MHz) of simultaneous enhancements at both altitudes. BHFIL were observed at an altitude between the matching height (Rietveld et al., 2000) and the altitude where $f_P = f_{\mathrm{HF}}$. THFIL were observed at the reflection altitude.

We plot the backscattered power for all 16 HF pulses, with identified THFIL, observed on the October 18th, 2017, at the altitude of the strongest BHFIL and THFIL and relate this to the difference between f_{HF} and f_{dbl} on the bottomside and topside ionosphere, $\Delta f = f_{\mathrm{HF}} - f_{\mathrm{dbl}}$, in Figure 2. Solid lines indicate the mean of the observations of the backscattered ion line spectra power. In the upper panel we relate all observations of HFIL to f_{dbl} on the bottomside ionoshpere. The lower panel shows the same data where the BHFIL are related to the bottomside f_{dbl}, while the THFIL are shown relative to f_{dbl} on the topside ionosphere. The slight difference in the mean calculations (solid lines) of the two panels is due to the bining algorithm. THFIL occur primarily when f_{HF} is between 75 and 160 kHz below f_{dbl} on the bottomside, and the strongest THFIL occurred when no BHFIL were observed. In the lower panel we observe that the THFIL were strongest when f_{HF} was between 100 kHz below and 10 kHz above the f_{dbl} on the topside ionosphere. A narrow local maximum of the THFIL is also seen when f_{HF} is ≈ 70–90 kHz above f_{dbl} on the topside. From the upper panel it is apparent that these THFIL occurred when f_{HF} was at or just below the f_{dbl} on the bottomside. BHFIL also have a maximum here. Looking at the development of each HF pulse separately as illustrated for one pulse, in Figure 1, we see that the THFIL coincidental with the strongest BHFIL, are not part of the prolonged main THFIL visible from $\Delta f \approx -0.6$ to $\Delta f \approx -2.0$. These THFIL were visible as a "flare" of enhancement for ∼5–10 s and faded thereafter, for some pulses (HF pulses starting at 10:07:30, 10:15:00, 11:00:00, 11:52:30, 12:00:00 and 12:07:30 UT), before disappearing and growing later during the HF pulse as f_{HF} was stepped downward.

In the example shown in Figure 1 the strongest THFIL is observed when f_{HF} is well below f_{dbl} on the bottomside. This is seen for all THFIL observed on October 18th and is also noticeable from the comparison of all pulses, in the top panel of Figure 2. Here we see that the solid orange line, indicating the mean backscattered power of all THFIL, has a wide local maximum well below f_{dbl} on the bottomside (zero on abscissa). Comparing the mean of the THFIL and BHFIL (orange and purple dots and lines) it is also clear that THFIL predominantly appeared when no BHFIL were observed and that, although the BHFIL were generally stronger than the THFIL, the strongest THFIL did not occur simultaneous to the strongest BHFIL. The narrow peak of the orange and purple solid lines in the top panel show that both BHFIL and THFIL

have a local maximum when f_{HF} is just below f_{dbl} on the bottomside. Figure 2 also shows that all THFIL have a comparable enhancement for comparable Δf, and that the enhancements develop and increase as Δf increases and the BHFIL begin to fade. The same data is shown in the lower panel of Figure 2 now arranged such that the THFIL (orange) are shown in relation to f_{dbl} on the topside, while the BHFIL (purple) are unchanged and shown in relation to f_{dbl} on the bottomside. The THFIL have a maximum when f_{HF} is just below f_{dbl} at the topside ionosphere.

The BHFIL in case A appear when f_{HF} is just below or at f_{dbl} in the bottomside ionosphere, in approximately the same range of Δf for f_{dbl} on the bottomside (Δf between ∼−100 and ∼6 kHz), as THFIL for Δf to f_{dbl} on the topside. Hence, as seen in the example in Figure 1, the strongest THFIL do not appear simultaneous to the strongest BHFIL (as in case B), but at f_{HF} where BHFIL have faded or disappeared completely. Consistent with the ion line spectra, the strongest enhancements, shown at two topside- and two bottomside altitudes in the middle panels of Figure 1, are observed at the resonance altitude, where $f_{HF} = f_P$, for the THFIL and between the matching height and the resonance altitude for BHFIL at the bottomside. At both the altitudes of THFIL and BHFIL, two well developed shoulders are seen, and we interpret these as decay lines of the parametric decay instability (PDI). These are more pronounced at the bottomside enhancements. A visible, but weak, central feature typical for the oscillating two stream instability (OTSI) (i.e., Kuo et al., 1997; Stubbe et al., 1992) is observed at the bottomside, while for the strongest THFIL the spectrum is filled in between the ion acoustic shoulders.

Downstepping HF pulses made on the October 19th, 2017, shown in the right column of Figure 3, are comparable to HF pulses where case A THFIL were observed. Although ion line spectra of the BHFIL (not shown) of these pulses are comparable to those of the case A observations as well as the range of the frequency steps in relation to f_{dbl} on the bottomside ionosphere, no THFIL were observed. The lower panels of Figure 3 indicate f_{dbl} on the top and bottomside ionosphere in relation to f_{HF}. Here we see that the range of frequency steps used in the downstepping experiment did not extend to or well below the topside f_{dbl}, the frequency range where we expect case A THFIL.

3.2. Case B: October 19th Observations

Figure 3 shows all HF pulses from 10.00.00 UT to 10.50.00 UT on 19th October in chronological order. Upper panels are the same as the upper right panel in Figure 1, showing the evolution of the mean ion line power at all altitudes, during a 2 min Heating on period with 5 s resolution. f_{HF} and the double resonance frequencies are indicated in the lower panels. As the direction of the frequency stepping in the experiment alternated between increasing and decreasing frequency for every Heating on pulse, the left column in the Figure shows all pulses where f_{HF} was stepped upward. It is only in these four pulses that we observe THFIL. During the HF pulses where f_{HF} was stepped downward, shown in the right column, only BHFIL are observed and no THFIL. In the top panel of the left column, showing the HF pulse starting at 10:06:00 UT, the THFIL appear weakly around 269 km for the initial 10 s frequency step. No THFIL are observed for the next 6 steps, until $f_{HF} = 5.44$ MHz and faint THFIL are observed for the two frequency steps just below and at the double resonance frequency. The second panel on the left shows slightly stronger THFIL around the same altitude for the fist frequency step. Weak THFIL are visible for three frequency steps of f_{HF} around the double resonance frequency, for $f_{HF} = 5.44$, 5.46 and 5.48 MHz. In the next two rows on the left column, showing HF pulses starting at 10:30.00 UT and 10:42:00 UT, THFIL are visible from Heating on and through all frequency steps until f_{HF} reaches the double resonance frequency around $f_{dbl} = 5.48$ MHz, where the THFIL fade.

Figure 4 is in the same format as Figure 1, but showing one of the four HF pulses of case B, in more detail. The backscattered power of BHFIL and THFIL increases as f_{HF} is increased stepwise and approaches the f_{dbl} on the bottomside ionosphere. The strongest THFIL are observed simultaneous to the strongest BHFIL at the altitude of the respective plasma resonance frequency, $f_P = f_{HF}$, rather than the matching height (Rietveld et al., 2000), which is ∼7 km lower in altitude on the bottomside for the duration of the experiment on this day. While weaker than the BHFIL, the THFIL show a comparable development as the BHFIL, increasing in intensity while f_{HF} is stepped upward to the bottomside f_{dbl} and fading when $f_{HF} > f_{dbl}$. These case B observations are consistent with observations made in 2016 (Rexer et al., 2018).

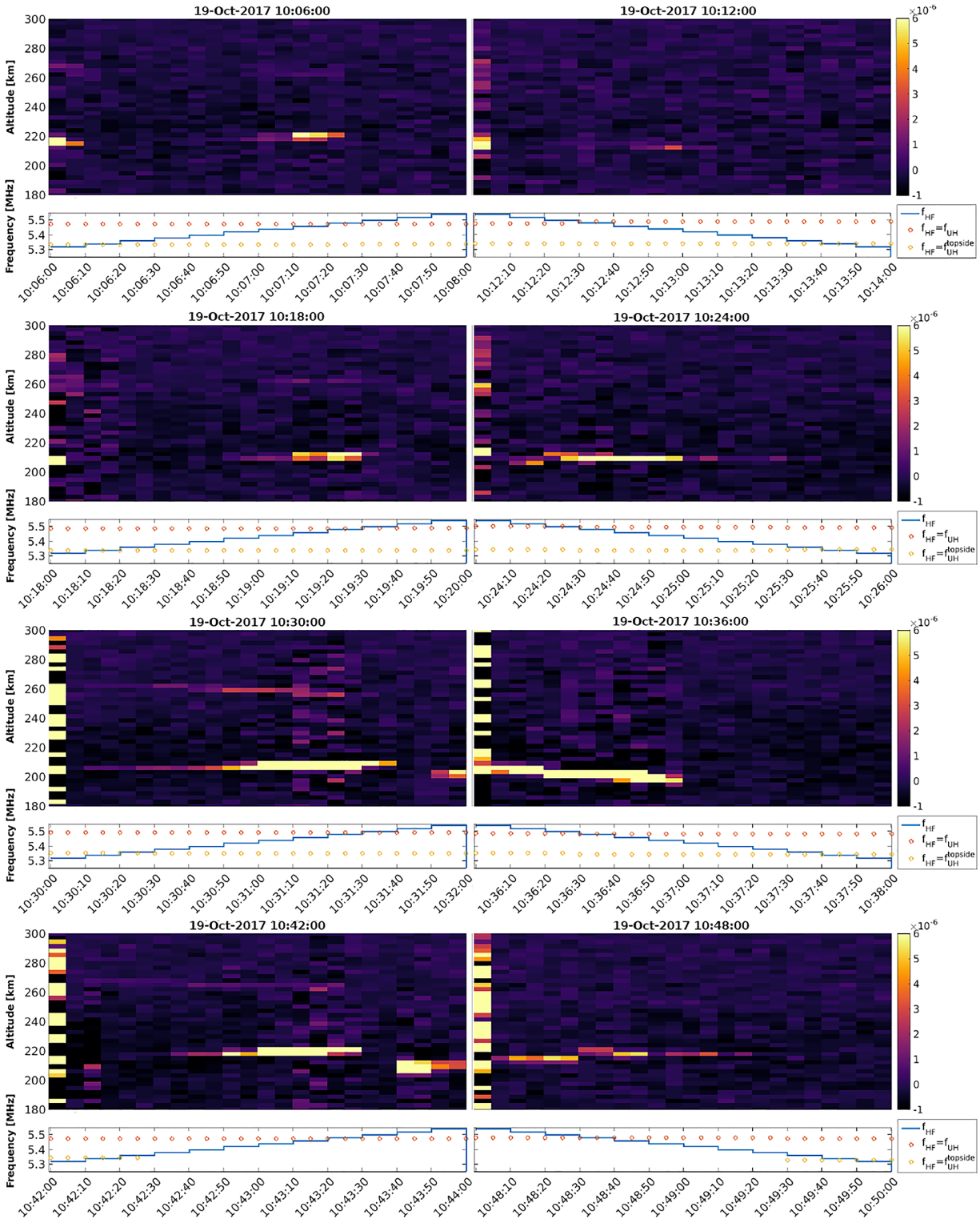

Figure 3. Case B: Time evolution of the averaged backscattered power in the ion line spectra for consecutive heating on pulses on October 19th, 2017. The bottom panels show f_{HF} and double resonance frequency. Case B enhancements are observed in high frequency pulses where f_{HF} is stepped upward (left column).

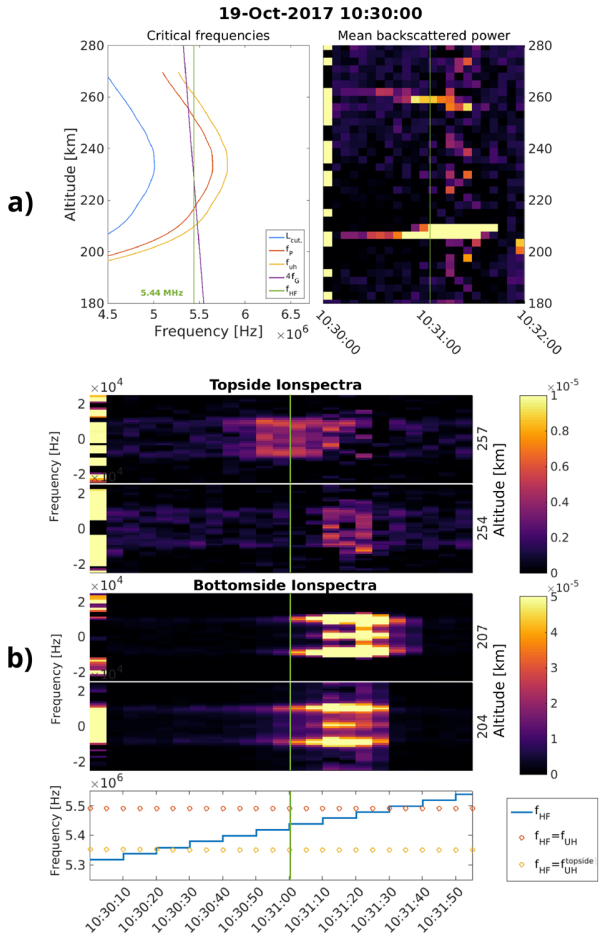

Figure 4. Example of a typical observations of case B. (a) The left panel shows the critical frequencies calculated from the observed natural Langmuir waves. The blue, red and yellow lines indicate the L mode cutoff, the local plasma frequency, and the local upper hybrid frequency, respectively. The purple line shows the fourth harmonic of the electron gyrofrequency, while the green vertical line indicates the frequency of the transmitted O mode pump wave. On the right the 5 s mean backscattered ion line power, with a 3 km altitude resolution, during a 2 min HF on pulse is shown. The vertical green line in the top right panel plot indicates the time to which the left panel plot corresponds. (b) The four upper panels show the topside ion line spectra and the bottomside ion line spectra with the frequency on the vertical axis, for the two altitudes of the strongest topside high frequency ion lines (254 and 257 km) and BHFIL (204 and 207 km). The bottom panel shows f_{HF} and the top- and bottomside fourth harmonic of the double resonance frequency. Green vertical lines indicate the time corresponding to the left panel of (a).

Figure 5 is the same as Figure 2, but for the case B data, with the 4 case B HF pulses from October 19th, 2017. Additionally, 33 HF pulses with THFIL, previously presented by Rexer et al. (2018), and all consistent with and categorized as case B, are added. We include the data again here to emphasize the case B characteristics and differences to case A. Case B has been previously discussed and the findings include observations that the case B THFIL are conditioned by the proximity of f_{HF} to f_{dbl} on the bottomside ionosphere. Additionally the THFIL only appear simultaneous to BFHIL and are generally weaker (Rexer et al., 2018). This is seen in the top panel of Figure 5. Relating the backscattered power of the THFIL to the topside f_{dbl}, shown in the lower panel, a small local maximum of the mean backscattered power of the THFIL can be observed when f_{HF} is close to f_{dbl} on the topside (zero on abscissa).

We have summarized the main characteristic of the BHFIL and THFIL for the two cases in Table 1.

4. Transionospheric Wave Propagation

Mjølhus and Flå (1984) adapted the theory of linear conversion of incident radiowaves into electrostatic waves, to ionospheric modification experiments, finding that an O mode wave transmitted into the horizontally stratified ionosphere can access the plasma resonance region through the radio window. That is, if $f_{\mathrm{HF}} > f_{L-\mathrm{cut}}$ the wave will propagate to the topside resonance region of the ionosphere, and continue through the topside radio window into space. Rays near θ_c are partially reflected and partially transmitted. Thus, partially penetrating rays at the bottomside radio window, will propagate to the topside ionosphere at an angle slightly off θ_c. These rays will be partially reflected at the topside radio window into a northward path (Mjølhus, 1990; Mjølhus & Flå, 1984).

Additionally, artificial radio windows can be generated at different locations by large scale, field aligned, density ducts induced by the pump wave (Leyser & Nordblad, 2009; Nordblad & Leyser, 2010). An incident O mode wave can be guided into the L mode along the geomagnetic field by ducts, with the same polarization as a ray at the critical angle in a horizontally stratified ionosphere. At $f_{\mathrm{HF}} = f_P$, with k exactly along the magnetic field, the O, Z and Langmuir dispersion surfaces connect, forming a radio window such that O mode waves guided into the L mode by large scale density irregularities will not change polarization. A wave, thus guided can pass the ionospheric density peak if $f > f_{L-\mathrm{cut}}$, and propagate to the topside resonance region, at different locations depending on the location and local parameters of the guiding density striation.

The dispersion properties of the upper hybrid waves is such that formation of small scale density striations, that can form a larger scale duct, decreases as the pump wave frequency approaches that of the double resonance frequency (i.e., Mjølhus, 1993; Robinson et al., 1996). Anomalous absorption is also at a minimum near or at harmonics of f_G (Stubbe et al., 1994). Consequently, and consistent with previous observations (Honary et al., 1999), coupling to Langmuir waves and ion acoustic waves is possible. Contrary to small scale density striations, large scale density ducts generated by the pump wave (i.e., A. Gurevich et al., 1998; Kelley et al., 1995) have a longer generation and decay time, on the order of minutes (Basu et al., 1997). Thus, guiding of the pump wave into the L mode, and hence transionospheric propagation, can be facilitated by these as they may exist in the plasma for several minutes, also when f_{HF} is stepped through f_{dbl}. Further, we propose that the physics described by (Mjølhus & Flå, 1984) concerning access to the plasma

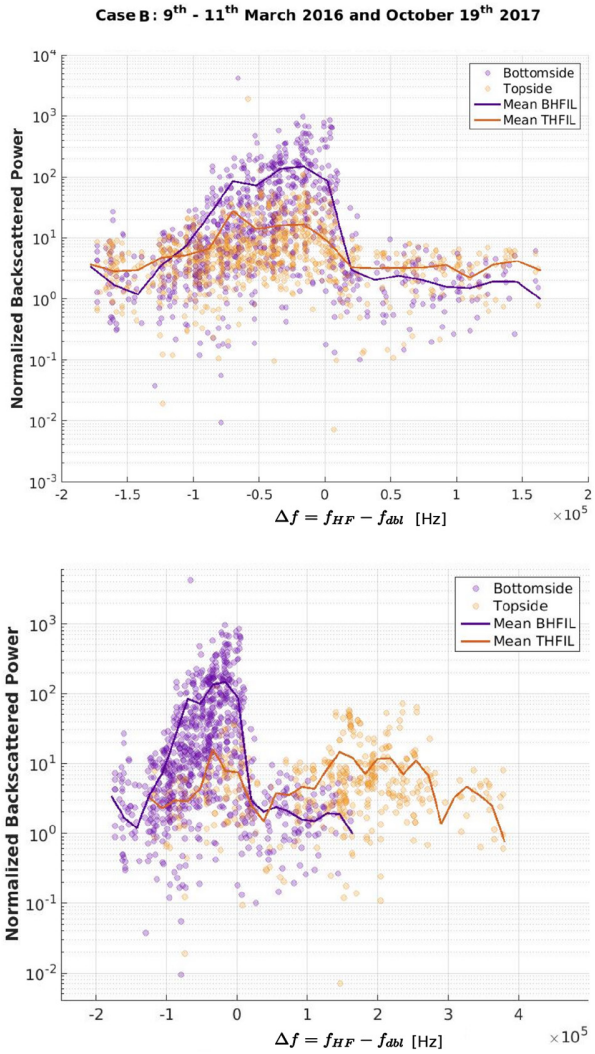

Figure 5. Same as Figure 2 but for the 4 case B high frequency (HF) pulses from October 19th, 2017 and 33 HF pulses with topside high frequency enhanced ion lines, previously presented by Rexer et al. (2018), and all categorized as case B.

resonance through radio windows in a horizontally stratified ionosphere is qualitatively applicable also to artificial radio windows due to the presence of density ducts.

5. Discussion

Figure 2 shows that case A THFIL predominantly appear when f_{HF} is just below or at f_{dbl} at the topside ionosphere, when $\Delta f = f_{\mathrm{HF}} - f_{dbl}$ on the topside is between −100 and 18 kHz. This resembles the dependence of the appearance of THFIL, on the proximity of f_{HF} to f_{dbl} on the bottomside in case B. Both cases of THFIL appear to be asymmetrically conditioned by the proximity of f_{HF} to a f_{dbl}. Contradictory to case B (and our previous observations (Rexer et al., 2018)), case A THFIL appear to be asymmetrically conditioned by the proximity of f_{HF} to f_{dbl} at the topside rather than the bottomside, as for case B.

Case B THFIL appear only simultaneous to stronger BHFIL and are conditioned by the proximity of f_{HF} to f_{dbl} on the bottomside ionosphere. Both THFIL and BHFIL are observed at the altitude where $f_P \approx f_{\mathrm{HF}}$, whereas the matching height is calculated to be approximately ≈6–7 km below the enhancements on the bottomside during the experiment. As the calculations of the matching height are based on the observations of the natural Langmuir waves in the plasma line spectra with a temporal resolution of 1 min, we interpret the observations of the BHFIL at the apparent resonance height to be an indication that large scale density ducts have formed. That is, the matching height is at a higher altitude within the duct, hence the BHFIL appear to be close to the resonance altitude.

In the bottom panel of Figure 5, showing the THFIL and BHFIL related to f_{dbl} at the top- and bottomside, respectively, we see a small local maximum of the case B THFIL when f_{HF} is close to f_{dbl} on the topside (zero on abscissa). This resembles the observations in case A, where THFIL appear to be conditioned by the proximity of f_{HF} to the topside f_{dbl}. It is possible that a similar relation as for case A exists, however, there are few datapoints in this region. As mentioned above, the lower panels of Figure 3 (case B THFIL in the left column) indicate that the range of frequency steps used did not include f_{HF} well below the topside f_{dbl}. It is apparent in the example in the top left panel of Figure 4, that the altitude difference between the bottomside and topside resonance height is≈50 km for case B from October 19th 2017 (≈70–100 km for the observation presented in Rexer et al. (2018)). This leads to a large difference between the top- and bottomside f_{dbl}, as f_G decreases with altitude. As we do not reach this frequency range below f_{dbl} at the topside ionosphere where one might expect THFIL, for these HF pulses, a definite conclusion about a possible relation to f_{dbl} on the topside, also for case B observations, cannot be drawn from these observations.

Further, distinct ion acoustic peaks are observed when $f_{\mathrm{HF}} < f_{dbl}$ on the bottomside and a sharp, distinct $\omega = 0$ peak, associated with the OTSI (i.e., Fejer, 1979; Kuo et al., 1997; Stubbe et al., 1992), in the BHFIL frequency spectra of case B. An example is shown in the middle panels of Figure 4. BHFIL frequency spectra from case A, shown in Figure 1, and BHFIL frequency spectra (not shown) from the downstepping HF pulses on the October 19th, 2017 (right column of Figure 3) have distinct ion acoustic shoulders, associated with PDIs, but only a weak or no $\omega = 0$ feature. Interestingly, although polarization and ERP of EISCAT Heating were the same for all HF pulses on October 19th, 2017, and the frequency steps were spanning the same frequency range, only alternating between stepping upward and downward, the BHFIL spectra for up stepping pulses show a clear and distinct central feature while BHFIL spectra for downstepping pulses show only well developed ion acoustic shoulders and no central feature. The threshold electric field of the

Table 1
Main Characteristics of BHFIL and THFIL for Case A and Case B

	BHFIL	THFIL
Case A		
Observed during f_{HF} downstepping experiments	• Predominantly appear for f_{HF} = 0–100 kHz below the bottomside f_{dbl} • Fade completely for $\Delta f < \sim -100$ kHz • Enhancement at altitude between matching height and resonance height • Weak and fading central feature in ion line spectra	• Predominantly appear when f_{HF} is between ≈ −100 and 18 kHz around the topside f_{dbl} • Growing enhancements as BHFIL fade • Enhancement at resonance height • Filled in ion line spectra/weak central feature
Case B		
Observed during f_{HF} upstepping experiments	• Strong enhancements when f_{HF} is 80 kHz below, and ∼9.8 kHz above the bottomside f_{dbl} • BHFIL abruptly disappear as f_{HF} increases above the bottomside f_{dbl} • Stronger than THFIL • Enhancement appears to be at the resonance height • Prominent, distinct central feature in ion line spectra	• Only appear simultaneous to BHFIL, when f_{HF} is 80 kHz below, and ∼9.8 kHz above f_{dbl} at the bottomside • Weaker then BHFIL • Enhancement at resonance height • Filled in ion line spectra/weak central feature

Abbreviations: BHFIL, bottomside HF-enhanced ion lines; HF, high frequency; THFIL, topside HF-enhanced ion lines

pump wave required to excite the OTSI is usually higher than that for the PDI (Robinson, 1989), indicating a possible difference in allocation of pump wave energy, a difference in *D*-region absorption or different mechanisms responsible for the BHFIL in the up stepping and down stepping HF pulses. The down stepping HF pulses on 19th October are comparable to HF pulses on 18th October, where case A THFIL were observed. We consider it likely that case A THFIL could have been generated also on the downstepping HF pulses on 19th October, had the f_{HF} stepping scheme extended to frequencies below f_{dbl} on the topside ionosphere as discussed above.

In case A, for the duration of the THFIL, f_{HF} is well below f_{dbl} at the bottomside. Consequently anomalous absorption is effective and less energy available for excitation of Langmuir waves and related nonlinear wave interactions at the bottomside plasma resonance (Stubbe et al., 1994). Conforming to this is the absence or very weak BHFIL observed during case A. The proximity of the f_{HF} to f_{dbl} at the topside, by propagation of the pump wave through an artificial radio window, allows for direct linear conversion of the pump wave here (Mjølhus & Flå, 1984). Furthermore, Mjølhus and Flå (1984) predict the formation of strongly nonlinear Langmuir wave field as a result of linear conversion in the resonance region. At exactly the radio window complete transmission occurs, while partial transmission and partial reflection occur for rays near this. It is possible then, that the close proximity of f_{HF} to the topside resonance allows for THFIL also in a suppressed pump field due to the anomalous absorption in the bottomside.

In case B f_{HF} is below f_{dbl} on the bottomside ionosphere for approximately 1 min and the duration of several frequency steps, permitting the development of large scale density ducts (Basu et al., 1997). The Weak BHFIL observed during this time are consistent with this, as the wave energy is absorbed by upper hybrid phenomena a few kilometer below the matching height and associated anomalous absorption (Robinson, 1989). Although we do not have direct observations of density ducts, we argue that it is likely they were excited by the pump wave. The large electron temperature enhancements we observe (up to ∼3500 K), during HF pulses are significantly larger than what is obtained with Ohmic heating alone (Bryers et al., 2013). Such anomalous heating is attributed to resonant heating effects at the upper hybrid resonance altitude, that are strongly coupled to the generation of field aligned density striations (A. V. Gurevich, 2007; A. V. Gurevich et al., 1996; Istomin & Leyser, 1997).

As f_{HF} approaches f_{dbl} on the bottomside, the growth of the density striations is suppressed (Honary et al., 1999; Huang & Kuo, 1994; Mjølhus, 1993; Robinson, 1989) and pump wave energy is guided by the remaining ducts to reach the resonance altitude, permitting coupling to Langmuir and ion acoustic waves.

This can be seen as an increase in the BHFIL power, observed near the resonance altitude, as f_{HF} approaches f_{dbl}. Hence, a larger portion of the pump wave energy reaches the topside resonance region, compared to case A, by propagation in the L mode guided by large scale density ducts. THFIL are therefore observed as a result of partial reflection of Z mode rays just outside the central ray in the density duct.

With the above discussion in mind the main difference between case A and case B appears to be the allocation of pump wave energy for the generation of BHFIL and the relative proximity of f_{HF} to a f_{dbl}, either on the topside or on the bottomside.

6. Conclusions

We have shown two cases, with different characteristics, of systematically recurring THFIL during an experiment at the EISCAT Heating facility on October 18th and 19th, 2017. A pump wave with an O mode polarization was transmitted in the magnetic zenith direction in a 2-min-on, 5-min-30-sec-off cycle, stepping through the double resonance frequency of the electron gyro frequency and the local upper hybrid frequency. Plasma parameters were obtained from the EISCAT UHF radar, allowing for high accuracy calculations of the altitude profile of the plasma-, upper hybrid-, and L mode cut-off frequencies. In case A, THFIL were observed when f_{HF} is at or below the double resonance frequency at the topside ionosphere. No or weak BHFIL were observed at the pump frequencies of the strongest THFIL. In case B observations the THFIL occur simultaneous to BHFIL, when f_{HF} is at or below the bottomside double resonance frequency. These are consistent with previous observations of THFIL made by Rexer et al. (2018) and Borisova et al. (2020). We interpret the observations as a result of pump wave guiding into the L mode by large scale density ducts to propagate through the ionospheric density peak. The pump wave may access the plasma resonance through these artificial radio windows in the magnetic zenith direction, in the same manner as Mjølhus and Flå (1984) describe theoretically for natural radio windows in a horizontally stratified ionosphere. We suggest that the main difference between the two characteristic cases of THFIL is the amount of available pump wave energy that reaches the topside resonance region and the relative proximity of the pump wave frequency to the double resonance frequency at the topside resonance region for case A and the bottomside resonance region for case B.

Data Availability Statement

The data of EISCAT UHF radar during the experiment can be obtained from EISCAT https://portal.eiscat.se/schedule/. The EISCAT ISR analysis tool GUISDAP is available at https://eiscat.se/scientist/user-documentation/guisdap/.

Acknowledgments
EISCAT is an international association supported by research organizations in China (CRIRP), Finland (SA), Japan (NIPR and ISEE), Norway (NFR), Sweden (VR), and the United Kingdom (UKRI).

References

Basu, S., Costa, E., Livingston, R. C., Groves, K. M., Carlson, H. C., Chaturvedi, P. K., & Stubbe, P. (1997). Evolution of subkilometer scale ionospheric irregularities generated by high-power HF waves. *Journal of Geophysical Research*, *102*(A4), 7469–7475. https://doi.org/10.1029/96JA03340

Borisova, T. D., Blagoveshchenskaya, N. F., Kalishin, A. S., Häggström, M. I., & Rietveld, M. T. (2020). Excitation of Langmuir and ion–acoustic turbulence in the high-latitude ionosphere by a high-power HF radio wave simultaneously below and above the F 2-layer maximum. *Radiophysics and Quantum Electronics*, *62*(12), 793–806. https://doi.org/10.1007/s11141-020-10025-z

Bryers, C. J., Kosch, M. J., Senior, A., Rietveld, M. T., & Singer, W. (2013). A comparison between resonant and nonresonant heating at EISCAT. *Journal of Geophysical Research: Space Physics*, *118*(10), 6766–6776. https://doi.org/10.1002/jgra.50605

Budden, K. G. (1980). The theory of radio windows in the ionosphere and magnetosphere. *Journal of Atmospheric and Terrestrial Physics*, *42*(3), 287–298. https://doi.org/10.1016/0021-9169(80)90036-7

Chen, F. (1983). *Introduction to plasma physics and controlled fusion* (2nd ed.). Springer.

Eliasson, B. (2008). Full-scale simulation study of the generation of topside ionospheric turbulence using a generalized Zakharov model. *Geophysical Research Letters*, *35*(11), 1–5. https://doi.org/10.1029/2008GL033866

Eliasson, B., & Leyser, T. B. (2015). Numerical study of upper hybrid to Z-mode leakage during electromagnetic pumping of groups of striations in the ionosphere. *Annales Geophysicae*, *33*(8), 1019–1030. https://doi.org/10.5194/angeo-33-1019-2015

Ellis, G. R. (1956). The Z propagation hole in the ionosphere. *Journal of Atmospheric and Terrestrial Physics*, *8*, 43–54. https://doi.org/10.1016/0021-9169(56)90090-3

Fejer, J. A. (1979). Ionospheric modification and parametric instabilities. *Reviews of Geophysics*, *17*(1), 135–153. https://doi.org/10.1029/RG017i001p00135

Ganguly, S., & Gordon, W. E. (1983). Heater enhanced topside plasma line. *Geophysical Research Letters*, *10*(10), 977–978. https://doi.org/10.1029/gl010i010p00977

Gurevich, A., Hagfors, T., Carlson, H., Karashtin, A., & Zybin, K. (1998). Self-oscillations and bunching of striations in ionospheric modifications. *Physics Letters, Section A: General, Atomic and Solid State Physics*, *239*(6), 385–392. https://doi.org/10.1016/S0375-9601(98)00006-1

Gurevich, A. V. (2007). Nonlinear effects in the ionosphere. *Uspekhi Fizicheskih Nauk, Russian Academy of Sciences*, *177*(11), 1145–1177. https://doi.org/10.3367/UFNr.0177.200711a.1145

Gurevich, A. V., Lukyanov, A. V., & Zybin, K. P. (1996). Anomalous absorption of powerful radio waves on the striations developed during ionospheric modification. *Physics Letters, Section A: General, Atomic and Solid State Physics*, *211*(6), 363–372. https://doi.org/10.1016/0375-9601(95)00970-1

Gurevich, A. V., Zybin, K. P., & Lukyanov, A. V. (1995). Stationary striations developed in the ionospheric modification. *Physical Review Letters*, *75*(13), 2622–2625. https://doi.org/10.1103/physrevlett.75.2622

Hagfors, T., & Lehtinen, M. (1981). Electron temperature derived from incoherent scatter radar observations of the plasma line frequency. *Journal of Geophysical Research*, *86*(A1), 119. https://doi.org/10.1029/ja086ia01p00119

Honary, F., Robinson, T., Wright, D., Stocker, A., Rietveld, M., & McCrea, I. (1999). First direct observations of the reduced striations at pump frequencies close to the electron gyroharmonics. *Annales Geophysicae*, *17*, 1235–1238. https://doi.org/10.1007/s00585-999-1235-6. Retrieved from http://hdl.handle.net/2381/12174

Huang, J., & Kuo, S. P. (1994). A theoretical model for the broad upshifted maximum in the stimulated electromagnetic emission spectrum. *Journal of Geophysical Research*, *99*(A10), 19569–19576. https://doi.org/10.1029/94ja01261

Isham, B., Hagfors, T., Mishin, E., Rietveld, M. T., La Hoz, C., Kofman, W., & Leyser, T. B. (1999). A search for the location of the HF excitation of enhanced ion acoustic and Langmuir waves with EISCAT and the Tromso Heater. *Radiophysics and Quantum Electronics*, *42*(7), 533–543. https://doi.org/10.1007/bf02677559

Isham, B., Kofman, W., Hagfors, T., Nordling, J., Thidé, B., LaHoz, C., & Stubbe, P. (1990). New phenomena observed by EISCAT during an RF ionospheric modification experiment. *Radio Science*, *25*(3), 251–262. https://doi.org/10.1029/RS025i003p00251

Isham, B., Rietveld, M., Hagfors, T., La Hoz, C., Mishin, E., Kofman, W., et al. (1999). Aspect angle dependence of HF enhanced incoherent backscatter. *Advances in Space Research*, *24*(8), 1003–1006. https://doi.org/10.1016/s0273-1177(99)00555-4. Retrieved from http://linkinghub.elsevier.com/retrieve/pii/S0273117799005554

Istomin, Y. N., & Leyser, T. B. (1997). Small-scale magnetic field-aligned density irregularities excited by a powerful electromagnetic wave. *Physics of Plasmas*, *4*(3), 817. https://doi.org/10.1063/1.872175. Retrieved from http://scitation.aip.org/content/aip/journal/pop/4/3/10.1063/1.872175

Istomin, Y. N., & Leyser, T. B. (2001). Diffraction of electromagnetic waves by small scale geomagnetic field-aligned density striations. *Physics of Plasmas*, *8*(10), 4577–4584. https://doi.org/10.1063/1.1399325

Kelley, M. C., Arce, T. L., Salowey, J., Sulzer, M., Armstrong, W. T., Carter, M., & Duncan, L. (1995). Density depletions at the 10-m scale induced by the Arecibo heater. *Journal of Geophysical Research*, *100*(A9), 17367–17376. https://doi.org/10.1029/95ja00063

Kosch, M. J., Mjlhus, E., Ashrafi, M., Rietveld, M. T., Yeoman, T., & Nozawa, S. (2011). Angular dependence of pump-induced bottomside and topside ionospheric plasma turbulence at EISCAT. *Journal of Geophysical Research*, *116*(3), 1–9. https://doi.org/10.1029/2010JA016014

Kuo, S. P., Lee, M. C., & Kossey, P. (1997). Excitation of oscillating two stream instability by upper hybrid pump waves in ionospheric heating experiments at Tromso. *Geophysical Research Letters*, *24*(23), 2969–2972. https://doi.org/10.1029/97GL03054

Leyser, T. B., James, H. G., Gustavsson, B., & Rietveld, M. T. (2018). Evidence of L-mode electromagnetic wave pumping of ionospheric plasma in geomagnetic Zenith. *Annales Geophysicae*, *36*, 900167. https://doi.org/10.1029/2009GL041438

Leyser, T. B., & Nordblad, E. (2009). Self-focused radio frequency L wave pumping of localized upper hybrid oscillations in high-latitude ionospheric plasma. *Geophysical Research Letters*, *36*(24), 1–4. https://doi.org/10.1029/2009GL041438

Mishin, E., Hagfors, T., & Isham, B. (2001). A generation mechanism for topside enhanced incoherent backscatter during high frequency modification experiments in. *Tromsø Geophysical Research Letters*, *28*(3), 479–482. https://doi.org/10.1029/2000GL000122

Mjølhus, E. (1990). On linear conversion in a magnetized plasma. *Radio Science*, *25*(6), 1321–1339.

Mjølhus, E. (1993). On the small scale striation effect in ionospheric radio modification experiments near harmonics of the electron gyro frequency. *Journal of Atmospheric and Terrestrial Physics*, *55*(6), 907–918. https://doi.org/10.1016/0021-9169(93)90030-3

Mjølhus, E., & Flå, T. (1984). Direct access to plasma resonance in ionospheric radio experiments. *Journal of Geophysical Research*, *89*(A6), 3921–3928. https://doi.org/10.1029/JA089iA06p03921

Nordblad, E., & Leyser, T. B. (2010). Ray tracing analysis of L mode pumping of the ionosphere, with implications for the magnetic zenith effect. *Annales Geophysicae*, *28*(9), 1749–1759. https://doi.org/10.5194/angeo-28-1749-2010

Rexer, T., Gustavsson, B., Leyser, T., Rietveld, M., Yeoman, T., & Grydeland, T. (2018). First observations of recurring HF-enhanced topside ion line spectra near the fourth Gyroharmonic. *Journal of Geophysical Research*, *123*, 1–15. https://doi.org/10.1029/2018JA025822

Rietveld, M. T., Isham, B., Grydeland, T., La Hoz, C., Leyser, T. B., Honary, F., et al. (2002). HF-pump-induced parametric instabilities in the auroral E-region. *Advances in Space Research*, *29*(9), 1363–1368. https://doi.org/10.1016/S0273-1177(02)00186-2

Rietveld, M. T., Isham, B., Kohl, H., La Hoz, C., & Hagfors, T. (2000). Measurements of HF-enhanced plasma and ion lines at EISCAT with high-altitude resolution. *Journal of Geophysical Research*, *105*(A4), 7429–7439. https://doi.org/10.1029/1999JA90047610.1029/1999JA900476

Rietveld, M. T., Senior, A., Markkanen, J., & Westman, A. (2016). New capabilities of the upgraded EISCAT high-power HF facility. *Radio Science*, *51*(9), 1533–1546. https://doi.org/10.1002/2016RS006093

Robinson, T. R. (1989). The heating of the high latitude ionosphere by high power radio waves. *Physics Reports*, *179*(2–3), 79–209. https://doi.org/10.1016/0370-1573(89)90005-7

Robinson, T. R., Honary, F., Stocker, A. J., Jones, T. B., & Stubbe, P. (1996). First EISCAT observations of the modification of F-region electron temperatures during RF heating at harmonics of the electron gyro frequency. *Journal of Atmospheric and Terrestrial Physics*, *58*(1–4), 385–395. https://doi.org/10.1016/0021-9169(95)00043-7

Stubbe, P. (1996). Review of ionospheric modification experiments at Troms˜. *Journal of Atmospheric and Terrestrial Physics*, *58*(1–4), 349–368. https://doi.org/10.1016/0021-9169(95)00041-0

Stubbe, P., Kohl, H., & Rietveld, M. T. (1992). Langmuir turbulence and ionospheric modification. *Journal of Geophysical Research*, *97*(A5), 6285–6297. https://doi.org/10.1029/91ja03047

Stubbe, P., Stocker, A. J., Honary, F., Robinson, T. R., & Jones, T. B. (1994). Stimulated electromagnetic emissions an anomalous HF wave absorption near electron gyroharmonics. *Journal of Geophysical Research*, *99*(A4), 6233–6246. https://doi.org/10.1029/94ja00023

Tjulin, A. (2017). EISCAT Experiments. *EISCAT Scientific Association*(March). Retrieved from https://www.eiscat.se/wp-content/uploads/2017/04/Experiments.pdf

PAPER III

Electron heating by HF pumping of high-latitude ionospheric F-region plasma near magnetic zenith

Leyser, T. T., Gustavsson, B., **Rexer, T.**, and Rietveld, M. M., Annales Geophysicae, 38, 297–307, doi: 10.5194/angeo-38-297-2020, 2020

Ann. Geophys., 38, 297–307, 2020
https://doi.org/10.5194/angeo-38-297-2020

Annales Geophysicae
Open Access
EGU

Electron heating by HF pumping of high-latitude ionospheric F-region plasma near magnetic zenith

Thomas B. Leyser[1], **Björn Gustavsson**[2], **Theresa Rexer**[2], **and Michael T. Rietveld**[3]

[1]Swedish Institute of Space Physics, Uppsala, Sweden
[2]Institute for Physics and Technology, The Arctic University of Norway, Tromsø, Norway
[3]EISCAT Scientific Association, Ramfjordmoen, Norway

Correspondence: Thomas B. Leyser (thomas.leyser@irfu.se)

Received: 19 November 2019 – Discussion started: 25 November 2019
Accepted: 2 February 2020 – Published: 6 March 2020

Abstract. High-frequency electromagnetic pumping of ionospheric F-region plasma at high and mid latitudes gives the strongest plasma response in magnetic zenith, antiparallel to the geomagnetic field in the Northern Hemisphere. This has been observed in optical emissions from the pumped plasma turbulence, electron temperature enhancements, filamentary magnetic field-aligned plasma density irregularities, and in self-focusing of the pump beam in magnetic zenith. We present results of EISCAT (European Incoherent SCATter association) Heating-induced magnetic-zenith effects observed with the EISCAT UHF incoherent scatter radar. With heating transmitting a left-handed circularly polarized pump beam towards magnetic zenith, the UHF radar was scanned in elevation in steps of 1.0 and 1.5° around magnetic zenith. The electron energy equation was integrated to model the electron temperature and associated electron heating rate and optimized to fit the plasma parameter values measured with the radar. The experimental and modelling results are consistent with pump wave propagation in the *L* mode in magnetic zenith, rather than in the *O* mode.

1 Introduction

A powerful high-frequency (HF) electromagnetic wave transmitted from the ground into the ionospheric F region stimulates the strongest plasma response on long timescales in the direction antiparallel to the geomagnetic field in the Northern Hemisphere as seen from the HF transmitter. This magnetic zenith effect has been observed in several ways for a range of pump frequencies in experiments at high and mid latitudes.

In experiments with EISCAT (European Incoherent SCATter association) high-power HF facility Heating in Norway in 1999, pump-induced optical emissions were imaged unambiguously for the first time (Brändström et al., 1999). Gustavsson et al. (2001) presented tomography-like estimates of the volume distribution of the 630.0 nm emissions from these experiments and found that the emissions intensified and self-focused towards magnetic zenith during the 4 min pumping. Kosch et al. (2000) observed that while the HF beam was directed vertically, the region of maximum optical emissions was displaced towards magnetic zenith as seen from EISCAT Heating. The authors also noted that published data of coherent HF radar scatter off geomagnetic field-aligned density irregularities tend to maximize in the magnetic field-aligned direction.

Radio tomography and scintillations using amplitude and phase measurements on the ground of VHF signals from orbiting satellites were used to study HF pump-induced electron density modifications in experiments with the mid-latitude Sura HF facility in Russia. Small-scale filamentary magnetic field-aligned plasma density irregularities were found to be strongest in magnetic zenith, both when the Sura beam was vertical and at an angle in between the vertical and magnetic zenith (Tereshchenko et al., 2004). Further, initial experiments with the Sura HF beam directed either 12° south of vertical or 16° both showed the strongest optical emissions at 630.0 nm near magnetic zenith at 18–19° south (Grach et al., 2007).

Rietveld et al. (2003) scanned the EISCAT Heating beam between three elevations from vertical to near magnetic zenith and found that electron temperature enhancements were almost always strongest in the magnetic zenith position. When the EISCAT UHF radar was scanned between the same positions, the strongest electron heating was always observed near magnetic zenith. In addition, optical emission at 630.0 nm was localized near magnetic zenith and HF coherent radar scatter off geomagnetic field-aligned density striations maximized when the Heating beam was in magnetic zenith. Blagoveshchenskaya et al. (2006) too observed the strongest field-aligned density striations when the Heating beam was in magnetic zenith.

Honary et al. (2011) examined the temporal evolution of the magnetic zenith effect as observed in the electron temperature measured by the EISCAT UHF radar. The beams from the Heating facility and the UHF radar were alternatively directed vertically and in magnetic zenith. Maximum temperature enhancements were observed when both the Heating and radar beams were in magnetic zenith. Further, these electron temperature enhancements reached a stationary state already within 10 s after pump-on in the 60 s on–90 s off pump cycle.

The magnetic zenith effect in optical emissions has also been observed in experiments with the HAARP (High frequency Active Auroral Research Program) facility in Alaska, USA (Pedersen and Carlson, 2001; Pedersen et al., 2003). Further, Pedersen et al. (2008) determined the optical emission production efficiency as a function of angle by HF beam-swinging experiments. The maximum emission efficiency occurred exactly in the geomagnetic field-aligned position.

Kosch et al. (2007) observed self-focusing of the pump beam in magnetic zenith in experiments at HAARP. The pump-induced optical emissions at 557.7 nm collapsed from a cone of approximately 22 to 9° within tens of seconds after pump-on while cycling the pump 60 s on–60 s off.

In the present treatment we report experimental results on the magnetic zenith effect obtained with the EISCAT Heating facility (Rietveld et al., 2016). The F-region plasma response to the HF pumping was observed with the EISCAT UHF incoherent scatter radar that was scanned in steps of either 1.0° or 1.5° around magnetic zenith to measure the electron temperature and other plasma parameter values. Nonlinear least squares analysis was used to fit electron temperature profiles obtained from integrating the electron energy equation with a parameterized heat source to measured plasma parameters, taking into account heat conduction, electron heating and cooling. The analysis gave the electron heating rate as a function of altitude and elevation angle. The results are consistent with the pump wave propagating in the L mode in magnetic zenith and in the O mode at angles deviating from zenith.

2 Experiment setup

The EISCAT Heating experiments were performed during daytime in November 2014 and October 2017. The Heating facility transmitted a left-handed circularly polarized wave (LHCP, often referred to as O mode) in a beam directed towards magnetic zenith ($\sim 78°$ elevation south) and cycling 150 s on–85 s off. The Heating beam width at -3 dB was $\sim 6°$. The term "left-handed" is defined with reference to the geomagnetic field direction: the electric field rotates in the opposite sense to the gyromotion of electrons.

Plasma parameter values in the F region were obtained with the EISCAT UHF incoherent scatter radar. The radar measurements utilized the Beata modulation scheme which includes a 32 bit binary alternating code with a baud length of 20 µs. The UHF radar beam was scanned in steps of 1.0° in the experiment in November 2014 and in steps of 1.5° in October 2017, between eight elevations around magnetic zenith in the plane containing the vertical and with a duration of 5 s in each position. The radar beam width was $\sim 0.5°$. The pump cycle of 150 s on–85 s off enabled appropriate coverage of the radar measurements throughout the pump-on time, so that after several pump cycles under stable ionospheric conditions the temporal evolution during the pumping could be obtained at all elevations. The radar data analysis provided 5 s temporal resolution and 15–20 km range resolution, depending on the range.

3 Experimental results

Figure 1 displays measured height profiles for the electron concentration ($\widetilde{N}_e$), electron temperature ($\widetilde{T}_e$) and ion temperature ($\widetilde{T}_i$) for the experiment on 25 November 2014 (the tilde denotes measured parameters as opposed to modelled ones). For this case the pump frequency is $f_0 = 6.30$ MHz, which is approximately half way between the fourth and fifth electron gyroharmonics in the F region. The transmitted power was 818 kW. For some unknown technical reason, Heating did not transmit a circularly polarized wave during this experiment: the effective radiated power (ERP) was 242 MW in LHCP and 157 MW in right-handed circular polarization (RHCP), assuming a perfectly conducting ground. However, electron heating effects from pumping with LHCP dominate over those with RHCP. Bryers et al. (2013) estimated the height-integrated heating source for O-mode pumping to be approximately a factor of 3 larger than for X-mode pumping, for a pump duty cycle of 50 % and the O-mode pump frequency not near an electron gyroharmonic, with the X-mode frequency near a gyroharmonic (their Fig. 5), however. In addition, the ERP in our experiments for LHCP was larger than for RHCP. We therefore consider the measured heating effects to be representative of pure LHCP pumping.

The $\widetilde{N}_e$ profile in Fig. 1a is stable throughout the displayed time interval and does not show modulations due to the pumping. However, the $\widetilde{T}_e$ profile in Fig. 1b exhibits clear pump-induced modulations. The HF pumping is marked by white boxes and the red zigzag line indicates the radar elevation scan. The $\widetilde{T}_i$ shown in Fig. 1c only exhibits weak pump-induced modulations. The ionospheric conditions and response to the HF pumping in the experiments on 24 October 2017 were similar to those shown in Fig. 1. However, whereas for 2014 the ionospheric critical frequency $foF2$ was near 8 MHz, well above f_0, $foF2$ was near f_0 in 2017.

The used pump cycle in combination with the radar scan cycle enabled measurement of the temporal evolution of the ionospheric parameters at all radar elevation angles throughout the pumping. Figure 2 shows the temporal evolution of height profiles of $\widetilde{T}_e$ for the different elevation angles of the UHF radar, starting at $t = 5$ s after pump-on for the experiments on 25 November 2014. Such measurements require reasonably stable ionospheric conditions during several pump cycles (see Fig. 1), as the radar, scanning eight elevations between 75.2 and 82.2°, samples the interaction region at a given elevation at different times after pump-on in different pump pulses. With measurements at sufficiently many pump pulses the temporal evolution can then be traced throughout the duration of pump-on ($t = 0$–150 s) at all elevations.

As seen in Fig. 2, $\widetilde{T}_e$ enhancements occurred already within the first few seconds of pump-on. The high $\widetilde{T}_e$ around 300 km in the first 5 s data dump is likely not real but due to HF enhanced ion acoustic lines on the topside ionosphere. During the following few tens of seconds $\widetilde{T}_e$ was further enhanced at all elevations and in a wider altitude range. Notice also the slow conduction of electron heat toward increasing altitudes with time, up to 300–400 km altitude, as can be seen in Fig. 1 too. The strongest $\widetilde{T}_e$ enhancements occurred at the elevations 77.2 to 79.2°, around magnetic zenith (∼ 78°). This is also where the $\widetilde{T}_e$ enhancements extended toward the highest altitudes. Differences in the enhanced $\widetilde{T}_e$ profiles can be discerned even though the radar elevation changes by only 1.0°.

Figure 3 displays $\widetilde{T}_e$ height profiles versus time for the experiment on 24 October 2017. As for Fig. 2, the high $\widetilde{T}_e$ around 300 km in the first 5 s data dump is likely not real. In this experiment $f_0 = 6.2$ MHz, which again is approximately half way between the fourth and fifth electron gyroharmonics in the F region. The transmitted power was 734 kW and the ERP was 471 MW (LHCP). The radar was scanned in steps of 1.5° from 74.56 to 85.06°, which is a larger range of elevations than that covered by the 1.0° steps in Fig. 2. $\widetilde{T}_e$ enhancements due to the HF pumping again occurred already in the first 5 s radar data integration after pump-on and $\widetilde{T}_e$ was the highest at elevations 77.56 and 79.06°, closest to magnetic zenith (∼ 78°). The gaps in the plots are because the ionospheric conditions were not stable long enough to give sufficient data to obtain the full temporal evolution at all elevations. However, the results for $\widetilde{T}_e$ are similar to those in Fig. 2 for the experiments on 25 November 2014.

4 Electron heating model

To get information on the source that underlies the observed electron temperature enhancements, we model the electron heating rate through the fluid equations (Shoucri et al., 1984). As the measurements of the UHF incoherent scatter indicate no major pump-induced effects in $\widetilde{N}_e$ and $\widetilde{T}_i$ (Fig. 1), the fluid equations can be reduced to the electron energy equation:

$$\frac{3}{2}N_e k_B\left(\frac{\partial T_e}{\partial t} + (\boldsymbol{v}_e\cdot\hat{\boldsymbol{z}})\frac{\partial T_e}{\partial z}\right) + N_e k_B T_e \frac{\partial}{\partial z}(\boldsymbol{v}_e\cdot\hat{\boldsymbol{z}}) = \frac{\partial}{\partial z}\left(\kappa_e\frac{\partial T_e}{\partial z}\right) + Q_{HF} + Q_e - L_e, \quad (1)$$

where $T_e(z,t)$ is the modelled electron temperature, $\hat{\boldsymbol{z}}$ is the unit vector in the direction of the geomagnetic field, k_B is Boltzmann's constant, $\kappa_e(T_e,z,t)$ is the electron heat conductivity, Q_{HF} is the HF pump wave energy deposition to the electrons, $Q_e(z,t)$ is the background electron heating rate (mainly from photoelectrons), and $L_e(T_e,z,t)$ is the electron cooling rate due to elastic and inelastic collisions with ions and neutrals.

With negligible plasma drift along the geomagnetic field as measured with the UHF radar, the convective terms in Eq. (1) can be neglected, giving (Löfås et al., 2009; Gustavsson et al., 2010)

$$\frac{3}{2}N_e k_B\frac{\partial T_e}{\partial t} = \frac{\partial}{\partial z}\left(\kappa_e\frac{\partial T_e}{\partial z}\right) + Q_{HF} + Q_e - L_e. \quad (2)$$

The heating rate of the electrons due to the electromagnetic pump wave consists of two parts:

$$Q_{HF} = Q_\Omega + Q_{AA}, \quad (3)$$

where Q_Ω is the ohmic heating due to collisional damping of the pump wave and Q_{AA} is the heating due to the anomalous absorption of the wave associated with the excitation of, for example, upper hybrid turbulence and associated small-scale density striations. The ohmic heating rate is the time-averaged product of the pump electric field $\boldsymbol{E}_0$ and induced electric current $\boldsymbol{\sigma}_{ij}\boldsymbol{E}_0$, where $\boldsymbol{\sigma}_{ij}$ is the conductivity tensor: $Q_\Omega = (1/2)Re[\boldsymbol{E}_0^*\cdot(\boldsymbol{\sigma}_{ij}\boldsymbol{E}_0)]$ (Gustavsson et al., 2010). At the relatively high ERP levels used in the experiments, Q_{AA} gives the dominating contribution to Q_{HF} and may be several times larger than Q_Ω (Bryers et al., 2013).

In the present treatment we obtain a model $T_e(z,t)$ of the observed $\widetilde{T}_e(z,t)$ by integrating the electron energy Eq. (2). The electron heating rate $Q_{HF}(z,t)$ due to the HF pumping is modelled by a one-dimensional and asymmetric Gaussian along the geomagnetic field. $Q_{HF}(z,t)$ has its maximum Q_m at range z_0 and has independent upper (σ_u) and lower (σ_l)

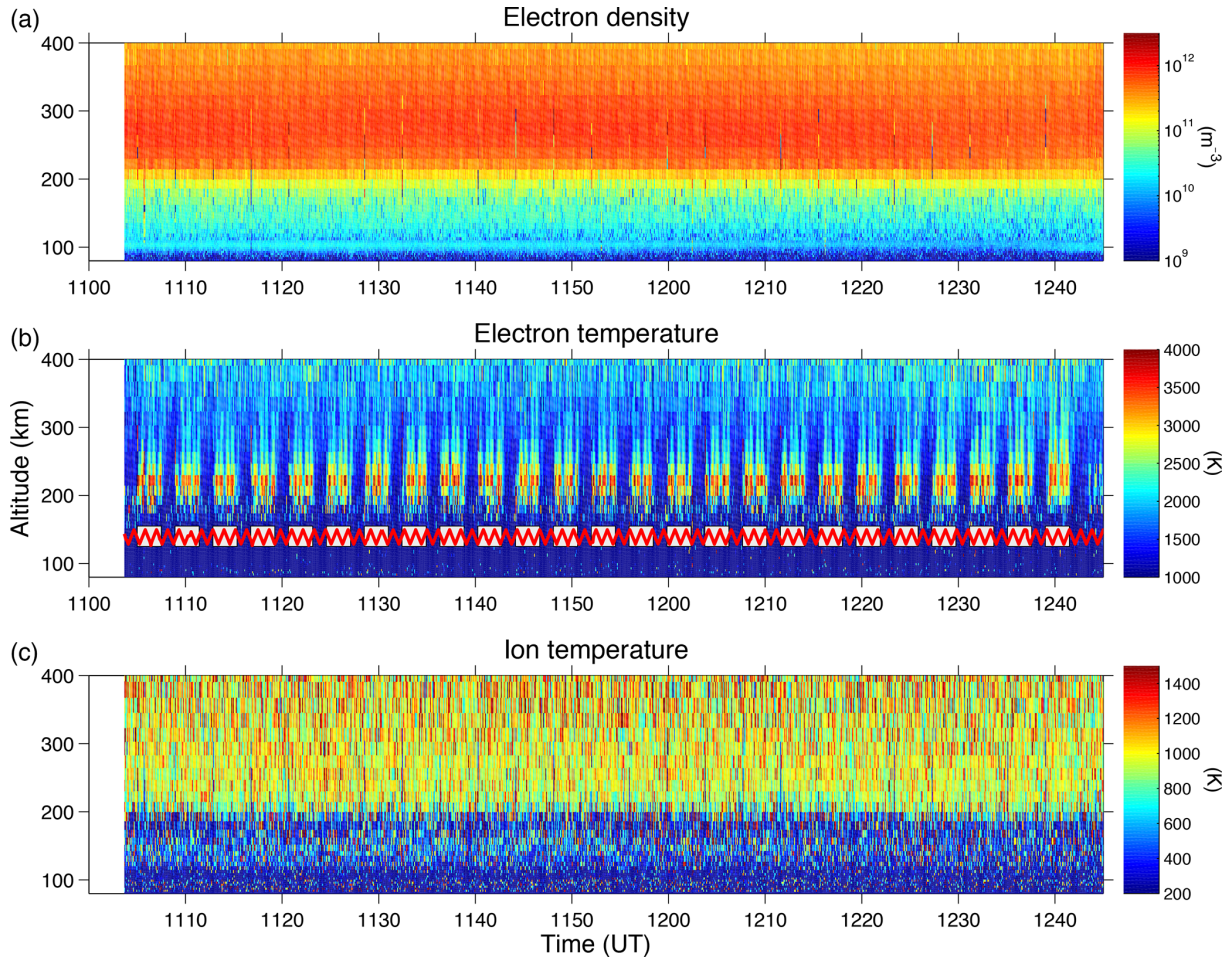

Figure 1. Height profiles as a function of time of $\widetilde{N}_e$ **(a)**, $\widetilde{T}_e$ **(b)** and $\widetilde{T}_i$ **(c)** during pump cycling on 25 November 2014. The white boxes in **(b)** show pump-on and the red zigzag line indicates the elevation of the UHF radar which was scanned between 75.2 and 82.2° in 1.0° steps.

half-widths (Senior et al., 2012; Bryers et al., 2013):

$$Q_{\mathrm{HF}}(z,t) = \begin{cases} Q_{\mathrm{m}} \exp\left[-(z-z_0)^2/\sigma_{\mathrm{l}}^2\right] \\ \times \left\{1 - \exp\left[-(t-t_{\mathrm{on}})/\tau\right]\right\}, & z < z_0, \\ Q_{\mathrm{m}} \exp\left[-(z-z_0)^2/\sigma_{\mathrm{u}}^2\right] \\ \times \left\{1 - \exp\left[-(t-t_{\mathrm{on}})/\tau\right]\right\}, & z \geq z_0, \end{cases} \tag{4}$$

where $t_{\mathrm{on}} \leq t \leq t_{\mathrm{off}}$ is the time during which HF pumping occurs. This leads to a parameter estimation problem in the model parameters Q_{m}, z_0, σ_{l}, σ_{u}, and τ that we solved by weighted nonlinear least squares:

$$\mathrm{par}_{\mathrm{HF}} = \arg\min \sum \left[\frac{\widetilde{T}_e(z,t) - T_e(z,t,\mathrm{par}_{\mathrm{HF}})}{\sigma_{\widetilde{T}_e}} \right]^2, \tag{5}$$

where $T_e(z,t,\mathrm{par}_{\mathrm{HF}})$ is obtained by integrating Eq. (2) with $Q_{\mathrm{HF}}(z,t,\mathrm{par}_{\mathrm{HF}})$ and $\sigma_{\widetilde{T}_e}$ is the standard deviation of the observed electron temperature.

When integrating Eq. (2) we used the observed range profiles for $\widetilde{T}_i$ and $\widetilde{N}_e$ as they evolve in time at each elevation. For example, L_e depends on both T_i and N_e and both the left-hand side of Eq. (2) and κ_e depend on N_e. As the initial condition we took a smoothed $\widetilde{T}_e$ range profile measured just before pump-on. Further, we used mixed boundary conditions, taking at the lower boundary $T_e = \widetilde{T}_e(z = 150\,\mathrm{km}, t)$ as given by the UHF radar measurements at $z = 150\,\mathrm{km}$ slightly before pump-on at $t = t_{\mathrm{on}}$ and at the upper boundary $\partial T_e/\partial z(z = 500\,\mathrm{km}, t) = 0$. The fixed temperature at the lower boundary follows from the observations with the additional theoretical justification that at such low altitudes T_e and T_i are both approximately equal to the neutral temperature due to the high collision frequencies. The upper boundary condition too is based on the observations and corresponds to a balance between upward heat flux out from the ionosphere and downward heat flux from the magnetosphere into the ionosphere.

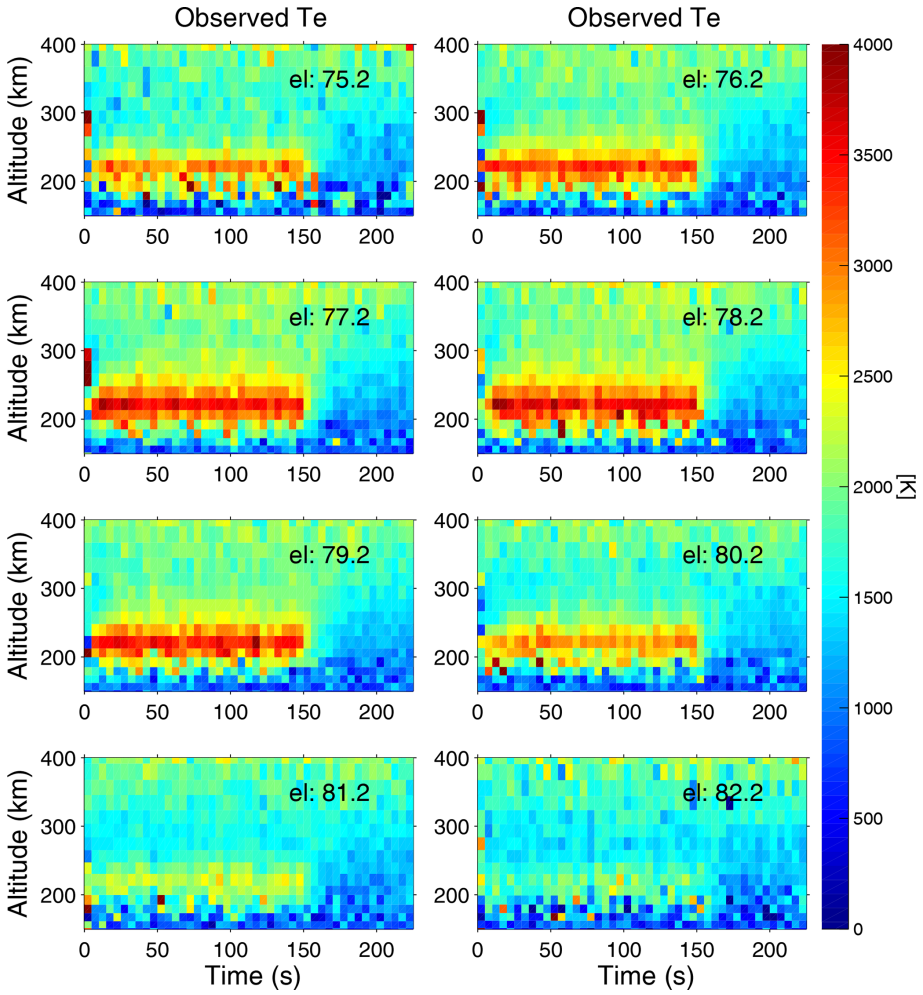

Figure 2. Height profiles of $\widetilde{T}_e$ (colour coded) versus time for the different elevation angles of the UHF radar between 75.2 and 82.2° on 25 November 2014 (11:03:45–13:00:00 UT). Pump-on was from $t = 0$ to $t = 150$ s.

5 Modelling results

The temporal evolution of the modelled T_e altitude profile for the elevation angles scanned by the radar is obtained by integrating Eq. (2) with the optimal parameters for $Q_{HF}(z,t)$. The results are shown in Figs. 4 and 5, which correspond to the measurements in Figs. 2 and 3, respectively. $T_e(z,t)$ is enhanced for all elevations already within the first seconds after pump-on at $t = 0$ s. Slow conduction of the electron heat is seen both upward and downward in altitude and $T_e(z,t)$ reaches the highest values near magnetic zenith ($\sim 78°$). The modelling results in Figs. 4 and 5 agree qualitatively with the measurements in Figs. 2 and 3, respectively.

Figure 6 displays the corresponding Q_{HF} versus elevation angle for the experiment on 25 November 2014 (Fig. 2) in panels (a) and (b) and for 24 October 2017 (Fig. 3) in panels (c) and (d). Figure 6a and c show the column-integrated Q_{HF} (blue) as well as the profile of the transmitted Heating beam (red) and Fig. 6b and d depict the altitude profiles of Q_{HF}. These modelling results are for the case after that steady state was reached in the 150 s pump-on period. The white and black lines in Fig. 6b and d show the altitudes of the plasma and upper hybrid resonances, respectively, as obtained from the ion and plasma lines. The altitude separation between the two resonances is larger in Fig. 6d for which f_0 was near $foF2$ than in Fig. 6b for which f_0 was well below $foF2$.

The column-integrated Q_{HF} in Fig. 6a is maximum at 78.2° and in Fig. 6c at 77.5°, which are the same elevations at which the observed electron temperature reached the highest values (Figs. 2 and 3, respectively). Also, the column-integrated Q_{HF} is maximum at the elevation closest to magnetic zenith ($\sim 78°$, labelled by MZ in the plots).

Further, as seen in Fig. 6a and c, the angular extent of the Q_{HF} profile is smaller than that of the Heating beam. Q_{HF} follows the profile of the Heating beam at elevations lower than magnetic zenith ($\sim 78°$), while at higher elevations it is more confined to magnetic zenith than the Heating beam. For

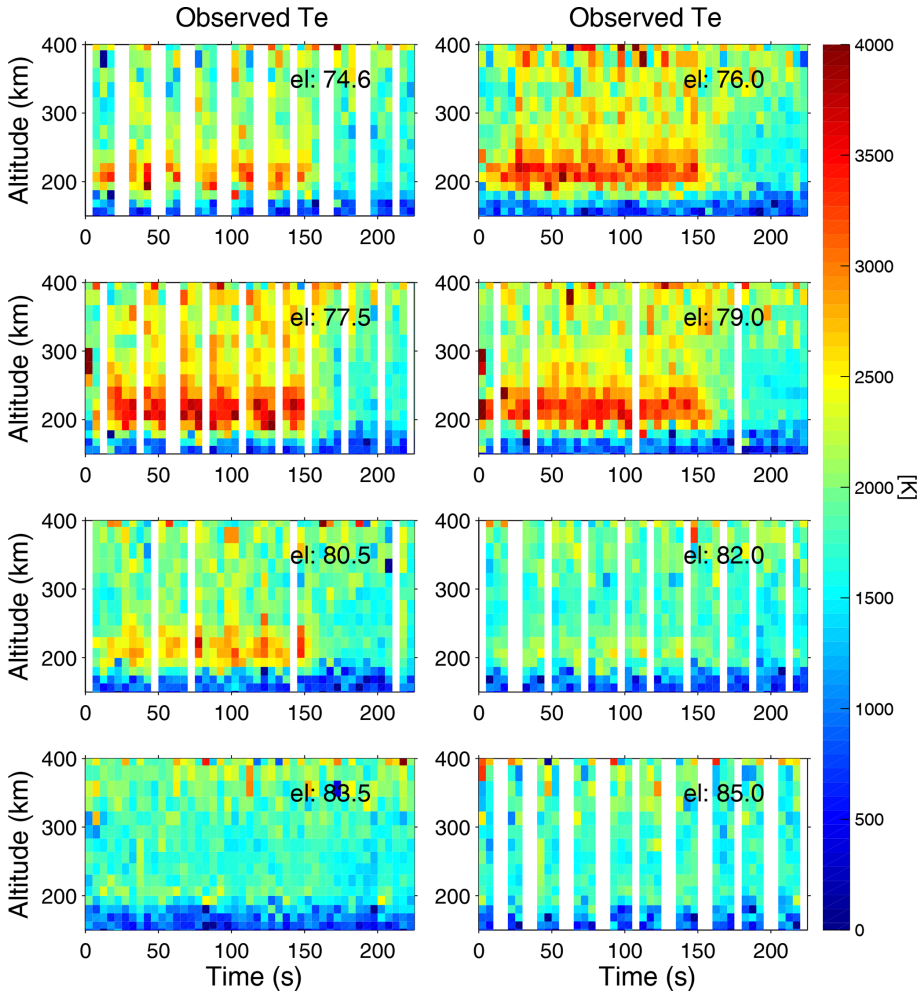

Figure 3. Height profiles of $\widetilde{T}_e$ (colour coded) versus time for the different elevation angles of the UHF radar between 74.56 and 85.06° on 24 October 2017 (12:00:00–12:43:00 UT). Pump-on was from $t = 0$ to $t = 150$ s.

reference, the Spitze angle is about 6° from the vertical or at about 84° elevation.

As seen in Fig. 6b and d, the altitude profile of Q_{HF} is generally asymmetric, with Q_{HF} decreasing steeply with increasing altitude above the maximum and declining more gradually with decreasing altitude below the maximum. Only in Fig. 6d for 77.5° (at magnetic zenith) does Q_{HF} decrease more slowly toward high altitudes than toward lower altitudes. Also, Q_{HF} decreases steeply for increasing elevations beyond about 80°, towards the vertical. This decrease in Q_{HF} with increasing elevation is steeper than what would be expected from the point view of the width of the Heating beam in vacuum (see Fig. 6a and c).

It is notable that Q_{HF} reaches larger values at the two elevations next to magnetic zenith compared to at the elevation nearest to magnetic zenith. In Fig. 6b, Q_{HF} is slightly higher at 77.2 and 79.2° than at 78.2°, while the Q_{HF} profile is more extended in altitude at 78.2°. Figure 6d shows larger differences, with Q_{HF} higher at 76.0 and 79.0° than at 77.5°, while the Q_{HF} profile is more extended in altitude at 77.5°. Thus, despite the maximum of the Q_{HF} profile being slightly lower at magnetic zenith compared to at the two nearest neighbouring elevations, the column-integrated Q_{HF} is maximum at magnetic zenith (Fig. 6a and c) for both experiments.

6 Discussion

We have presented experimental and modelling results concerning electron heating and the ionospheric plasma response to HF pumping near magnetic zenith. The experiments were performed with the EISCAT Heating facility and measurements of the plasma response were done with the EISCAT UHF incoherent scatter radar. The Heating beam was tilted in the magnetic zenith direction and the UHF radar was scanned between eight positions around this direction to study the electron-heating efficiency. The electron heating rate $Q_{HF}(z,t)$ and associated electron temperature $T_e(z,t)$ due to the HF pumping were modelled by integrating the en-

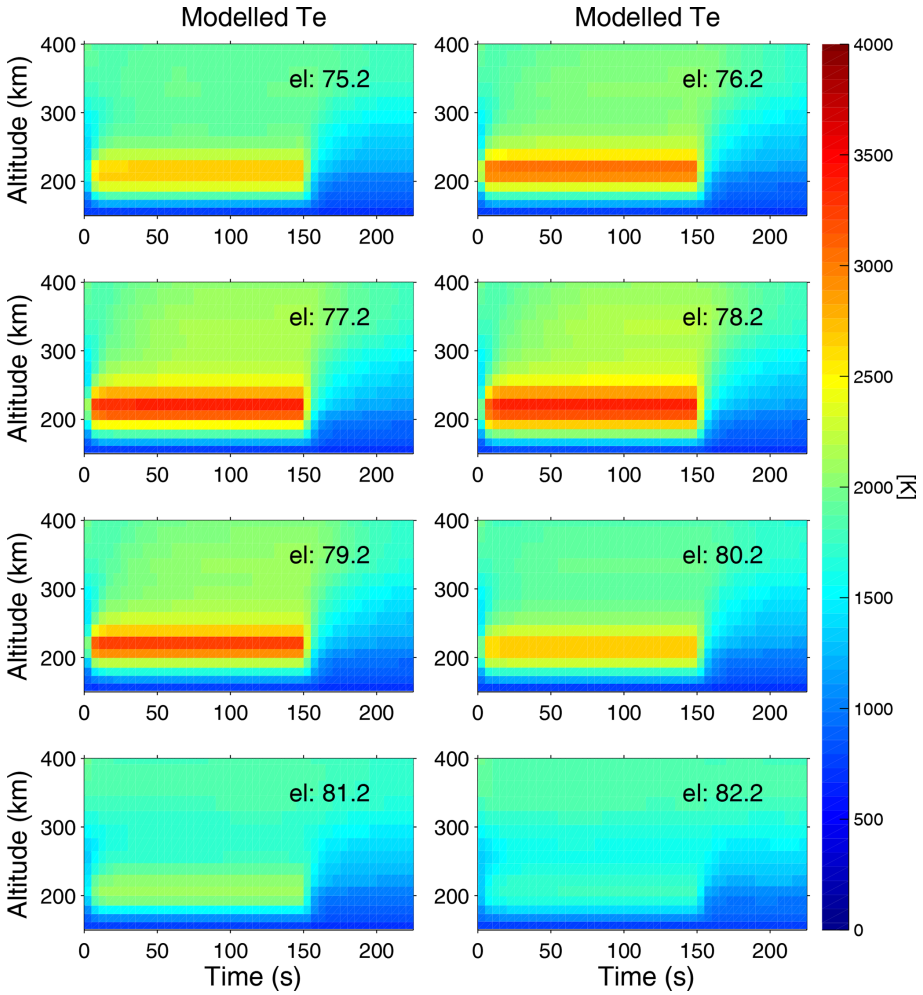

Figure 4. Modelled temporal evolution of the altitude profile of the electron temperature $T_e(z,t)$ for the different elevation angles in the experiments on 25 November 2014 (Fig. 2).

ergy Eq. (2) and fitting the model parameters with respect to the measurements of $\widetilde{N}_e$, $\widetilde{T}_e$ and $\widetilde{T}_i$.

Differences in the plasma response were observed for radar elevations differing by only 1° (Fig. 2). The pump-induced measured $\widetilde{T}_e(z,t)$ enhancements (Figs. 2 and 3), the modelled $T_e(z,t)$ (Figs. 4 and 5) and the associated column-integrated Q_{HF} (Fig. 6) were all found to maximize in the magnetic zenith direction ($\sim 78°$ elevation). Further, the angular width of the Q_{HF} profile, with a full width at half maximum (FWHM) of about 4° around magnetic zenith, was less than that of the HF beam, which suggests that some focusing of the Heating beam occurred.

Pedersen et al. (2008) obtained the angular distribution of the optical emission production efficiency by HF beam-swinging experiments at HAARP. The optical emission production efficiency peaked at magnetic zenith with a FWHM of 7°, for which the HAARP beam width and many other experiment variables were accounted. This FWHM of 7° is larger than the two cases for Q_{HF} in Fig. 6. The HAARP experiments used an ERP of 32.1 MW at 2.83 MHz and 42.4 MW at 3.3 MHz, thus, both lower ERP and lower f_0 than in the present EISCAT experiments. It is plausible that self-focusing effects were larger at the higher ERP in the present experiments, which could give a narrower region of pump-induced enhancements.

It has been proposed that filamentary plasma density ducts can guide a transmitted LHCP wave, entering the ionosphere in the O mode, as an L-mode wave along the geomagnetic field (Leyser and Nordblad, 2009; Nordblad and Leyser, 2010). The L mode is an LHCP electromagnetic wave mode with the wave vector parallel or anti-parallel to the ambient magnetic field. For a homogeneous and cold magnetized plasma the refractive index ($n_\parallel$) parallel to the ambient magnetic field is given by $n_\parallel^2 = 1 - f_p^2/f(f+f_e)$, where f_p is the electron plasma frequency and f_e is the electron gyrofrequency. Whereas the O mode has a cutoff at $f_p = f_0$, the L mode has the cutoff frequency $f_L = -f_e/2 + (f_p^2 + f_e^2/4)^{1/2}$, which corresponds to $f_p \approx f_0 + f_e/2$ for $f_p^2 \gg f_e^2$

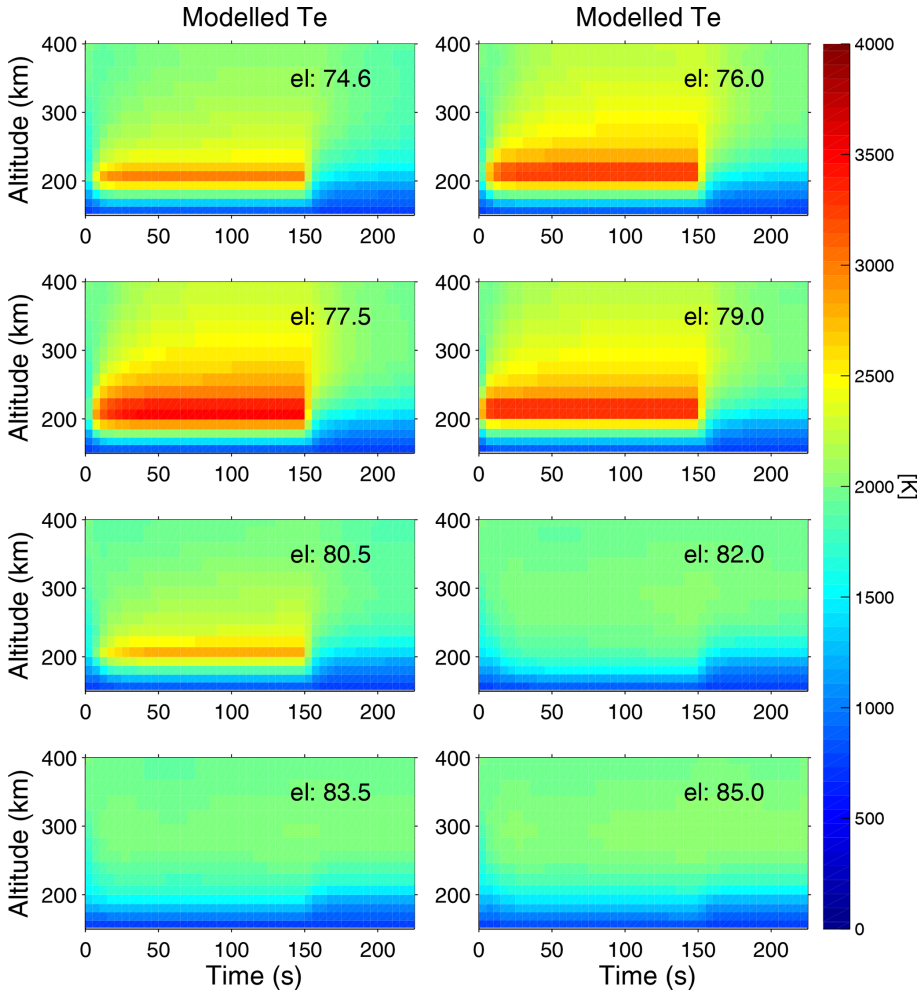

Figure 5. Modelled temporal evolution of the altitude profile of the electron temperature $T_e(z,t)$ for the different elevation angles in the experiments on 24 October 2017 (Fig. 3).

for a pump wave at frequency $f = f_0$. Thus, an electromagnetic wave in the L mode can propagate at higher plasma densities than in the O mode.

L-mode propagation can occur when the background plasma density gradient near the plasma resonance is parallel to the geomagnetic field, instead of the density gradient for example being vertical as in a horizontally stratified ionosphere. Such a condition with the density gradient being magnetic field-aligned can occur in density ducts, either natural or pump-induced. In the L mode the pump wave can propagate upwards, passing through the plasma resonance on its way to the cutoff at $f_p \approx f_0 + f_e/2$ if the plasma is sufficiently dense. With its perpendicular electric field, strong pumping of upper hybrid phenomena localized in small-scale density striations and related anomalous electron heating can occur at higher altitudes and deeper into the plasma compared to the case of an O-mode wave which therefore could contribute to the strong plasma response observed in magnetic zenith (Leyser and Nordblad, 2009; Nordblad and Leyser, 2010).

The HF pump-induced electron heating rate Q_{HF} obtained for our experiments exhibited an interesting dependence on the elevation angle near magnetic zenith (Fig. 6). Q_{HF} is maximum at the elevations next to magnetic zenith. At magnetic zenith, the Q_{HF} profile is more extended in altitude, such that the column-integrated Q_{HF} is maximum in this direction. These results are consistent with the pump wave propagating in the L mode in magnetic zenith and in the O mode at angles deviating from the zenith direction. As a wave in the L mode propagates to higher altitudes than in the O mode, electron heating can occur in a more extended altitude range for L-mode propagation, thereby giving maximum column-integrated electron heating in magnetic zenith. The large difference in the Q_{HF} profile between magnetic zenith and the adjacent elevations is consistent with that the pump wave in the O mode has a much lower reflection height than in the L mode; the O-mode reflection height

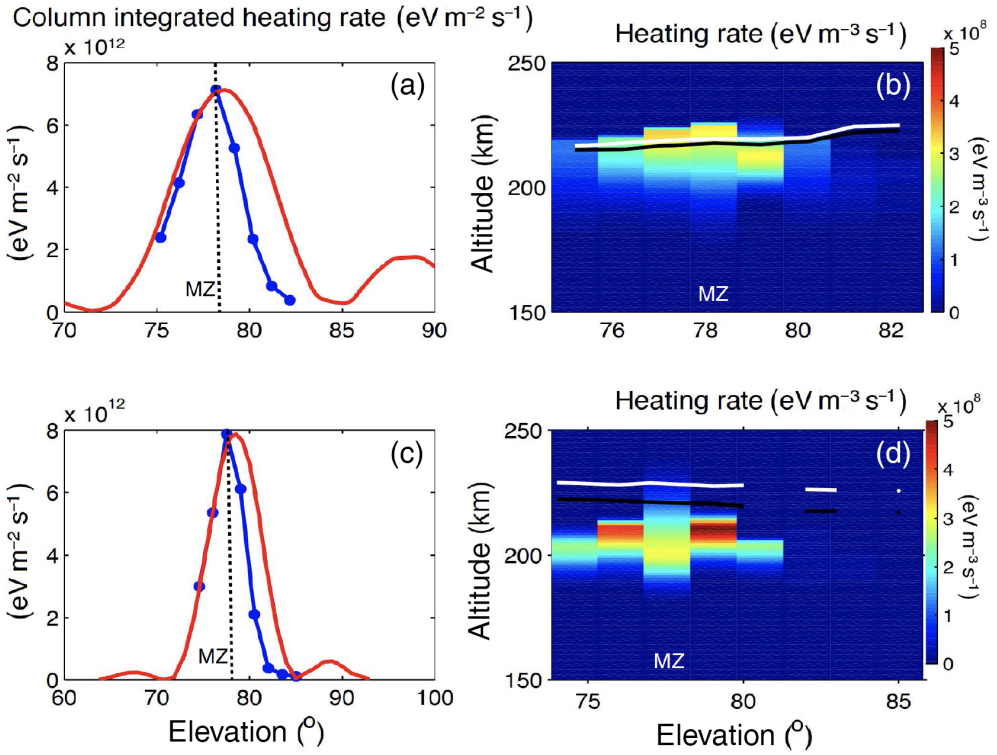

Figure 6. Modelled electron heating rate Q_{HF} (eV m^{-3} s^{-1}) during steady state versus radar elevation angle for 25 November 2014 **(a, b)** and 24 October 2017 **(c, d)**. Panels **a** and **c** display the column-integrated Q_{HF} (blue dots, with connecting lines to guide the eye) and the relative intensity of the transmitted Heating beam (red) assumed to propagate in vacuum. The elevation corresponding to magnetic zenith is indicated by the dashed line and labelled MZ. Panels **b** and **d** show the altitude profiles of Q_{HF}. The white line indicates the altitude of the plasma resonance where $f_{\mathrm{p}} = f_0$ and the black line shows the upper hybrid resonance height at which the upper hybrid frequency equals f_0. Note that the elevation scale is different in panels **a** and **b** and **c** and **d**.

is well below the plasma resonance for elevations near magnetic zenith. In magnetic zenith the pump wave is guided by magnetic field-aligned density ducts in the L mode, but at the adjacent elevations the pump wave makes too large an angle to the magnetic field for trapping of the HF wave in the duct, and thus guiding, to occur so that instead the pump wave propagates in the O mode.

Evidence of L-mode propagation of the EISCAT Heating beam has previously been obtained as transionospheric propagation for $f_0 < foF2 < f_0 + f_{\mathrm{e}}/2$, in which case an L-mode wave would not be reflected but pass through the ionospheric plasma density peak. This was observed by direct measurement on the CASSIOPE spacecraft (Leyser et al., 2018) and indirectly by EISCAT UHF radar observations of ion acoustic lines in the topside ionosphere (Rexer et al., 2018).

Figure 6 also displays the altitude of the plasma resonance (white lines in Fig. 6b and d). The position of the Q_{HF} profile relative to the plasma resonance is not fully understood. In Fig. 6b, Q_{HF} is maximum slightly above the plasma resonance at magnetic zenith. This is consistent with a pump wave in the L mode being able to propagate well above the plasma resonance, whereas an O-mode wave cannot. Further, an L-mode wave has its electric field perpendicular to the geomagnetic field all the way up to its reflection height, so that pumping of upper hybrid turbulence can occur in an extended altitude range. In the O mode, on the other hand, the electric field turns to parallel to the geomagnetic field close to the reflection height, which favours excitation of Langmuir turbulence that generally causes less electron heating than upper hybrid turbulence.

However, in Fig. 6d all electron heating appears to occur well below even the upper hybrid resonance height (black line). In this case $foF2$ was near f_0, whereas for Fig. 6b it was well above f_0, which is consistent with that the altitude separation between the plasma and upper hybrid resonances is larger in Fig. 6d. We do not have any explanation for why electron heating seemed to occur at such low altitudes in this case.

Gurevich et al. (2002) developed a theory for self-focusing of the electromagnetic pump wave propagating in the O mode on geomagnetic field-aligned density striations. An important mechanism in the nonlinear pump beam self-focusing is the trapping of pump rays near the magnetic zenith direction in the large-scale density depletions within the beam, as previously was found in numerical studies (Gurevich et al.,

1999). The results were shown to be consistent with observations of pump-induced optical emissions at HAARP (Pedersen et al., 2003). However, the possibility of propagation of the pump wave in the L mode, deeper into the plasma than what is possible in the O mode, was not considered. Whereas the nonlinear self-focusing of the pump beam is an important mechanism, particularly for guiding the pump beam in magnetic zenith, it does as it stands not seem to account for the difference that we have found in the altitude distribution of the electron heating rate in magnetic zenith compared to that just about 1° away from this direction (Fig. 6). We therefore suggest that such theories for self-focusing are developed to include the possibility of L-mode propagation.

7 Conclusions

The EISCAT Heating facility was used to pump ionospheric F-region plasma by cycling 150 s on–85 s off with an LHCP HF beam directed in magnetic zenith. Plasma parameter values were measured with the EISCAT UHF incoherent scatter radar that was scanned in steps of 1.0° (November 2014) and 1.5° (October 2017) in elevation around magnetic zenith. The temporal evolution of the electron temperature profile was modelled by integrating the electron energy equation, which was used to fit the measured plasma parameter values with a model electron heating rate.

The observed electron temperature enhancements and the associated column-integrated electron heating rate and modelled electron temperature all exhibit maxima in magnetic zenith. In addition, the altitude range of electron heating is more extended in magnetic zenith than for elevations deviating from the zenith direction. These results are consistent with pump wave propagation in the L mode rather than purely O mode and suggest the importance of L-mode propagation for understanding magnetic zenith effects.

Data availability. Access to the raw data may be provided upon reasonable request to the authors.

Author contributions. BG, TBL and MTR performed the experiments. BG developed the theoretical model and performed the numerical analysis. TR contributed to the data analysis and data presentation. TBL carried out most of the interpretation and prepared the paper. All the co-authors helped in the interpretation of the results, read the paper and commented on it.

Competing interests. The authors declare that they have no conflict of interest.

Acknowledgements. EISCAT is an international association supported by research organizations in China (CRIRP), Finland (SA), Japan (NIPR and ISEE), Norway (NFR), Sweden (VR), and the United Kingdom (UKRI).

Review statement. This paper was edited by Nick Sergis and reviewed by two anonymous referees.

References

Blagoveshchenskaya, N. F., Borisova, T., Kornienko, V., Leyser, T., Rietveld, M., and Thidé, B.: Artificial field-aligned irregularities in the nightside auroral ionosphere, Adv. Space Res., 38, 2503–2510, https://doi.org/10.1016/j.asr.2004.12.008, 2006.

Brändström, B. U. E., Leyser, T. B., Steen, Å., Rietveld, M. T., Gustavsson, B., Aso, T., and Ejiri, M.: Unambiguous evidence of HF pump-enhanced airglow at auroral latitudes, Geophys. Res. Lett., 26, 3561–3564, 1999.

Bryers, C. J., Kosch, M. J., Senior, A., Rietveld, M. T., and Singer, W.: A comparison between resonant and nonresonant heating at EISCAT, J. Geophys. Res., 118, 6766–6776, https://doi.org/10.1002/jgra.50605, 2013.

Grach, S. M., Kosch, M. J., Yashnov, V. A., Sergeev, E. N., Atroshenko, M. A., and Kotov, P. V.: On the location and structure of the artificial 630-nm airglow patch over Sura facility, Ann. Geophys., 25, 689–700, https://doi.org/10.5194/angeo-25-689-2007, 2007.

Gurevich, A., Carlson, H., Kelley, M., Hagfors, T., Karashtin, A., and Zybin, K.: Nonlinear structuring of the ionosphere modified by powerful radio waves at low latitudes, Phys. Lett. A, 251, 311–321, 1999.

Gurevich, A., Zybin, K., Carlson, H., and Pedersen, T.: Magnetic zenith effect in ionospheric modifications, Phys. Lett. A, 305, 264–274, https://doi.org/10.1016/S0375-9601(02)01450-0, 2002.

Gustavsson, B., Sergienko, T., Rietveld, M. T., Honary, F., Steen, Å., Brändström, B. U. E., Leyser, T. B., Aruliа, A., Aso, T., and Ejiri, M.: First tomographic estimate of volume distribution of enhanced airglow emission caused by HF pumping, J. Geophys. Res., 106, 29105–29123, https://doi.org/10.1029/2000JA900167, 2001.

Gustavsson, B., Rietveld, M. T., Ivchenko, N. V., and Kosch, M. J.: Rise and fall of electron temperatures: Ohmic heating of ionospheric electrons from underdense HF radio wave pumping, J. Geophys. Res., 115, A12332, https://doi.org/10.1029/2010JA015873, 2010.

Honary, F., Borisov, N., Beharrell, M., and Senior, A.: Temporal development of the magnetic zenith effect, J. Geophys. Res., 116, A06309, https://doi.org/10.1029/2010JA016029, 2011.

Kosch, M. J., Rietveld, M. T., Hagfors, T., and Leyser, T. B.: High-latitude HF-induced airglow displaced equatorwards of the pump beam, Geophys. Res. Lett., 27, 2817–2820, https://doi.org/10.1029/2000GL003754, 2000.

Kosch, M. J., Pedersen, T., Mishin, E., Starks, M., Gerken-Kendall, E., Sentman, D., Oyama, S., and Watkins, B.: Temporal evolution of pump beam self-focusing at the High-Frequency Active Auroral Research Program, J. Geophys. Res., 112, A08304, https://doi.org/10.1029/2007JA012264, 2007.

Leyser, T. B. and Nordblad, E.: Self-focused radio frequency *L* wave pumping of localized upper hybrid oscillations in high-latitude ionospheric plasma, Geophys. Res. Lett., 36, L24105, https://doi.org/10.1029/2009GL041438, 2009.

Leyser, T. B., James, H. G., Gustavsson, B., and Rietveld, M. T.: Evidence of *L*-mode electromagnetic wave pumping of ionospheric plasma near geomagnetic zenith, Ann. Geophys., 36, 243–251, https://doi.org/10.5194/angeo-36-243-2018, 2018.

Löfås, H., Ivchenko, N., Gustavsson, B., Leyser, T. B., and Rietveld, M. T.: F-region electron heating by *X*-mode radiowaves in underdense conditions, Ann. Geophys., 27, 2585–2592, https://doi.org/10.5194/angeo-27-2585-2009, 2009.

Nordblad, E. and Leyser, T. B.: Ray tracing analysis of *L* mode pumping of the ionosphere, with implications for the magnetic zenith effect, Ann. Geophys., 28, 1749–1759, https://doi.org/10.5194/angeo-28-1749-2010, 2010.

Pedersen, T., Esposito, R., Starks, M., and McCarrick, M.: Quantitative determination of HF radio-induced optical emission production efficiency at high latitudes, J. Geophys. Res., 113, A11316, https://doi.org/10.1029/2008JA013502, 2008.

Pedersen, T. R. and Carlson, H. C.: First observations of HF heater-produced airglow at the High Frequency Active Auroral Research Program facility: Thermal excitation and spatial structuring, Radio Sci., 36, 1013–1026, https://doi.org/10.1029/2000RS002399, 2001.

Pedersen, T. R., McCarrick, M., Gerken, E., Selcher, C., Sentman, D., Carlson, H. C., and Gurevich, A.: Magnetic zenith enhancement of HF radio-induced airglow production at HAARP, Geophys. Res. Lett., 30, 1169, https://doi.org/10.1029/2002GL016096, 2003.

Rexer, T., Gustavsson, B., Leyser, T., Rietveld, M., Yeoman, T., and Grydeland, T.: First Observations of Recurring HF-Enhanced Topside Ion Line Spectra Near the Fourth Gyroharmonic, J. Geophys. Res.-Space, 123, 8649–8663, https://doi.org/10.1029/2018JA025822, 2018.

Rietveld, M. T., Kosch, M. J., Blagoveshchenskaya, N. F., Kornienko, V. A., Leyser, T. B., and Yeoman, T. K.: Ionospheric electron heating, optical emissions, and striations induced by powerful HF radio waves at high latitudes: Aspect angle dependence, J. Geophys. Res., 108, 1141, https://doi.org/10.1029/2002JA009543, 2003.

Rietveld, M. T., Senior, A., Markkanen, J., and Westman, A.: New capabilities of the upgraded EISCAT high-power HF facility, Radio Sci., 51, 1533–1546, https://doi.org/10.1002/2016RS006093,2016.

Senior, A., Rietveld, M. T., Yeoman, T. K., and Kosch, M. J.: The dependence of F-region electron heating on HF radio pump power: Measurements at EISCAT Tromsø, J. Geophys. Res.-Space, 117, A04309, https://doi.org/10.1029/2011JA017267, 2012.

Shoucri, M. M., Morales, G. J., and Maggs, J. E.: Ohmic heating of the polar F region by HF pulses, J. Geophys. Res., 89, 2907–2917, https://doi.org/10.1029/JA089iA05p02907, 1984.

Tereshchenko, E. D., Khudukon, B. Z., Gurevich, A. V., Zybin, K. P., Frolov, V. L., Myasnikov, E. N., Muravieva, N. V., and Carlson, H. C.: Radio tomography and scintillation studies of ionospheric electron density modification caused by a powerful HF-wave and magnetic zenith effect at mid-latitudes, Phys. Lett. A, 325, 381–388, https://doi.org/10.1016/j.physleta.2004.03.055, 2004.